UNIVERSITY OF
BIRMINGHAM

Synthesis and Characterisation of Chemically Modified Schafarzikite and Pyrochlore Minerals

by

Mariana J. Whitaker

Supervisor: Professor Colin Greaves

A thesis submitted to the
University of Birmingham
for the degree of
Doctor of Philosophy

The School of Chemistry
College of Engineering and Physical Sciences
University of Birmingham
December 2012

UNIVERSITY OF
BIRMINGHAM

Synthesis and Characterisation of Chemically Modified Schafarzikite and Pyrochlore Minerals

by

Mariana J. Whitaker

Supervisor: Professor Colin Greaves

A thesis submitted to the
University of Birmingham
for the degree of
Doctor of Philosophy

The School of Chemistry
College of Engineering and Physical Sciences
University of Birmingham
December 2012

Abstract

Schafarzikite, $FeSb_2O_4$, is a tetragonal mineral (space group $P4_2/mbc$) belonging to a family of compounds with the general formula MX_2O_4. Schafarzikite has successfully been synthesised and chemically modified in various different ways. Lead has been substituted onto the pyramidal X sites to form compounds of formulation $FeSb_{2-x}Pb_xO_4$ (x = 0.2-0.75), excess oxygen ions have been incorporated into the structure to form $FeSb_{2-x}Pb_xO_{4+y}$ and compounds with mixed octahedral M ions, $Fe_{1-x}Mg_xSb_2O_4$, have been prepared. The modifications give rise to changes in the magnetic ordering and magnetic structures and the conductivity of $FeSb_{2-x}Pb_xO_4$ is increased with respect to that of schafarzikite.

Pyrochlores (space group Fd-3m) have the general formula $A_2B_2O_7$. The structures of $Bi_{2-x}Fe_x(FeSb)O_7$ (x = 0.1, 0.2, 0.3) and $Nd_{1.8}Fe_{0.2}(FeSb)O_7$ have been studied and found to undergo static displacive disorder in the A_2O' chains. Pyrochlore materials are magnetically frustrated and the samples $Bi_{2-x}Fe_x(FeSb)O_7$ (x = 0.1, 0.2, 0.3) display spin-glass behaviour. The magnetic properties of RE_2CrSbO_7 pyrochlores have also been investigated because, despite the inherent magnetic frustration in the pyrochlore structure, Ho_2CrSbO_7 is known to order magnetically at 10 K. Neutron diffraction showed that the Ho^{3+} moments form an ordered spin-ice arrangement while the Cr^{3+} moments order ferromagnetically.

Acknowledgements

Firstly I would like to thank my supervisor, Professor Colin Greaves, for all his help and support throughout my PhD. I would like to thank him for giving me such an interesting project but also for making my PhD so enjoyable by being kind, friendly and always willing to help.

I would also like to thank Professor Frank Berry, not only for his help with Mössbauer spectroscopy, but also for his support and enthusiasm throughout the project.

I would also like to express my gratitude to all the members of the Greaves group. We have had many interesting discussions and I feel very lucky to have gone through my PhD with such a friendly and welcoming group.

Many thanks go to all the staff and students on Floor 5 because, as well as always helping me with work and equipment, they have made the 5th floor a social and enjoyable place to work. I have made some great friends here and I would like to thank them for making my experience in Birmingham such a happy one.

Thanks also go to Michael Parkes and the people in Physics for help with the MPMS and to Emma Suard at the ILL and Vladimir Pomjakushin at the PSI for their help with the neutron diffraction facilities. I am also grateful to Advantage West Midlands and the European Regional Development Fund for equipment and to the EPSRC and the University of Birmingham for funding.

Finally I would like to thank the people closest to me including my parents, my sister and my friends for their constant encouragement and for always being there to listen, to help and to support me.

Table of Contents

1 Introduction 1

1.1 Functional Metal Oxides 1

1.1.1 Effects of Cation Substitution in Metal Oxides 1

1.2 Structure Types 2

1.2.1 Schafarzikite 2

1.2.1.1 Orthorhombic Distortion in Pb_3O_4 4

1.2.2 Pyrochlore 5

1.3 Charge Ordering and the Verwey Transition 7

1.4 One Dimensional Metals 10

1.5 Magnetic Interactions 10

1.5.1 Superexchange 14

1.5.2 Magnetic Properties of MX_2O_4 17

1.5.3 Magnetic Properties of Pyrochlores 21

1.6 Project Aims 23

1.7 References 25

2 Experimental Techniques 28

2.1 Synthesis Methods 28

2.1.1 Solid State Synthesis 28

2.2 X-ray Diffraction 28

2.3 Neutron Diffraction 31

2.4 Rietveld Refinement 35

2.5 SQUID Magnetometry 37

2.6 Mössbauer Spectroscopy 38

2.7 Thermogravimetric Analysis 40

2.8 AC Impedance 41

2.9 Scanning Electron Microscopy 41

2.10 Raman Spectroscopy 42

2.11 References 44

3 Lead-Substituted Schafarzikites, $FeSb_{2-x}Pb_xO_4$ 45

3.1 Background 45

3.1.1 Cation Substitution in the Schafarzikite Structure 45

3.2 Synthesis 46

3.3 Results and Discussion 47

3.3.1 Sample Preparation and Structural Characterisation 47

3.3.2 Magnetic Properties 55

3.3.3 Electronic Conductivity 72

3.4 Conclusions 75

3.5 References 76

4 Oxygen Insertion in $FeSb_{2-x}Pb_xO_4$ 77

4.1 Background 77

4.2 Synthesis 80

4.3 Results and Discussion 81

4.3.1 Sample Preparation and Structural Characterisation 81

4.3.2 Magnetic Properties 94

4.4 Conclusions 101

4.5 References 102

5 Mixed Magnesium Iron Schafarzikites, $Fe_{1-x}Mg_xSb_2O_4$ 103

5.1 Background 103

5.2 Synthesis 104

5.3 Results and Discussion 105

5.3.1 Structural Characterisation 105

5.3.2 Scanning Electron Microscopy (SEM) Study 110

5.3.3 Oxygen Insertion 114

5.3.4 Magnetic Properties 122

5.4 Conclusions 125

5.5 References 126

6 Displacements and Disorder in $A_{1-x}Fe_x(FeSb)O_7$ Pyrochlores 127

6.1 Background 127

6.1.1 Static Displacive Disorder 127

6.2 Synthesis 129

6.3 Results and Discussion 130

6.3.1 Sample Preparation and Structural Characterisation 130

6.3.2 Magnetic Properties 140

6.4 Conclusions 145

6.5 References 146

7 Magnetic Properties of RE_2CrSbO_7 Pyrochlores 147

7.1 Background 147

7.2 Synthesis 150

7.3 Results and Discussion 151

7.3.1 Sample Preparation 151

7.3.2 Structural Characterisation 154

7.3.3 Magnetic Properties 158

7.4 Conclusions 170

7.5 References 171

8 Conclusions and Further Work 172

8.1 Conclusions 172

8.2 Further Work 174

8.3 References 177

List of Publications Arising from this Thesis 178

1 Introduction

1.1 Functional Metal Oxides

Functional materials, in contrast to structural materials, are those with inherent physical properties that allow them to perform specific, useful functions other than bearing a load. This includes electrical, magnetic, thermal and optical properties and these materials are therefore widely used for many different applications. Some examples of functional materials are ionic conductors used for batteries and fuel cells, thermoelectrics used for power generation, phosphors used in lighting and semiconductors used in many electronic devices. A large class of functional materials is the mixed metal oxides and due to the range of important applications that functional metal oxides are used for, there is much ongoing research to enhance these materials, to develop new, interesting materials and to understand better the relationship between structure and properties.

1.1.1 Effects of Cation Substitution in Metal Oxides

One of the most well-studied and technologically-important structure types is the perovskite ABO_3 structure. Perovskites and perovskite-related materials exhibit many interesting and useful properties and some well known examples include the ferroelectric material $BaTiO_3$, the high-temperature ceramic superconductors, such as $YBa_2Cu_3O_7$, and the colossal-magnetoresistive (CMR) manganese-based materials. The perovskite structure consists of corner-linked BO_6 octahedra and 12-coordinate A cations, and substituting cations onto the A sites allows control over the oxidation state of the B-site cations which can drastically affect the physical properties of the materials. Examples of perovskite materials are $LaMnO_3$, which contains only Mn^{3+}, and $CaMnO_3$, which contains only Mn^{4+}. These materials are both antiferromagnetic insulators but the mixed Mn^{3+}/Mn^{4+} compound $La_{1-x}Ca_xMnO_3$ is ferromagnetic and displays CMR behaviour. This

demonstrates the effect that cation substitution can have on a material by allowing control over the oxidation states and fine tuning of the properties. This method allows many interesting new materials with varying properties to be prepared.

1.2 Structure Types

In this work two interesting structure types derived from naturally-occurring mixed-metal oxide minerals are studied: the schafarzikite, MX_2O_4, structure and the pyrochlore, $A_2B_2O_7$, structure.

1.2.1 Schafarzikite

Schafarzikite, $FeSb_2O_4$, is a tetragonal mineral with space group $P4_2/mbc$ (no. 135) and unit cell parameters a = 8.59 Å and c = 5.91 Å[1]. Schafarzikite belongs to a family of compounds isostructural with red lead, Pb_3O_4, which have the general formula MX_2O_4 where M = Pb^{4+}, Sn^{4+} and X = Pb^{2+} or M = Mn^{2+}, Fe^{2+}, Co^{2+}, Ni^{2+}, Cu^{2+}, Zn^{2+}, Mg^{2+} and X = Sb^{3+}, As^{3+}.[2-4] The structure consists of rutile-type chains of edge-sharing MO_6 octahedra along the c-axis which are separated and linked by trigonal-pyramidal Sb^{3+} cations (Fig. 1.1). The Sb^{3+} cations bond to three oxygen ions and have lone pairs of electrons which point out into the channels between the octahedral chains. The atomic positions for the general MX_2O_4 schafarzikite structure in $P4_2/mbc$ are given in Table 1.1.

***Table 1.1**: Atomic positions for MX_2O_4 in $P4_2/mbc$*

	Wyckoff Position	*x*	*y*	*z*
Fe1	4*d*	0	½	¼
Sb1	8*h*	*x*	*y*	0
O1	8*g*	*x*	*x* + ½	¼
O2	8*h*	*x*	*y*	0

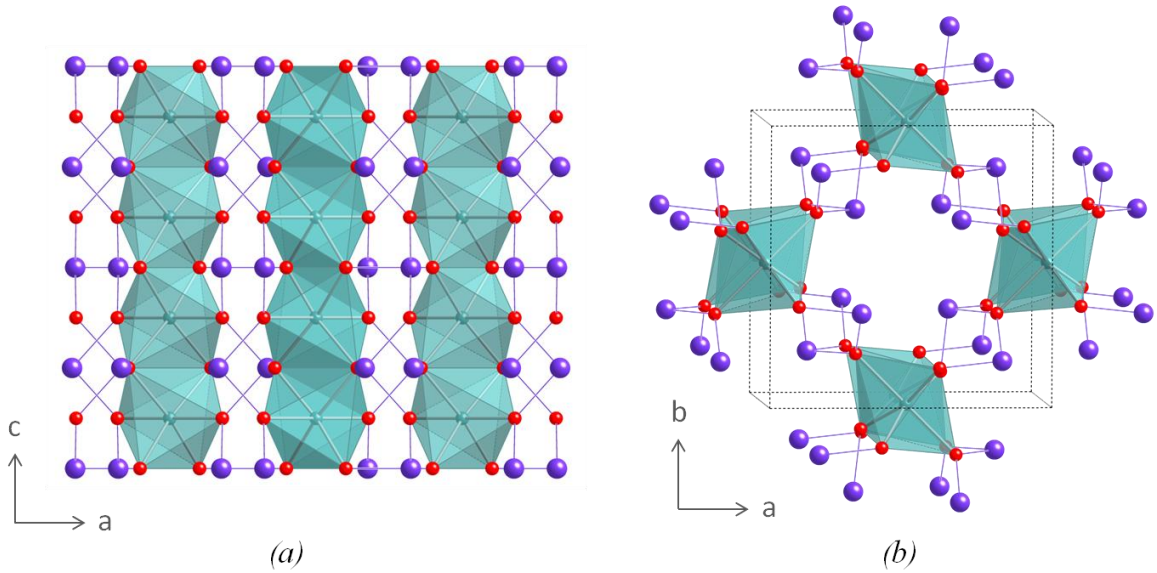

***Fig. 1.1**: The structure of schafarzikite, $FeSb_2O_4$ (a) showing the edge-linked chains and (b) looking down the c-axis. FeO_6 octahedra are shaded. Fe ions are located within the octahedra, O ions are shown as red spheres and Sb ions are shown as purple spheres.*

The schafarzikite structure is interesting for many reasons and one of these is its relationship to the rutile structure. The rutile structure (Fig. 1.2) has an MO_2 stoichiometry and the same edge-linking chains of MO_6 octahedra along the *c*-axis that are found in schafarzikite. However in the schafarzikite structure these chains are separated and linked by cations in pyramidal sites. The presence of a significantly different second cation that will not mix with the M cations in the octahedral chains could potentially provide a way of controlling the M oxidation state in the chains which is not possible in the rutile structure. Therefore structural modifications by cation substitution at the pyramidal site could be made for the schafarzikite materials to alter the properties as has been done for perovskites. Other interesting features arise due to the separation of the chains. The intrachain Fe-Fe distance (2.96 Å) is much shorter than the nearest Fe-Fe distance within the layers perpendicular to the chains (6.07 Å) suggesting that some one-dimensional character could be expected in schafarzikite. Low dimensional materials are of interest for electronic devices because they can have new and unusual electronic and magnetic properties which are anisotropic.

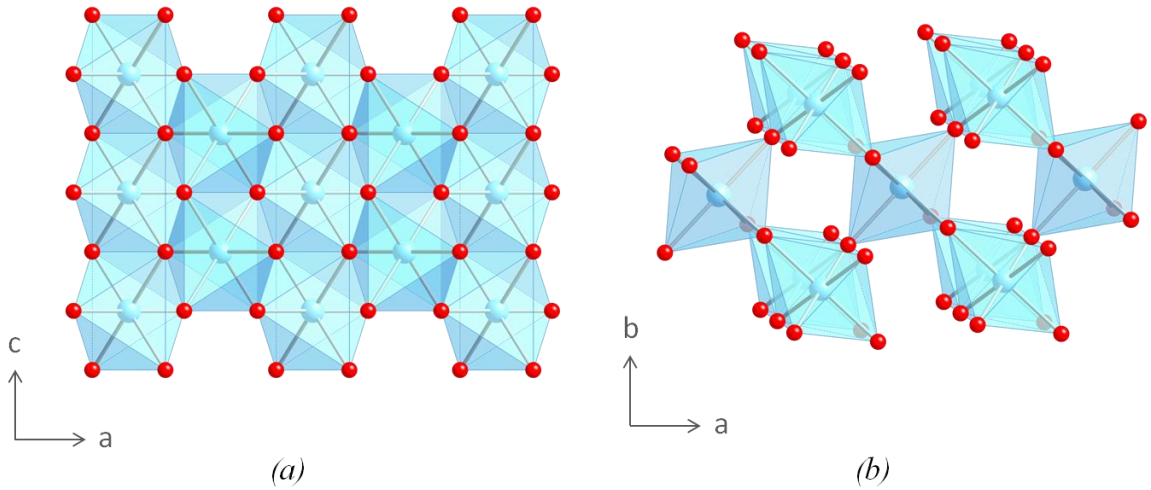

***Fig. 1.2**: The rutile, MO_2, structure (a) showing the edge-linked chains and (b) looking down the c-axis. MO_6 octahedra are shaded, M ions are located within the octahedra and O ions are shown as red spheres.*

The separation of the chains in schafarzikite also gives rise to channels within the structure along the *c*-axis. Insertion of ions into these channels to give mixed oxidation state materials may also be possible. Modifications of the schafarzikite structure in this way have not been studied before. There is only one previous report exploring substitutions on the pyramidal site;[5] this was for the material $MnSb_2O_4$ which was unsuccessful and is discussed further in Section 3.1.1.

1.2.1.1 Orthorhombic Distortion in Pb_3O_4

As mentioned previously the MX_2O_4 schafarzikites are isostructural with Pb_3O_4, which has Pb^{4+} ions within the octahedral chains and Pb^{2+} ions on the pyramidal sites. Pb_3O_4 is tetragonal at room temperature but undergoes a tetragonal to orthorhombic transition at 170 K[6-7]. The tetragonal structure has space group $P4_2/mbc$ and unit cell parameters a = 8.811(5) Å and c = 6.563(3) Å,[6] and the orthorhombic structure has space group *Pbam* (no. 55) and unit cell parameters a = 9.124(1) Å, b = 8.467(1) Å and c = 6.5667(5) Å[7]. So far no similar transitions have been observed for any other MX_2O_4 schafarzikite materials[3]. The structure of the similar compound $SnPb_2O_4$ was studied at various temperatures using X-ray and neutron diffraction.[2] No phase transition was seen

but both tetragonal and orthorhombic structures were reported at each temperature, the latter only having small differences in the *a*- and *b*-parameters.

1.2.2 Pyrochlore

The term pyrochlore refers to a family of mixed oxides isostructural with the mineral pyrochlore, $NaCaNb_2O_6F$. The general formula is $A_2B_2O_7$ (or $A_2B_2O_6O'$ to distinguish between the two crystallographically different O1 and O2 sites) where A is a larger 8-coordinate cation and B is a smaller 6-coordinate cation. The structure is shown in Fig 1.3. There are various different ways of describing the pyrochlore structure and two examples are given here: it can be described as two interlinking networks of BO_6 octahedra and A_2O' chains or as an oxygen-deficient fluorite superstructure. Pyrochlores have cubic symmetry with space group *Fd*-3*m* (no. 227) and unit cell *a*-parameter between 10-11 Å.[8]

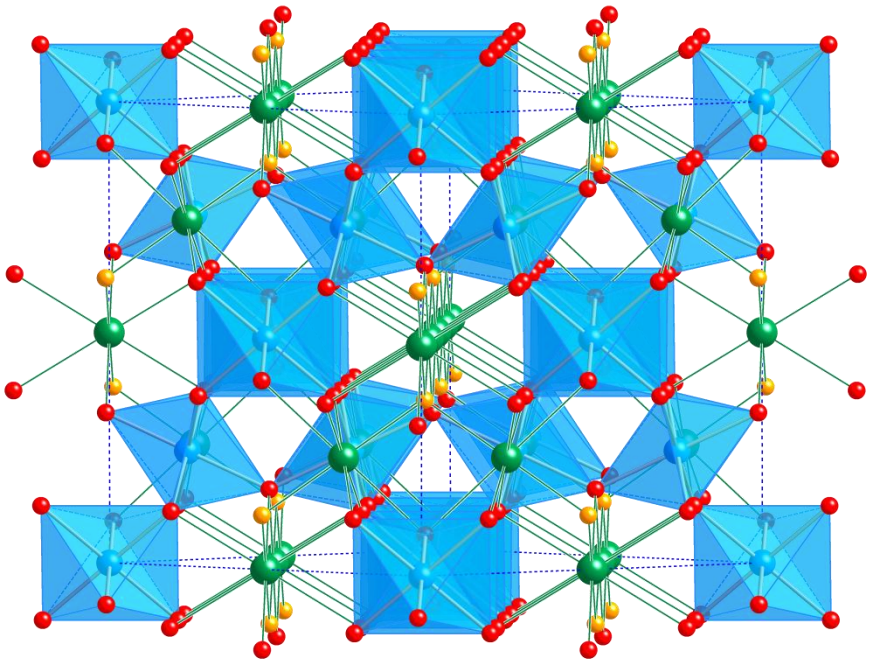

***Fig. 1.3**: The pyrochlore $A_2B_2O_7$ structure: A-cations are shown in green, BO_6 octahedra are shaded, O1 anions are shown in red and O2 anions are shown in orange.*

The atomic positions for the pyrochlore structure are given in Table 1.2, the only variable positional parameter in the structure is the O1 *x*-value which falls between 0.319 and 0.343[9]. There are different possible choices of origin for the pyrochlore structure but most commonly the B-cation is chosen and this is used as the origin throughout this work.

***Table 1.2**: Atomic positions for the pyrochlore $A_2B_2O_7$ structure in Fd-3m (origin at the B-site)*

	Wyckoff Position	*x*	*y*	*z*
A	16*d*	½	½	½
B	16*c*	0	0	0
O1	48*f*	*x*	⅛	⅛
O2	8*b*	⅜	⅜	⅜

The geometry around the A-cations is described as scalenohedral rather than cubic because the A-ion forms six longer A-O1 bonds and two shorter A-O2 bonds (Fig. 1.4a). The B-ion forms six equal B-O1 bonds and although the BO_6 units will be referred to as octahedra they are distorted and therefore are in fact trigonal antiprisms (Fig. 1.4b).

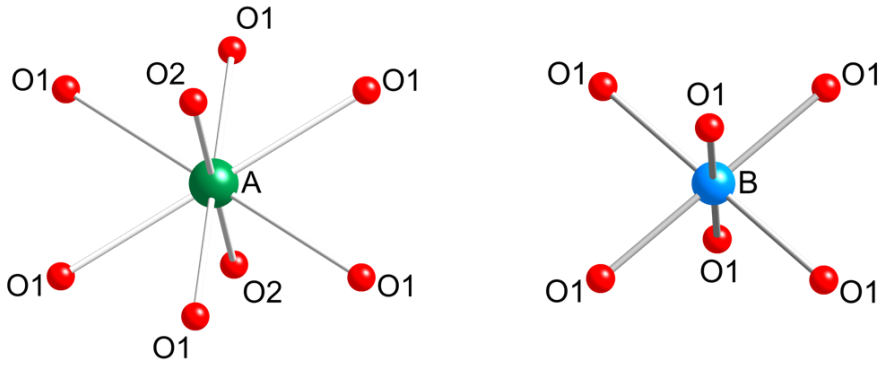

***Fig. 1.4**: Coordination environment around cations in the pyrochlore structure showing (a) the 8-coordinate A-ion and (b) the 6-coordinate B-ion.*

Mixed metal oxides with the pyrochlore structure are well studied and of great interest because of their susceptibility to chemical modifications. Pyrochlores can be substituted at the A-, B- and O-sites and can tolerate vacancies at the A and O2 sites giving

a large number of possible compositions with a range of useful properties[8-9]. This includes insulators, semiconductors and metals, and even superconductivity has been observed in some compounds[10], first for the material $Cd_2Re_2O_7$[11]. Piezoelectrics, dielectrics and ferroelectrics are also found. As for their magnetic properties, ferromagnetic and antiferromagnetic ordering is seen but pyrochlores are geometrically frustrated and can often display unusual magnetic behaviour at low temperatures[12]. The magnetic properties of pyrochlores are discussed further in Section 1.5.3.

1.3 Charge Ordering and the Verwey Transition

Charge ordering is a phenomenon which is sometimes seen in materials which have ions of the same element present in different oxidation states. The material undergoes a transition at a particular temperature, T_{CO}, where the oxidation states become localised and order, breaking the symmetry of the material. Above this temperature an average oxidation state is observed and all the ion sites are equivalent. Charge ordering was first discovered in magnetite, Fe_3O_4, below the Verwey transition which occurs at around 120 K[13], but since then has also been observed in other interesting metal-oxide materials such cuprates, manganites and nickelates[14-16].

Magnetite, Fe_3O_4, has a cubic inverse-spinel structure (space group *Fd*-3*m*). Spinel has the general formula AB_2O_4 and consists of a cubic close packed array of oxide ions with A^{2+} cations on the tetrahedral sites and B^{3+} cations on the octahedral sites. In the inverse spinel structure, all the A-cations and half the B-cations occupy the octahedral sites and the remaining half of the B-cations occupy the tetrahedral sites. The inverse spinel structure can therefore be written as $[A^{2+}B^{3+}]_{oct}(B^{3+})_{tet}O_4$ and the formula for Fe_3O_4 as $[Fe^{2+}Fe^{3+}]_{oct}(Fe^{3+})_{tet}O_4$. There are similarities between schafarzikite and magnetite because both materials contain edge-sharing chains of FeO_6 octahedra; in magnetite the chains

contain equal amounts of Fe^{2+} and Fe^{3+} ions whereas in schafarzikite they contain Fe^{2+} ions only.

Magnetite is a very interesting material and has been the subject of numerous studies because in 1939 it was discovered by Verwey that Fe_3O_4 undergoes a charge ordering transition at *ca*. 120 K[13], now known as the Verwey transition. It is a first order transition where the resistivity increases by two orders of magnitude, a magnetic transition is seen, there is a peak in the specific heat and the structure distorts from cubic symmetry (Fig. 1.5)[13, 17-19].

Verwey's original theory was that above the transition temperature, T_v, there is a continuous interchange of electrons between the iron ions and an averaged distribution of Fe^{2+} and Fe^{3+}, giving rise to electrical conductivity. Then below T_v the Fe^{2+} and Fe^{3+} ions order and the electrons become localised causing the conductivity to decrease and Fe_3O_4 to become an insulator.[17-18] Although Verwey's theory is still generally regarded as a valid explanation for the observed change in properties at T_v, there is still much debate and questioning over the transition and many aspects that are still not well understood. Details such as the driving force for the transition, the mechanisms for charge transport and how exactly the ions order, and finding evidence to prove charge ordering, have been investigated for many years. The low-temperature crystal structure was also the subject of much discussion but has recently been solved[20-21]. One of the main problems when studying the low-temperature crystal structure of Fe_3O_4 is in obtaining single crystals of sufficiently high quality as microtwinning of domains is seen below T_v.[21] Verwey originally proposed a low-temperature structure that, although reported as tetragonal[18], was later reclassified as orthorhombic[22] and the structure now reported is a monoclinic supercell with *Cc* (no. 9) space group symmetry and 224 atoms[20-21].

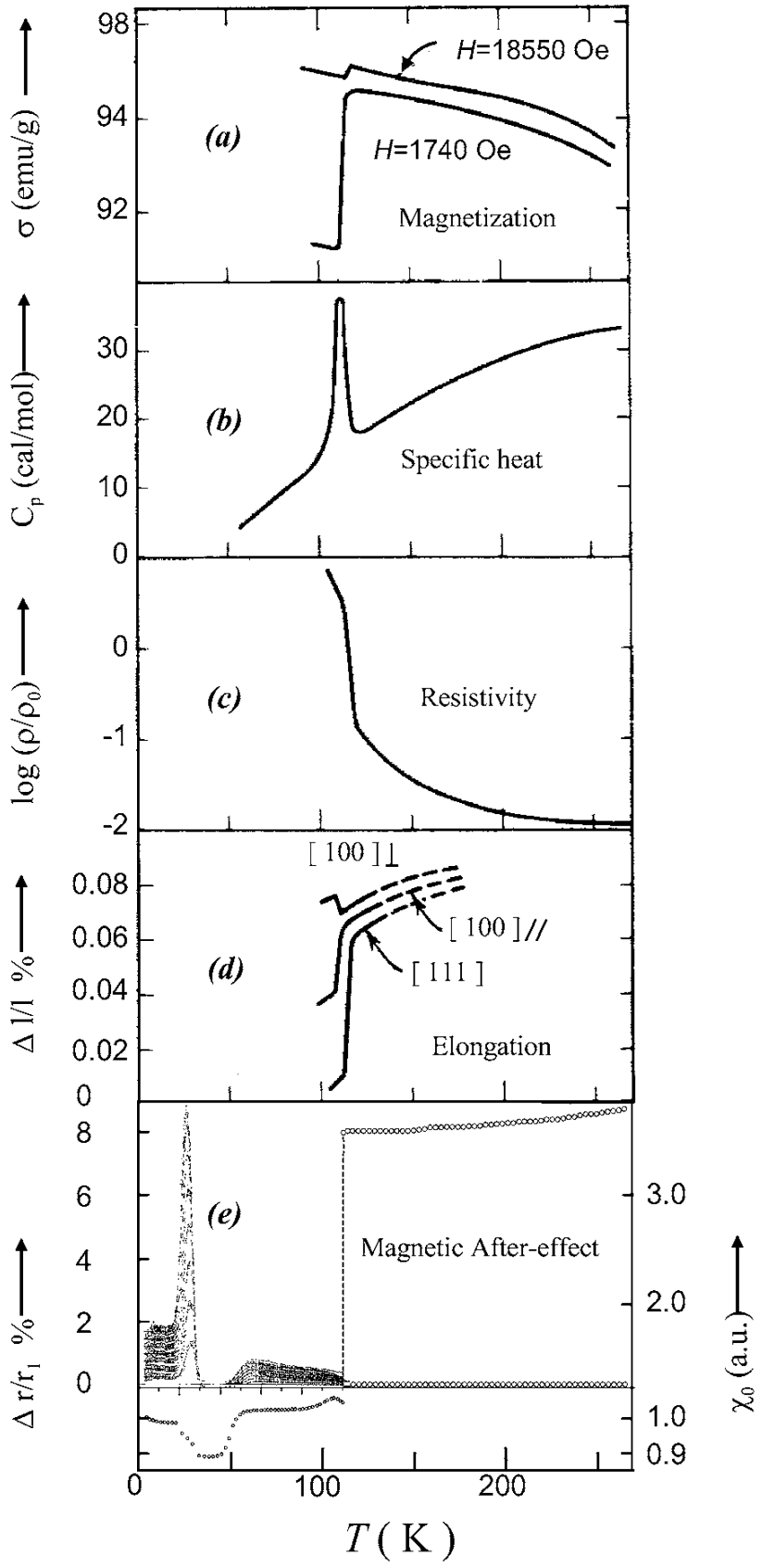

***Fig. 1.5**: Experimental data showing the effects of the Verwey transition taken from a 2002 review article by Friedrich Walz[19]. (a) Magnetisation, (b) specific heat, (c) resistivity, (d) thermal expansion along selected directions and (e) magnetic after-effect data are shown.*

1.4 One Dimensional Metals

As discussed in Section 1.2.1, the schafarzikite structure is related to the rutile structure (Fig. 1.2). Although the rutile structure cannot be modified and controlled in the same way as the perovskite structure, rutile materials still show some interesting properties. An example of this is the rutile materials VO_2 and NbO_2 which display some one-dimensional properties due to the metal-metal distances in the edge-sharing octahedral chains along the *c*-axis being shorter than those between the chains. The vanadium and niobium ions both have d^1 electronic configurations so one electron per metal ion and a half-filled band. The structures therefore undergo Peierls type metal to insulator transitions at low temperatures[23-24], the exact origins of which are still debated[25-26].

The transition in VO_2 is seen at 340 K. Above this temperature VO_2 displays metallic behaviour and has the tetragonal rutile structure with space group $P4_2/mnm$ (no. 136) and intrachain V-V distances of 2.87 Å.[27] Below 340 K two V-V distances of 2.65 Å and 3.12 Å are seen as the vanadium ions form pairs which are tilted with respect to the *c*-axis[27]. This gives a monoclinic structure with space group $P2_1/c$ (no. 12) and VO_2 becomes semiconducting.[23, 27]

The transition in NbO_2 occurs at 1080 K, the structure distorts from the tetragonal rutile structure to a structure with a distorted tetragonal body-centred lattice and a change from metallic to semiconducting behaviour is observed.[24, 26, 28]

1.5 Magnetic Interactions

Magnetic fields are produced when charges are in motion. In a magnetic material the electron spinning and orbiting the nucleus of an atom generates a magnetic field. There are different types of magnetism that can occur in a magnetic material which are studied by measuring the response of the material to an applied magnetic field. When reporting magnetic data, there are two systems of units that are commonly used[29]: the international

system of units (SI) and the centimeter-gram-second system of units (cgs). The magnetic data in this thesis are all reported using the cgs system. The response of a volume of space to a magnetic field, H (measured in Oersted, Oe), is its magnetic induction or magnetic flux density, B (measured in Gauss, G), and these two values are related by the permeability of the volume, μ, or the permeability of free space, μ_o, in a vacuum (Equation 1.1). In the cgs system, as μ_o is set as 1, H and B are numerically equal.

$$B = \mu_o H \tag{1.1}$$

The contribution from the interaction of the sample with the applied field is known as the magnetisation, M, and is also taken into account. This is an intrinsic property of the sample, reported in electromagnetic units (emu), but it is often divided by volume, mass or moles to give units of emu cm^{-3}, emu g^{-1} or emu mol^{-1} respectively. Using the SI system the relationship between B, H and M is:

$$B = \mu_o H + \mu_o M \tag{1.2}$$

However, when using the cgs system, there is a factor of 4π that must be taken into account to give:

$$B = H + 4\pi M \tag{1.3}$$

The response of a sample to an applied magnetic field is usually reported as its magnetic susceptibility, χ, which is the ratio of the magnetisation to the field:

$$\chi = \frac{M}{H} \tag{1.4}$$

The magnetisation is negative for diamagnetic materials as they are repelled by magnetic fields and positive for paramagnetic materials as they are attracted to magnetic

fields. Diamagnetism is present in all materials as it arises from the motion of paired electron in their orbitals but it is usually very weak and not observed. An exception to this is in superconducting materials which are perfect diamagnets and show very strong diamagnetic effects. Paramagnetism is seen in materials which have unpaired electrons; each atom with unpaired electrons has a magnetic moment and in a paramagnet these moments do not interact strongly with one another. The moments are randomly orientated and fluctuating due to the thermal energy but when an external magnetic field is applied they will attempt to line up with the field. The magnetic susceptibility, χ, is inversely proportional to temperature, T, and this is described by the Curie law (where C is the Curie constant):

$$\chi = \frac{C}{T} \tag{1.5}$$

In this work materials which order magnetically are studied. Magnetic ordering arises when the moments interact with one another and their spins align giving rise to a magnetic transition at a particular temperature. Above the transition temperature the moments are randomly aligned and the materials behave paramagnetically. Some different types of magnetic ordering are shown schematically in Fig. 1.6.

In a ferromagnetic material the magnetic moments all line up in the same direction (Fig. 1.6a) causing the magnetic susceptibility to increase at the transition temperature, called the Curie temperature, T_c. In an antiferromagnetic material the ordering temperature is known as the Néel temperature, T_N, and at this temperature the moments align antiparallel (Fig. 1.6b) causing a decrease to be seen in the susceptibility. Other types of magnetic ordering are also possible, for example Fe_3O_4, which was discussed in Section 1.3, is a ferrimagnet. Ferrimagnetic ordering is shown in Fig. 1.6c and arises when ions with different-sized magnetic moments order antiferromagnetically. In Fe_3O_4 the

octahedral Fe^{2+} and Fe^{3+} ions are aligned parallel to one another but antiparallel to the tetrahedral Fe^{3+} ions so the moments therefore do not cancel out and an increase is observed in the susceptibility. Another type of ordering that gives rise to an increased susceptibility at the ordering temperature is canted antiferromagnetism (Fig. 1.6d). The moments are aligned antiferromagnetically but do not cancel out as they are all slightly tilted in one direction causing there to be an overall magnetic moment.

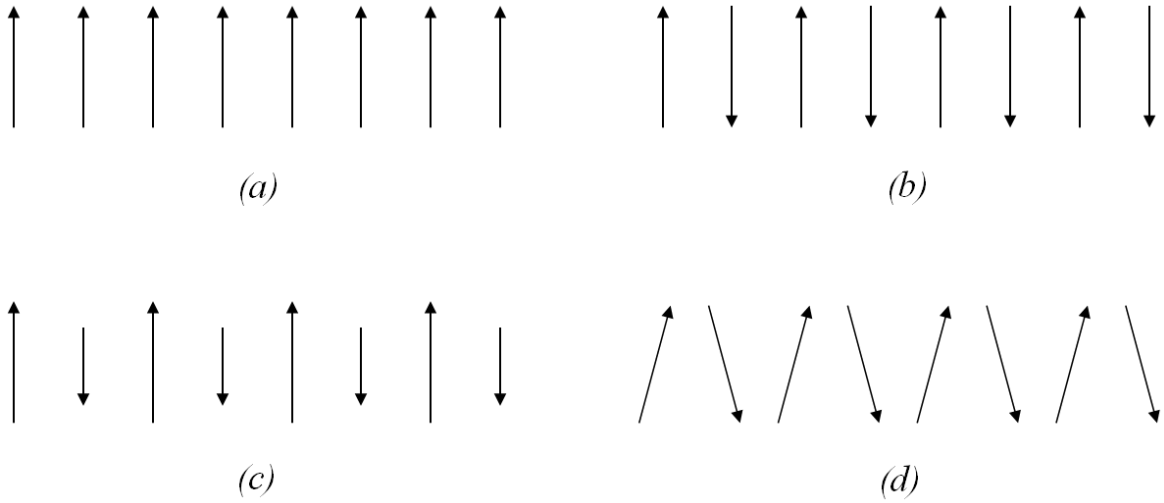

Fig. 1.6*: Diagrams to represent different types of magnetic ordering showing (a) ferromagnetism, (b) antiferromagnetism, (c) ferrimagnetism and (d) canted antiferromagnetism.*

The Curie law is modified to take into account the interactions between magnetic moments to give the Curie-Weiss law:

$$\chi = \frac{C}{T - \theta} \tag{1.6}$$

Plots of inverse susceptibility against temperature that follow the Curie-Weiss law are linear in the high temperature paramagnetic region then a deviation is seen at the ordering temperature. The plot (Fig. 1.7) can be used to calculate magnetic moments and to obtain the Weiss temperature, θ, the sign of which indicates whether the interactions

occurring in the material are ferromagnetic (positive value of θ) or antiferromagnetic (negative value of θ).

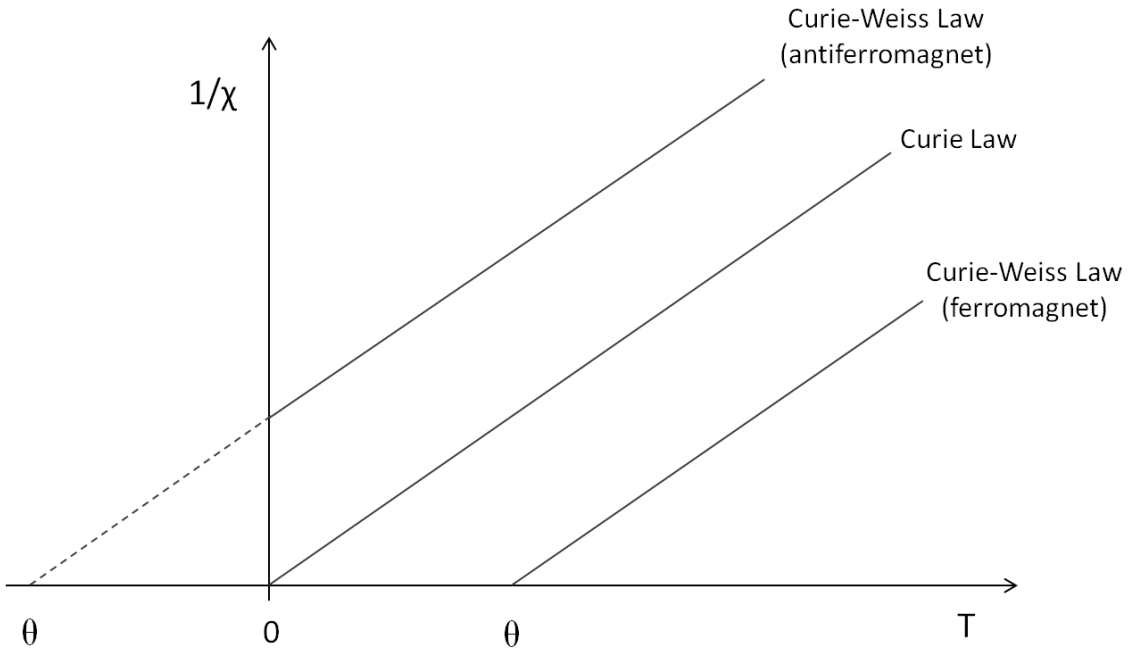

Fig. 1.7*: Plot of inverse susceptibility against temperature showing the Curie law for paramagnetic materials and the Curie-Weiss law for ferromagnetic and antiferromagnetic materials.*

1.5.1 Superexchange

To rationalise the ways in which magnetic materials order, the interactions between magnetic ions need to be considered. Magnetic ions in metal-oxide materials can either interact directly if they are close enough, for example in face- or edge-sharing chains, or indirectly through the oxide ions. The interaction through oxide ions is known as superexchange where virtual electron transfer occurs between the metal *d*-orbitals and oxygen 2*p* orbitals.[30-33] The type of ordering resulting from superexchange interactions depends on the geometry of the ions and the electron configuration of the metal ions. Various types of magnetic superexchange interactions are shown in Fig. 1.8.

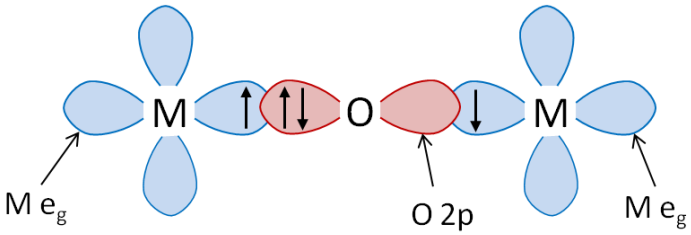

(a)

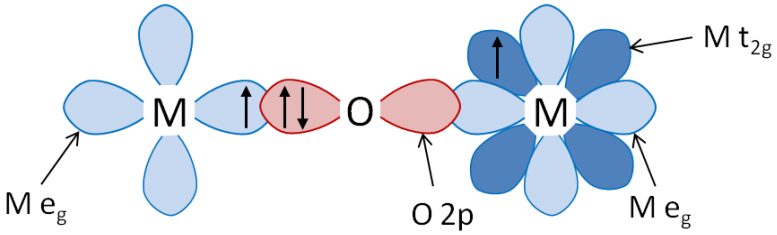

(b)

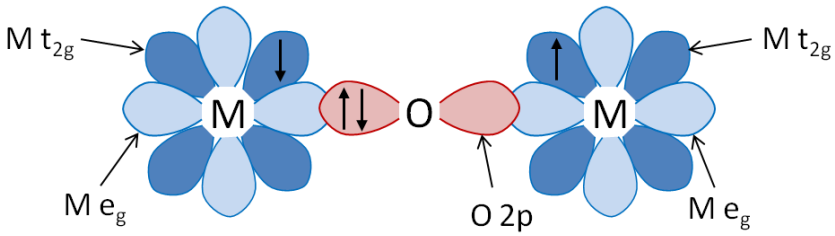

(c)

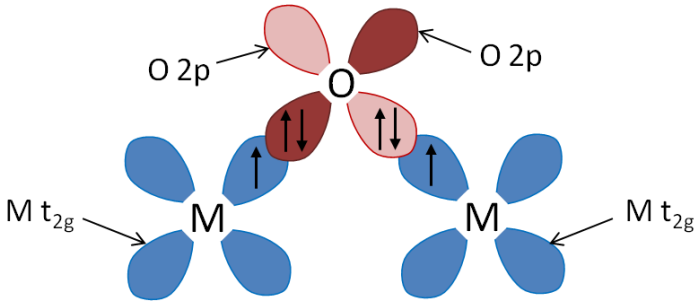

(d)

***Fig. 1.8**: Magnetic superexchange diagrams showing: (a) 180 ° AFM e_g-2p-e_g superexchange, (b) 180 ° FM e_g-2p-t_{2g} superexchange (c) 180 ° AFM t_{2g}-2p-t_{2g} superexchange and (d) 90 ° FM t_{2g}-2p-2p-t_{2g} superexchange.*

In Fig. 1.8a, 180 ° antiferromagnetic (AFM) superexchange is shown. This type of exchange arises from metal ions with unpaired electrons in the e_g orbitals which directly overlap with the 2*p* orbital on the intermediate oxygen. One metal transfers some up-spin to the oxygen 2*p* orbital and to accommodate this, up-spin is transferred from the O 2*p* orbital to the other metal which, due to the Pauli exclusion principle, will align its unpaired electron antiparallel giving overall AFM ordering. In Fig. 1.8b the situation is shown where one metal ion has an unpaired electron in the e_g orbital and the other has empty e_g orbitals. In this case partially filled t_{2g} orbitals contribute to the superexchange interaction. As for the first example, some up-spin is transferred from the e_g orbital to the O 2*p* orbital which then transfers up-spin to the e_g orbital on the second metal ion. The unpaired electron in the t_{2g} orbital then aligns itself parallel to the up-spin transferred which gives overall ferromagnetic (FM) ordering. Fig. 1.8c shows another 180 ° AFM superexchange interaction but this time both the metal ions have empty e_g orbitals and unpaired electrons in the t_{2g} orbitals. Spin of opposite directions is transferred to each metal from the O 2*p* orbital and the electrons in the t_{2g} orbitals will align parallel to the spin transferred.

The final example of magnetic superexchange interactions is the most important when considering magnetic ions in edge-sharing octahedral chains such as those found in the rutile, spinel and schafarzikite structures discussed previously. This is the 90 ° FM superexchange interaction (Fig. 1.8d) which occurs through two oxygen 2*p* orbitals. Although the electrons are localised and only virtual electron transfer is occurring, the interaction can be more easily understood by imagining complete electron transfer. In a 90 ° interaction it is now the t_{2g} orbitals which overlap with the oxygen 2*p* orbitals. Each oxygen 2*p* orbital will transfer an electron of the same spin to the metal t_{2g} orbitals so that the remaining O 2*p* electrons are aligned parallel to one another. The metal t_{2g} orbitals must align their unpaired electrons antiparallel to the electrons transferred which overall

gives FM ordering. This type of superexchange is weaker than the 180 ° AFM exchange shown in Fig. 1.8a because the interaction is occurring through two oxygen orbitals rather than one. In edge-sharing chains the metal ions are also much closer together and if the direct interactions between them are strong this will dominate the type of magnetic ordering that is observed. Superexchange interactions alone may therefore not be enough to predict the overall magnetic ordering of the system.

1.5.2 Magnetic Properties of MX_2O_4

From the series of MX_2O_4 compounds, $MnSb_2O_4$, $FeSb_2O_4$ and $NiSb_2O_4$ are known to order magnetically; all three compounds display antiferromagnetic behaviour at low temperatures[34-37]. The magnetic transition is seen in schafarzikite, $FeSb_2O_4$, at a Néel temperature, T_N, of around 45 K[34, 37]. Below this temperature $FeSb_2O_4$ displays predominantly A-type antiferromagnetic ordering. The modes of antiferromagnetic ordering for the MX_2O_4 structures are shown in Fig. 1.9 and are analogous to those for perovskites[38]. In an A-type structure the magnetic moments are aligned antiparallel within the octahedral chains along the *c*-axis and parallel within the layers perpendicular to the chains. The moments in $FeSb_2O_4$ are aligned perpendicular to the *c*-axis but they are non-collinear and have a small component along *c*.[34, 37]

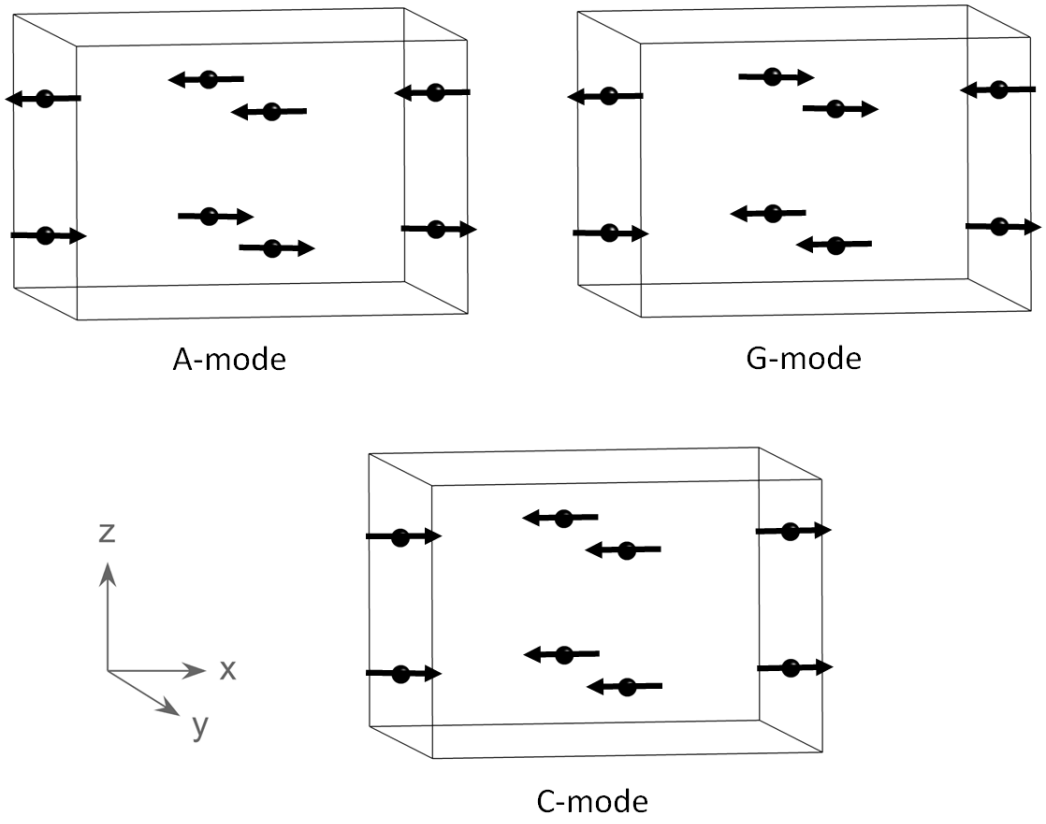

***Fig 1.9**: The three antiferromagnetic modes for MX_2O_4 structures. The magnetic moments are shown here to be aligned along the x-axis.*

$MnSb_2O_4$ also exhibits A-type antiferromagnetic order with a Néel temperature of around 60 K[35-36]. The moments are collinear and lie in the *ab* plane. $NiSb_2O_4$ orders antiferromagnetically at approximately 46 K[35-36], the moments are collinear and are aligned primarily along the *c*-axis. Unlike $FeSb_2O_4$ and $MnSb_2O_4$ the ordering is C-type (Fig. 1.9). In a C-type magnetic structure the moments are aligned parallel within the chains along the *c*-axis and antiparallel within the layers. In the final antiferromagnetic mode, the G-mode (Fig 1.9), the moments are aligned antiparallel in both the chains and the layers.

The differences in magnetic ordering can be rationalised by considering how the transition metal cations interact with one another. The magnetic ions within a chain can interact by direct cation-cation exchange (Fig 1.10a) and through 90º M-O-M

superexchange interactions (Fig 1.10b). Within a layer the ions interact through much weaker M-O-Sb-O-M links, giving long range magnetic order.

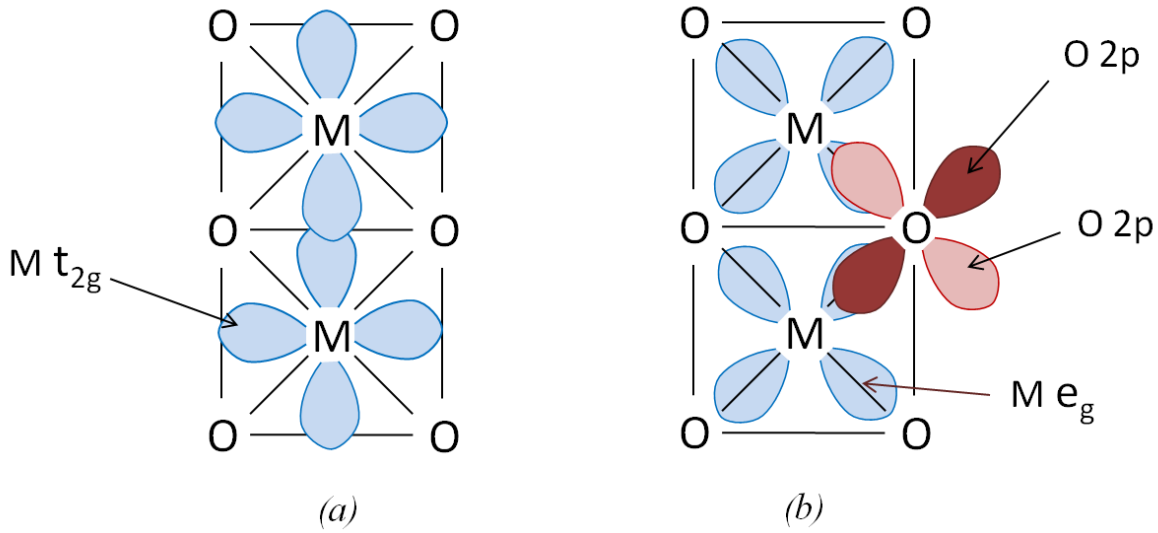

***Fig. 1.10**: Mechanisms of magnetic exchange throughout the chains of MO_6 octahedra. Magnetic moments on adjacent ions in a chain can interact by (a) direct cation-cation exchange and (b) 90° superexchange interactions.*

As the octahedra in the chains share edges, the t_{2g} orbitals on neighbouring transition metal ions point directly towards each other and overlap (Fig. 1.10a). If the unpaired electrons between the two cation centres are arranged antiferromagnetically, this will maximise the electronic charge in this region and stabilise the bonding[39]. This exchange mechanism competes with the 90º superexchange interaction which favours ferromagnetic ordering (Section 1.5.1). In $MnSb_2O_4$ and $FeSb_2O_4$ the Mn^{2+} (d^5) and Fe^{2+} (d^6) t_{2g} orbitals are partially filled and antiferromagnetic coupling is observed throughout the octahedral chains which is consistent with direct exchange occurring between adjacent ions. In $NiSb_2O_4$ the Ni^{2+} (d^8) t_{2g} orbitals are completely filled and therefore there is no direct exchange occurring and the ordering seen within the chains is ferromagnetic, as predicted by the superexchange interactions.

This type of direct exchange is also seen for the related compound $MnPb_2O_4$.[40] $MnPb_2O_4$ has a slightly different structure from $FeSb_2O_4$: it is tetragonal with space group $P\bar{4}2_1c$ (no. 114) and the MnO_6 octahedra form zigzag chains along the *c*-axis which are linked by Pb^{2+} ions in pyramidal sites (Fig 1.11)[41]. It is an interesting material because it is piezoelectric and also has magnetic properties. The moments on the Mn^{4+} ions order antiferromagnetically below $T_N = 18$ K[40]; the moments align antiparallel both within the chains and within the layers perpendicular to the chains. The octahedra share edges and antiferromagnetic ordering within the chains would be expected for Mn^{4+} as it has a d^3 configuration and therefore three unpaired electrons in the t_{2g} orbitals.

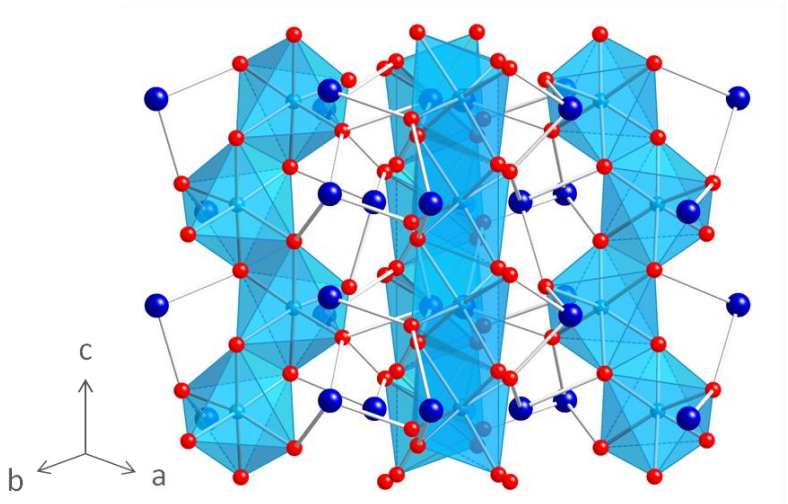

***Fig. 1.11**: The structure of $MnPb_2O_4$. MnO_6 octahedra are shaded. Mn ions are located within the octahedra, O ions are shown as red spheres and Pb ions are shown as dark blue spheres.*

1.5.3 Magnetic Properties of Pyrochlores

As mentioned in Section 1.2.2 there are many different ways of describing the pyrochlore structure. It is useful when looking at magnetic properties to view the structure as two sublattices of A_4 and B_4 corner-sharing tetrahedra (Fig. 1.12). If these sites are occupied by magnetic ions the tetrahedral relationship can cause them to be frustrated giving unusual magnetic properties.

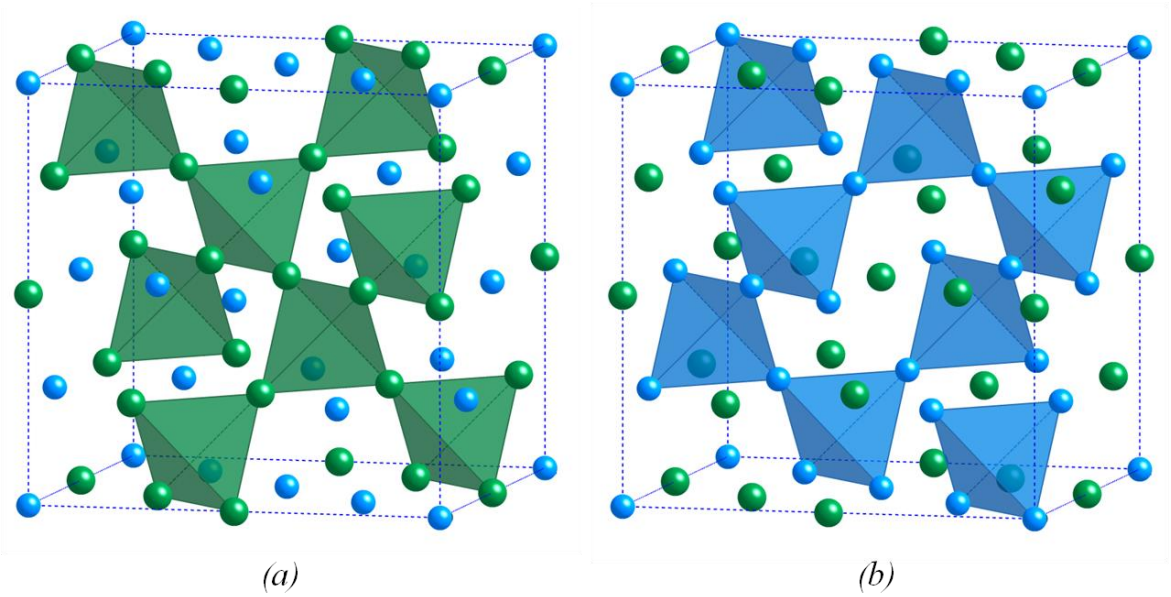

***Fig. 1.12**: The pyrochlore structure showing the A- and B-cations only. The tetrahedral arrangement of (a) A-cations (green) and (b) B-cations (blue) is shown.*

Triangles and tetrahedra of magnetic atoms are described as frustrated because they cannot form an antiferromagnetic ground state. It can be seen from Fig. 1.13 that it is impossible for all the nearest neighbour interactions to be antiferromagnetic. There are therefore competing antiferromagnetic and ferromagnetic interactions and no single lowest energy ground state.

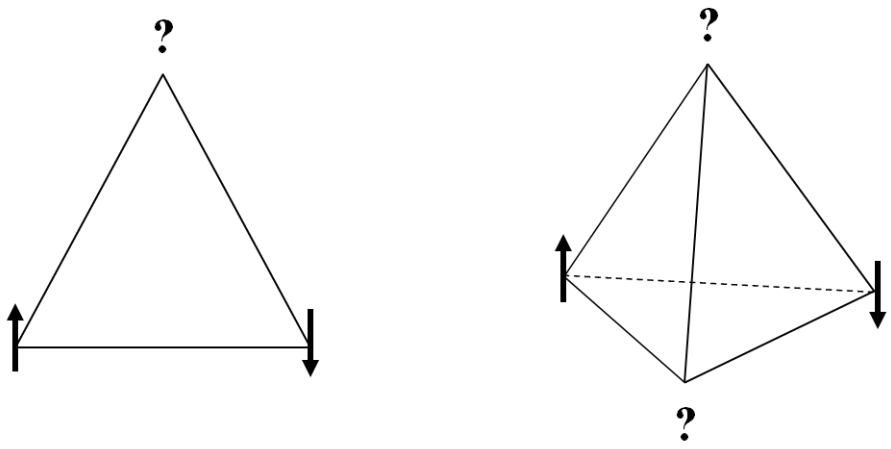

***Fig. 1.13**: Geometric frustration shown by antiferromagnetic arrangement of spins on a triangle and on a tetrahedron.*

Although magnetic pyrochlore materials are highly geometrically frustrated there are still some materials which exhibit long-range magnetic ordering at low temperatures[12]. Some examples of this are the material $Er_2Ti_2O_7$ which orders below T_N = 1.173 K to an antiferromagnetic state where the moments are perpendicular to the ⟨111⟩ axes[42], the material $Gd_2Sn_2O_7$ in which the Gd^{3+} moments are aligned parallel to the edges of the tetrahedron below a Néel temperature of around 1 K[43] and the material $Tb_2Sn_2O_7$ which displays magnetic ordering below 0.87 K with both ferromagnetic and antiferromagnetic character[44]. Other interesting magnetic pyrochlores are those which contain magnetic ions on both the A and B sites of the structure, such as $A_2Ru_2O_7$ (where A = rare earth), as they can interact with one another influencing the magnetic properties. In the material $Er_2Ru_2O_7$ both the Ru^{4+} and Er^{3+} moments order magnetically at temperatures of 90 K and 10 K respectively and the moments are arranged antiferromagnetically along the ⟨110⟩ directions[45]. The rare-earth ions in the pyrochlore structure will often only order at very low temperatures of around 1 K or lower, as seen for the materials mentioned above, and it was suggested that the increased ordering temperature of the Er^{3+} moments in $Er_2Ru_2O_7$ is due to the interaction with Ru^{4+} moments[45].

Due to the geometric frustration, some more unusual types of magnetic behaviour are also seen such as spin-glass, spin-ice and spin-liquid. In a spin-glass material there is no long-range ordering but the random orientation of disordered magnetic moments becomes frozen-in below the glass transition temperature, T_f. Some pyrochlore oxides exhibit spin-ice behaviour which is a frustrated magnetic state where the nearest neighbour interactions are ferromagnetic but the moments are constrained to lie along the ⟨111⟩ axis[46]. Spin-ice materials have many degenerate ground states and do not show any long-range ordering down to very low temperatures. The spin-ice magnetic state has been confirmed for three pyrochlore compounds $Ho_2Ti_2O_7$,[47] $Dy_2Ti_2O_7$ [48] and $Ho_2Sn_2O_7$.[49] Spin-glasses and spin-ices are discussed in more detail in Sections 6.3.2 and 7.1 respectively. A few pyrochlore materials such as $Tb_2Ti_2O_7$, $Yb_2Ti_2O_7$, $Er_2Sn_2O_7$ and $Pr_2Ir_2O_7$ are being investigated as possible spin-liquid materials[12]. Spin-liquids are very disordered, the magnetic spins are highly correlated but are described as fluid-like because they fluctuate even down to temperatures of 0 K.[50]

1.6 Project Aims

In this thesis the synthesis, structure and magnetic properties of materials derived from schafarzikite and pyrochlore minerals are studied. As mentioned in Section 1.2.1 schafarzikite has a very interesting, yet little-studied, structure type and by making chemical modifications to $FeSb_2O_4$ many new materials with a range of properties could potentially be prepared. Modifications could be made by substituting ions on to the pyramidal Sb^{3+} sites to control the iron oxidation state, by making substitutions at the octahedral Fe^{2+} site giving mixed cations within the chains or by inserting ions such as O^{2-} into the channels between the octahedral chains, again modifying the cation oxidation state. There is a large range of unexplored possibilities and the aim of this work is to investigate how making changes to the structure alters the properties and therefore better

understand structure property relationships. Properties that could be explored are magnetic ordering, electronic and ionic conductivity, the possibility of Fe^{2+}/Fe^{3+} charge ordering, low dimensionality and thermoelectric properties.

Pyrochlores, in contrast to schafarzikite materials, have been very well studied and a large number of materials are known which exhibit a diverse range of properties. As well as the synthesis and study of some new pyrochlore materials, the properties of some known pyrochlore minerals will be explored further in this work. The stability of some previously-reported pyrochlore materials and distortions which occur in the structure will be investigated along with their magnetic properties. As discussed in Section 1.5.3 many pyrochlores do not show long-range ordering due to the geometric frustration present in the pyrochlore lattice and those that do often will only display magnetic ordering at extremely low temperatures of $T \leq 1$ K. The magnetic properties of pyrochlore materials that have been reported to show magnetic ordering at relatively high temperatures will be investigated. Materials containing magnetic ions on both the A- and B-sites of the structure will be prepared to explore any interactions that occur between them and how this may influence the magnetic properties.

1.7 References

1. R. Fischer and F. Pertlik, *Tschermaks Mineral. Petrogr. Mitt.*, 1975, **22**, 236.

2. J. R. Gavarri, J. P. Vigouroux, G. Calvarin and A. W. Hewat, *J. Solid State Chem.*, 1981, **36**, 81.

3. J. R. Gavarri, *J. Solid State Chem.*, 1982, **43**, 12.

4. J. R. Gavarri, R. Chater and J. Ziółkowski, *J. Solid State Chem.*, 1988, **73**, 305.

5. A. M. Abakumov, M. G. Rozova, E. V. Antipov, J. Hadermann, G. Van Tendeloo, M. Lobanov, M. Greenblatt, M. Croft, E. V. Tsiper, A. Llobet, K. A. Lokshin and Y. Zhao, *Chem. Mater.*, 2005, **17**, 1123.

6. J. R. Gavarri and D. Weigel, *J. Solid State Chem.*, 1975, **13**, 252.

7. J. R. Gavarri, G. Calvarin and D. Weigel, *J. Solid State Chem.*, 1975, **14**, 91.

8. M. A. Subramanian, G. Aravamudan and G. V. Subba Rao, *Prog. Solid St. Chem.*, 1983, **15**, 55.

9. M. A. Subramanian and A. W. Sleight, in *Handbook on the Physics and Chemistry of Rare Earths*, eds. K. A. Gschneidner Jr. and L. Eyring, Elsevier Science Publishers B.V., Editon, 1993, vol. 16, p. 225-248.

10. Z. Hiroi, J. Yamaura, S. Yonezawa and H. Harima, *Physica C*, 2007, **460**, 20.

11. H. Sakai, K. Yoshimura, H. Ohno, H. Kato, S. Kambe, R. E. Walstedt, T. D. Matsuda, Y. Haga and Y. Ōnuki, *J. Phys.: Condens. Matter*, 2001, **13**, L785.

12. J. S. Gardner, M. J. P. Gingras and J. E. Greedan, *Rev. Mod. Phys.*, 2010, **82**, 53.

13. E. J. W. Verwey, *Nature*, 1939, **144**, 327.

14. J. P. Attfield, *Solid State Sciences*, 2006, **8**, 861.

15. N. Kumar and C. N. R. Rao, *Chem. Phys. Chem.*, 2003, **4**, 439.

16. J. M. Tranquada, *J. Phys. Chem. Solids*, 1998, **59**, 2150.

17. E. J. Verwey and P. J. Haayman, *Physica*, 1941, **9**, 979.

18. E. J. Verwey, P. W. Haayman and F. C. Romeijn, *J. Chem. Phys.*, 1947, **15**, 181.

19. F. Walz, *J. Phys.: Condens. Matter*, 2002, **14**, R285.

20. M. S. Senn, J. P. Wright and J. P. Attfield, *Nature*, 2012, **481**, 173.

21. M. S. Senn, I. Loa, J. P. Wright and J. P. Attfield, *Phys. Rev. B*, 2012, **85**, 125119.

22. L. R. Bickford, *Phys. Rev.*, 1950, **78**, 449.

23. F. J. Morin, *Phys. Rev. Lett.*, 1959, **3**, 34.

24. R. F. Janninck and D. H. Whitmore, *J. Phys. Chem. Solids*, 1966, **27**, 1183.

25. J. M. Booth and P. S. Casey, *Phys. Rev. Lett.*, 2009, **103**, 086402.

26. V. Eyert, *Europhys. Lett.*, 2002, **58**, 851.

27. J. B. Goodenough, *J. Solid State Chem.*, 1971, **3**, 490.

28. T. Sakata, K. Sakata and I. Nishida, *Phys. Stat. Sol.*, 1967, **20**, K155.

29. L. H. Bennett, C. H. Page and L. J. Swartzendruber, *J. Res. Nat. Bur. Stand.*, 1978, **83**, 9.

30. J. B. Goodenough and A. L. Loeb, *Phys. Rev.*, 1955, **98**, 391.

31. J. B. Goodenough, *Phys. Rev.*, 1955, **100**, 564.

32. J. B. Goodenough, *J. Phys. Chem. Solids*, 1958, **6**, 287.

33. J. Kanamori, *J. Phys. Chem. Solids*, 1959, **10**, 87.

34. J. A. Gonzalo, D. E. Cox and G. Shirane, *Phys. Rev.*, 1966, **147**, 415.

35. J. R. Gavarri, G. Calvarin and B. Chardon, *J. Solid State Chem.*, 1983, **47**, 132.

36. J. R. Gavarri and A. W. Hewat, *J. Solid State Chem.*, 1983, **49**, 14.

37. R. Chater, J. R. Gavarri and A. Hewat, *J. Solid State Chem.*, 1985, **60**, 78.

38. E. O. Wollan and W. C. Koehler, *Phys. Rev.*, 1955, **100**, 545.

39. J. B. Goodenough, *Phys. Rev.*, 1960, **117**, 1442.

40. S. A. J. Kimber and J. P. Attfield, *J. Mater. Chem.*, 2007, **17**, 4885.

41. A. Teichert and H. K. Müller-Buschbaum, *Z. Anorg. Allg. Chem.*, 1991, **598/599**, 319.

42. A. Poole, A. S. Wills and E. Lelièvre-Berna, *J. Phys.: Condens. Matter*, 2007, **19**, 452201.

43. A. S. Wills, M. E. Zhitomirsky, B. Canals, J. P. Sanchez, P. Bonville, P. Dalmas de Réotier and A. Yaouanc, *J. Phys.: Condens. Matter*, 2006, **18**, L37.

44. I. Mirebeau, A. Apetrei, J. Rodríguez-Carvajal, P. Bonville, A. Forget, D. Colson, V. Glazkov, J. P. Sanchez, O. Isnard and E. Suard, *Phys. Rev. Lett.*, 2005, **94**, 246402.

45. N. Taira, M. Wakeshima, Y. Hinatsu, A. Tobo and K. Ohoyama, *J. Solid State Chem.*, 2003, **176**, 165.

46. S. T. Bramwell and M. J. P. Gingras, *Science*, 2001, **294**, 1495.

47. M. J. Harris, S. T. Bramwell, D. F. McMorrow, T. Zeiske and K. W. Godfrey, *Phys. Rev. Lett.*, 1997, **79**, 2554.

48. A. P. Ramirez, A. Hayashi, R. J. Cava, R. Siddharthan and B. S. Shastry, *Nature*, 1999, **399**, 333.

49. K. Matsuhira, Y. Hinatsu, K. Tenya and T. Sakakibara, *J. Phys.: Condens. Matter*, 2000, **12**, L649.

50. L. Balents, *Nature*, 2010, **464**, 199.

2 Experimental Techniques

2.1 Synthesis Methods

2.1.1 Solid State Synthesis

All the materials were synthesised using the ceramic method. Synthesis details are provided for specific compounds in the individual results chapters. Stoichiometric amounts of high-purity metal and metal oxide powders were ground together using a pestle and mortar then heated in a furnace to promote a solid-state reaction. The powders react in the solid state by diffusion of ions at the interface of the solids and therefore it is important that the reactants are mixed and ground thoroughly to maximise surface contact throughout the mixture; materials are also reground between heat treatments for this reason. Diffusion is achieved by heating the powders at high temperatures; in this work temperatures between 550 °C and 1200 °C were used. For some of the materials prepared, reactions within evacuated sealed silica tubes were necessary to achieve the desired oxidation states: the schafarzikite-related materials contain Fe^{2+} and Sb^{3+} which become oxidised when heated in air.

2.2 X-ray Diffraction

X-rays are electromagnetic radiation with a wavelength of around 1 Å, and since this is similar to the distance between atoms in a solid they can be scattered by crystalline materials to give structural information. The X-rays interact with electrons to give a diffraction pattern that is characteristic for a particular solid. Further information about the details of X-ray diffraction can be found in the literature[1-3].

The X-rays are produced by bombarding a metal target, usually copper, with a beam of electrons which, for those with sufficient energy, will ionise electrons from the 1*s* orbital, the *K*-shell, of Cu leaving a core hole. An electron from a higher-energy orbital

will then drop down to fill the hole, emitting X-ray radiation of a particular wavelength corresponding to the energy of the transition. If the higher energy orbital is a 2*p* orbital this gives the *K*α transition which provides a doublet (*K*α_1 and *K*α_2) with two slightly different energies due to the two possible spin states of the 2*p* electron ($_{\alpha}$ = 1.5406 Å and $_{\alpha}$ = 1.5443 Å). The transitions from higher-energy orbitals are present against a background of white radiation and a Ni filter or a crystal monochromator can be used to filter out the unwanted radiation. A Ni filter will absorb radiation with a wavelength above 1.488 Å as this corresponds to the energy needed to ionise the 1*s* electrons of Ni. This lies between the energy of the Cu *K*α transition and the next intense line in the X-ray spectrum of Cu, the *K*β transition, therefore a Ni filter absorbs Cu *K*β radiation and most of the white radiation leaving the Cu *K*α doublet to be used in the diffraction experiment. A crystal monochromator is a large single crystal and is used to provide radiation of a single wavelength. It is oriented so that a strongly diffracting set of lattice planes is at the Bragg angle to the incident beam and the Bragg angle is calculated to diffract X-rays arising from the more intense *K*α_1 transition.

In this study room temperature diffraction data were collected using monochromated radiation (Cu Kα_1, wavelength 1.5406 Å) and Bruker D8 diffractometers. One of the two diffractometers used was operating in transmission mode and the other diffractometer was operating in reflection mode. The diffractometers each use a curved germanium crystal monochromator and a moveable 3 °2θ position sensitive detector; a step size of approximately 0.02 ° was used.

In a powder, crystals are present in many random orientations and X-rays are diffracted from those at the correct angle to give a diffraction pattern showing intensity versus angle (in º2θ) of the diffracted beam. Information can be obtained from the positions, intensities and shapes of the peaks in the pattern. The peak positions, or

d-spacings, show how far apart planes of diffracting atoms are from one another and therefore give the size of the unit cell; the intensities give information about the positions of atoms within the unit cell and the types of atom present whereas the peak shapes are affected by the size and shape of the crystallites.

As it is the electrons that X-rays interact with, heavy atoms scatter the X-ray beam more strongly than light atoms. The power of an atom to scatter an incident beam of radiation is given by its form factor (or scattering factor), *f*, which for X-ray diffraction is proportional to atomic number. The consequence of this is that, when using X-rays, light atoms can be difficult to locate and it can be hard, or impossible, to differentiate between elements with similar atomic numbers. The form factor also depends on the scattering angle and on the X-ray wavelength. This is because phase differences between waves scattered from different parts of the atom cause partial destructive interference. The phase differences are increased at higher 2θ values and cause more cancellation for shorter X-ray wavelengths. X-ray diffraction patterns therefore have weak intensities at high angles.

The interactions of waves scattered from all the atoms in the unit cell are described by the structure factor, F_{hkl}:

$$F_{hkl} = \sum_j f_j \exp\left[2\pi i\left(hx_j + ky_j + lz_j\right)\right] \tag{2.1}$$

The structure factor can be calculated for a particular *hkl* reflection using the atomic coordinates and form factors of all the atoms. The intensity of the reflection is proportional to the square of the structure factor:

$$I_{hkl} \propto {F_{hkl}}^2 \tag{2.2}$$

To calculate the intensity of a reflection, several additional factors must be taken into account:

- Thermal motion: diffraction experiments record average atomic positions but in reality the atoms move about their equilibrium positions causing their scattering power to fall off more quickly
- Anomalous dispersion: the X-rays can cause some elements to fluoresce which reduces their scattering power
- Multiplicity of the Bragg planes: the number of equivalent *hkl* planes
- Absorption correction: some of the X-rays are absorbed by the sample rather than scattered
- The Lorentz correction: this relates to the time for which various lattice planes are in the correct position to satisfy Braggs law
- Polarisation correction: the unpolarised X-ray beam can become partially polarised by the diffraction process

2.3 Neutron Diffraction

Neutrons can also be used to investigate crystalline structures as they are predominantly scattered by atomic nuclei to give a diffraction pattern similar to that of X-rays.[4] However there are some important differences between the two techniques.

There are two ways in which neutrons are generated for use in diffraction experiments: in a reactor or by spallation. Neutron powder diffraction measurements were carried out at the Institut Laue-Langevin (ILL) in Grenoble, France and at the Paul Scherrer Institut (PSI) in Villigen, Switzerland each of which generate neutrons in a different way.

At the ILL high-energy neutrons are produced in a nuclear reactor from the fission reaction of highly enriched ^{235}U. Heavy water, D_2O, is used as a moderator to equilibrate the neutrons at ambient temperatures providing thermal neutrons with wavelengths of 1-2 Å that can be used for diffraction.

The PSI uses a spallation source; a high-energy proton beam is accelerated in a cyclotron and then fired at a heavy-metal target causing it to release neutrons. At the PSI this is a lead target in a tube within a moderator tank of D_2O which slows the neutrons down producing thermal neutrons. The PSI resembles a reactor although it is a spallation source.

Once the thermal neutrons have been generated they are led to the instruments through evacuated beam tubes. They pass through a collimator and then the wavelength is selected by reflection from a specific plane of a crystal monochromator.

This differs from X-ray diffraction because a broad spectrum of neutron wavelengths is produced and the desired wavelength is selected by the monochromator. Therefore most of the neutrons are not used, giving a weaker beam of radiation. Neutrons also penetrate further into materials than X-rays and for these reasons larger samples sizes and longer collection times are required for neutron diffraction studies.

Constant-wavelength neutron powder diffraction (NPD) data were collected from samples in vanadium cans at the ILL in France, using the high-resolution powder diffractometer D2B (Fig. 2.1) at 298 K and 4 K using a wavelength of 1.5943 Å, and at the PSI in Switzerland, using the high-resolution powder diffractometer for thermal neutrons (HRPT) (Fig. 2.2) at 300 K, 50 K, 2 K and 1.5 K using a wavelength of 1.8857 Å. D2B uses a Ge crystal monochromator and 128 200 mm high ^{3}He counting tube detectors at 1.25 º intervals to take measurements within a range of 5 to 165 º2θ.[5] HRPT uses a Ge crystal monochromator and a large position sensitive ^{3}He detector with 1600 (25 x 64) wires with an angular separation of 0.1 º; measurements can be taken up to 165 º2θ.[6-7] The NPD data reported in Chapter 3 were collected at the ILL and the NPD data reported in Chapters 4, 6 and 7 were collected at the PSI.

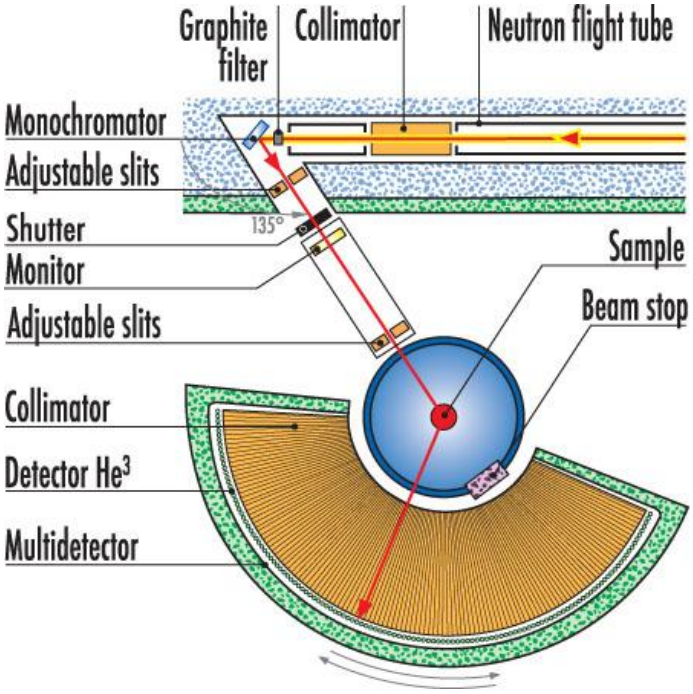

***Fig. 2.1**: Diagram of D2B instrument layout.*[5]

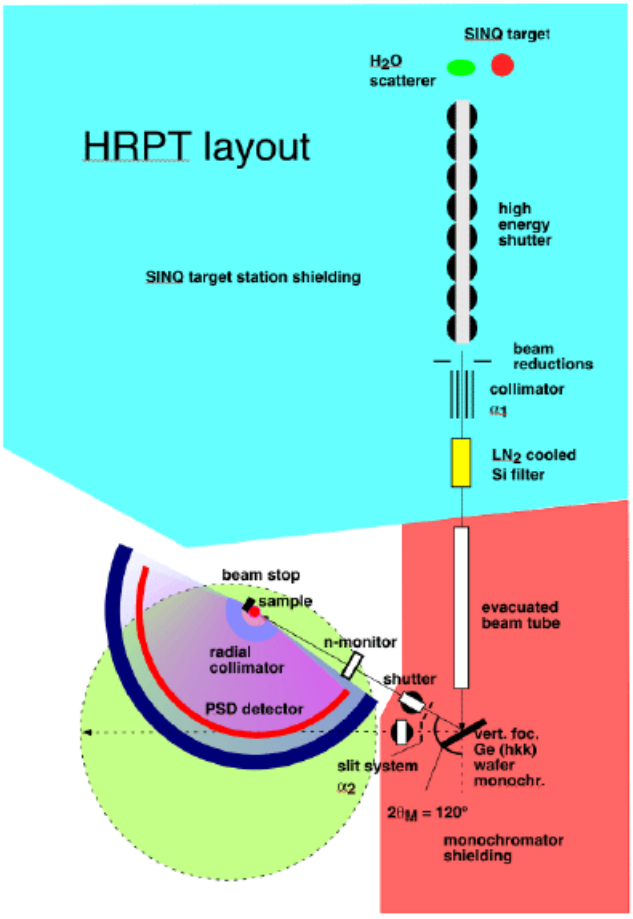

***Fig. 2.2**: Diagram of HRPT instrument layout.*[6]

Neutrons are scattered by the nuclei, rather than the electron cloud, resulting in some significant differences between NPD and X-ray diffraction. The nucleus is much smaller than the electron cloud and can be regarded as a point scatterer. The form factor, therefore, does not decrease with increasing º2θ and neutron diffraction patterns remain intense at high angles. The scattering powers of atoms do not increase linearly with atomic number; light atoms can be strong neutron scatterers, and isotopes of the same element can scatter very differently from one another. Consequently, neutron diffraction can be used to distinguish between elements with similar atomic numbers and to locate accurately light atoms within a crystal structure.

The structure factor for neutrons is similar to that for X-rays (Equation 2.1) but the form factor, f, is replaced by the neutron scattering length, b:

$$F_{hkl} = \sum_j b_j \exp\left[2\pi i\left(hx_j + ky_j + lz_j\right)\right] \tag{2.3}$$

In this work mixed metal oxides were studied containing heavy elements, including Sb, Pb, Bi and various lanthanides, whose strong scattering dominates X-ray diffraction patterns. Neutron diffraction is required in addition to X-ray diffraction to obtain accurate oxygen positions and bond lengths. The majority of compounds prepared also order magnetically and neutrons, unlike X-rays, can be used to study magnetic structures.

Neutrons posses a magnetic moment and can therefore interact with unpaired electrons revealing the magnetic properties of a material. Neutron diffraction can detect the ordering of electron spins which gives rise to increased intensity of various reflections and, depending on the type of ordering, the presence of additional Bragg peaks. Neutron diffraction measurements can be taken at various temperatures to study materials above and below magnetic ordering transitions. Because the magnetic scattering arises from the interaction with electrons and not nuclei, the atoms have a form factor, similar to that for

X-ray diffraction, which decreases with increasing scattering angle. However the form factors are not identical as neutrons are only scattered by the unpaired electrons, rather than all the electrons, causing the intensity to fall off more rapidly.

2.4 Rietveld Refinement

Rietveld refinements were performed on both X-ray- and neutron-diffraction data using the General Structure Analysis System (GSAS)[8] and the graphical user interface EXPGUI[9].

Rietveld refinement uses a least-squares method to get the best fit between an entire observed pattern and an entire calculated pattern by adjusting variables that relate to the crystal structure and to the instrument.[10-12]

Powder diffraction patterns are made up of independent diffraction peaks and in all patterns, except the simplest ones, these peaks show some degree of overlap with one another. Each peak has its own height, position, width and integrated area and using the total integrated intensity of the groups of overlapping peaks leads to a loss of information. The Rietveld method uses a diffraction data file which has the intensity recorded typically at thousands of equal steps; in this case the steps are in scattering angle, º2θ. All the individual points are used in the refinement to get the maximum amount of information from the diffraction pattern.

As the structure is being refined, a reasonably good starting model is needed whose structure is put into the program and is refined along with profile parameters, such as the peak shape and halfwidth, to give the best fit with the observed pattern. All the individual points are compared with the calculated pattern, and the residual, S_y, which represents the difference between the observed and calculated intensities, is minimised in the least-squares refinement:

$$S_y = \sum w_i\left(y_i(obs) - y_i(calc)\right)^2 \tag{2.4}$$

- w_i = weighting factor = $1/y_i$
- $y_i(obs)$ = observed intensity at step i
- $y_i(calc)$ = calculated intensity at step i

To assess the fit between the calculated data and the observed data, several R-values are used.[12]

$$R_p = \frac{\sum|y_i(obs) - y_i(calc)|}{\sum y_i(obs)} \tag{2.5}$$

$$R_{wp} = \left\{\frac{\sum w_i\left(y_i(obs) - y_i(calc)\right)^2}{\sum w_i\left(y_i(obs)\right)^2}\right\}^{1/2} \tag{2.6}$$

$$R_e = \left\{\frac{n-p}{\sum w_i\left(y_i(obs)\right)^2}\right\}^{1/2} \tag{2.7}$$

- R_p = R-pattern, R_{wp} = R-weighted pattern, R_e = R-expected
- n = number of observations
- p = number of parameters

The goodness of fit is given as a value of χ^2:

$$\chi^2 = \left(\frac{R_{wp}}{R_e}\right)^2 \tag{2.8}$$

For a good fit, values of χ^2 should normally be between 1 and 4.

2.5 SQUID Magnetometry

The magnetisation of a material can be measured using a magnetic property measurement system (MPMS). The MPMS includes the following superconducting components: a superconducting magnet, a superconducting detection coil, a superconducting quantum interference device (SQUID) and a superconducting magnetic shield which surrounds the SQUID.

The SQUID is a very sensitive magnetometer which can detect small changes in magnetic fields. It consists of a superconducting loop containing one or two Josephson junctions[13]. The magnetic field from the sample is not directly detected using the SQUID; an external magnetic field is applied using the superconducting magnet then a measurement is taken by moving the sample slowly though a system of superconducting detection coils. The magnetic moment of the sample induces a change in the magnetic flux of the coils which are connected to the SQUID with superconducting wires. This gives a change in the current and produces variations in the SQUID output voltage proportional to the magnetic moment of the sample.

Magnetic data were collected using a Quantum Design MPMS[14]. Zero-field cooled and field cooled data were collected between 5 and 300 K using applied fields of 100, 500 or 1000 Oe. Measurements were taken at 5 K intervals using sweep mode and a heating rate of 10 K per min. For the spin-glass study of $Bi_{2-x}Fe_x(FeSb)O_7$ in Chapter 6 and for the sample Ho_2CrSbO_7 in Chapter 7, more detailed magnetic data were obtained by taking measurements at smaller intervals and using slower heating rates.

Hysteresis measurements were taken at 5 K between -20000 and +20000 Oe and between -50000 and 50000 Oe.

2.6 Mössbauer Spectroscopy

Mössbauer spectroscopy is a technique in which γ-radiation is used to probe transitions within atomic nuclei. Nuclear energy levels are modified by their surrounding environments and Mössbauer spectroscopy can therefore be used to provide chemical, structural and magnetic information about a material.[15] Although the Mössbauer effect has been detected in many isotopes only some are suitable for practical use and most commonly ^{57}Fe is studied. All the Mössbauer data reported in this work were collected and interpreted by Professor Frank J. Berry.

The decay of radioactive nuclei in excited states produces γ-rays which can be absorbed by nuclei of the same isotope, provided that their energies are not affected by nuclear recoil. To detect subtle changes in the nuclear energy levels, the γ-ray energy is modified using the Doppler Effect: the γ-ray source is vibrated back and forth relative to the absorber. The resultant Mössbauer spectrum shows γ-ray transmission, or absorption, against velocity in mm s^{-1}. The parameters obtained from a Mössbauer spectrum are the chemical isomer shift, the quadrupole splitting and the magnetic hyperfine splitting.

The chemical isomer shift, δ, arises when the nuclei in the absorber and the source are in different environments. The energy gap between their ground and excited states is therefore different, shifting the absorbed γ-ray energy from zero velocity by a value, δ, (Fig. 2.3). This is due to the electric monopole interaction between the nuclear and electronic charges; it is affected by changes in electron density at the nucleus and can therefore be used to investigate oxidation states and covalency effects. For example in ^{57}Fe Mössbauer spectroscopy Fe^{2+} has a more positive isomer shift than Fe^{3+} because it has more *d*-electrons which provide greater screening of the nucleus from the outer *s*-electrons.

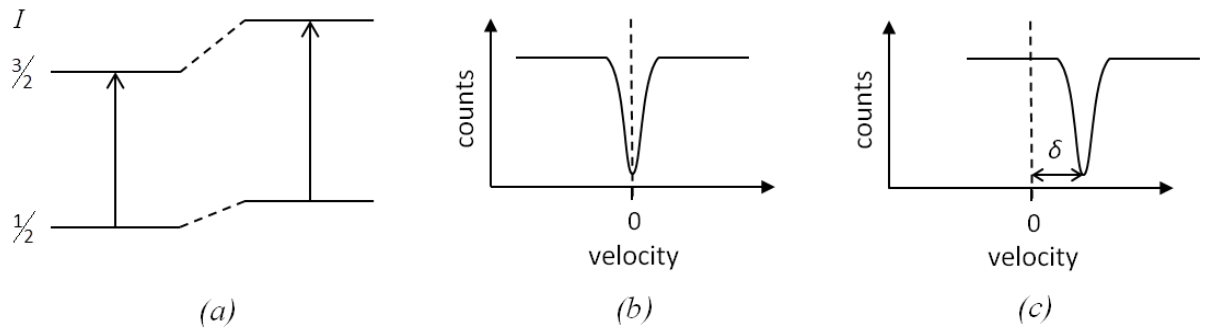

***Fig. 2.3**: (a) Modification of ^{57}Fe nuclear energy levels by chemical isomer shift and the transition that occurs, (b) Mössbauer spectrum with sample and source in the same environment and (c) the effect of chemical isomer shift on the Mössbauer spectrum.*

The quadrupole splitting, Δ, is seen if a nucleus has a nuclear spin quantum number, $I > ½$ as it will have a non-spherical charge distribution and a nuclear quadrupole moment. If an asymmetric electric field is present, from an asymmetric arrangement of electrons or surrounding atoms, the nuclear quadrupole moment will interact with it causing the nuclear energy levels to split. This results in splitting of absorption lines in the Mössbauer spectrum by an amount, Δ, and gives information about bonding and local structure. For ^{57}Fe a two-line spectrum is seen as the excited state splits into two substates giving rise to two possible transitions (Fig. 2.4). High spin Fe^{2+} has a larger quadrupole splitting than high spin Fe^{3+} as Fe^{2+} has an asymmetric d^6 configuration whereas Fe^{3+} has a symmetric d^5 configuration.

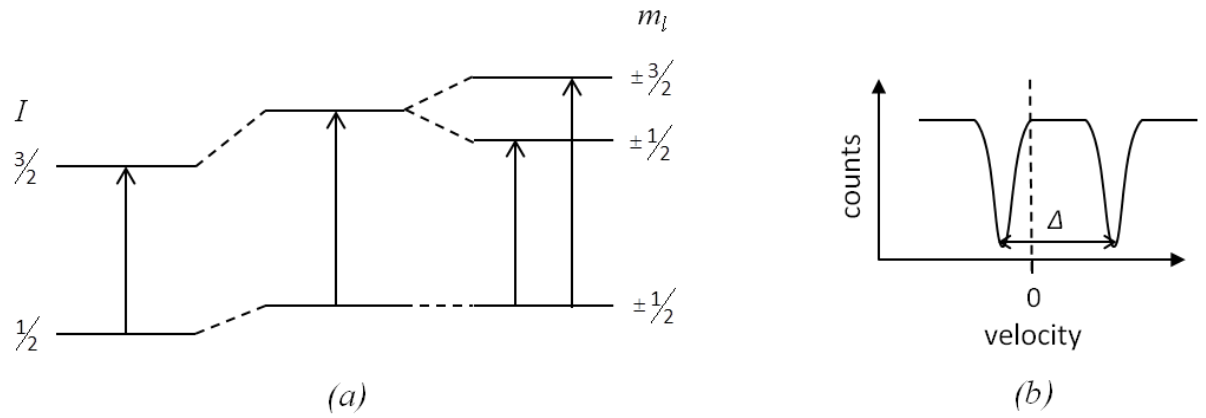

***Fig. 2.4**: (a) The effect of quadrupole splitting on the nuclear energy levels of ^{57}Fe and the transitions that occur and (b) the resultant Mössbauer spectrum.*

The magnetic hyperfine splitting is observed because nuclei with spin, $I > 0$ interact with magnetic fields via a magnetic dipole interaction. This interaction splits the absorption lines in the Mössbauer spectrum as it removes the degeneracy of the nuclear energy levels causing them to split into $2I + 1$ substates. The magnetic hyperfine field at the nucleus is caused by the spin of unpaired electrons therefore the magnetic splitting gives information about electronic structure and magnetic properties. In ^{57}Fe the ground state splits into two substates and the excited state splits into four substates resulting in six possible transitions and a six line spectrum due to selection rules (Fig. 2.5).

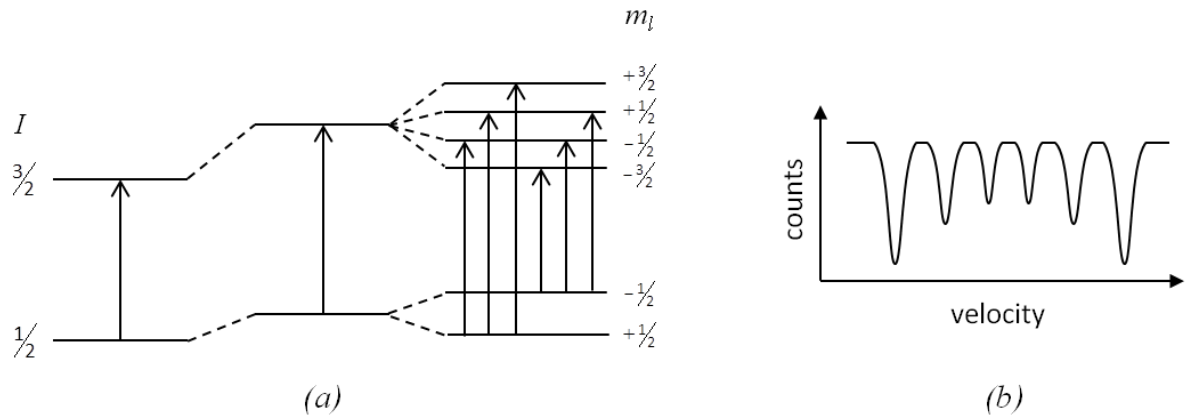

***Fig. 2.5**: (a) The effect of magnetic splitting on the nuclear energy levels of ^{57}Fe and the transitions that occur, (b) the resultant Mössbauer spectrum.*

2.7 Thermogravimetric Analysis

Thermogravimetric analysis (TGA) is used to measure precise changes in the mass of a sample as a function of temperature or time. The sample is heated at a constant rate in a controlled atmosphere under the flow of a gas such as nitrogen, oxygen or hydrogen. A decrease in mass may be seen if the sample decomposes or if volatiles are lost, which can be measured by linking the thermogravimetric analyser to a mass spectrometer; however if the sample becomes oxidised or adsorbs gas molecules an increase in mass is observed.

In this work a Netzsch STA 449 F1 Jupiter thermogravimetric analyser was used; samples of around 100 mg were heated at a rate of 10 ºC per minute in an oxygen atmosphere.

2.8 AC Impedance

Impedance is a measure of a samples ability to oppose the flow of current. Electrodes are attached to opposite sides of a pelletized sample and an alternating voltage is applied. The current is measured and a plot which gives the capacitance and resistance of the sample is obtained from which the conductivity can be calculated.

AC impedance measurements were made using a Solartron S1 1260 Impedance/Gain-phase analyser between 300 and 450 K. Cylindrical pellets were prepared using an 8 mm diameter die with an axial force of around 1 tonne. After sintering in sealed tubes at 600 ºC, pellets with 60-70% theoretical density were formed. Opposite faces were coated with silver, to which electrical contacts were made using spring tensioned electrodes.

2.9 Scanning Electron Microscopy

Scanning electron microscopy (SEM) is used to study the morphology of a sample. An electron beam is shone across the sample surface and backscattered electrons and electrons emitted from the atoms are detected to give an image of the sample. SEM is used to study structures on the μm scale and can be used to investigate the size and shapes of particles in a powder or a pellet. The experiment takes place within an evacuated chamber and as the sample must be electrically conductive and grounded it often has to be coated with a thin layer of gold or graphite to prevent the accumulation of charge at the surface.

On some instruments, elemental analysis is possible as well as imaging. Bombarding the sample with high energy electrons causes the elements to emit X-rays

whose energy can be measured in a technique known as energy-dispersive X-ray spectroscopy (EDS). The X-ray emission spectra are characteristic of a particular element therefore the types of element present and relative amounts within a selected area can be determined. This is useful for investigating materials in which the elemental composition across the sample may not be uniform.

In this study a Jeol 6060 SEM with Oxford Inca EDS was used to study carbon coated powder samples.

2.10 Raman Spectroscopy

Raman spectroscopy is used to study the vibrational motions of atoms within a molecule or a crystal lattice.[16] Monochromatic light from a laser is shone onto the sample and two different scattering processes occur (Fig. 2.6). The majority of the light is reemitted by Rayleigh scattering and the wavelength remains unchanged, however some of the light undergoes Raman scattering and is shifted to lower energy (Stokes shift) or higher energy (anti-Stokes shift). The Raman scattering is detected to give a Raman spectrum showing the vibrational frequencies as the shift in energy (in cm^{-1}) from that of the incident radiation. For a vibrational mode to be Raman active the motions of the atoms must produce a change in the polarisability of the molecule. The number of modes expected to be seen depends on the symmetry of the molecule and can be determined using group theory.

Room temperature Raman measurements were taken using a Renishaw Invia Raman Microscope and a 532 nm laser.

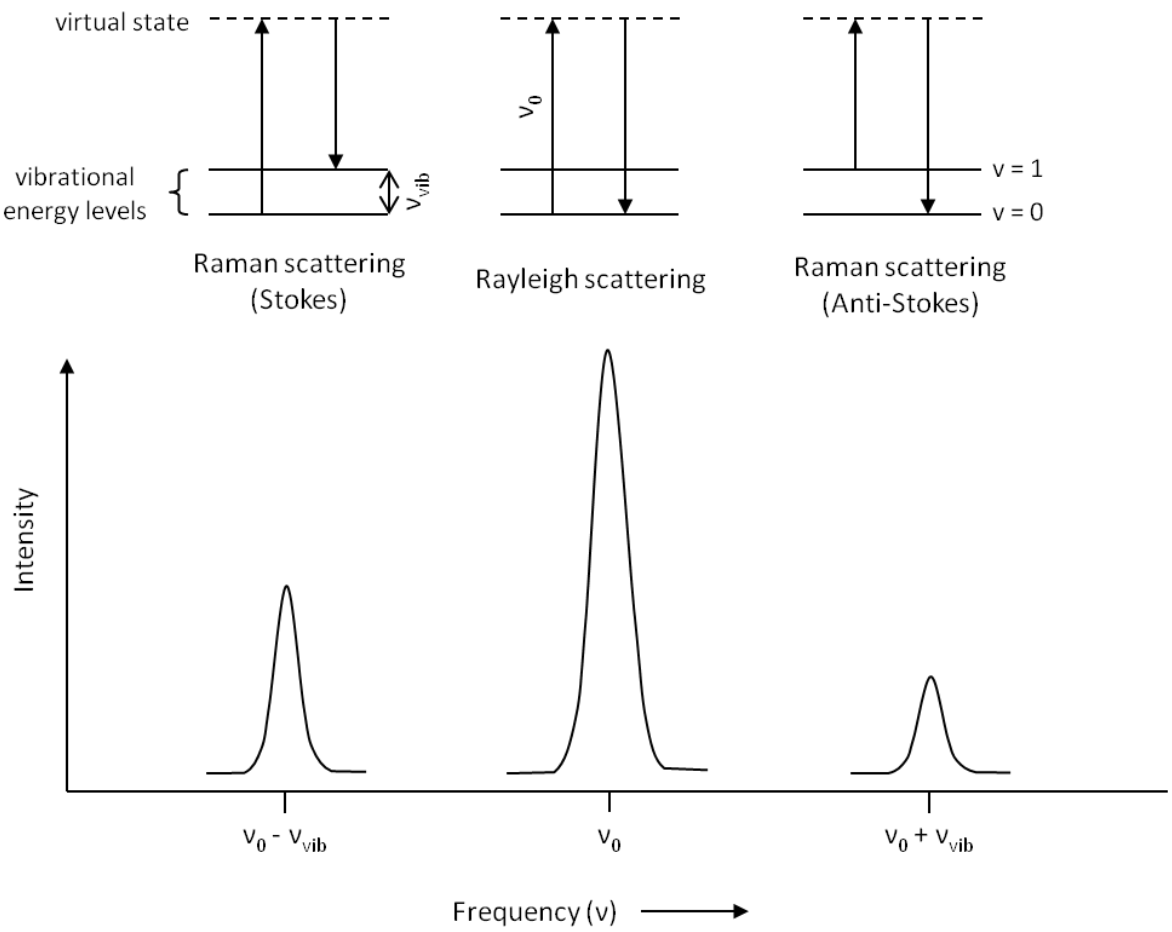

***Fig. 2.6**: Diagram showing the different scattering processes that can occur and the resultant spectrum.*

2.11 References

1. A. R. West, *Basic Solid State Chemistry*, Second edn., John Wiley & Sons Ltd., Chichester, 1999.

2. L. E. Smart and E. A. Moore, *Solid State Chemistry: An Introduction*, Third edn., CRC Press, Taylor and Francis Group, Boca Raton, FL, 2005.

3. R. E. Dinnebier and S. J. L. Billinge, *Powder Diffraction: Theory and Practice*, The Royal Society of Chemistry, Cambridge, 2008.

4. G. E. Bacon, *Neutron Diffraction*, Second edn., Clarendon Press, Oxford, 1962.

5. http://www.ill.eu/instruments-support/instruments-groups/instruments/d2b/

6. http://sinq.web.psi.ch/sinq/instr/hrpt/index.html

7. G. F. P. Fischer, M. Koch, M. Könnecke, V. Pomjakushin, J. Schefer, R. Thut, N. Schlumpf, R. Bürge, U. Greuter, S. Bondt and E. Berruyer, *Physica B*, 2000, **276-278**, 146.

8. A. C. Larson and R. B. V. Dreele, General Structure Analysis System (GSAS), Los Alamos National Laboratory Report LAUR 86-748, 1994

9. B. H. Toby, *J. Appl. Cryst.*, 2001, **34**, 210.

10. H. M. Rietveld, *Acta Cryst.*, 1967, **22**, 151.

11. H. M. Rietveld, *J. Appl. Cryst.*, 1969, **2**, 65.

12. R. A. Young, *The Rietveld Method*, Oxford University Press, Oxford, 1995.

13. B. D. Josephson, *Rev. Mod. Phys.*, 1974, **46**, 251.

14. M. McElfresh, *Fundamentals of Magnetism and Magnetic Measurements featuring Quantum Design's Magnetic Property Measuring System*, Quantum Design, 1994.

15. D. P. E. Dickson and F. J. Berry, *Mössbauer Spectroscopy*, Cambridge University Press, Great Britain, 1986.

16. E. Bright Wilson Jr, J. C. Decius and P. C. Cross, *Molecular Vibrations: The Theory of Infrared and Raman Vibrational Spectra*, Dover Publications, Inc., New York, 1980.

3 Lead-Substituted Schafarzikites, $FeSb_{2-x}Pb_xO_4$

3.1 Background

The structure of $FeSb_2O_4$ was described in detail in Section 1.2.1 and is shown in Fig. 3.1. Schafarzikite belongs to a family of compounds isostructural with red lead, Pb_3O_4, which have the general formula MX_2O_4 where M = Pb^{4+}, Sn^{4+} and X = Pb^{2+} or M = Mn^{2+}, Fe^{2+}, Co^{2+}, Ni^{2+}, Cu^{2+}, Zn^{2+}, Mg^{2+} and X = Sb^{3+}, As^{3+}.[1-3]

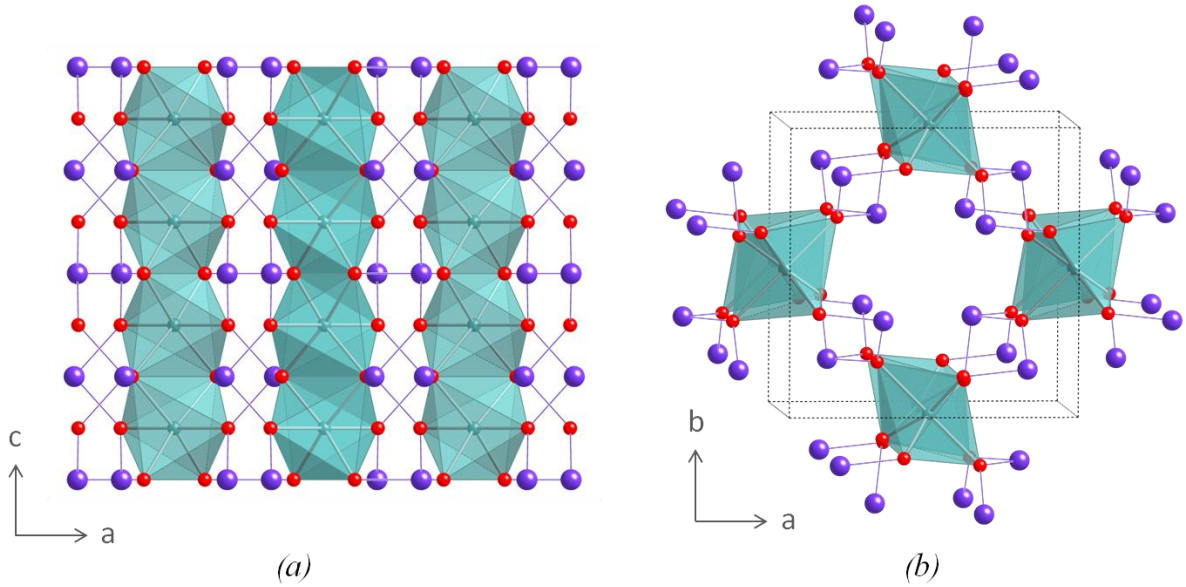

***Fig. 3.1**: The structure of schafarzikite, $FeSb_2O_4$ (a) showing the edge-linked chains and (b) looking down the c-axis. FeO_6 octahedra are shaded. Fe ions are located within the octahedra, O ions are shown as red spheres and Sb ions are shown as purple spheres.*

3.1.1 Cation Substitution in the Schafarzikite Structure

Due to the chemical similarities of Sb^{3+} and Pb^{2+} in the MX_2O_4 schafarzikites, chemical modification of the structure may be possible by substituting Pb^{2+} for Sb^{3+} with consequential oxidation of transition metal cations. So far there has only been one report of lead substitution in MX_2O_4 structures, for the compound $MnSb_2O_4$, but this resulted in oxidation of Sb^{3+}, rather than Mn^{2+}, ions[4]. The Pb^{2+} ions replaced Sb^{3+} ions on the pyramidal sites and to compensate for the loss of charge, Sb^{3+} ions were oxidised to Sb^{5+} ions. The Sb^{5+} ions then replaced Mn^{2+} ions in the octahedral chains to give multi-phase

products with the schafarzikite phase being $(Mn_{1-x}Sb_x)(Sb_{1-y}Pb_y)_2O_4$ (where x = 0-0.372 and y = 0-0.608)[4]. As the average cation size is increasing on the pyramidal sites and decreasing on the octahedral sites there are competing trends for the change in unit cell size which cause the MO_6 octahedra to become distorted. The introduction of non-magnetic Sb^{5+} ions onto the octahedral sites also resulted in a loss of magnetic ordering at higher lead concentrations. Cation ordering of the Mn^{2+} and Sb^{5+} ions occurred throughout the chains, presumably driven by electrostatic repulsions between the highly charged antimony ions.

In this chapter the successful formation of lead substituted schafarzikites, $FeSb_{2-x}Pb_xO_4$, is reported. The Sb^{3+} ions are replaced by Pb^{2+} ions inducing oxidation of Fe^{2+} to Fe^{3+} for charge balance. The synthesis, structure, magnetic and electrical properties have been investigated.

3.2 Synthesis

$FeSb_2O_4$ was prepared by heating stoichiometric amounts of Fe_2O_3 (99+ %), Sb_2O_3 (99 %) and Sb metal in an alumina crucible within an evacuated, sealed silica tube at 700 °C for 12 hours with one intermediate regrind.

The lead-substituted variants, $FeSb_{2-x}Pb_xO_4$, (x = 0.2, 0.25, 0.3, 0.4, 0.45, 0.5, 0.55, 0.6, 0.7 and 0.75) were prepared by heating $FeSb_2O_4$ with Fe_2O_3 (99+ %), Sb_2O_3 (99 %) and PbO (≥99.0 %) in the correct proportions with a 3 % molar excess of Sb_2O_3 (to compensate for a loss due to volatilisation) at 550 °C for one week with one intermediate regrind. The sample $FeSb_{1.8}Pb_{0.2}O_4$ required further regrinding and was reheated at 600 °C for 38 hours. The reactions were all carried out in alumina crucibles within evacuated, sealed silica tubes.

3.3 Results and Discussion

3.3.1 Sample Preparation and Structural Characterisation

All the samples of $FeSb_{2-x}Pb_xO_4$ (x = 0-0.75) were confirmed to be single phase from X-ray powder diffraction data (Fig. 3.2). The highest lead content successfully substituted into the structure was for the compound $FeSb_{1.25}Pb_{0.75}O_4$ in which 75 % of the Fe^{2+} is oxidised to Fe^{3+}. Formation of the pure Fe^{3+} sample, $FeSbPbO_4$, was also attempted but a mixed iron antimony lead pyrochlore was formed along with a secondary lead-substituted schafarzikite phase.

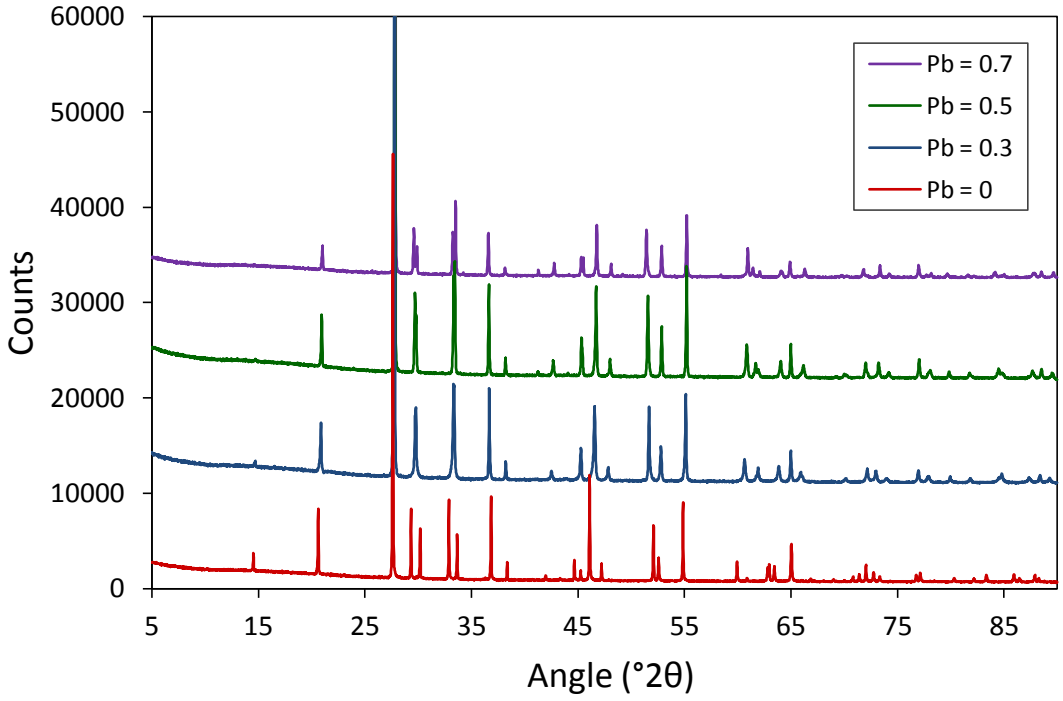

***Fig. 3.2**: Stack plot of X-ray powder diffraction patterns for $FeSb_{2-x}Pb_xO_4$ where x = 0, 0.3, 0.5, 0.7.*

Mössbauer spectra were recorded from the samples and interpreted by Professor Frank J. Berry. ^{121}Sb Mössbauer spectra of $FeSb_2O_4$ and $FeSb_{1.5}Pb_{0.5}O_4$ showed that antimony was only present in the +3 oxidation state, characterised by a single resonance at δ = 11.84 mm s^{-1}. ^{57}Fe Mössbauer studies on initial samples of $FeSb_{2-x}Pb_xO_4$ found that the Fe^{2+}:Fe^{3+} ratios were incorrect. The sample $FeSb_{1.5}Pb_{0.5}O_4$ was shown to have significantly

more Fe^{3+} than Fe^{2+} (Fe^{3+}:Fe^{2+} ≈ 2:1) which suggested that there was a deficiency of either lead or antimony in the sample. As antimony oxide is fairly volatile it was assumed to be the latter and the formation of a schafarzikite with antimony vacancies, $FeSb_{2-x}O_4$, was attempted. This was unsuccessful and instead $FeSb_2O_4$ was formed with Fe_3O_4 and other small impurities. The lead substituted samples were remade using a small excess of Sb_2O_3 to compensate for the loss and ^{57}Fe Mössbauer spectroscopy measurements were retaken. The ^{57}Fe Mössbauer spectrum of $FeSb_{1.5}Pb_{0.5}O_4$ recorded at 298 K is shown in Fig. 3.3 and is best fit to two quadrupole split absorptions. The first doublet has a chemical isomer shift, δ, of 0.49(2) mm s^{-1} and quadrupole splitting, Δ, of 0.87(4) mm s^{-1}; it is characteristic of Fe^{3+} and accounts for 58 % of the spectral area. The second doublet has δ = 1.01(2) mm s^{-1} and Δ = 1.74(4) mm s^{-1}; it is characteristic of Fe^{2+} and accounts for 42 % of the spectral area. Within the errors (±5 %) the result is indicative of nearly equal amounts of iron in each oxidation state and is consistent the composition $FeSb_{1.5}Pb_{0.5}O_4$. The ^{57}Fe Mössbauer spectrum of $FeSb_2O_4$ is reported in the literature.[5]

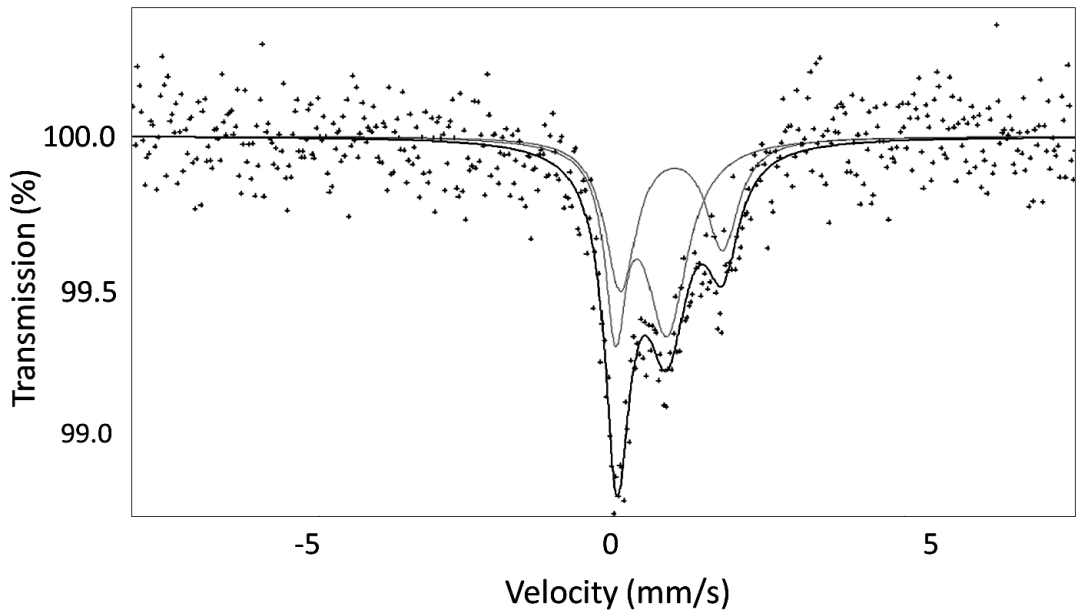

***Fig. 3.3**: ^{57}Fe Mössbauer spectrum recorded from $FeSb_{1.5}Pb_{0.5}O_4$ at 298 K.*

Structure refinement based on X-ray powder diffraction (XRPD) and neutron powder diffraction (NPD) data used $FeSb_2O_4$ [6] as a starting model with the tetragonal space group $P4_2/mbc$. Rietveld refinements of XRPD data for $FeSb_2O_4$ and $FeSb_{1.5}Pb_{0.5}O_4$ are shown in Fig. 3.4. Refined parameters included the background, zero-point error, scale factor, unit cell parameters, atomic positions, thermal parameters, Sb/Pb fractional occupancy and profile parameters relating to the halfwidth, asymmetry and crystallite size. As the Sb and Pb atoms share the same site their atomic coordinates were constrained to be equal and the overall occupancy of the site was constrained to 1.

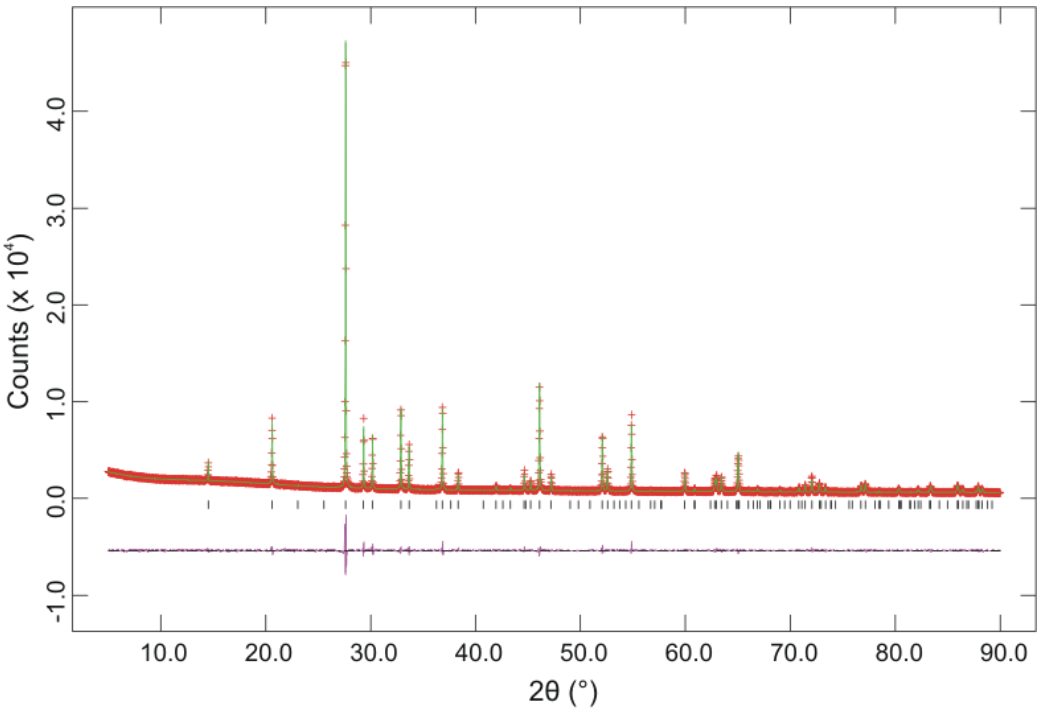

(a)

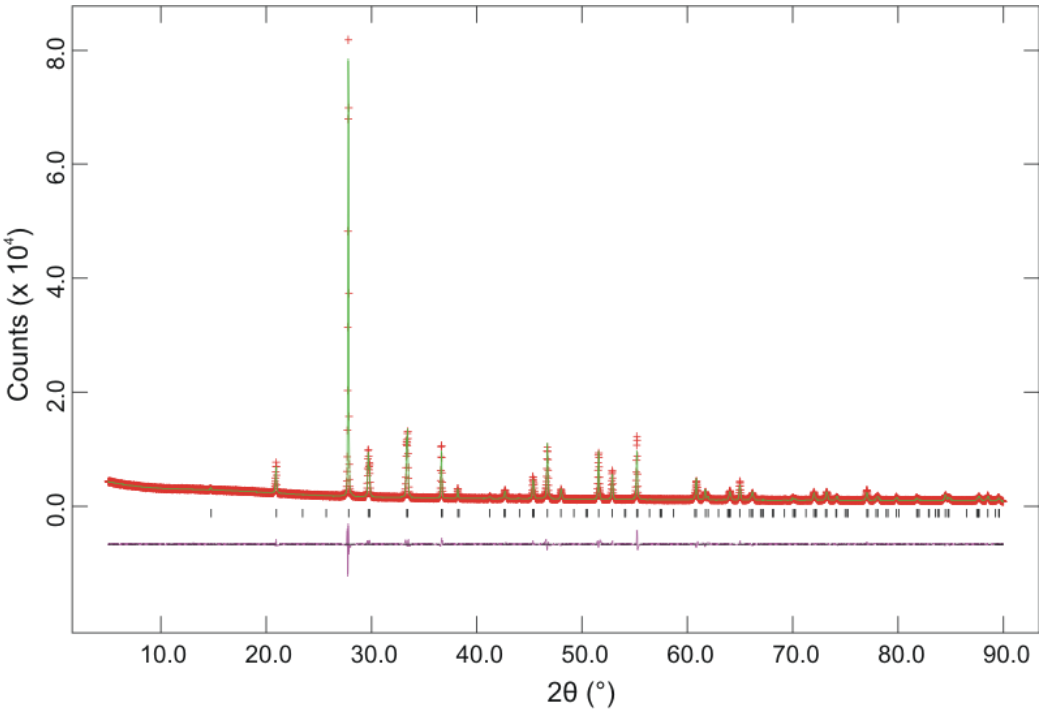

(b)

***Fig. 3.4**: Observed, calculated and difference plots for room temperature XRPD data recorded from (a) $FeSb_2O_4$ and (b) $FeSb_{1.5}Pb_{0.5}O_4$.*

For the X-ray data, as the compounds contain light oxygen atoms along with heavy antimony and lead atoms, the thermal parameters were unreliable and were therefore all constrained to be equal. The unit cell parameters and volume, obtained from the structural refinements of XRPD data of $FeSb_{2-x}Pb_xO_4$, are shown in Table 3.1.

***Table 3.1**: Unit cell parameters from Rietveld refinement of XRPD data for $FeSb_{2-x}Pb_xO_4$*

Sample	*a* (Å)	*c* (Å)	volume (Å³)
$FeSb_2O_4$	8.59621(7)	5.91014(5)	436.729(9)
$FeSb_{1.8}Pb_{0.2}O_4$	8.5388(2)	5.9524(2)	434.00(3)
$FeSb_{1.75}Pb_{0.25}O_4$	8.5135(2)	5.9650(1)	432.34(2)
$FeSb_{1.7}Pb_{0.3}O_4$	8.4973(1)	5.98891(9)	432.42(2)
$FeSb_{1.6}Pb_{0.4}O_4$	8.4763(1)	5.99696(8)	430.87(1)
$FeSb_{1.55}Pb_{0.45}O_4$	8.4720(1)	6.00688(8)	431.14(1)
$FeSb_{1.5}Pb_{0.5}O_4$	8.4678(1)	6.01050(8)	430.98(1)
$FeSb_{1.45}Pb_{0.55}O_4$	8.4595(1)	6.01494(9)	430.45(2)
$FeSb_{1.4}Pb_{0.6}O_4$	8.4607(1)	6.0233(1)	431.17(2)
$FeSb_{1.3}Pb_{0.7}O_4$	8.4577(1)	6.03652(9)	431.81(2)

There are two competing trends for the change in unit cell size as more lead is introduced into the structure which are reflected by the change in unit cell parameters. The Sb^{3+} ions are being replaced by larger Pb^{2+} ions, increasing the overall size on the pyramidal sites, but the Fe^{2+} ions are being oxidised to smaller Fe^{3+} ions, decreasing the overall size on the octahedral sites (ionic radii[7]: Sb^{3+} = 0.76 Å, Pb^{2+} = 0.98 Å, Fe^{2+} = 0.78 Å, Fe^{3+} = 0.645 Å). This causes the *a*-parameter to decrease and the *c*-parameter to increase. The unit cell volume decreases as *x* increases but in a non-linear fashion and the difference in volume for Pb contents of 0.25-0.7 is small. These changes can be explained further by looking at the bond lengths and angles which are obtained accurately using neutron diffraction data. Rietveld refinements of room temperature NPD data for $FeSb_2O_4$ and $FeSb_{1.5}Pb_{0.5}O_4$ are shown in Fig. 3.5 and the refined structural parameters for $FeSb_{2-x}Pb_xO_4$ where x = 0, 0.3, 0.45, 0.5 and 0.7 are summarised in Table 3.2.

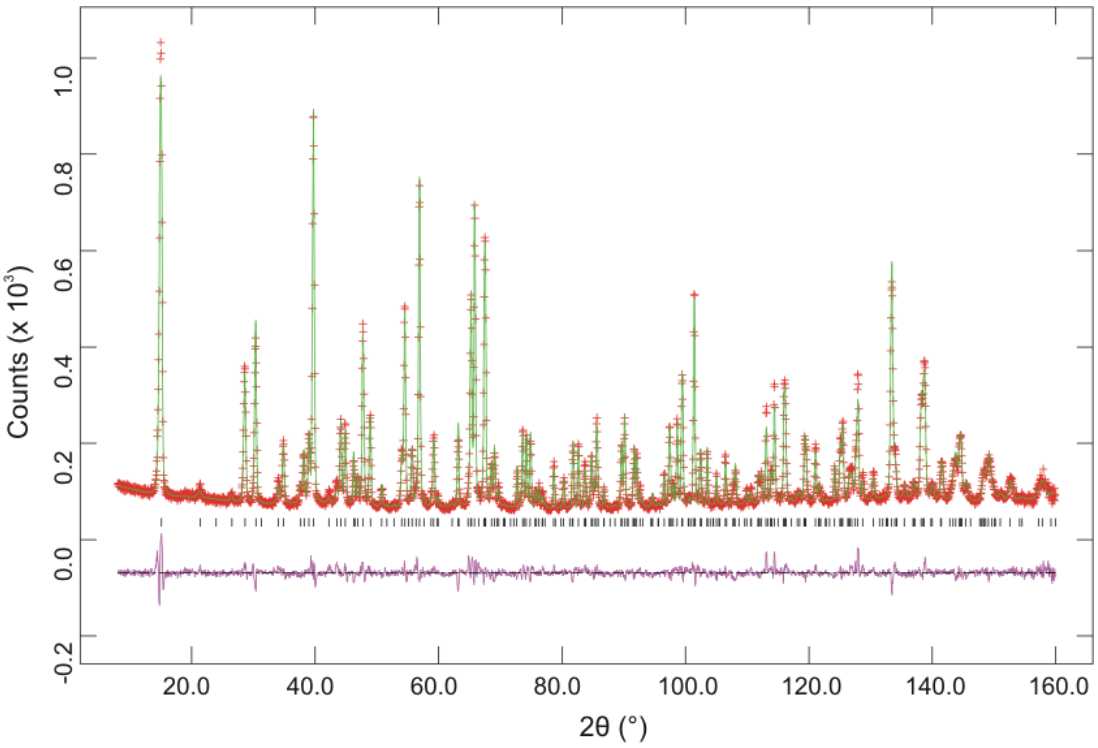

(a)

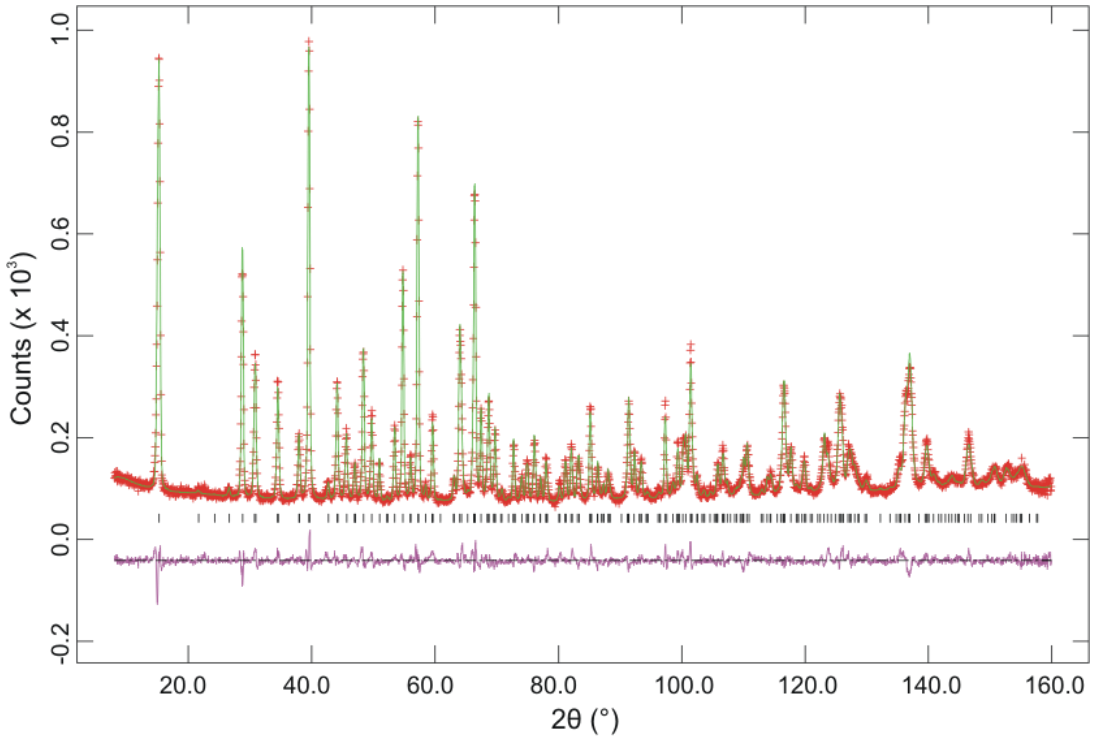

(b)

***Fig. 3.5**: Observed, calculated and difference plots for high resolution NPD data recorded from (a) $FeSb_2O_4$ and (b) $FeSb_{1.5}Pb_{0.5}O_4$ at 298 K.*

***Table 3.2**: Structural parameters refined from high resolution NPD data for $FeSb_{2-x}Pb_xO_4$ at 298 K*

		$FeSb_2O_4$	$FeSb_{1.7}Pb_{0.3}O_4$	$FeSb_{1.55}Pb_{0.45}O_4$	$FeSb_{1.5}Pb_{0.5}O_4$	$FeSb_{1.3}Pb_{0.7}O_4$
a (Å)		8.61574(9)	8.5032(3)	8.4850(2)	8.4833(2)	8.4671(2)
c (Å)		5.92069(8)	5.9935(2)	6.0153(1)	6.0210(1)	6.0425(2)
volume (Å³)		439.50(1)	433.36(2)	433.07(2)	433.31(1)	433.20(2)
Fe	U_{iso} (Å²)	0.0123(3)	0.0068(4)	0.0098(3)	0.0098(3)	0.0081(4)
Sb/Pb	*x*	0.1772(2)	0.1685(4)	0.1657(3)	0.1649(2)	0.1605(3)
Sb/Pb	*y*	0.1648(2)	0.1613(4)	0.1596(3)	0.1588(3)	0.1583(3)
Sb/Pb	U_{iso} (Å²)	0.0127(3)	0.0129(6)	0.0179(4)	0.0177(4)	0.0166(6)
O1	*x*	0.6794(1)	0.6763(2)	0.6748(2)	0.6743(2)	0.6733(2)
O1	*y*	0.1794(1)	0.1763(2)	0.1747(2)	0.1743(2)	0.1733(2)
O1	U_{iso} (Å²)	0.0196(4)	0.0199(6)	0.0221(4)	0.0219(4)	0.0190(5)
O2	*x*	0.0999(2)	0.0967(3)	0.0973(2)	0.0975(2)	0.0968(3)
O2	*y*	0.6419(2)	0.6366(3)	0.6361(3)	0.6359(2)	0.6334(3)
O2	U_{iso} (Å²)	0.0155(4)	0.0151(6)	0.0186(5)	0.0184(5)	0.0161(6)
Sb occupancy		-	0.84(1)	0.750(8)	0.748(8)	0.67(1)
Pb occupancy		-	0.16(1)	0.250(8)	0.252(8)	0.33(1)
Fe-O1 (Å) x 2		2.187(2)	2.120(3)	2.097(2)	2.092(2)	2.075(3)
Fe-O2 (Å) x 4		2.104(1)	2.066(2)	2.068(2)	2.069(2)	2.057(2)
Fe-O2-Fe (°) x 1		89.43(6)	93.0(1)	93.31(9)	93.38(9)	94.5(1)
O2-Fe-O2(°) x 2		90.57(6)	87.0(1)	86.96(9)	86.62(9)	85.5(1)
O2-Fe-O2(°) x 2		91.08(6)	94.5(1)	94.77(9)	94.80(9)	95.9(1)
Sb/Pb-O1(Å) x 2		1.997(2)	2.039(3)	2.060(2)	2.068(2)	2.080(2)
Sb/Pb-O2(Å) x 1		1.927(3)	2.008(4)	2.022(3)	2.025(3)	2.066(3)
χ^2		3.885	3.289	3.129	3.505	4.549
R_{wp}		0.058	0.052	0.051	0.052	0.061
R_F^2		0.061	0.037	0.038	0.040	0.053

As more lead is introduced into the schafarzikite structure the FeO_6 octahedra become increasingly distorted (Fig. 3.6); this is seen by the deviation in O2-Fe-O2 angles from 90 °. With increasing levels of lead, all the Fe-O bond lengths decrease consistent with the presence of more Fe^{3+} ions. This is mainly seen for the Fe-O1 (apical) bond length which causes the FeO_6 octahedra to contract in the *a*-direction. The Fe-O2 (equatorial) bonds also contract slightly but to a lesser extent. As the Fe ions are found in octahedral edge-linked chains along the *c*-axis, the increasing *c*-parameter directly reflects an increase in Fe-Fe distances. This is caused by an increasing repulsion throughout the chains due to the presence of more highly charged Fe^{3+} ions. This is also observed by the change in Fe-O2-Fe bond angle which increases as the FeO_6 octahedra expand in the *c*-direction and limits the reduction possible in the Fe-O2 bond lengths. As Pb substitutes for Sb, the Sb/Pb position is altered and longer Sb/Pb-O bond lengths are observed due to the increased size and reduced charge on the pyramidal sites. The shorter Fe-O1 bonds are dominant over the longer Sb/Pb-O bonds in the *ab* plane and an overall contraction is seen in the *a*-direction with increasing lead content.

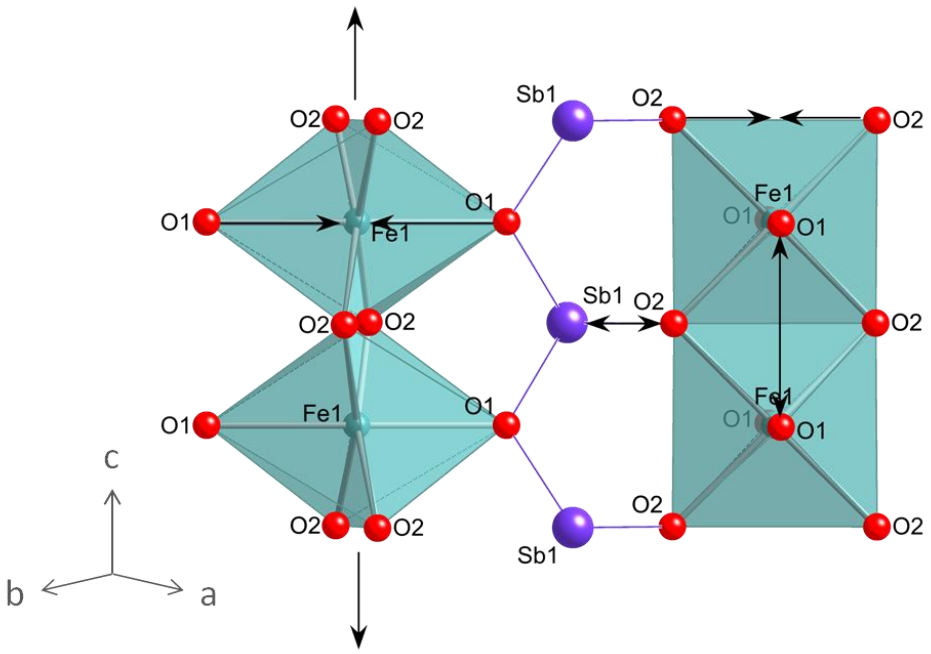

***Fig. 3.6**: Changes in $FeSb_{2-x}Pb_xO_4$ bond lengths and angles as the lead content is increased.*

3.3.2 Magnetic Properties

Field cooled (FC) and zero-field cooled (ZFC) susceptibility measurements were taken for $FeSb_{2-x}Pb_xO_4$ between 5 and 300 K using an applied field of 1000 Oe; plots of susceptibility versus temperature are shown in Fig. 3.7-3.12.

Antiferromagnetic (AFM) ordering was seen in $FeSb_2O_4$, as expected[8], by a decrease in the magnetic susceptibility at around 45 K (Fig. 3.7). At *ca*. 125 K an anomaly is observed in the susceptibility data below which the FC and ZFC susceptibilities diverge and this can be attributed to the Verwey transition in Fe_3O_4. The presence of ferrimagnetic Fe_3O_4 impurities is a common problem when synthesising schafarzikite[8-9] and the peak at *ca*. 125 K is seen in the susceptibility plots of all the lead-substituted samples. However the amount of Fe_3O_4 present in $FeSb_{2-x}Pb_xO_4$ is small, it is a trace impurity, as it is below the levels of detection by XRPD and NPD.

The magnetic susceptibility data for all the lead-substituted variants of $FeSb_2O_4$ showed a transition between *ca*. 50 and 70 K to a magnetically ordered state with a ferromagnetic component (Fig. 3.8-3.12). A small increase in the susceptibility is seen at the transition temperature, with a divergence of FC and ZFC susceptibilities at lower temperatures, but the ferromagnetic (FM) component is small and is therefore consistent with a canted AFM structure for $FeSb_{2-x}Pb_xO_4$. The transition temperature is shown to increase with increasing lead, and Fe^{3+}, content (Table 3.3) due to an increase in exchange interactions.

Table 3.3*: Approximate magnetic ordering temperatures from SQUID magnetometry data*

Sample	Transition Temperature (K)
$FeSb_2O_4$	45
$FeSb_{1.8}Pb_{0.2}O_4$	51
$FeSb_{1.7}Pb_{0.3}O_4$	56
$FeSb_{1.6}Pb_{0.4}O_4$	58
$FeSb_{1.5}Pb_{0.5}O_4$	69
$FeSb_{1.4}Pb_{0.6}O_4$	69

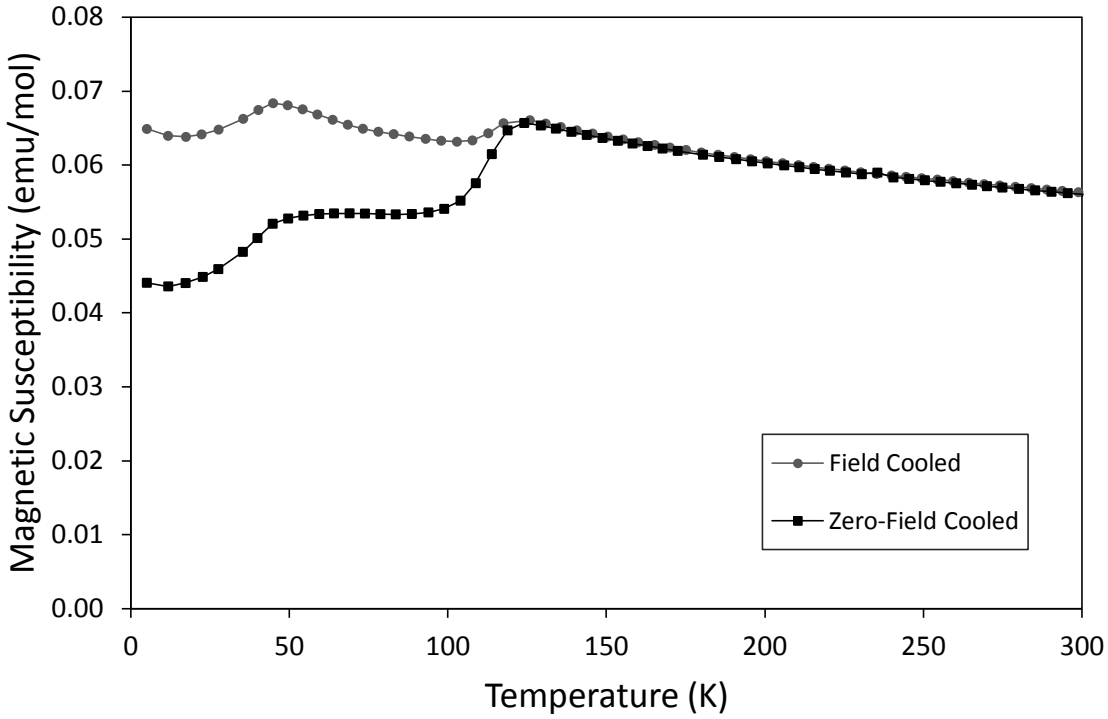

***Fig. 3.7**: Variation of magnetic susceptibility with temperature for $FeSb_2O_4$.*

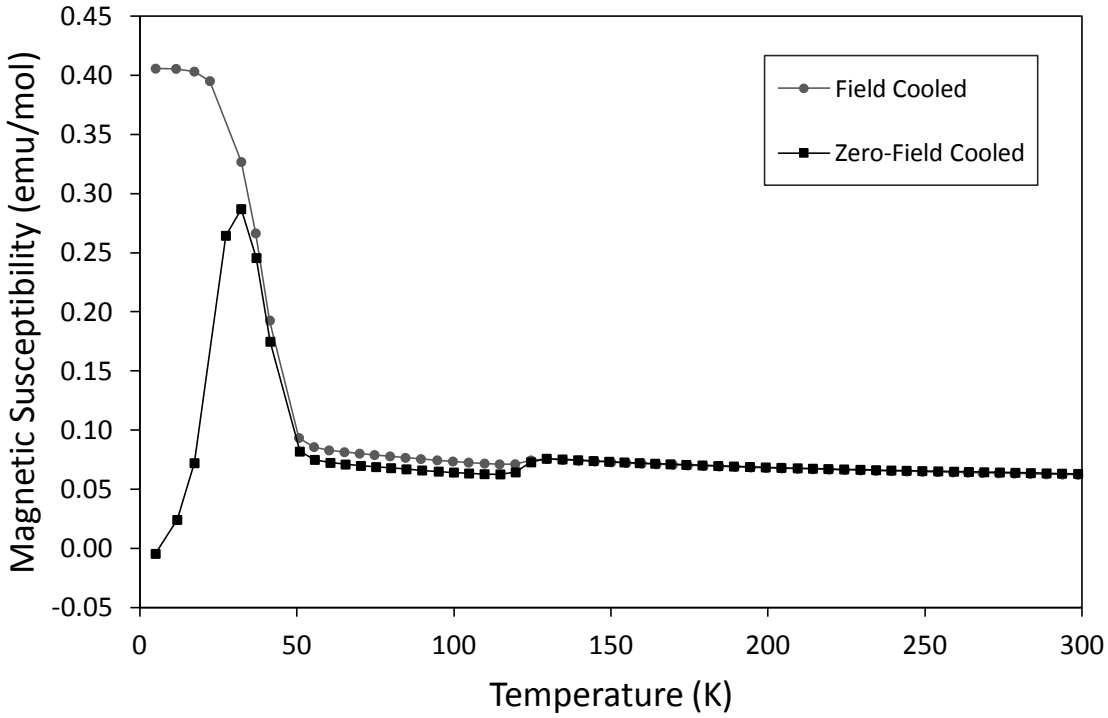

***Fig. 3.8**: Variation of magnetic susceptibility with temperature for $FeSb_{1.8}Pb_{0.2}O_4$.*

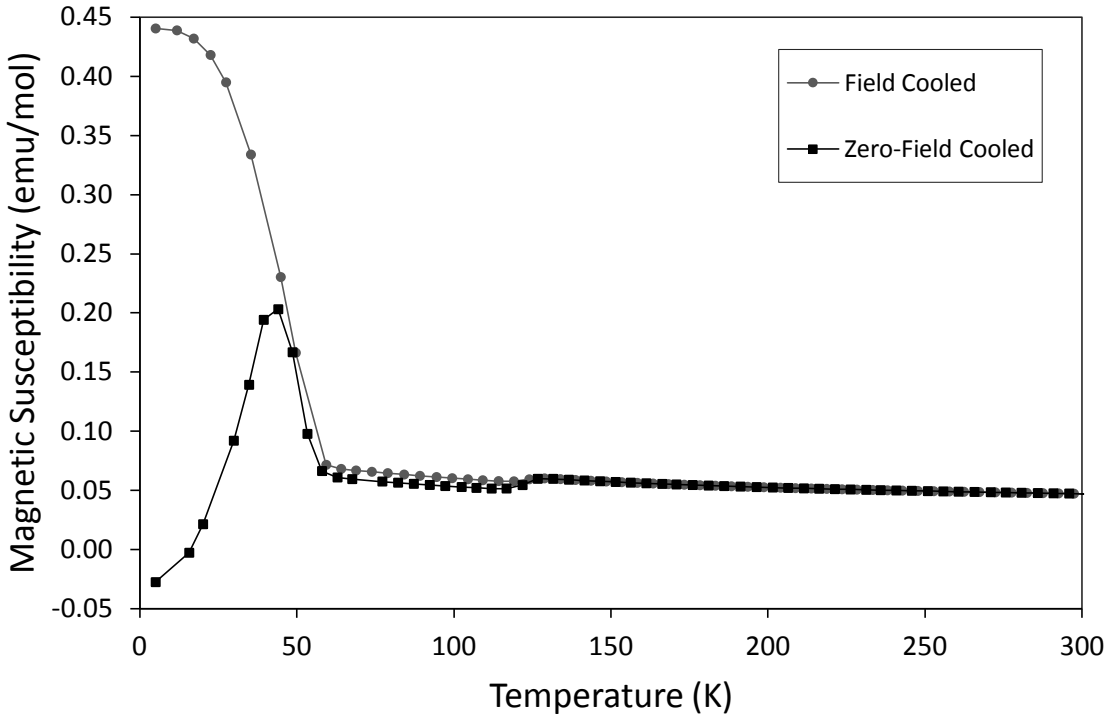

***Fig. 3.9**: Variation of magnetic susceptibility with temperature for $FeSb_{1.7}Pb_{0.3}O_4$.*

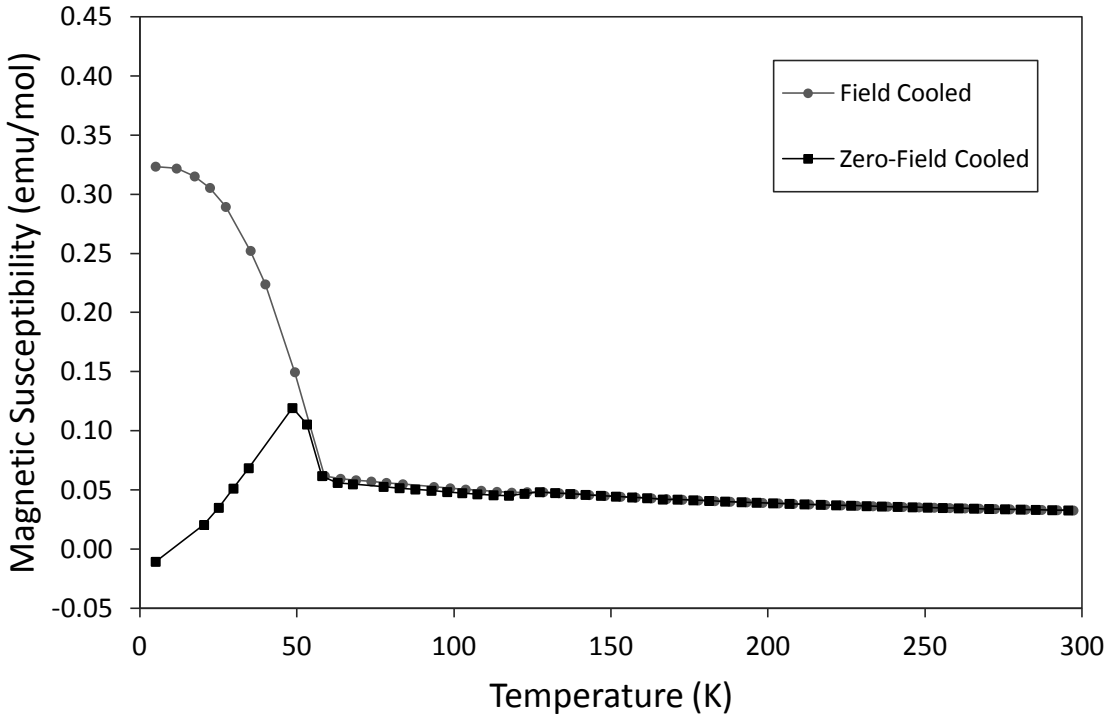

***Fig. 3.10**: Variation of magnetic susceptibility with temperature for $FeSb_{1.6}Pb_{0.4}O_4$.*

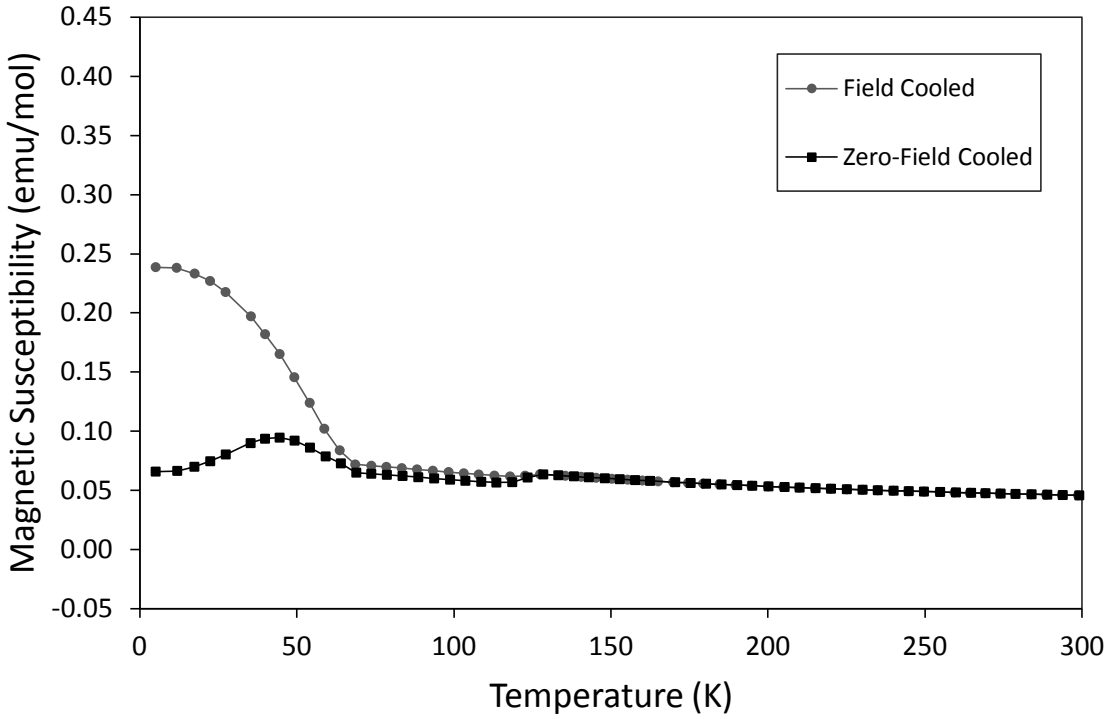

***Fig. 3.11**: Variation of magnetic susceptibility with temperature for $FeSb_{1.5}Pb_{0.5}O_4$.*

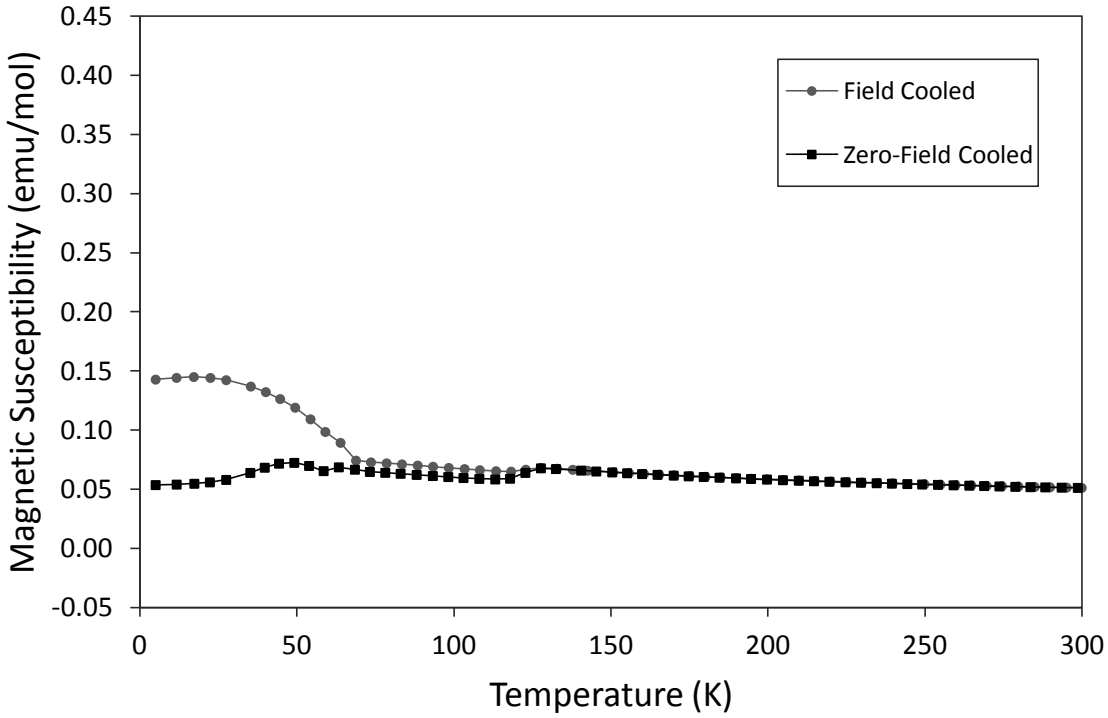

***Fig. 3.12**: Variation of magnetic susceptibility with temperature for $FeSb_{1.4}Pb_{0.6}O_4$.*

For some of the scans the ZFC data is actually seen to drop below zero at low temperatures. This type of behaviour has been studied previously in the compound $CoCr_2O_4$ and was found to be the result of trapped magnetic flux in the SQUID superconducting magnet[10]. The trapped flux causes the sample to be cooled in a small applied field, rather than a true zero field, which has the opposite sign of the last field applied before reducing to zero. This behaviour has also been observed in the similar schafarzikite compounds $CoSb_2O_4$ and $CoSb_{1.5}Pb_{0.5}O_4$[11] and can be counteracted by applying a negative field before setting the field to zero and running the measurement.

For refinement using the NPD data recorded at 4 K, the nuclear structure was refined using the space group $P4_2/mbc$ and the magnetic structure was refined as a separate, purely magnetic phase using the space group $P1$ (no. 1) so that the directions of the magnetic moments were not restricted by symmetry. As described in Section 1.5.2 and Fig. 1.9 there are three types of antiferromagnetic ordering possible, considering the interactions within the chains along the *c*-axis and between the chains in the layers perpendicular to *c*:

- A-type: AFM ordering in the chains, FM ordering within the layers
- C-type: FM ordering in the chains, AFM ordering within the layers
- G-type: AFM ordering within both the chains and the layers

Rietveld refinements for $FeSb_2O_4$ and $FeSb_{1.5}Pb_{0.5}O_4$ based on NPD data at 4 K are shown in Fig. 3.13; the lower angle region (10-40 °2θ) is shown in Fig. 3.14. The best fit for $FeSb_2O_4$ was obtained using a model with the moments aligned perpendicular to the *c*-axis and A-type magnetic ordering. The A-type magnetic ordering is evident from the presence of the (111) peak and increased intensity of the {021} peak (Fig. 3.14a).

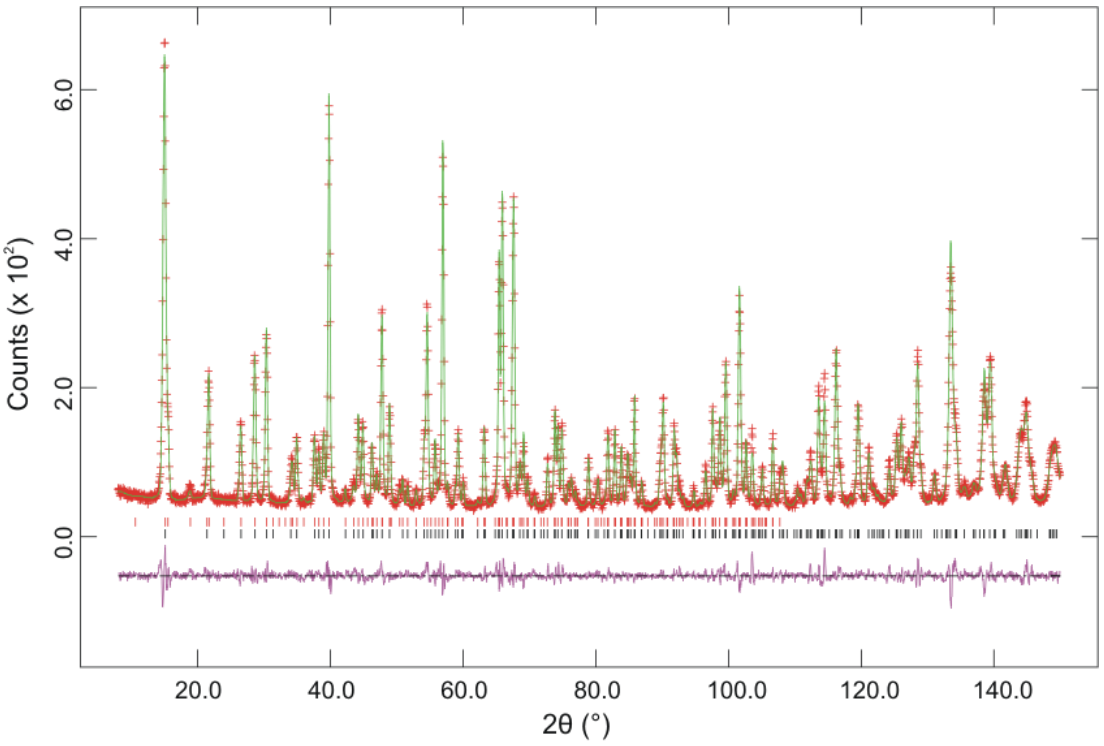

(a)

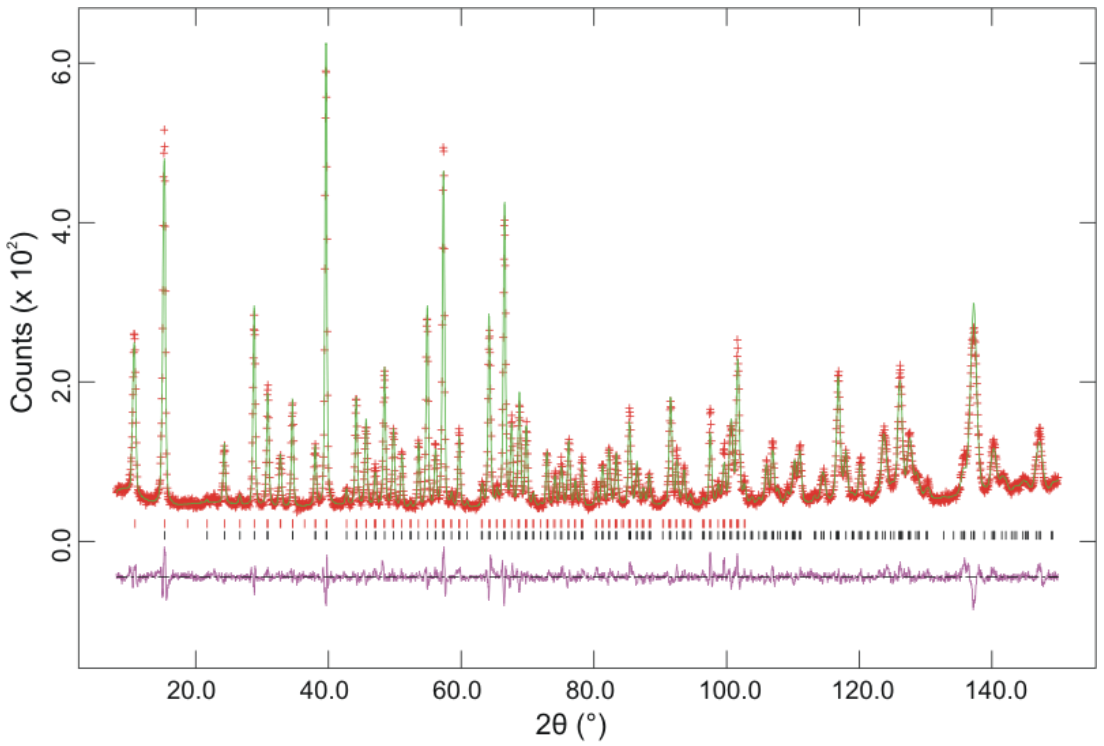

(b)

***Fig. 3.13**: Observed, calculated and difference plots for high resolution NPD data recorded from (a) $FeSb_2O_4$ and (b) $FeSb_{1.5}Pb_{0.5}O_4$ at 4 K.*

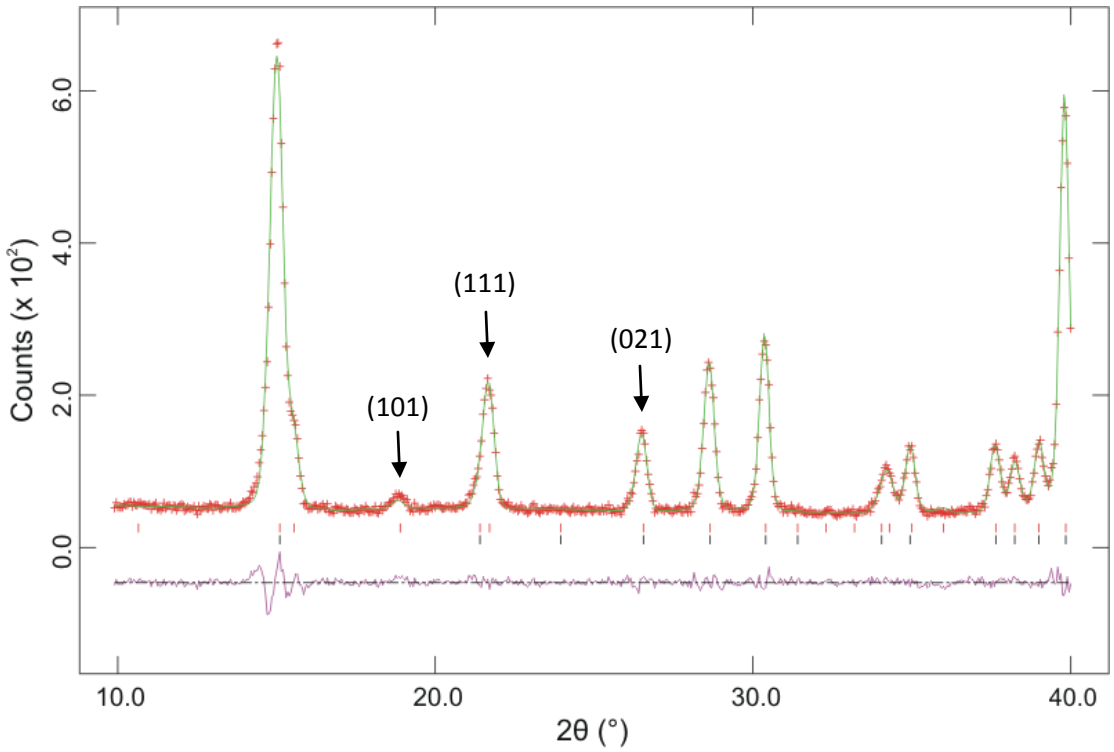

(a)

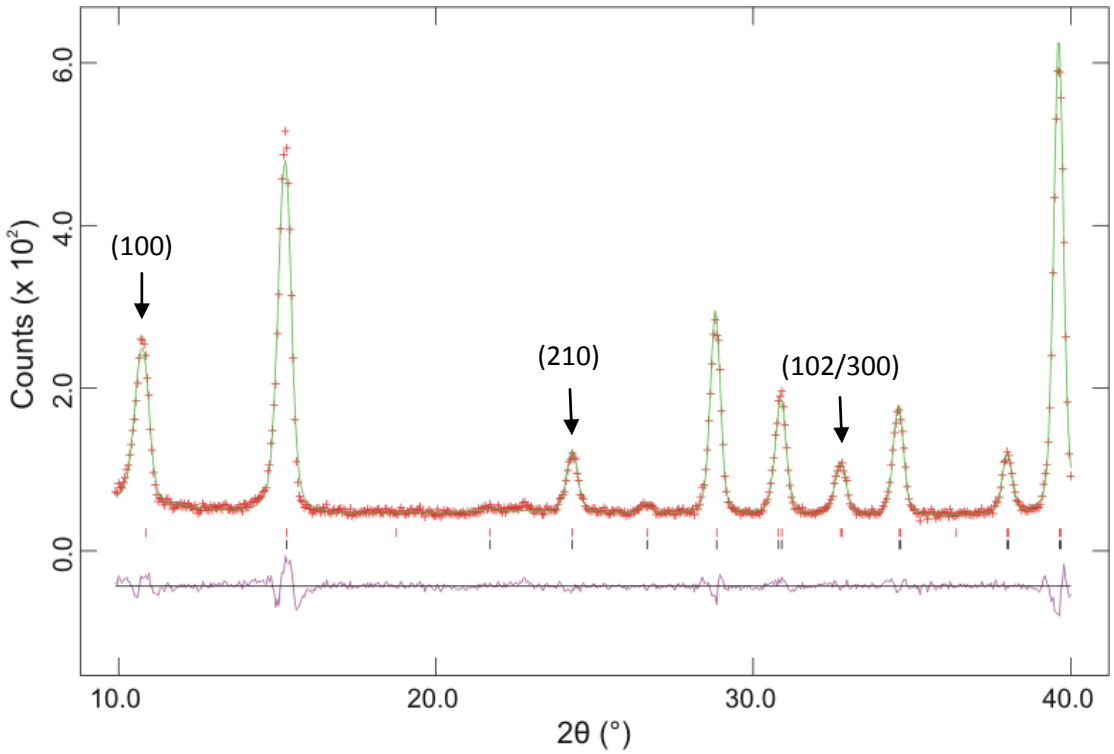

(b)

***Fig. 3.14**: Observed, calculated and difference plots (between 10 and 40 °2θ) for high resolution NPD data recorded from (a) $FeSb_2O_4$ and (b) $FeSb_{1.5}Pb_{0.5}O_4$ at 4 K.*

Previous work on neutron diffraction data of $FeSb_2O_4$ reported that the low temperature magnetic structure is predominantly A-type, but that C-type and G-type components are also present.[8] These three modes are combined to give a magnetic structure with orthorhombic symmetry and small moments along the *y*- and *z*-axes in addition to the major component along *x*.[8] As the {100} peak is absent there is no evidence for a C-type component in the sample studied here, but a peak just below 19 ° θ could be indexed as the {101} peak which would indicate a G-type component (Fig. 3.14a). This peak could also be due to Fe_3O_4 impurities, which were shown to be present from the SQUID magnetometry data, as it is close to the position of the most intense magnetic reflection of magnetite. However, the peak is absent from the room temperature (Fig. 3.15) data and a refinement with Fe_3O_4 added as an impurity phase did not model the peak well, indicating that it relates to a bulk feature.

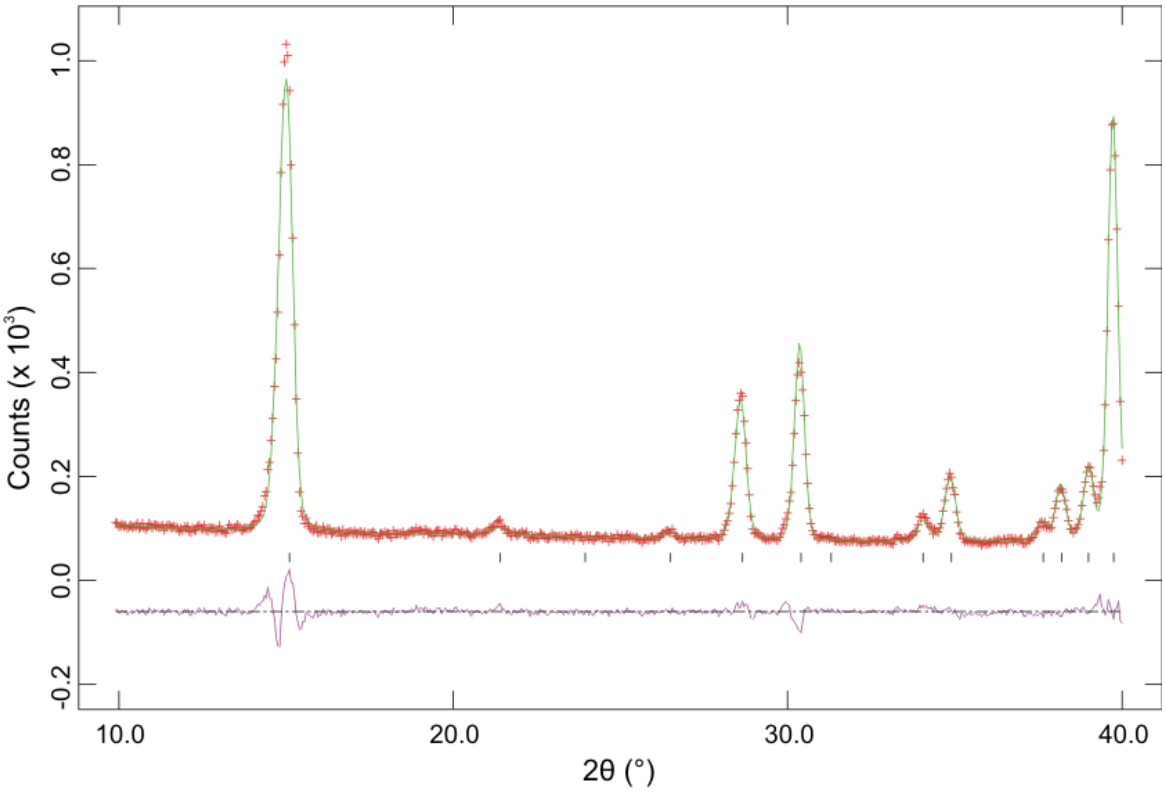

***Fig. 3.15**: Low angle region of observed, calculated and difference plots for high resolution NPD data recorded from $FeSb_2O_4$ at 298 K.*

A Rietveld refinement was therefore carried out using a model with both A-type and G-type magnetic ordering. The two magnetic ordering modes can be combined to give a single AFM phase which is shown in Fig. 3.16a. The moments are predominantly aligned along the *x*-axis, with A-type ordering, but they are non-collinear and have a small component along the *z*-axis which gives rise to a G-type component, and the {101} peak, while the overall moment remains equal to zero. The final refinement, using this model, gave a moment for each Fe ion of 3.62(3) μ_B in the *x*-direction and 1.24(7) μ_B in the *z*-direction and an overall moment of 3.83(4) μ_B. This is similar to the moments reported in the literature[8-9] although the moment along the *z*-axis is larger than that reported previously of 0.5 μ_B[9].

NPD data were taken at 4 K from four of the lead substituted schafarzikites: $FeSb_{1.7}Pb_{0.3}O_4$, $FeSb_{1.55}Pb_{0.45}O_4$, $FeSb_{1.5}Pb_{0.5}O_4$ and $FeSb_{1.3}Pb_{0.7}O_4$. The Rietveld refinements of NPD data for $FeSb_{1.5}Pb_{0.5}O_4$ shown in Fig. 3.13b and Fig. 3.14b are typical of all the lead-containing samples. The nuclear and magnetic structures were refined separately as described above for $FeSb_2O_4$. It can be seen from the NPD data that $FeSb_{2-x}Pb_xO_4$ have a different magnetic structure to that of the parent material, $FeSb_2O_4$. The {101} and (111) peaks have disappeared and the intensity of the {021} peak is greatly reduced. In addition to this the {100}, {210} and {102/300} peaks are present showing that the lead substituted samples have a purely C-type magnetic structure (Fig. 3.16b). The changes in the magnetic structure can be rationalised by considering the different exchange interactions occurring in the materials.

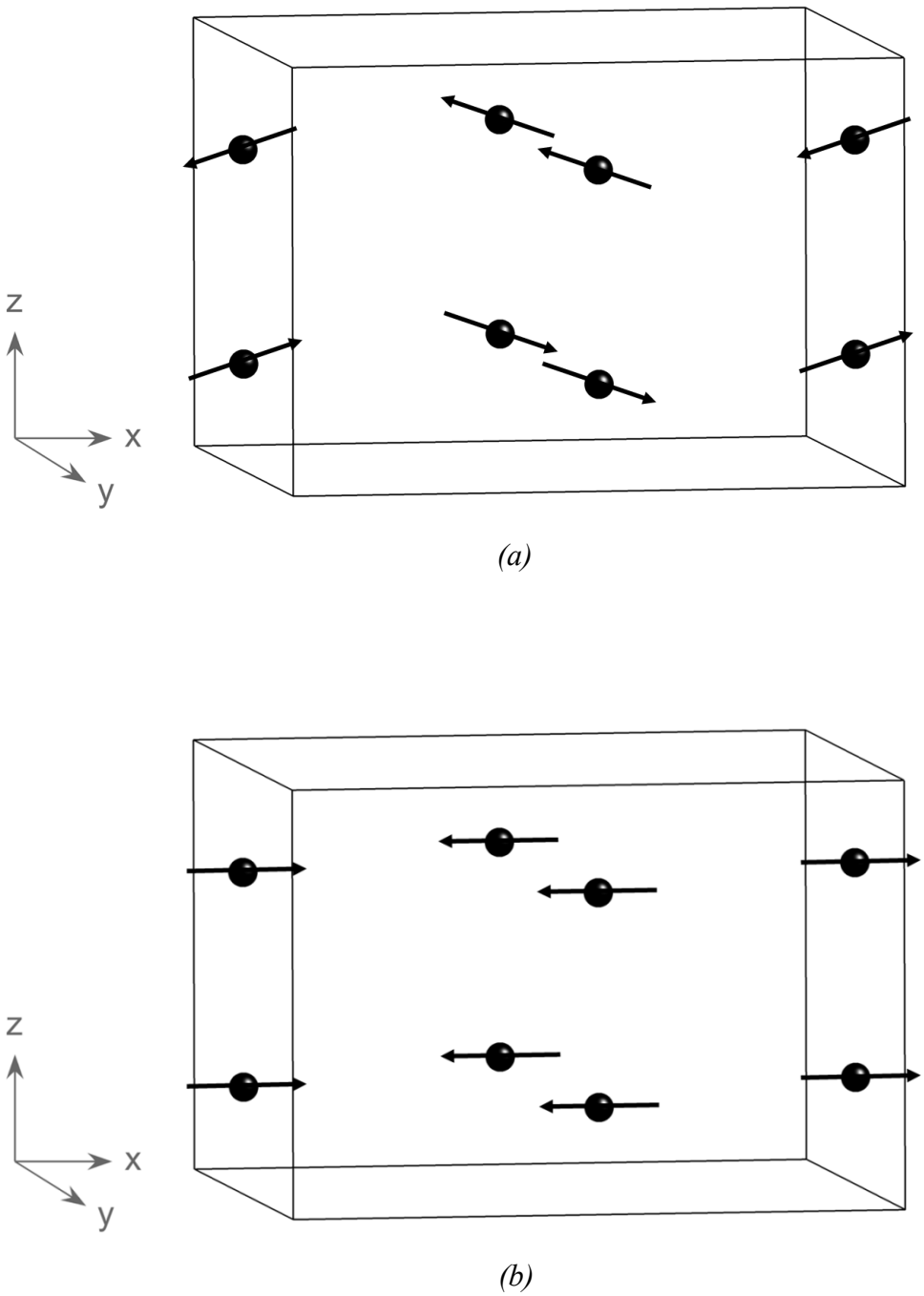

***Fig. 3.16**: Magnetic structure models (a) for $FeSb_2O_4$ showing predominantly A-type ordering with a G-type component and (b) for $FeSb_{2-x}Pb_xO_4$ showing C-type ordering.*

As described in Section 1.5.2 and Fig. 1.10, within a chain the Fe ions interact both directly through the t_{2g} orbitals and also through 90 º Fe-O-Fe superexchange interactions, and within a layer the Fe ions interact through weaker Fe-O-Sb/Pb-O-Fe links. The A-type ordering of $FeSb_2O_4$ was explained by the partially filled t_{2g} orbitals which favour AFM ordering within the FeO_6 chains (Section 1.5.2). Introducing lead into $FeSb_2O_4$ results in partial oxidation of Fe^{2+} giving a mixed Fe^{2+}/Fe^{3+} oxidation state throughout the chains and C-type magnetic order. The FM ordering within the chains can then either be explained by a reduction in the direct exchange or by a double exchange mechanism. Direct exchange occurs as the t_{2g} orbitals on neighbouring Fe ions within the edge-sharing chains point directly at each other. With increasing lead content the t_{2g} overlap decreases due to the *d*-orbital contraction in Fe^{3+} and the increase in Fe-Fe distance along *c*. This could then cause the 90 ° superexchange interaction, which favours FM interactions, to become dominant. A double exchange mechanism[12], by which electron migration between Fe^{2+} and Fe^{3+} ions can occur, is possible throughout the chains of $FeSb_{2-x}Pb_xO_4$ as a result of the mixed Fe^{2+}/Fe^{3+} oxidation state (Fig. 3.17). As Fe^{2+} has a d^6 configuration and Fe^{3+} has a d^5 configuration, a parallel arrangement of spins throughout the chains allows electron transfer between neighbouring Fe ions and is therefore favoured over an antiparallel arrangement. In $FeSb_2O_4$, as all the Fe is present as Fe^{2+}, this is not possible.

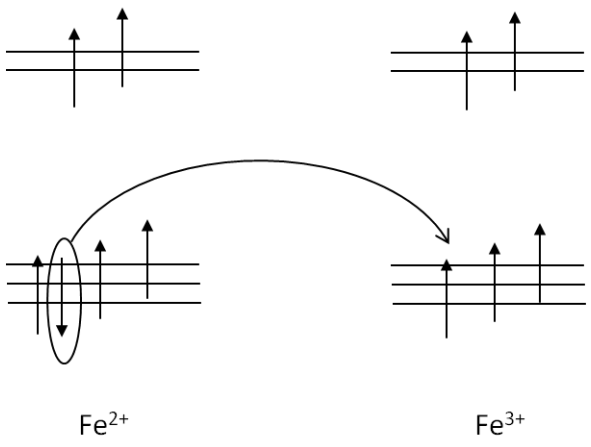

***Fig. 3.17**: Double exchange mechanism.*

Once the magnetic ordering of $FeSb_{2-x}Pb_xO_4$ had been established as being C-type, different magnetic refinements were carried out to determine the direction of the moments. For most of the lead substituted schafarzikites (x = 0.3-0.5) the best fits were obtained using magnetic models which had the moments aligned predominantly along the x-axis, possibly with a smaller component along the z-axis, but for the sample $FeSb_{1.3}Pb_{0.7}O_4$ the fit was significantly better when the moments were aligned along the z-axis with a small component along x. The results from different magnetic refinements are summarised in Table 3.4. The data suggest that the moment tilts away from x with increasing Pb content. The magnetic susceptibility data indicated that the compounds are canted antiferromagnets so models with canting were applied, but the canted moment was very small with high error showing that the ferromagnetic component is too small to be detected from NPD data.

The overall magnetic moments from the best fits to the data are given in Table 3.5 with unit cell parameters and selected bond angles. From $FeSb_{1.7}Pb_{0.3}O_4$ to $FeSb_{1.3}Pb_{0.7}O_4$ the moment increases with increasing lead content but the moment for schafarzikite, $FeSb_2O_4$, is higher than those for the lead substituted samples. As Fe^{2+} has a d^6 configuration and Fe^{3+} has a d^5 configuration, the moment arising from the electron spin is expected to increase with higher levels of lead due to the presence of more Fe^{3+} and therefore more unpaired electrons. However this is assuming that there is no orbital contribution to the magnetic moment. This is the case for Fe^{3+}, but Fe^{2+} has a triply degenerate T ground state and therefore a significant orbital contribution which causes the moment to increase. Although $FeSb_{2-x}Pb_xO_4$ also contain Fe^{2+} ions, and could therefore also be expected to have an orbital contribution to the moment, the bond angles given in Table 3.5 indicate that a major distortion of the FeO_6 octahedra occurs between $FeSb_2O_4$ and $FeSb_{1.7}Pb_{0.3}O_4$ which would lift the degeneracy of the T ground state. This would

quench the orbital contribution and reduce the moment which explains why a higher moment is observed in schafarzikite compared to all the lead substituted samples. The octahedra continue to distort as more lead is introduced into the structure and the moment increases as expected due to the increase in the Fe oxidation state. The NPD magnetic moments are all lower than the ideal values based on spin (4 μ_B for Fe^{2+} and 5 μ_B for Fe^{3+}) because of covalency and quantum mechanical effects[13].

***Table 3.4**: Summary of results from various magnetic models refined from high resolution neutron powder diffraction data from $FeSb_{2-x}Pb_xO_4$ at 4 K*

$FeSb_2O_4$

Magnetic Form Factor	Model	Moment (μ_B)	χ^2
Fe^{2+}	A-type along *x*	3.61(3)	3.17
	A-type along *z*	3.61(4)	4.78
	A-type along *x* and *z*	3.56(5), 0.6(3)	3.17
	A-type along *x* and G-type along *z*	3.62(3), 1.24(7)	3.09

$FeSb_{1.7}Pb_{0.3}O_4$

Magnetic Form Factor	Model	Moment (μ_B)	χ^2
Fe^{2+}	C-type along *x*	2.91(4)	3.57
	C-type along *z*	2.12(3)	3.75
	C-type along *x* and *z*	2.8(1), 0.7(3)	3.57

$FeSb_{1.5}Pb_{0.5}O_4$

Magnetic Form Factor	Model	Moment (μ_B)	χ^2
Fe^{3+}	C-type along *x*	3.54(5)	3.32
	C-type along *z*	2.69(5)	3.79
	C-type along *x* and *z*	3.10(9), 1.3(1)	3.27

$FeSb_{1.3}Pb_{0.7}O_4$

Magnetic Form Factor	Model	Moment (μ_B)	χ^2
Fe^{3+}	C-type along *x*	4.20(4)	5.03
	C-type along *z*	3.46(3)	3.22
	C-type along *x* and *z*	1.3(2), 3.29(4)	3.15

***Table 3.5**: Magnetic moments, unit cell parameters and selected bond angles refined from high resolution neutron powder diffraction data from $FeSb_{2-x}Pb_xO_4$ at 4 K*

	$FeSb_2O_4$	$FeSb_{1.7}Pb_{0.3}O_4$	$FeSb_{1.55}Pb_{0.45}O_4$	$FeSb_{1.5}Pb_{0.5}O_4$	$FeSb_{1.3}Pb_{0.7}O_4$
Total Moment (μ_B)	3.83(4)	2.90(3)	3.29(4)	3.36(9)	3.54(8)
a (Å)	8.6150(1)	8.4957(2)	8.4751(2)	8.4728(2)	8.4584(2)
c (Å)	5.90327(9)	5.9786(2)	5.9997(2)	6.0053(2)	6.0287(2)
O2-Fe-O2(°) x 2	90.80(7)	88.2(1)	87.1(1)	86.7(1)	85.9(1)
O2-Fe-O2(°) x 2	90.96(7)	93.5(1)	94.5(1)	94.9(1)	95.5(1)
Fe-O2-Fe (°) x 1	89.20(7)	91.9(1)	92.9(1)	93.3(1)	94.1(1)

^{57}Fe Mössbauer spectra have been recorded from the sample $FeSb_{1.5}Pb_{0.5}O_4$ between 300 K and 20 K (Table 3.6 and Fig. 3.18). The magnetic properties of $FeSb_2O_4$ from ^{57}Fe Mössbauer studies can be found in the literature and are not discussed here[14-17]. The spectra at 300 K and 77 K show two quadrupole split absorptions, one corresponding to Fe^{2+} and one corresponding to Fe^{3+}, consistent with oxidation of half the Fe^{2+} to Fe^{3+}. At 62 K it can be seen from Fig. 3.18 that the material is beginning to order magnetically which is in agreement with the estimate from SQUID magnetometry data of T_N = 69 K. At 62 K and 50 K the spectra show a quadrupole split Fe^{2+} absorption and three magnetically split sextet absorptions: one with a small magnetic hyperfine field and a chemical isomer shift characteristic of Fe^{2+}, and two with chemical isomer shifts characteristic of Fe^{3+}. Below 50 K a single Fe^{2+} sextet and two Fe^{3+} sextets are seen.

For Fe^{2+}, the quadrupole interaction is larger than the magnetic interaction and therefore dominates the spectrum. At 62 K and 50 K, the non-magnetic Fe^{2+} quadrupole-split absorption arises from Fe^{2+} ions which are surrounded by other Fe^{2+} ions and therefore only experience weak magnetic couplings within this temperature range. The Fe^{2+} ions interacting with neighbouring Fe^{3+} ions give the magnetically split Fe^{2+} component with small magnetic hyperfine field.

The Fe^{3+} sextets between 62 K and 20 K are also broad and this is because of the various magnetic exchange interactions of different strengths occurring throughout the structure. These can be attributed to the interactions occurring with neighbouring Fe^{2+} or Fe^{3+} ions. Within the octahedral chains the Fe^{3+} ion can either have two Fe^{2+} neighbours, two Fe^{3+} neighbours or one Fe^{2+} and one Fe^{3+} neighbour. Each of these scenarios gives rise to magnetic exchange interactions of slightly different strengths and, in addition to this, magnetic exchange interactions, which occur within the layers, are weaker than those within the chains. A range of magnetic coupling strengths are therefore experienced by a given Fe^{3+} ion which do not give discrete sextets but result in broadening of the Fe^{3+} sextets. As the temperature decreases the magnetic hyperfine fields for the stronger Fe^{3+} couplings become saturated and the linewidths sharpen.

***Table 3.6**: ^{57}Fe Mössbauer parameters recorded from $FeSb_{1.5}Pb_{0.5}O_4$ between 300 and 20 K*

Temperature (K)	Assignment	$\delta \pm 0.02$ (mm/s)	$\Delta \pm 0.02$ (mm/s)	$H \pm 0.5$ (T)	Area $\pm$ 3 %
300	Fe^{3+}	0.45	0.85	-	66
	Fe^{2+}	0.95	1.90	-	34
77.4	Fe^{3+}	0.50	0.82	-	54
	Fe^{2+}	1.16	2.67	-	46
62	Fe^{3+}	0.48	0.12	34.7	28
	Fe^{3+}	0.40	-0.16	28.0	20
	Fe^{2+}	1.15	0.10	15.0	43
	Fe^{2+}	1.15	2.66	-	9
50	Fe^{3+}	0.47	0.10	39.8	31
	Fe^{3+}	0.40	-0.16	33.5	21
	Fe^{2+}	1.15	0.10	18.0	42
	Fe^{2+}	1.14	2.66	-	6
45	Fe^{3+}	0.51	0.08	43.5	30
	Fe^{3+}	0.40	-0.16	38.7	19
	Fe^{2+}	1.15	0.08	18.0	51
40	Fe^{3+}	0.50	1.10	45.4	31
	Fe^{3+}	0.40	-0.16	41.1	23
	Fe^{2+}	1.15	0.10	20.5	47
35	Fe^{3+}	0.47	0.10	46.4	30
	Fe^{3+}	0.40	-0.16	42.5	20
	Fe^{2+}	1.15	0.10	20.1	50
30	Fe^{3+}	0.52	0.04	47.6	28
	Fe^{3+}	0.40	-0.18	43.6	18
	Fe^{2+}	1.15	0.10	25.8	54
20	Fe^{3+}	0.53	0.08	49.3	26
	Fe^{3+}	0.40	-0.18	45.5	20
	Fe^{2+}	1.15	0.10	27.3	54

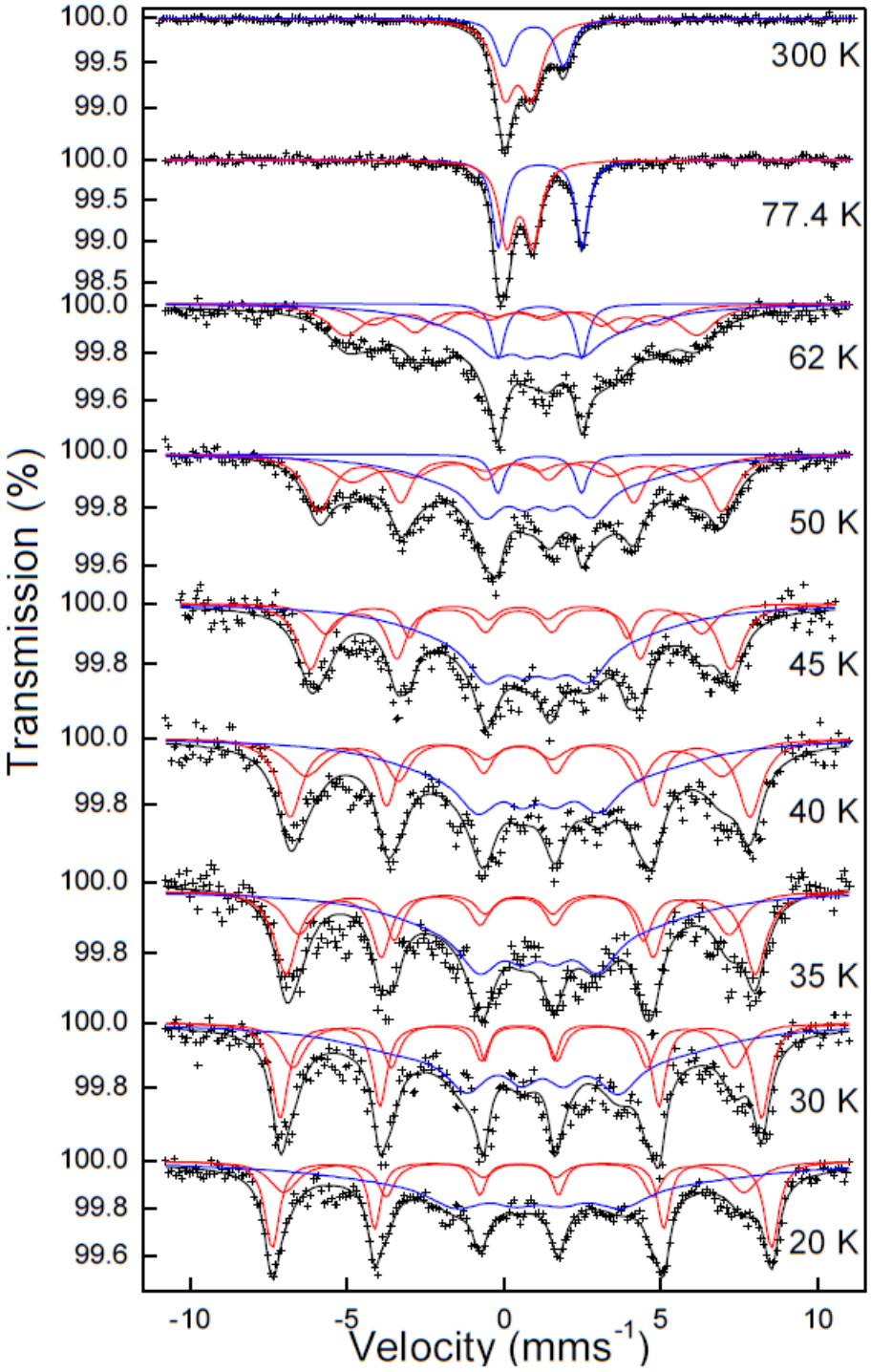

Fig. 3.18: *^{57}Fe Mössbauer spectra recorded between 300 K and 20 K from $FeSb_{1.5}Pb_{0.5}O_4$. The Fe^{2+} components are shown in blue and the Fe^{3+} components are shown in red.*

3.3.3 Electronic Conductivity

Polycrystalline samples of $FeSb_{2-x}Pb_xO_4$ (x = 0, 0.25, 0.5 and 0.75) were prepared for conductivity measurements and were shown to be single phase from XRPD data. Thermogravimetric analysis (TGA) was used to measure the stability of the samples to heating in an oxygen atmosphere (Fig. 3.19) before taking conductivity measurements.

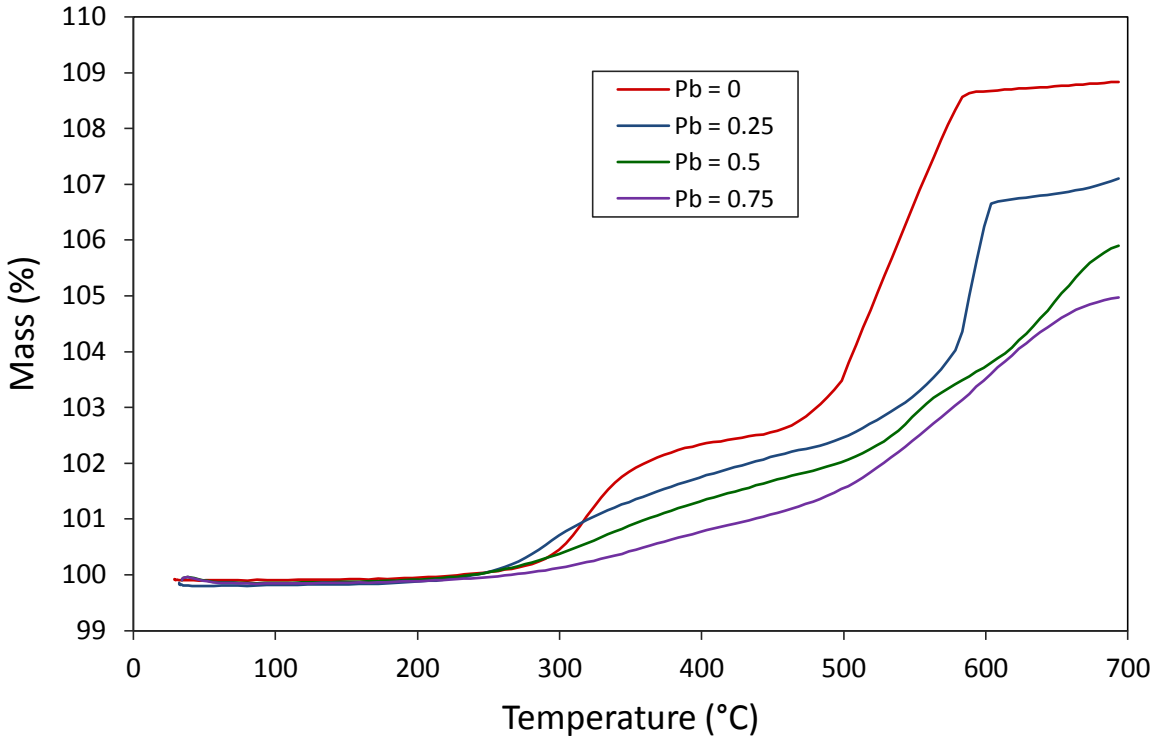

***Fig. 3.19**: Thermogravimetric analysis of $FeSb_{2-x}Pb_xO_4$ (x = 0, 0.25, 0.5 and 0.75).*

Measurements were taken between 30 °C and 700 °C and the data show that the samples were completely stable with respect to oxidation up to 200 °C. Conductivity measurements, using AC impedance, were therefore taken between 20 °C and 200 °C in air. Above 200 °C the mass of the samples increases as they take up oxygen. It can be seen from Fig. 3.19 that the mass increase occurs in two stages and this is discussed further in Chapter 4.

When analysing the conductivity data, the resistance values arising from bulk and grain boundary contributions were difficult to separate. Two overlapping semicircles

corresponding to bulk and grain boundary resistances could be seen in the impedance plots for $FeSb_2O_4$ between 300 and 350 K but they could no longer be resolved at higher temperatures. For the lead-substituted samples the two semicircles could not be resolved at any temperature so only the higher resistance semicircle with a capacitance value typical of a grain boundary response could be fitted. The capacitance values suggest that the resistance obtained from the first semicircle (observed for $FeSb_2O_4$ only at lower temperatures) arises from the bulk sample and that the main contribution observed in the impedance plots arises from grain boundaries.

As the contributions from the bulk and the grain boundaries were difficult to separate the total resistance, determined by taking intercept of the impedance spectrum with the real axis, was used. The variation in conductivity (σ), calculated from the total pellet resistance, with temperature (T) is therefore shown Fig. 3.20. The conductivity is seen to increase with temperature and the plots of log σ against 000/ T were linear for all samples consistent with thermally activated semiconducting behaviour. The activation energy obtained from the Arrhenius plots are reported in Table 3.7. The activation energy is lower and the conductivity is increased for the lead-substituted samples compared with schafarzikite. The highest conductivity is observed for $FeSb_{1.5}Pb_{0.5}O_4$ which has equal amounts of Fe^{2+} and Fe^{3+} in the chains. The lower value for $FeSb_{1.25}Pb_{0.75}O_4$ may be related to the fact that the contribution to the resistance from grain boundaries is high. The small Fe_3O_4 impurities found in these samples could also be a problem as Fe_3O_4 is metallic and has a high conductivity, and may affect the grain boundary resistance.

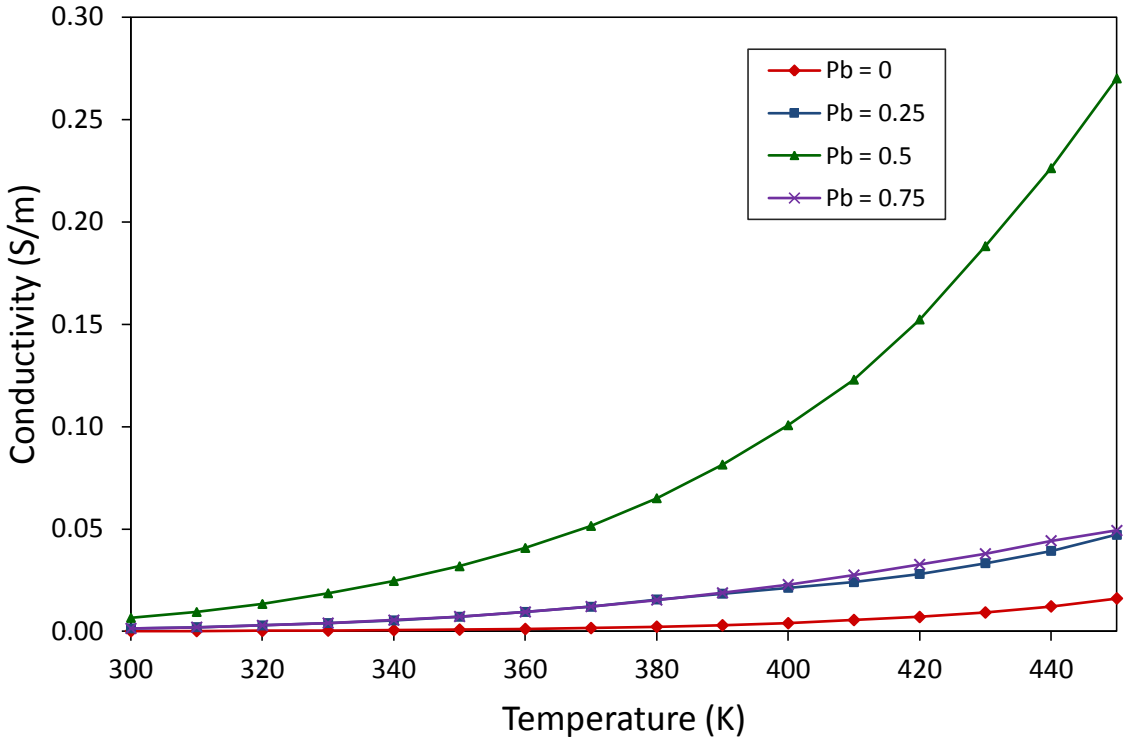

(a)

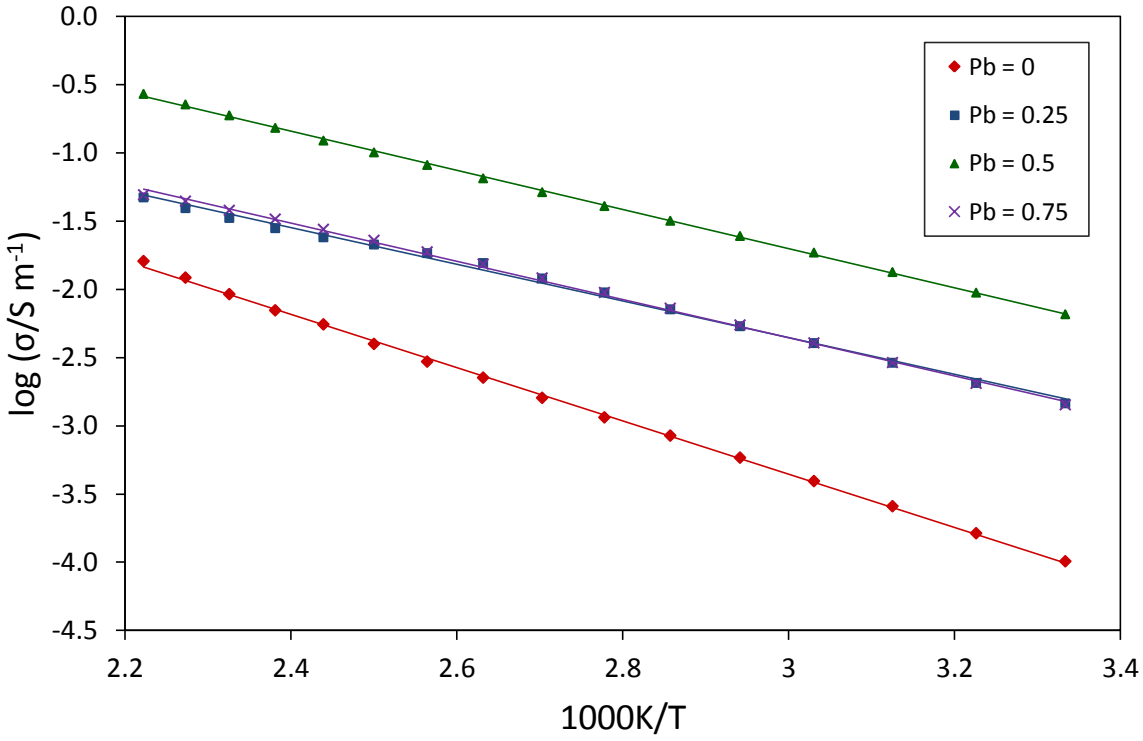

(b)

***Fig. 3.20**: Plots of (a) σ vs. T and (b) log σ vs. 1000/T for $FeSb_{2-x}Pb_xO_4$ (x = 0, 0.25, 0.5 and 0.75).*

***Table 3.7**: Activation energies obtained from the Arrhenius plot for $FeSb_{2-x}Pb_xO_4$*

Sample	Activation Energy, E_a (kJ mol^{-1})
$FeSb_2O_4$	37.4
$FeSb_{1.75}Pb_{0.25}O_4$	25.7
$FeSb_{1.5}Pb_{0.5}O_4$	27.5
$FeSb_{1.25}Pb_{0.75}O_4$	26.8

3.4 Conclusions

Schafarzikite was successfully synthesised and lead substituted into the structure to form $FeSb_{2-x}Pb_xO_4$ (x = 0-0.75). The samples were characterised using XRPD, Mössbauer spectroscopy and NPD and the structure was found to be similar to that of the parent material. As Pb^{2+} replaces Sb^{3+} on the pyramidal sites, and Fe^{2+} is oxidised to Fe^{3+} on the octahedral sites, there are two competing trends for the variation in unit cell parameters which cause the *a*-parameter to decrease and the *c*-parameter to increase. The magnetic properties of $FeSb_{2-x}Pb_xO_4$ were investigated using SQUID magnetometry, Mössbauer spectroscopy and low temperature NPD. $FeSb_2O_4$ was shown to be antiferromagnetic with predominantly A-type ordering, consistent with the literature. A G-type component was also seen to be present but there was no evidence for an additional C-type component. The magnetic structure of $FeSb_{2-x}Pb_xO_4$ was found to be different from that of the parent material; a canted antiferromagnetic structure is seen with C-type magnetic ordering. Conductivity measurements, using AC impedance, show that all the samples display semiconducting behaviour.

3.5 References

1. J. R. Gavarri, J. P. Vigouroux, G. Calvarin and A. W. Hewat, *J. Solid State Chem.*, 1981, **36**, 81.

2. J. R. Gavarri, *J. Solid State Chem.*, 1982, **43**, 12.

3. J. R. Gavarri, R. Chater and J. Ziółkowski, *J. Solid State Chem.*, 1988, **73**, 305.

4. A. M. Abakumov, M. G. Rozova, E. V. Antipov, J. Hadermann, G. Van Tendeloo, M. Lobanov, M. Greenblatt, M. Croft, E. V. Tsiper, A. Llobet, K. A. Lokshin and Y. Zhao, *Chem. Mater.*, 2005, **17**, 1123.

5. R. Bayliss, F. J. Berry, A. Bowden, C. Greaves and M. F. Thomas, *J. Phys.: Conf. Ser.*, 2010, **217**, 012049.

6. R. Fischer and F. Pertlik, *Tschermaks Mineral. Petrogr. Mitt.*, 1975, **22**, 236.

7. R. D. Shannon, *Acta Cryst.*, 1976, **A32**, 751.

8. J. A. Gonzalo, D. E. Cox and G. Shirane, *Phys. Rev.*, 1966, **147**, 415.

9. R. Chater, J. R. Gavarri and A. Hewat, *J. Solid State Chem.*, 1985, **60**, 78.

10. N. Kumar and A. Sundaresan, *Solid State Commun.*, 2010, **150**, 1162.

11. B. P. de Laune and C. Greaves, *J. Solid State Chem.*, 2012, **187**, 225.

12. C. Zener, *Phys. Rev.*, 1951, **82**, 403.

13. M. T. Hutchings and H. J. Guggenheim, *J. Phys. C: Solid State Phys.*, 1970, **3**, 1303.

14. M. Eibschütz and U. Ganiel, *Solid State Commun.*, 1968, **6**, 775.

15. F. Varret, P. Imbert, A. Gerard and F. Hartmann-Boutron, *Solid State Commun.*, 1968, **6**, 889.

16. G. A. Petitt and M. R. Meder, *Hyperfine Interactions*, 1978, **5**, 323.

17. R. D. Bayliss, F. J. Berry, B. P. de Laune, C. Greaves, Ö. Helgason, J. F. Marco, M. F. Thomas, L. Vergara and M. J. Whitaker, *J. Phys.: Condens. Matter*, 2012, **24**, 276001.

4 Oxygen Insertion in $FeSb_{2-x}Pb_xO_4$

4.1 Background

As described in Chapters 1 and 3, the structure of schafarzikite consists of edge-sharing chains of FeO_6 octahedra and trigonal pyramidal Sb^{3+} cations (Fig. 4.1a)[1]. The octahedral chains are separated and linked by the Sb^{3+} cations, opening up channels parallel to the *c*-axis into which the Sb^{3+} lone pairs point. The channels could potentially provide another way of modifying the structure by insertion of anions resulting in oxidation of Fe^{2+} to Fe^{3+}. This approach to structural modification in schafarzikites has never been investigated before but two closely related minerals are known, versiliaite and apuanite, which contain sulfide links within schafarzikite-type channels[2-3].

The structures of schafarzikite, versiliaite and apuanite are shown in Fig. 4.1a, b and c respectively; the unit cells are shown both along the *a*-axis and along the *c*-axis.

The structures of versiliaite and apuanite are derived from that of schafarzikite by replacing some of the Sb^{3+} on pyramidal sites with Fe^{3+} and adding a S^{2-} ion between two Fe^{3+} ions in adjacent chains. The Fe^{3+} ions on this site form FeO_3S tetrahedra and are therefore required to fulfill the tetrahedral bonding conditions. The insertion of sulfide ions into the structure then results in partial oxidation of Fe^{2+} to Fe^{3+} in the octahedral chains.[3]

In the versiliaite structure, every fourth Sb^{3+} ion is replaced and, as the Sb^{3+} lone pairs point out into the channels in alternating directions, all the pyramidal Fe^{3+} ions in a chain face the same direction resulting in the formation of isolated double-chain ribbons by Fe-S-Fe links (Fig. 4.1b and 4.2a). This gives an orthorhombic structure (space group *Pbam*) and doubling of the unit cell in the *c*-direction (a = 8.492(5), b = 8.326(5), c = 11.938(7)[3]).

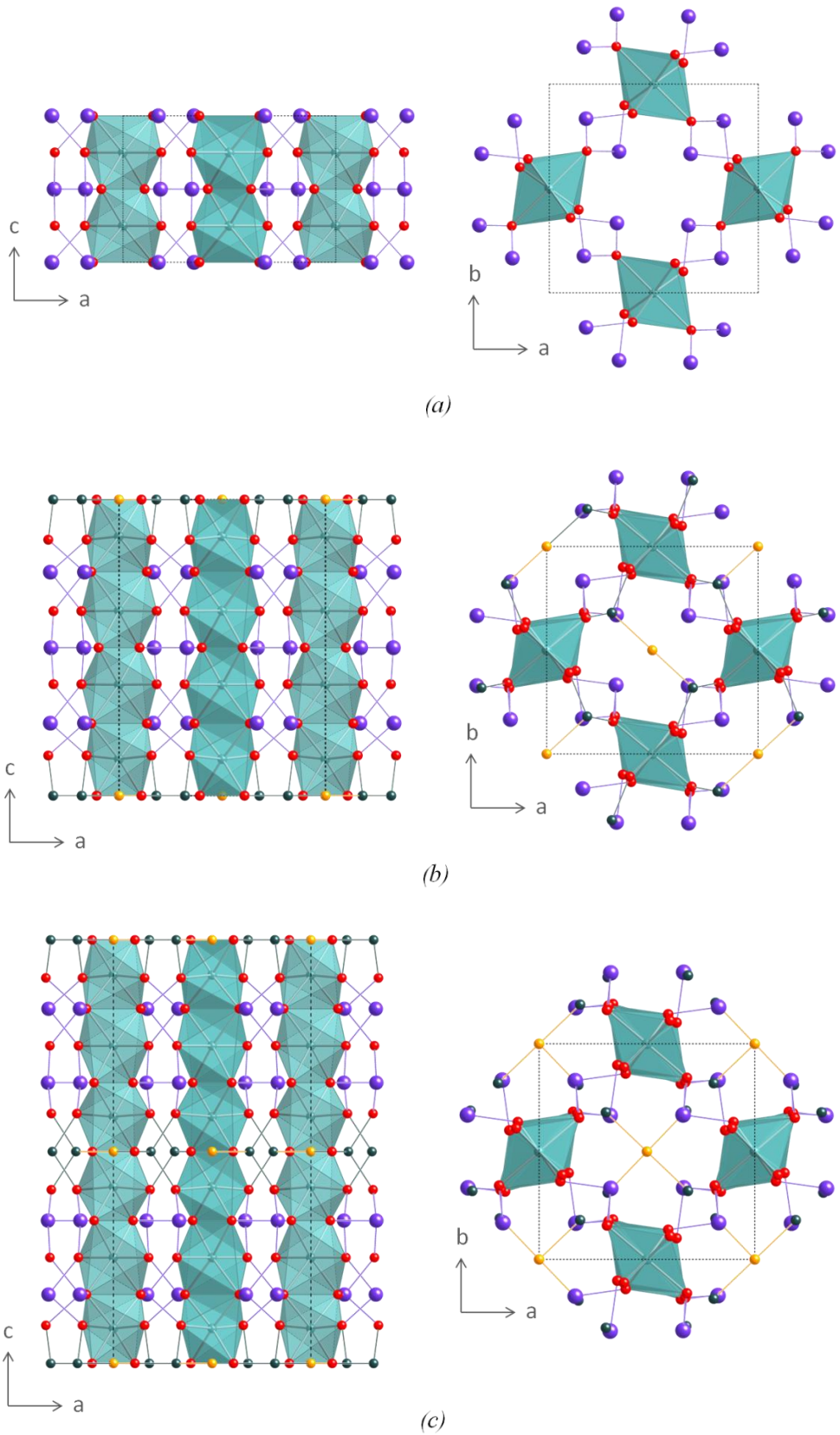

***Fig. 4.1**: Structure of (a) schafarzikite, (b) versiliaite and (c) apuanite unit cells. FeO_6 octahedra are shaded, O ions are shown as red spheres and Sb ions are shown as purple spheres. For versiliaite and apuanite, pyramidal Fe^{3+} ions are shown in dark green and S^{2-} ions are shown in orange.*

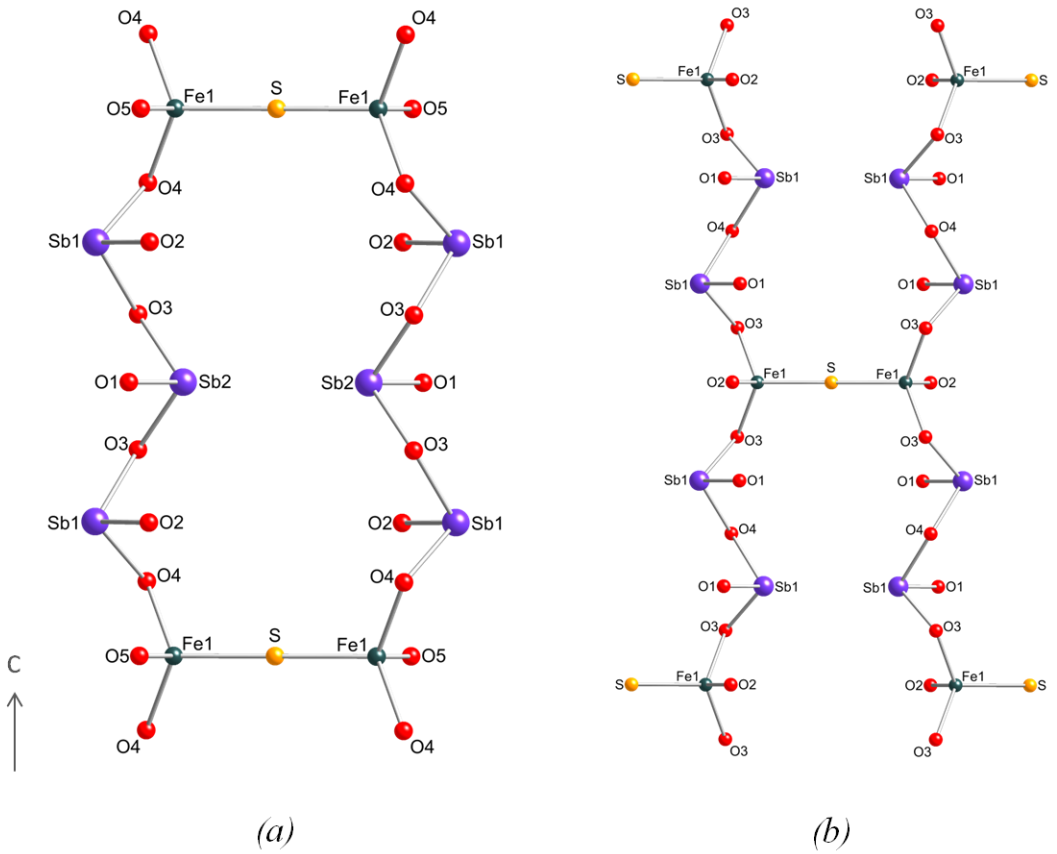

***Fig. 4.2**: Structures of schafarzikite-related minerals: the formation of (a) two chain ribbons in versiliaite and (b) infinite sheets in apuanite by Fe-S-Fe links is shown.*

In the apuanite structure, every third Sb^{3+} ion is replaced to give pyramidal Fe^{3+} ions within a chain facing in alternating directions (Fig. 4.2b). Infinite sheets are formed in (110) directions by the Fe-S-Fe links (Fig. 4.1c and 4.2b) resulting in a tetragonal structure (space group $P4_2/mbc$) and tripling of the unit cell (a = 8.372(5), c = 17.97(1)[3]).

The formulae of versiliaite and apuanite can be written as $Fe(Sb_{1.5}Fe_{0.5})O_4S_{0.25}$ and $Fe(Sb_{1.33}Fe_{0.67})O_4S_{0.33}$ respectively. Little research has been carried out on these materials: both versiliaite and apuanite have been investigated using Mössbauer spectroscopy[4] and apuanite has also been studied using Raman spectroscopy[5].

In this chapter insertion of oxygen into the schafarzikite structure is investigated. The lead-substituted schafarzikites, $FeSb_{2-x}Pb_xO_4$, have been shown to incorporate oxygen

into the structure when heated to intermediate temperatures (*ca*. 400 °C) in air and the synthesis, structure and magnetic properties of the resultant $FeSb_{2-x}Pb_xO_{4+y}$ are reported.

4.2 Synthesis

The lead substituted schafarzikites were prepared as described in Section 3.2. Oxygen inserted schafarzikites were formed when carrying out TGA measurements by heating small amounts of sample (*ca*. 100 mg) in flowing oxygen gas to 400 °C for 10 minutes. A larger 1-2 g sample of $FeSb_{1.25}Pb_{0.75}O_{4+x}$ was prepared for neutron diffraction by heating $FeSb_{1.25}Pb_{0.75}O_4$ to 400 °C in air for 12 minutes.

4.3 Results and Discussion

4.3.1 Sample Preparation and Structural Characterisation

A TGA study of the lead-substituted schafarzikites, $FeSb_{2-x}Pb_xO_4$, revealed that oxidation takes place in two stages (Fig. 3.19). The samples were heated to 700 °C in flowing oxygen gas and were shown to take up oxygen initially at around 300-400 °C, presumably corresponding oxidation of Fe^{2+} only[6], and then again at higher temperatures forming $FeSbO_4$, Sb_2O_4 and Pb-containing pyrochlore phases. To see whether oxygen was being incorporated into the original schafarzikite structure the samples were heated to 400 °C in flowing oxygen gas, held at this temperature for 10 minutes and then cooled down to room temperature (Fig. 4.3) and XRPD patterns were recorded from the products (Fig. 4.4).

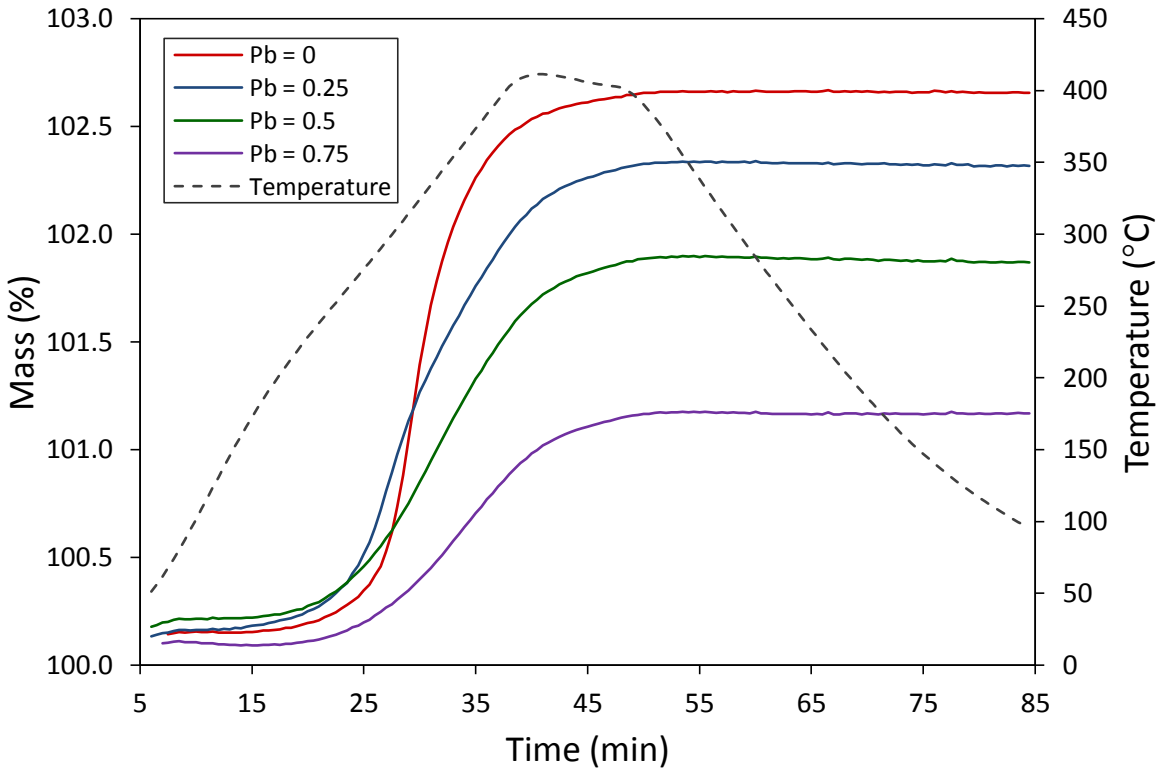

***Fig. 4.3**: Thermogravimetric analysis of $FeSb_{2-x}Pb_xO_4$ (x = 0, 0.25, 0.5, 0.75) up to 400 °C.*

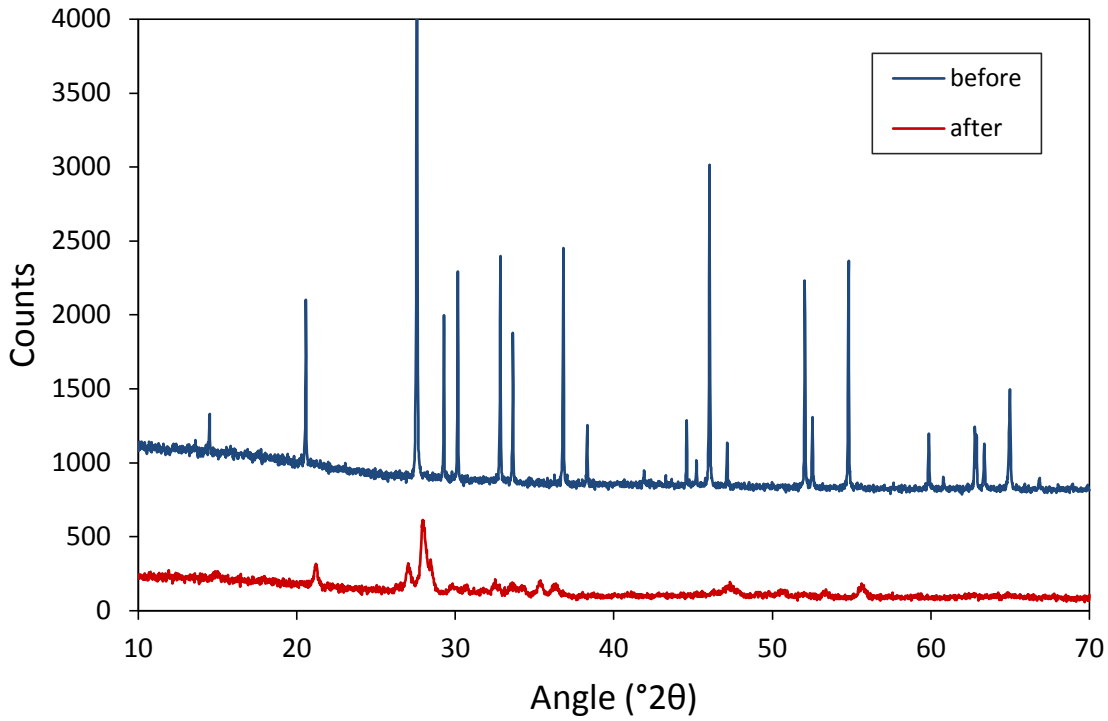

(a)

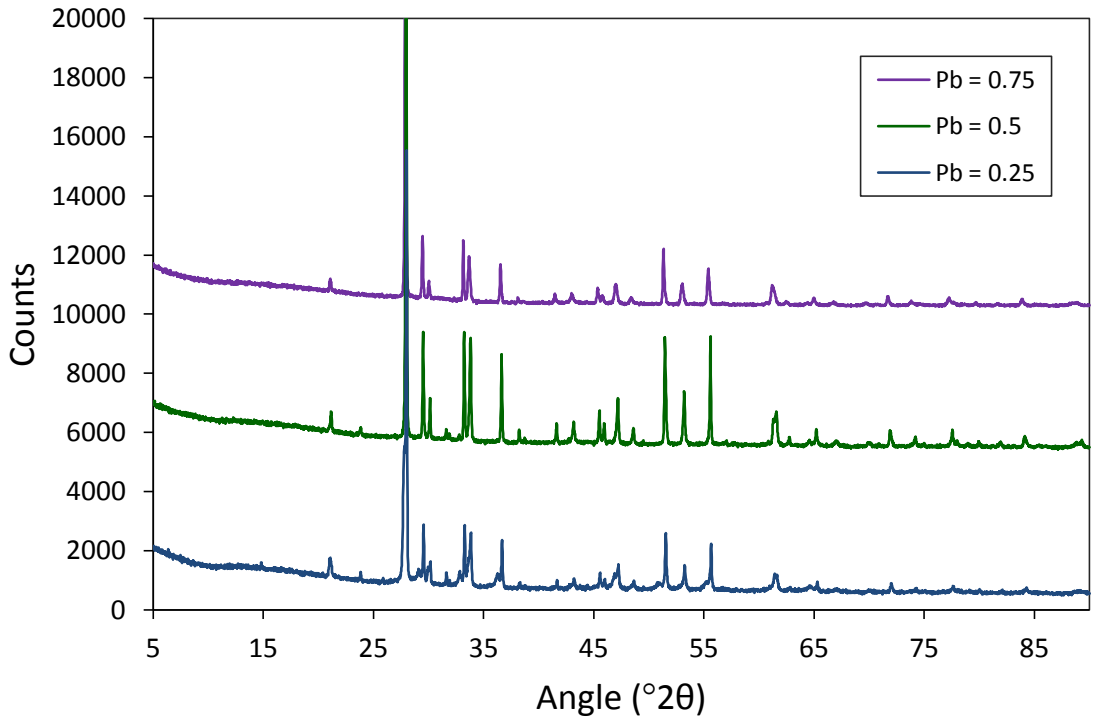

(b)

***Fig. 4.4**: Stack plots of XRPD patterns for (a) $FeSb_2O_4$ before and after heating to 400 °C in flowing oxygen gas and (b) $FeSb_{2-x}Pb_xO_4$ (x = 0.25, 0.5, 0.75) after heating to 400 °C in flowing oxygen gas.*

XRPD patterns of $FeSb_2O_4$ before and after heating to 400 °C in flowing oxygen gas are shown in Fig. 4.4a. The structure breaks down on insertion of oxygen but some peaks related to the original structure can still be seen. Insertion of excess oxygen into schafarzikite was therefore retried by heating $FeSb_2O_4$ in air in a furnace but this was unsuccessful. Evacuated sealed silica tube synthesis of $FeSb_2O_{4.5}$ was then attempted firstly by using stoichiometric amounts of Fe_2O_3 and Sb_2O_3 which was unsuccessful and secondly using stoichiometric amounts of $FeSbO_4$, Sb_2O_3 and Sb metal. A highly crystalline schafarzikite-related phase with unit cell parameters a = 8.240(1) Å and c = 5.9901(9) Å was formed by the second method with large Fe_2O_3, Sb_2O_3 and $FeSbO_4$ impurities. The unit cell parameters fit well with the trend seen for $FeSb_{2-x}Pb_xO_{4+y}$ (shown in Table 4.1 and discussed later) and indicate that an oxygen inserted schafarzikite phase can be made. To try and isolate the phase, $FeSb_2O_4$ which had already been heated in air to 300 °C for 30 minutes was heated in an evacuated, sealed silica tube for 48 hours at 650 °C and the same crystalline schafarzikite-related phase was formed but impurities were still present.

The X-ray diffraction patterns of $FeSb_{2-x}Pb_xO_4$ (x = 0.25, 0.5, 0.75) after heating to 400 °C are shown in Fig. 4.4b. The schafarzikite structure is maintained and the unit cell parameters have changed (Table 4.1) indicating that oxygen is being incorporated into the original structure. The oxygen insertion is shown to work best for the samples containing more lead; for samples with lower levels of lead there are increasing amounts of impurity phases present. For samples with a higher lead content there is less Fe^{2+} present therefore fewer oxygen ions will need to be accommodated by the structure to oxidise all the Fe^{2+} ions to Fe^{3+}.

***Table 4.1**: Unit cell parameters from Rietveld refinement of room temperature XRPD data for $FeSb_{2-x}Pb_xO_4$ (x = 0.25, 0.5, 0.75) before and after heating to 400 °C in flowing oxygen gas*

	a-parameter (Å)		*c*-parameter (Å)		volume (Å³)	
x	before	after	before	after	before	after
0.25	8.5135(2)	8.3505(8)	5.9650(1)	6.0201(6)	432.34(2)	419.8(1)
0.5	8.4678(1)	8.3597(3)	6.01050(8)	6.0323(2)	430.98(1)	421.56(4)
0.75	8.4556(1)	8.3924(3)	6.0371(1)	6.0486(2)	431.64(2)	426.01(4)

On insertion of oxygen into the structure of $FeSb_{2-x}Pb_xO_4$, a decrease in the *a*-parameter, an increase in the *c*-parameter and a decrease in the unit cell volume is seen for all the samples. As Fe^{2+} is being oxidised to Fe^{3+} (Ionic radii[7]: Fe^{2+} = 0.78 Å, Fe^{3+} = 0.645 Å) a decrease in the Fe-O bond lengths and unit cell size is expected. The expansion along *c* is explained, as it was for increasing lead substitution (Section 3.3.1), by the repulsion between highly charged Fe^{3+} ions causing an increase in the Fe-Fe distance within a chain. The intra-chain Fe-Fe distance is directly linked to the *c*-parameter (Fig. 4.1).

It was assumed that when the samples take up oxygen at 400 °C O^{2-} ions are inserted into the structure and all the Fe^{2+} is oxidised to Fe^{3+}. The expected relative molecular mass (RMM) and expected mass increase were therefore calculated and compared to the observed mass increase obtained from TGA data (Table 4.2, Fig. 4.3). Determination of errors from TGA is difficult and the error values reported in Table 4.2 have been determined by taking into account the likely errors when calculating percentage differences. The values show that the observed increase is actually higher than expected. This suggests that, as only Fe^{2+} is being oxidised at these temperatures, oxygen could be being taken up as peroxide, O_2^{2-}, ions which would double the expected mass increase. The mass increase is slightly more than double for the sample $FeSb_{1.25}Pb_{0.75}O_4$, but for the samples with lower lead contents the increase is less than double and for $FeSb_2O_4$ the mass increase is close to the expected value. This could indicate that at high lead (and low Fe^{2+})

levels the oxygen is taken up mostly as peroxide ions, at low lead (and high Fe^{2+}) levels, the oxygen is taken up mostly as oxide ions and between these situations there is a mix of oxide and peroxide ions in the structure.

***Table 4.2**: Expected and observed mass increases of $FeSb_{2-x}Pb_xO_4$ after oxygen insertion at 400 °C*

x	RMM $FeSb_{2-x}Pb_xO_4$	RMM $FeSb_{2-x}Pb_xO_{4+y}$	expected increase (%)	observed increase (%)
0	363.361	371.3605	2.20	2.49(3)
0.25	384.7185	390.7181	1.56	2.17(3)
0.5	406.076	410.0758	0.98	1.67(4)
0.75	427.4335	429.4334	0.47	1.08(2)

To find evidence for the presence of peroxide ions in the structure, Raman spectroscopy measurements were recorded from the samples before and after insertion of oxygen. The spectra recorded from $FeSb_{2-x}Pb_xO_4$ before insertion of oxygen are shown in Fig. 4.5-4.8. The schafarzikite and related antimonite minerals are characterized by a strong band at 660-680 cm^{-1} [5] and the spectrum recorded from schafarzikite (Fig. 4.5) agreed well with those reported in the literature[5-6].

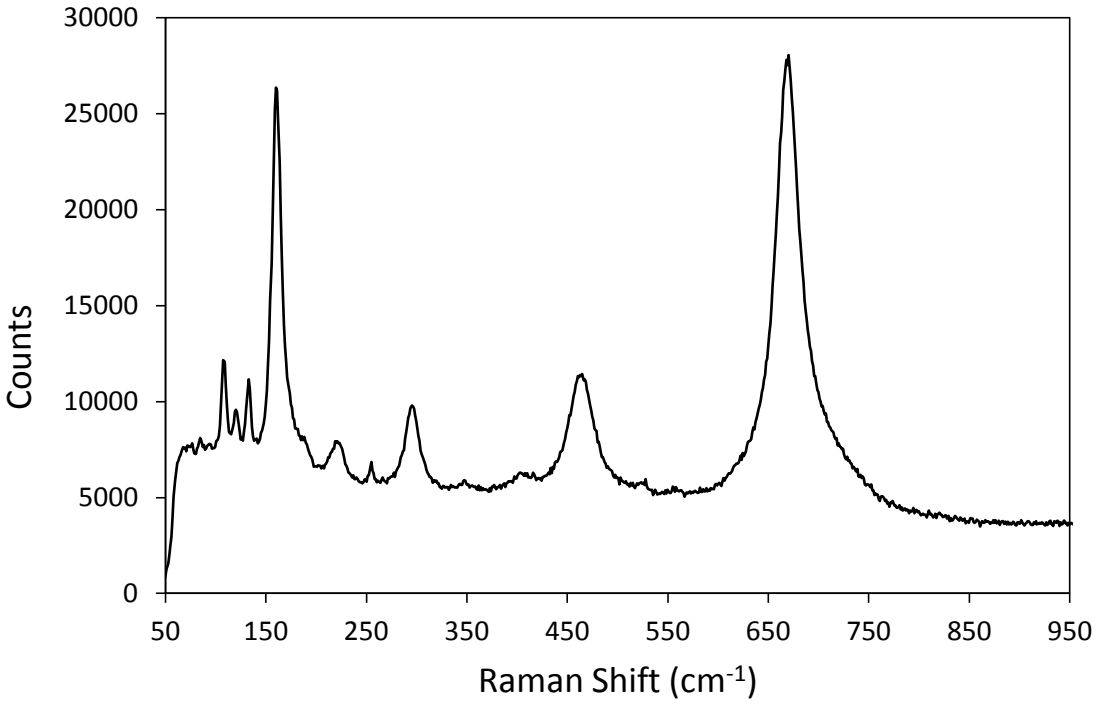

***Fig. 4.5**: Room temperature Raman spectra recorded from $FeSb_2O_4$ powder.*

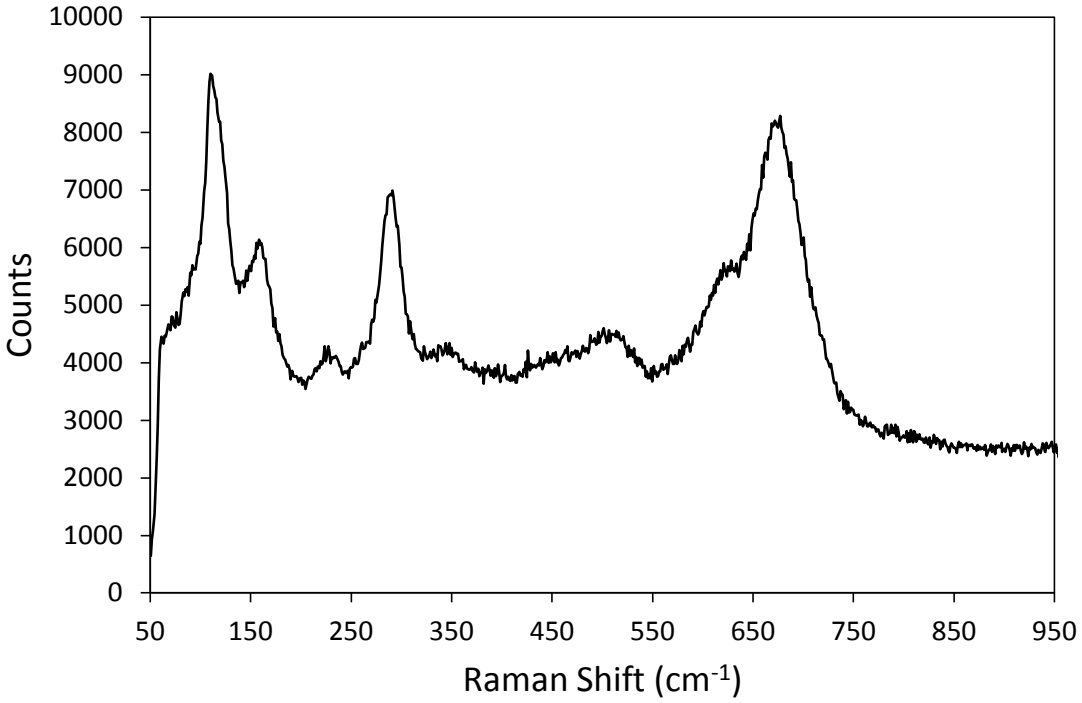

***Fig. 4.6**: Room temperature Raman spectra recorded from $FeSb_{1.75}Pb_{0.25}O_4$ powder.*

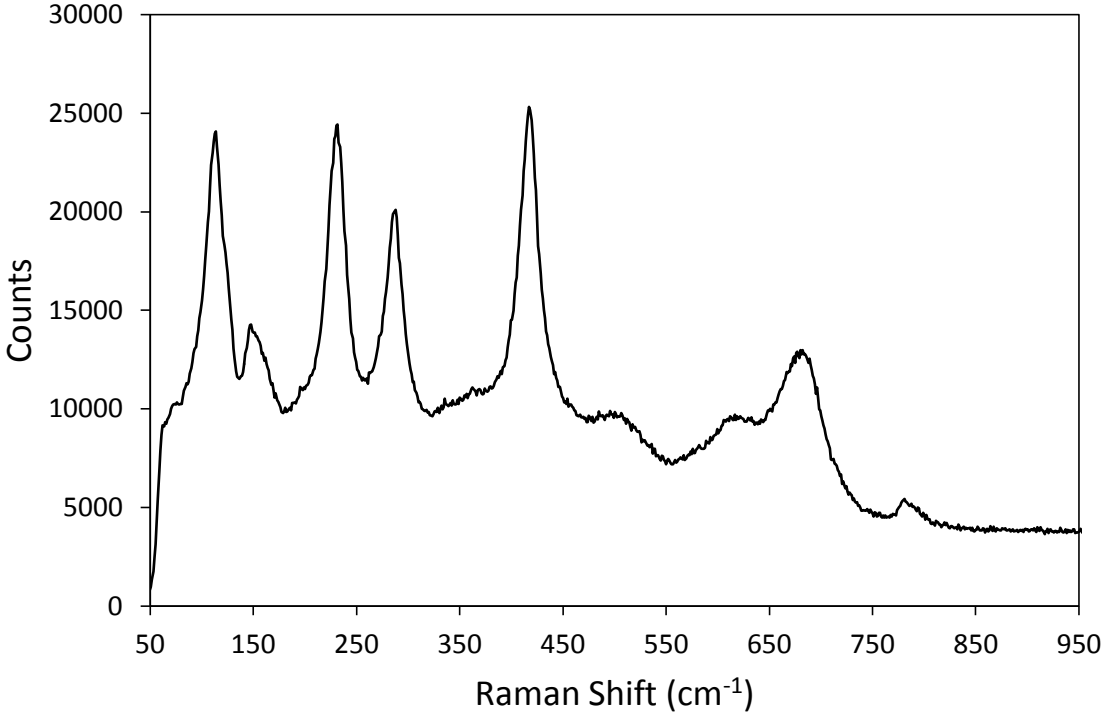

***Fig. 4.7**: Room temperature Raman spectra recorded from $FeSb_{1.5}Pb_{0.5}O_4$ pellet.*

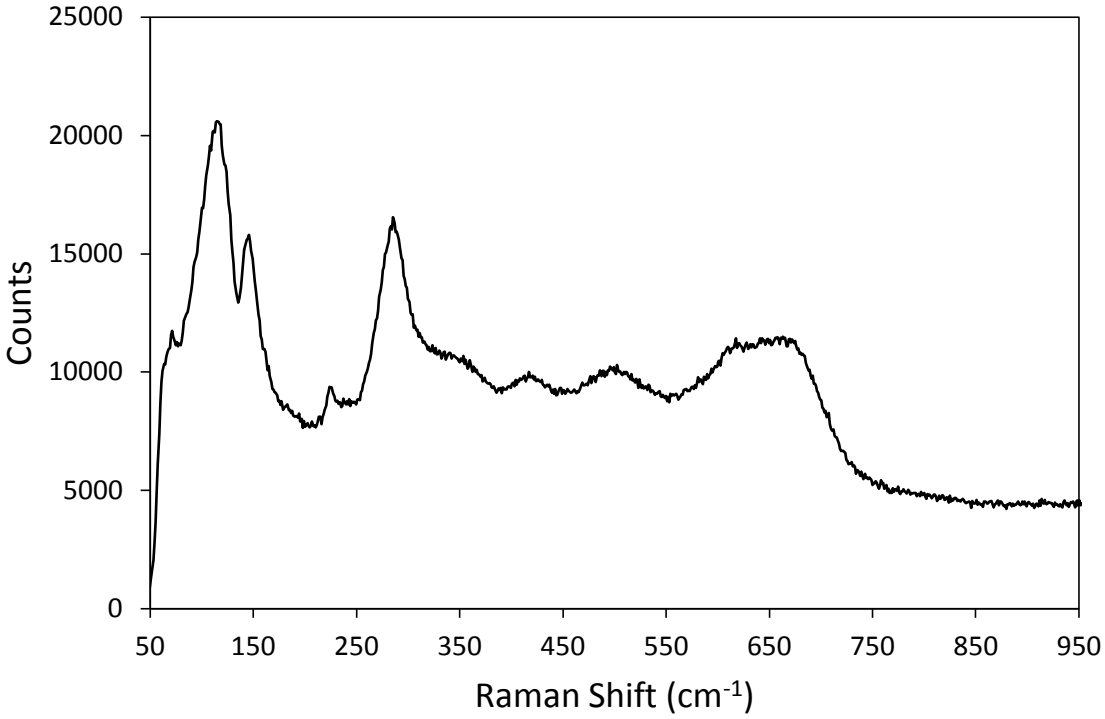

***Fig. 4.8**: Room temperature Raman spectra recorded from $FeSb_{1.25}Pb_{0.75}O_4$ powder.*

The mix of antimony and lead ions on the pyramidal sites of $FeSb_{2-x}Pb_xO_4$ (x = 0.25, 0.5, 0.75) causes the bands in the spectra to be broader than those for $FeSb_2O_4$. The band found at around 660-680 cm^{-1} corresponds to a vibration of Sb-O bonds[5] and a splitting of this band is seen for the lead substituted samples due to the presence of Pb-O, as well as Sb-O, bonds in the structure. Raman spectroscopy was performed on the oxygen inserted samples $FeSb_{1.5}Pb_{0.5}O_{4+x}$ and $FeSb_{1.25}Pb_{0.75}O_{4+x}$: the data are shown in Fig. 4.9 and compared to data obtained before insertion of oxygen. The results are inconclusive as the peaks are extremely broad. In metal dioxygen complexes peroxide shifts are found between 750 and 950 cm^{-1} [8-9] and in a known organometallic complex containing antimony bonded to peroxide ions a signal is observed at 798.6 cm^{-1} [10]. However in schafarzikite-type materials the peroxide peak may be shifted to lower wavenumbers due to the presence of heavier atoms and introduction of lead into the structure. No peaks are seen above 750 cm^{-1} but the signal could be masked by the broadening of the peak at *ca*. 680 cm^{-1}. To

study this further, neutron powder diffraction data were obtained from the sample $FeSb_{1.25}Pb_{0.75}Sb_2O_{4+x}$.

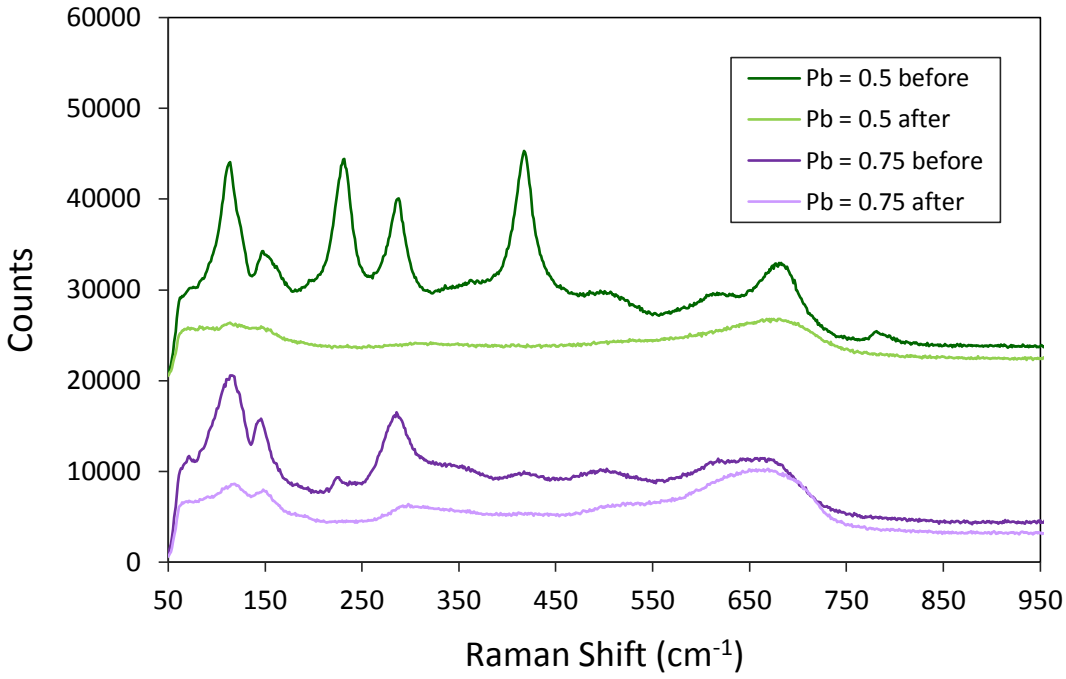

***Fig. 4.9**: Stack plot of room temperature Raman spectra recorded from $FeSb_{2-x}Pb_xO_4$ (x = 0.5, 0.75) before and after insertion of oxygen.*

A larger sample of $FeSb_{1.25}Pb_{0.75}O_{4+x}$ was prepared, as described in Section 4.2, by heating $FeSb_{1.25}Pb_{0.75}O_4$ in a furnace in air for 12 minutes. The XRPD pattern confirmed that this sample was the same as the oxygen inserted sample prepared using TGA. ^{57}Fe Mössbauer spectra were recorded at 298 K from the sample before and after heating in air. Before heating in air the sample, $FeSb_{1.25}Pb_{0.75}O_4$, was shown to contain 74 % Fe^{3+} and 26 % Fe^{2+}, in excellent agreement with the expected values. The Mössbauer spectrum recorded from the sample after heating in air (Fig. 4.10) showed that some Fe^{2+} still remained in the sample (5 %) while the rest of the iron had been oxidised to Fe^{3+} (95 %). However this is not surprising due to the short heating time used. The reason the sample was heated for such a short time was because longer heats were shown by XRPD to cause a loss of crystallinity.

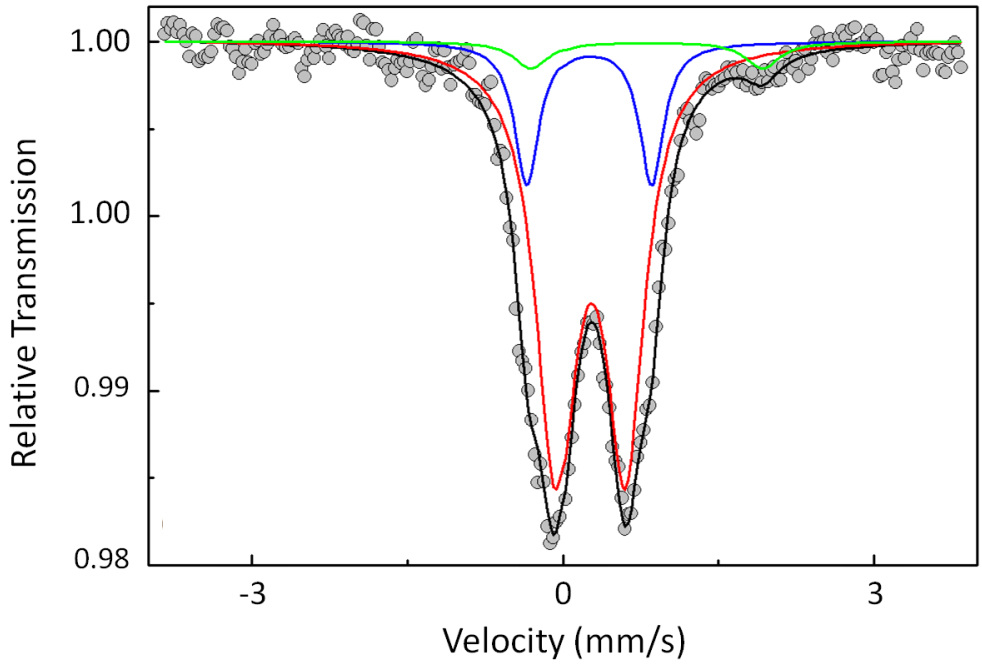

***Fig. 4.10**: ^{57}Fe Mössbauer spectrum recorded from $FeSb_{1.25}Pb_{0.75}O_{4+x}$ at 298 K.*

Structure refinement of NPD data was performed using the model obtained for $FeSb_{1.25}Pb_{0.75}O_4$ (space group $P4_2/mbc$) with no excess oxygen added and refining the unit cell along with other parameters as described for $FeSb_{2-x}Pb_xO_4$ in Section 3.3.1. The refinement gave a good fit with values of $\chi^2 = .6$, $R_{wp} = 0.055$ and $R_F^2 = 0.052$.

To locate oxygen ions in the structure, difference Fourier maps were plotted. Fourier maps can be calculated from data obtained during the Rietveld refinement. For each reflection the structure factor, F_{calc}, and phase are calculated; the observed intensity is also extracted which can be used to calculate an observed structure factor, F_{obs}. Using these values, calculated and observed maps of the structure can be plotted and by subtracting the calculated data from the observed data a difference Fourier map can be plotted which is used to find missing atoms in the structure. Two-dimensional difference Fourier maps were plotted at various intervals along the *c*-axis to locate the extra oxygen ions. The Fourier maps are shown in Fig. 4.11 and are compared with the structure of $FeSb_2O_4$.

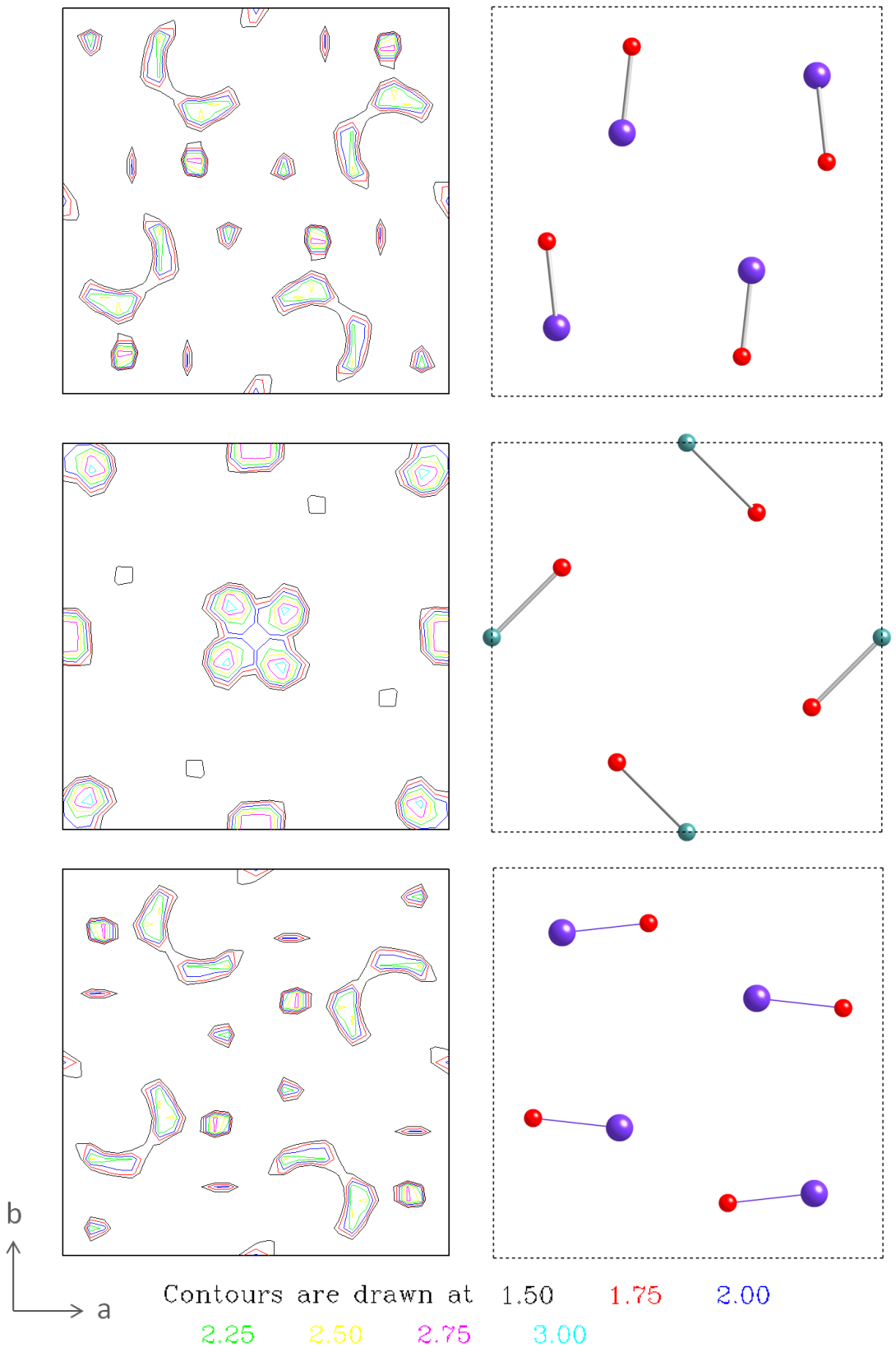

***Fig. 4.11**: Left hand side: 2D difference Fourier maps for $FeSb_{1.25}Pb_{0.75}O_{4+x}$ obtained from Rietveld refinement of room temperature NPD data at c = 0 Å (top), c = 1.5 Å (middle) and c = 3 Å (bottom). Right hand side: corresponding structure diagrams of $FeSb_2O_4$; Fe ions are shown as green spheres, Sb as purple spheres and O as red spheres.*

Three maps are shown at c = 0 Å, c = 1.5 Å and c = 3 Å which, since c = 6.04 Å, correspond to 0, ¼ and ½ along the c-axis respectively. The region of highest neutron scattering density not being accounted for in the model was found at c = ¼ and slightly off centre within the channels. Due to the space group symmetry, four oxygen ion positions are generated and this corresponds to a partially occupied 16*i* site (Fig. 4.12).

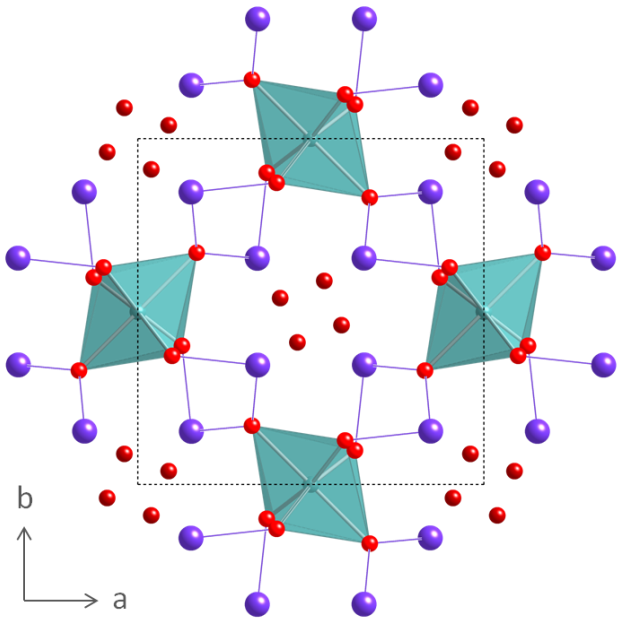

***Fig. 4.12**: The structure of $FeSb_{1.25}Pb_{0.75}O_{4+x}$ looking down the c-axis. FeO_6 octahedra are shaded. Fe ions are located within the octahedra, Sb/Pb ions are shown as purple spheres and O ions are shown as red spheres. The O3 ions within the channels are shown in dark red and only partially occupy a 16i site.*

A third oxygen position was therefore added to the model and the atomic coordinates and fractional occupancy were refined. The model fits the data well (Fig. 4.13), reducing the value of χ^2 to .900, and the parameters obtained from the refinement are summarised in Table 4.3. The Fourier maps initially plotted revealed a splitting of the O1 anion site as electron density was seen either side of the O1 anion in the *ab* plane. Anisotropic temperature factors were therefore used for this ion in all room temperature $FeSb_{1.25}Pb_{0.75}O_{4+x}$ refinements and gave larger values in the *a*-direction than in the *c*-direction (Table 4.3).

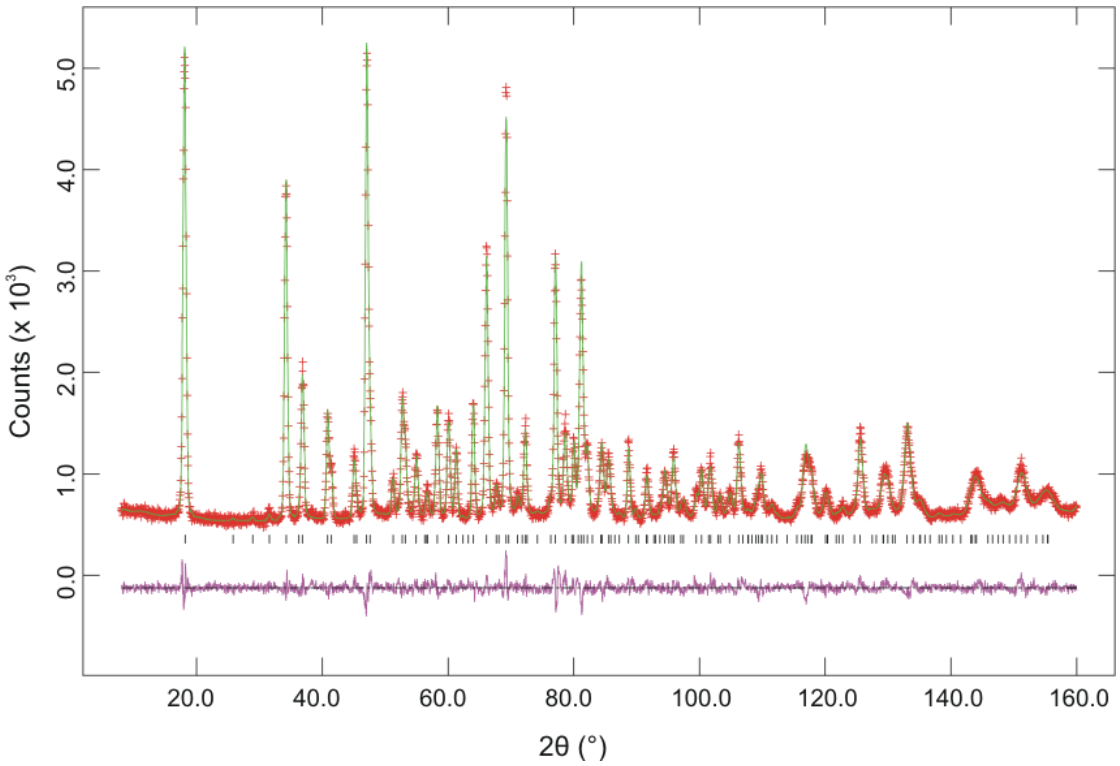

***Fig. 4.13**: Observed, calculated and difference plots for high resolution NPD data recorded from $FeSb_{1.25}Pb_{0.75}O_{4+x}$ at 298 K.*

Assuming all the Fe^{2+} is oxidised to Fe^{3+} by insertion of oxide ions, the composition of the sample would be $FeSb_{1.25}Pb_{0.75}O_{4.125}$ which gives half an excess oxygen ion per unit cell. Overall a fractional occupancy of 0.03125 would be expected on the O3 16*i* site. The fractional occupancy given from refinement of NPD data (Table 4.3) is slightly more than double the expected value. This, along with the value from TGA, supports the idea that oxygen is being taken up as peroxide. The bond lengths and angles obtained from the refinement show that a model with peroxide in the channels bonded to Sb ions is sensible. The Sb-O3 bond to the nearest of the four possible oxygen sites is 1.92(4) Å, the bond length between the O3 ions opposite one another is 1.63(4) Å and the Sb-O3-O3 bond angle is 118(2) °. Compared to other compounds these values look reasonable[10] and the O3-O3 bond length corresponds to a long peroxide bond as the O-O bond length of peroxo groups is typically 1.40-1.48 Å [11]. The coordination of the Sb^{3+}/Pb^{2+} ion and location of O3 ions is shown in Fig. 4.14.

***Table 4.3**: Structural parameters refined from high resolution NPD data for $FeSb_{1.25}Pb_{0.75}O_{4+x}$ at 298 K*

	Wyckoff Position	*x*	*y*	*z*	Fractional Occupancy	U_{iso} (Å²)
Fe	4*d*	0	0.5	0.25	1	0.0181(6)
Sb	8*h*	0.1538(3)	0.1547(3)	0	0.64(1)	0.0235(8)
Pb	8*h*	0.1538(3)	0.1547(3)	0	0.36(1)	0.0235(8)
O1	8*g*	0.6702(2)	0.1702(2)	0.25	1	*
O2	8*h*	0.0988(3)	0.6276(3)	0	1	0.0234(9)
O3	16*i*	0.539(4)	0.411(3)	0.259(6)	0.074(4)	0.05(1)
* U_{11}, U_{22} = 0.039(1), U_{33} = 0.029(2), U_{12} = -0.025(1), U_{13} = -0.010(1), U_{23} = 0.010(1)						
a (Å)				8.4057(3)		
c (Å)				6.0446(2)		
Volume (Å²)				427.09(4)		
Fe-O1 (Å) x 1				2.024(3)		
Fe-O2 (Å) x 4				2.031(2)		
Fe-O2-Fe (°) x 1				96.2(1)		
O2-Fe-O2 (°) x 2				83.8(1)		
O2-Fe-O2 (°) x 2				97.00(9)		
Sb/Pb-O1 (Å) x 2				2.114(2)		
Sb/Pb-O2 (Å) x 1				2.092(3)		
Sb/Pb-O3 (Å)				1.92(4)		
Sb-O3-O3 (°)				118(2)		
O3-O3 (Å)				1.63(4)		
χ^2, R_{wp}, R_F^2				1.900, 0.047, 0.036		

The Sb^{3+}/Pb^{2+} ion is equidistant to two peroxide ion groups within the channels and links can be formed between Sb^{3+}/Pb^{3+} ions in adjacent chains (Fig. 4.14). The Sb^{3+}/Pb^{2+} ions can form a bond to the O3 ion while the lone pair points into the channel. Due to the low levels of oxygen in the material long range ordering is not seen.

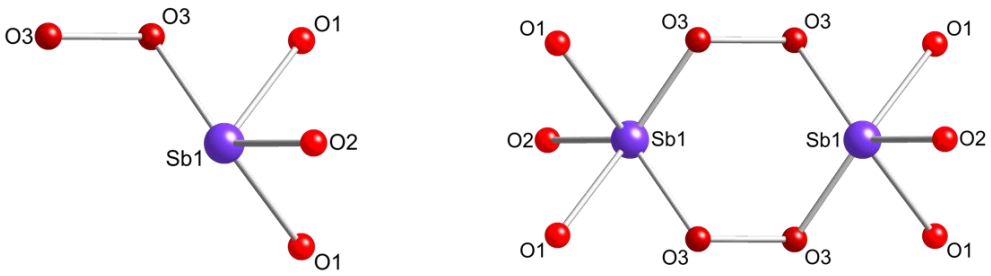

***Fig. 4.14**: Left: coordination of the Sb/Pb ion in $FeSb_{1.25}Pb_{0.75}O_{4+x}$ showing bonding to peroxide oxygen ions (O3) in the channels; right: location of O3 ions and possible links to Sb/Pb in adjacent chains.*

4.3.2 Magnetic Properties

Field cooled (FC) and zero-field cooled (ZFC) susceptibility measurements were taken between 5 and 300 K for the samples $FeSb_{1.5}Pb_{0.5}O_{4+x}$ and $FeSb_{1.25}Pb_{0.75}O_{4+x}$. An applied field of 500 Oe was used and plots of susceptibility versus temperature are shown in Fig. 4.15 and 4.16.

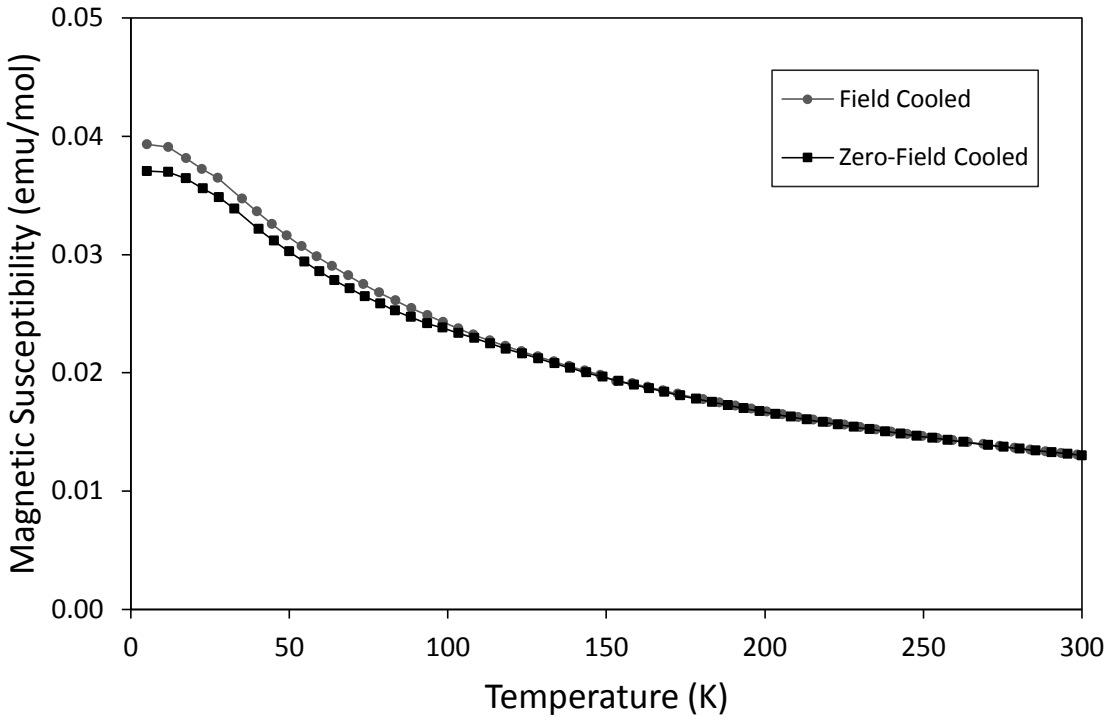

***Fig. 4.15**: Variation of magnetic susceptibility with temperature for $FeSb_{1.5}Pb_{0.5}O_{4+x}$.*

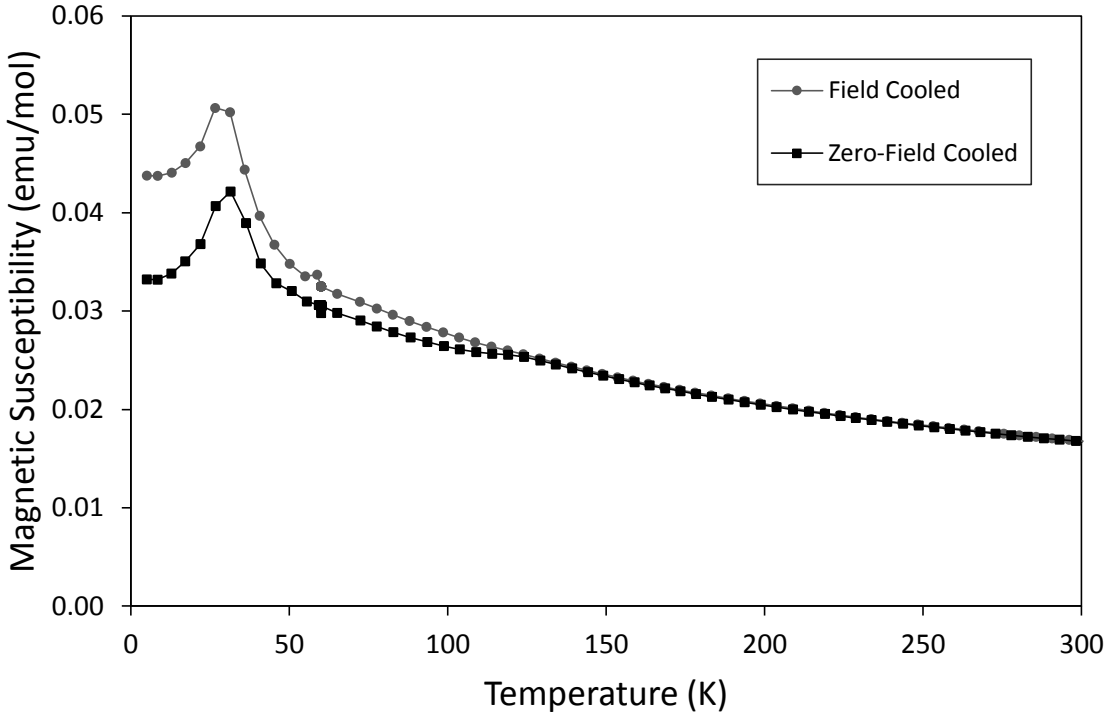

***Fig. 4.16**: Variation of magnetic susceptibility with temperature for $FeSb_{1.25}Pb_{0.75}O_{4+x}$.*

The masses of $FeSb_{2-x}Pb_xO_{4+y}$ given in Table 4.2 were used when calculating the susceptibility. Although there may be more oxygen in the structures than these masses account for, the amounts are uncertain and very small changes in mass would have negligible effects on the susceptibility values.

Transitions at around 120 K can be seen in both plots due to the Verwey transition in Fe_3O_4 impurities, as discussed in Section 3.3.2, which causes the FC and ZFC data to diverge. On insertion of oxygen ions, $FeSb_{1.5}Pb_{0.5}O_4$ is seen to lose the magnetic ordering seen in Fig. 3.11. However an antiferromagnetic transition is seen at *ca*. 36 K in $FeSb_{1.25}Pb_{0.75}O_{4+x}$, which is lower than the ordering temperatures observed previously for $FeSb_{2-x}Pb_xO_4$ (Table 3.3). The low ordering temperature and loss of ordering in $FeSb_{1.5}Pb_{0.5}O_{4+x}$ indicate that the exchange interactions have been weakened on insertion of oxygen ions and consequential oxidation of all Fe^{2+} to Fe^{3+}.

Refinement of NPD data recorded at 2 K was performed as described for the lead substituted schafarzikites: the nuclear and magnetic structures were refined as separate phases with $P4_2/mbc$ and $P1$ symmetry respectively so that the directions of the magnetic moments were not restricted by the tetragonal symmetry constraints. The final refinement is shown in Fig. 4.17.

When refining the 2 K NPD data, it was seen that the thermal parameters for all the atoms were higher than expected as they were close to the room temperature values. The Fourier map revealed splitting of the O1 site, as it did in the room temperature refinement, and changing the O1 temperature factor to an anisotropic one reduced the U_{iso} values for the other atoms. The O1 temperature factor was very large in the *a* and *b* directions, much larger than would be expected for a 2 K refinement, so for subsequent refinements the O1 anion was displaced onto a 16*i* site and the fractional occupancy set at 0.5. A summary of structural and magnetic parameters obtained from the refinement is given in Table 4.4. The U_{iso} value for the O3 anion is large but this is to be expected as these oxygen ions are disordered throughout the channels. The fractional occupancy of the O3 anion site is again consistent with oxygen being taken up as peroxide ions.

It can be seen from Fig. 4.17b that the {100} and {210} reflections are present which indicates the presence of C-type magnetic ordering (FM within the chains and AFM within the layers) and that the (111) and {021} reflections are also present consistent with A-type magnetic ordering (AFM within the chains and FM within the layers). There is no {101} peak which would be indicative of G-type magnetic ordering (AFM within both the chains and the layers). The two modes can be combined to give a non-collinear antiferromagnetic structure with both A- and C-type components. The final model, in which A-type ordering is seen along the *x*-axis with a strong C-type component along *z*, is shown in Fig. 4.18 and the magnetic moments are given in Table 4.4.

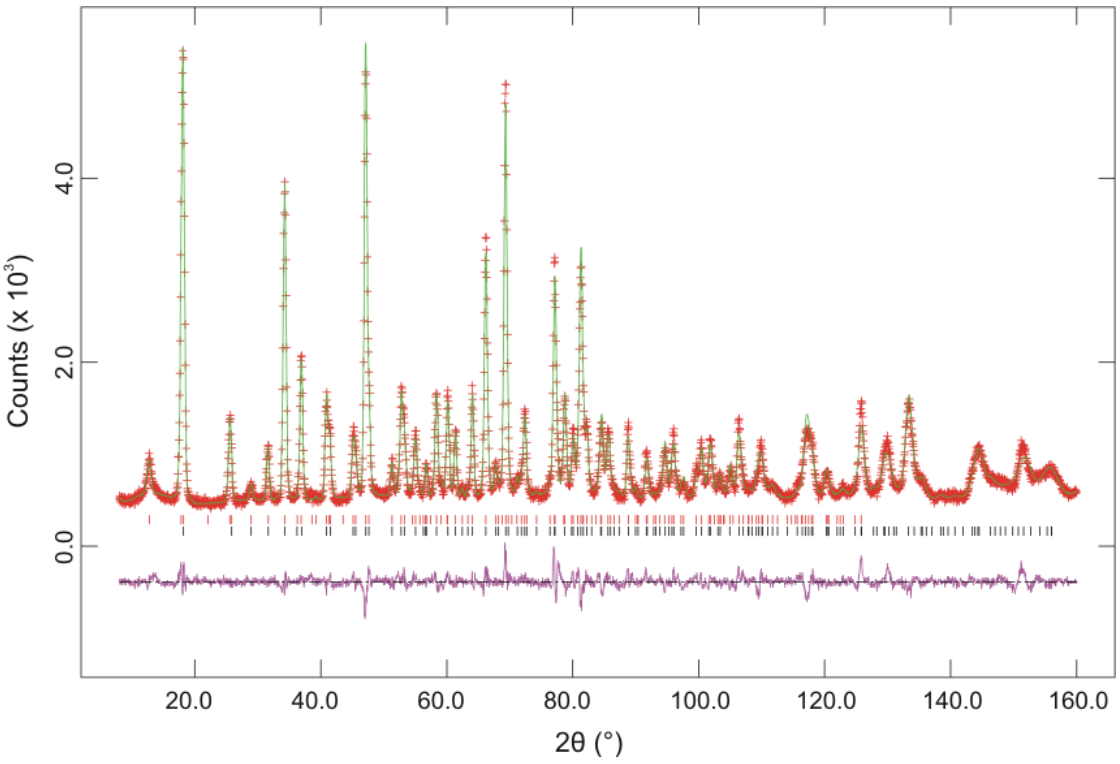

(a)

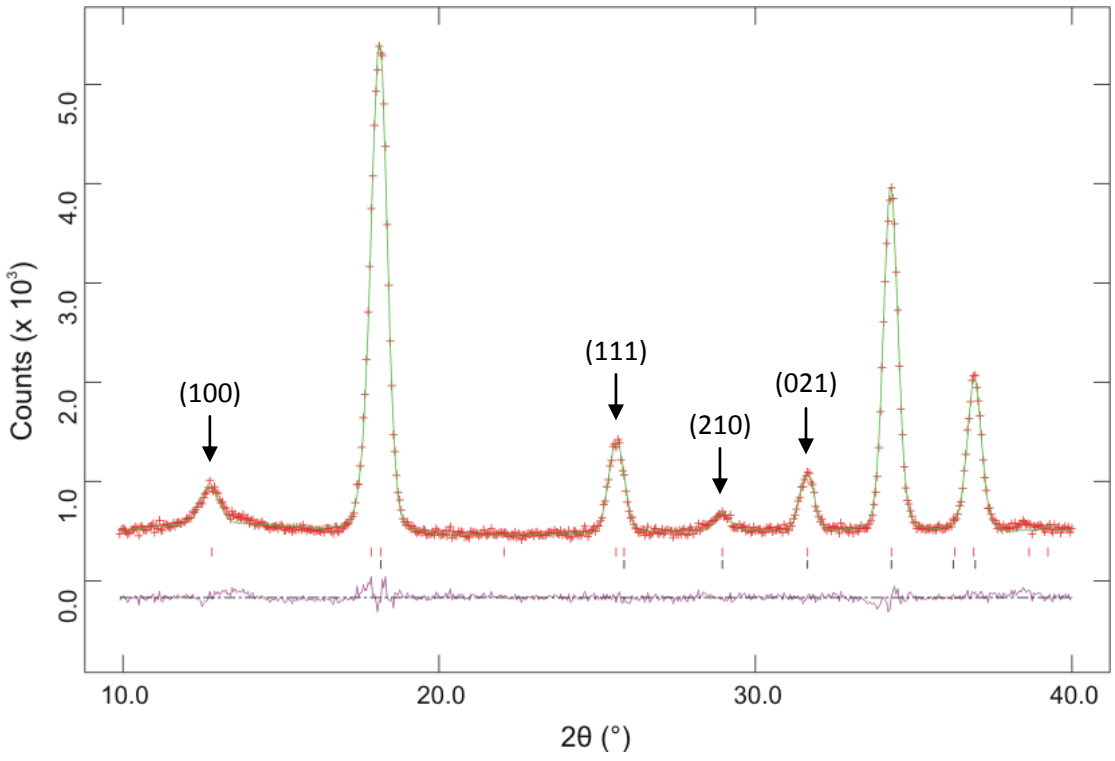

(b)

***Fig. 4.17**: Observed, calculated and difference plots for high resolution NPD data recorded from $FeSb_{1.25}Pb_{0.75}O_{4+x}$ at 2 K showing (a) the full plot from 10 to 160 °2θ and (b) 10 to 40 °2θ with magnetic reflections labelled.*

***Table 4.4**: Structural parameters and magnetic moments refined from high resolution neutron powder diffraction data from $FeSb_{1.25}Pb_{0.75}O_{4+x}$ at 2 K*

	Wyckoff Position	*x*	*y*	*z*	Fractional Occupancy	U_{iso} (Å²)
Fe	4*d*	0	0.5	0.25	1	0.0142(7)
Sb	8*h*	0.1546(3)	0.1544(3)	0	0.59(1)	0.0178(8)
Pb	8*h*	0.1546(3)	0.1544(3)	0	0.41(1)	0.0178(8)
O1	16*i*	0.6860(4)	0.1543(4)	0.240(1)	0.5	0.010(1)
O2	8*h*	0.0989(3)	0.6267(3)	0	1	0.0172(8)
O3	16*i*	0.541(4)	0.410(3)	0.253(7)	0.056(4)	0.03(1)

a (Å)	8.3946(3)
c (Å)	6.0383(3)
Volume (Å²)	425.52(5)
Fe-O1 (Å) x 1	2.030(3)
Fe-O2 (Å) x 4	2.025(2)
Fe-O2-Fe (°) x 1	96.4(1)
O2-Fe-O2 (°) x 2	83.6(1)
O2-Fe-O2 (°) x 2	97.2(1)
Sb/Pb-O1 (Å) x 2	2.064(5), 2.180(5)
Sb/Pb-O2 (Å) x 1	2.082(4)
Sb/Pb-O3 (Å)	1.88(4)
Sb-O3-O3 (°)	118(2)
O3-O3 (Å)	1.66(5)
Moment along *x* (μ_B)	2.67(3)
Moment along *z* (μ_B)	1.08(3)
Total moment (μ_B)	2.88(3)
χ^2, R_{wp}, R_F^2	2.861, 0.058, 0.050

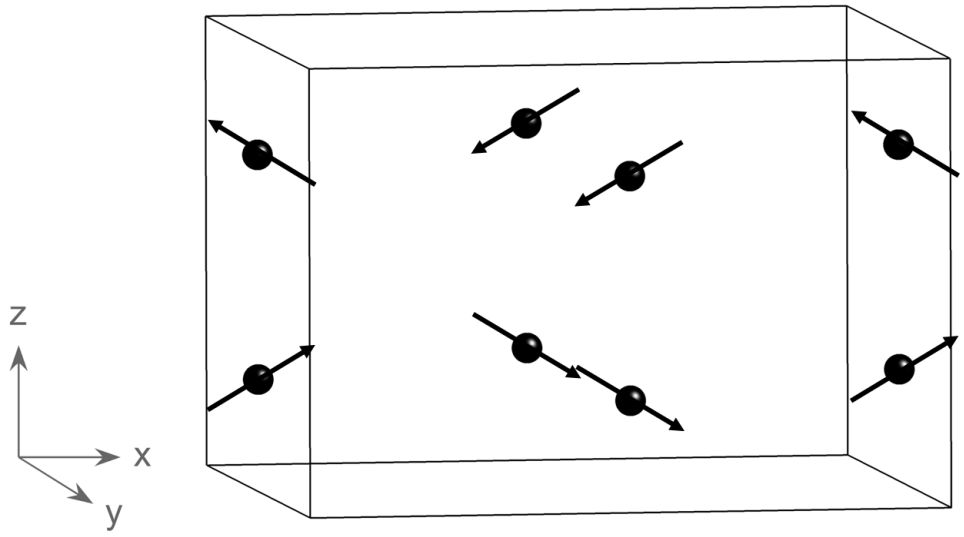

***Fig. 4.18**: Magnetic structure model for $FeSb_{1.25}Pb_{0.75}O_{4+x}$ showing A-type ordering along x with a strong C-type component along z.*

This is different from the magnetic structures of $FeSb_{2-x}Pb_xO_4$ before oxygen insertion, which show C-type magnetic ordering only. Of these samples the highest lead composition for which NPD data were collected was 0.7 and the magnetic structure of $FeSb_{1.3}Pb_{0.7}O_4$ is shown in Fig. 4.19 for comparison with $FeSb_{1.25}Pb_{0.75}O_{4+x}$.

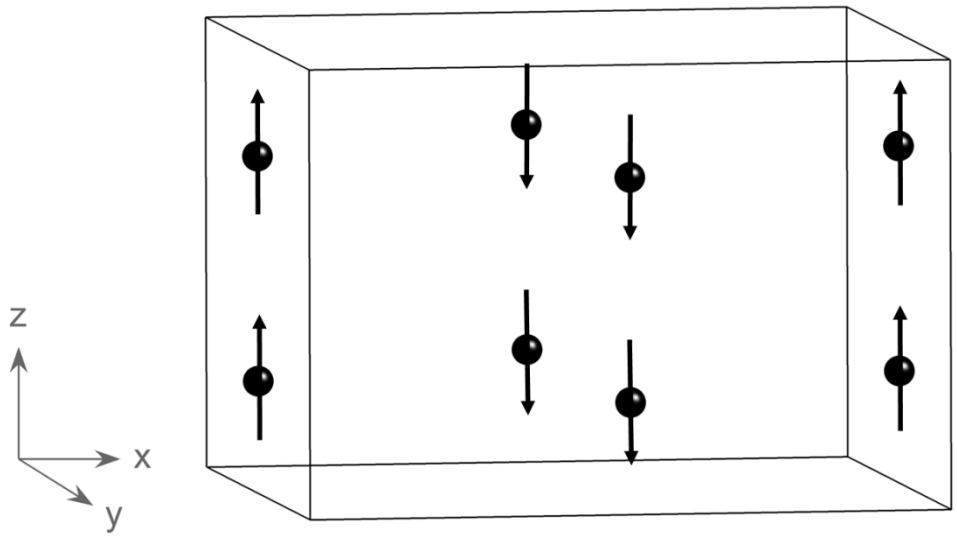

***Fig. 4.19**: Magnetic structure model for $FeSb_{1.3}Pb_{0.7}O_4$ showing C-type ordering. The moment is aligned predominantly along the z-axis with a small component along x (not shown).*

The magnetic moment in $FeSb_{1.3}Pb_{0.7}O_4$ lies predominantly along the *z*-axis with a small component along *x*. On insertion of oxygen the magnetic structure changes: the C-type component along *z* is still present but there is also an additional A-type component which lies along the *x*-axis. The change in magnetic ordering implies that the insertion of oxygen ions into the channels, and resultant oxidation of Fe^{2+} ions to Fe^{3+}, has caused a change in the exchange interactions occurring between the iron ions.

There are various ways in which magnetic ions in the schafarzikite structure can interact with one another, giving rise to long-range ordering throughout the materials. Almost all the iron is oxidised to Fe^{3+} in the oxygen-inserted samples (Fig. 4.10) which will have significant effects on the exchange interactions. The Fe ions within a chain can interact in three ways: directly through the t_{2g} orbitals, via a double-exchange mechanism and indirectly through 90 ° Fe-O-Fe superexchange interactions. The Fe ions within the layers interact through weaker Fe-O-Sb/Pb-O-Fe links. Direct cation-cation exchange is possible throughout the chains due to the edge-linking of FeO_6 octahedra. The t_{2g} orbitals on neighbouring Fe ions point directly at one another and the binding is stabilised if the electrons are aligned antiparallel, therefore favouring AFM ordering within the chains[12]. This interaction is reduced in the oxygen-inserted samples due to contraction of the Fe^{3+} *d*-orbitals and the increased Fe-Fe intra-chain distance (Table 4.1). This is the same effect that was seen when comparing the lead substituted samples to schafarzikite (Section 3.3.2) but the oxygen-inserted samples contain more Fe^{3+} and have even larger *c*-parameters. The double-exchange mechanism[13], whereby ferromagnetically-aligned Fe^{2+} and Fe^{3+} ions in a chain can exchange an electron, was possible for $FeSb_{2-x}Pb_xO_4$ due to the mixed Fe^{2+}/Fe^{3+} oxidation state. On insertion of oxygen almost all the Fe^{2+} (*ca*. 95 %) has been oxidised to Fe^{3+} so the mechanism is no longer possible. The 90° Fe^{3+}-O-Fe^{3+} superexchange interactions occur due to the interaction of Fe e_g electrons through two

O 2p orbitals. This type of exchange usually favours FM interactions but the possible involvement of t_{2g} electrons in Fe^{3+} causes uncertainty as to whether the interaction will favour FM or AFM ordering[14]. The mix of competing exchange interactions is complicated and overall a decreased ordering temperature and a mix of magnetic ordering modes are observed in $FeSb_{1.25}Pb_{0.75}O_{4+x}$.

4.4 Conclusions

Oxygen ions have successfully been inserted into the schafarzikite structure for the first time. When carrying out thermogravimetric analysis of $FeSb_{2-x}Pb_xO_4$ it was shown that at intermediate temperatures (*ca*. 400 °C) only Fe^{2+} is oxidised and the samples incorporate oxygen into the original structure. This was shown to work best for samples containing higher amounts of lead, at lower lead levels the amount of oxygen inserted is too great and the structure begins to break down. On insertion of oxygen a decrease was seen in the *a*-parameter and overall cell volume, due to the oxidation of Fe^{2+} to smaller Fe^{3+} ions, and an increase was seen in the *c*-parameter, due to enhanced Fe-Fe repulsions. TGA showed that the samples were taking up more oxygen than would be expected for oxidation by insertion of oxide, O^{2-}, ions and that the samples may also be taking up oxygen as peroxide, O_2^{2-}. Raman spectroscopy was used to try and confirm this but the results were inconclusive due to broadening of the peaks. NPD data recorded from the sample $FeSb_{1.25}Pb_{0.75}O_{4+x}$ were used to locate oxygen in the channels and a structure in which peroxide ions can form links between Sb^{3+}/Pb^{2+} ions on either side of the channels was suggested. Magnetic measurements showed that the magnetic properties of $FeSb_{2-x}Pb_xO_{4+y}$ change on insertion of oxygen: $FeSb_{1.5}Pb_{0.5}O_{4+x}$ loses its magnetic ordering and $FeSb_{1.25}Pb_{0.75}O_{4+x}$ orders at low temperatures to an antiferromagnetic state with both A- and C-type components whereas the $FeSb_{2-x}Pb_xO_4$ samples only show C-type ordering.

4.5 References

1. R. Fischer and F. Pertlik, *Tschermaks Mineral. Petrogr. Mitt.*, 1975, **22**, 236.

2. M. Mellini, S. Merlino and P. Orlandi, *Am. Mineral.*, 1979, **64**, 1230.

3. M. Mellini and S. Merlino, *Am. Mineral.*, 1979, **64**, 1235.

4. R. Bayliss, F. J. Berry, A. Bowden, C. Greaves and M. F. Thomas, *J. Phys.: Conf. Ser.*, 2010, **217**, 012049.

5. S. Bahfenne, L. Rintoul and R. L. Frost, *Am. Mineral.*, 2011, **96**, 888.

6. J. Sejkora, D. Ozdín, J. Vitáloš, P. Tuček, J. Čejka and R. Ďuďa, *Eur. J. Mineral.*, 2007, **19**, 419.

7. R. D. Shannon, *Acta Cryst.*, 1976, **A32**, 751.

8. S. Ahmad, J. D. McCallum, A. K. Shiemke, E. H. Appelman, T. M. Loehr and J. Sanders-Loehr, *Inorg. Chem.*, 1988, **27**, 2230.

9. M. Suzuki, T. Ishiguro, M. Kozuka and K. Nakamoto, *Inorg. Chem.*, 1981, **20**, 1993.

10. H. J. Breunig, T. Krüger and E. Lork, *Angew. Chem. Int. Ed. Engl.*, 1997, **36**, 615.

11. C. E. Housecroft and A. G. Sharpe, *Inorganic Chemistry*, Second edn., Pearson Education Limited, Harlow, 2005.

12. J. B. Goodenough, *Phys. Rev.*, 1960, **117**, 1442.

13. C. Zener, *Phys. Rev.*, 1951, **82**, 403.

14. J. Kanamori, *J. Phys. Chem. Solids*, 1959, **10**, 87.

5 Mixed Magnesium Iron Schafarzikites, $Fe_{1-x}Mg_xSb_2O_4$

5.1 Background

In Chapter 3 schafarzikite compounds were prepared in which Pb^{2+} ions were substituted for Sb^{3+} ions on the pyramidal sites. The schafarzikite structure can also be modified by substituting cations onto the octahedral sites. There are only a few previous reports of schafarzikite compounds with mixed octahedral site cations. One of these was for the series of compounds $(Mn_{1-x}Sb_x)(Sb_{1-y}Pb_y)_2O_4$, discussed in Section 3.1.1, in which introduction of Pb^{2+} ions into the structure of $MnSb_2O_4$ resulted in preferential oxidation of Sb^{3+} to give multi-phase products with a mixed Mn^{2+}/Sb^{5+} octahedral site occupancy in the schafarzikite product[1]. Another report was of mixed manganese vanadium schafarzikites, $Mn_{1-x}V_xSb_2O_4$ (x = 0-0.6)[2]. The changes in magnetic properties of $MnSb_2O_4$ were investigated on substituting with V^{2+}: $MnSb_2O_4$ is antiferromagnetic whereas the mixed Mn/V compounds all seem to have a ferromagnetic component from SQUID magnetometry data[2]. Samples within the series $Mg_{1-x}Ni_xSb_2O_4$ (x = 0.01-0.2) have also been synthesised to investigate the change in magnetic interaction between the Ni^{2+} ions[3]. X-ray diffraction data indicated that the samples were orthorhombic and magnetic susceptibility data showed that the magnetic interaction between Ni^{2+} ions is strong, even at low levels of x.[3] Finally the compound $Sn_{0.5}Pb_{0.5}Pb_2O_4$, which has a mix of Sn^{4+} and Pb^{4+} on the octahedral site and Pb^{2+} on the pyramidal site, is also known[4].

This chapter reports the formation of a series of schafarzikite compounds with mixed Fe^{2+} and Mg^{2+} cations on the octahedral site, $Fe_{1-x}Mg_xSb_2O_4$. The compound $MgSb_2O_4$ is already known to have the schafarzikite structure[5]. Insertion of oxygen into the channels of $Fe_{1-x}Mg_xSb_2O_4$, resulting in the oxidation of Fe^{2+} to Fe^{3+}, may be possible as described for $FeSb_{2-x}Pb_xO_4$ in Chapter 4. For $FeSb_2O_4$ the amount of oxygen incorporated into the material was too large for the original structure to be retained but

introducing Mg^{2+} ions into the structure should reduce the amount of oxygen required and therefore synthesis of $Fe_{1-x}Mg_xSb_2O_{4+y}$ could be successful. In this chapter the synthesis, structure, sample morphology, thermal stability and magnetic properties of $Fe_{1-x}Mg_xSb_2O_4$ are reported.

5.2 Synthesis

$Fe_{1-x}Mg_xSb_2O_4$ (x = 0.25, 0.5, 0.75) were prepared by heating stoichiometric amounts of Fe_2O_3 (99+ %), MgO, Sb_2O_3 (99 %) and Sb metal in an alumina crucible within an evacuated, sealed silica tube at 650 °C for 4 days.

$MgSb_2O_4$ was prepared by heating stoichiometric amounts of MgO and Sb_2O_3 (99 %) in an evacuated, sealed silica tube at 650 °C for 60 hours.

5.3 Results and Discussion

5.3.1 Structural Characterisation

Four magnesium containing compounds were prepared, $Fe_{1-x}Mg_xSb_2O_4$ (x = 0.25, 0.5, 0.75, 1), and were all shown to be single phase with the tetragonal schafarzikite structure from XRPD data (Fig. 5.1). The shift in peak positions indicated that Mg had successfully been substituted into the structure.

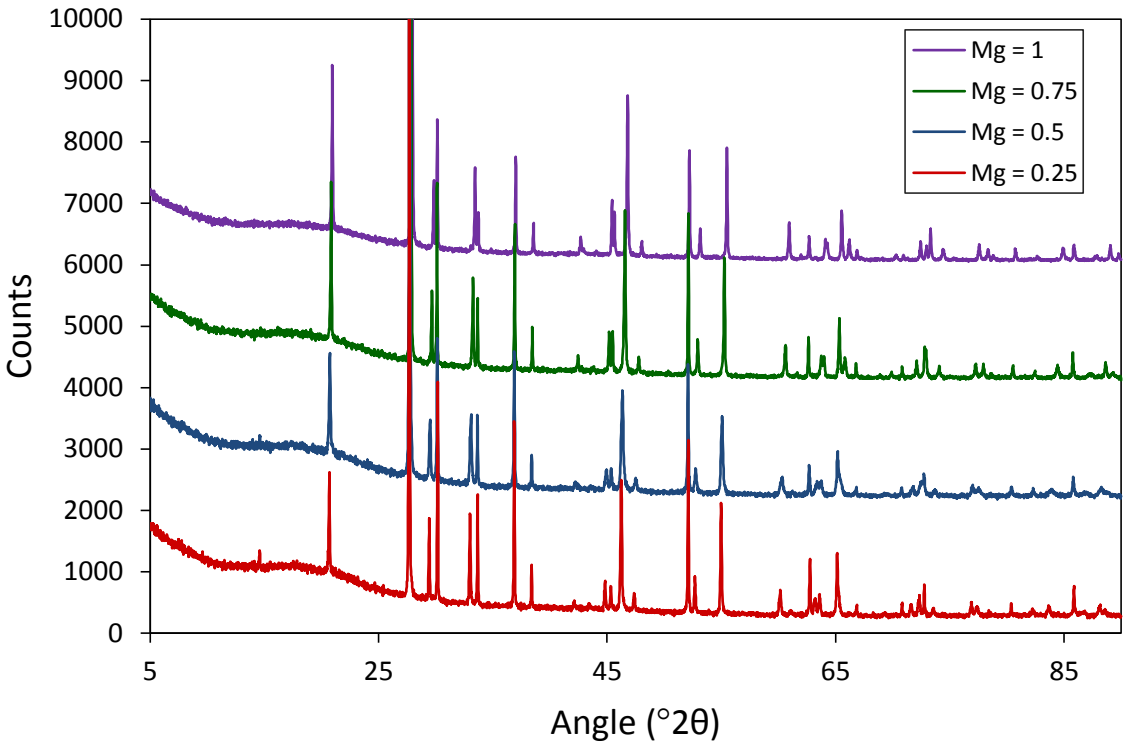

***Fig. 5.1**: Stack plot of X-ray powder diffraction patterns for $Fe_{1-x}Mg_xSb_2O_4$ (x = 0.25, 0.5, 0.75, 1).*

Rietveld refinements of XRPD data were performed as described previously (Section 3.3.1) using $FeSb_2O_4$ [6] as a starting model with tetragonal space group $P4_2/mbc$. The overall occupancy of the Fe/Mg site was constrained to 1 and the thermal parameters were set to remain equal for all the atoms. From the initial Rietveld refinement, it was seen that the widths and intensities of the peaks did not fit the data well. A closer look at the XRPD patterns for $Fe_{1-x}Mg_xSb_2O_4$ (x = 0.25, 0.5, 0.75) revealed anisotropic broadening of

the diffraction peaks (Fig. 5.2), for example the (220) and (310) reflections are broader than the (002) and (112) reflections.

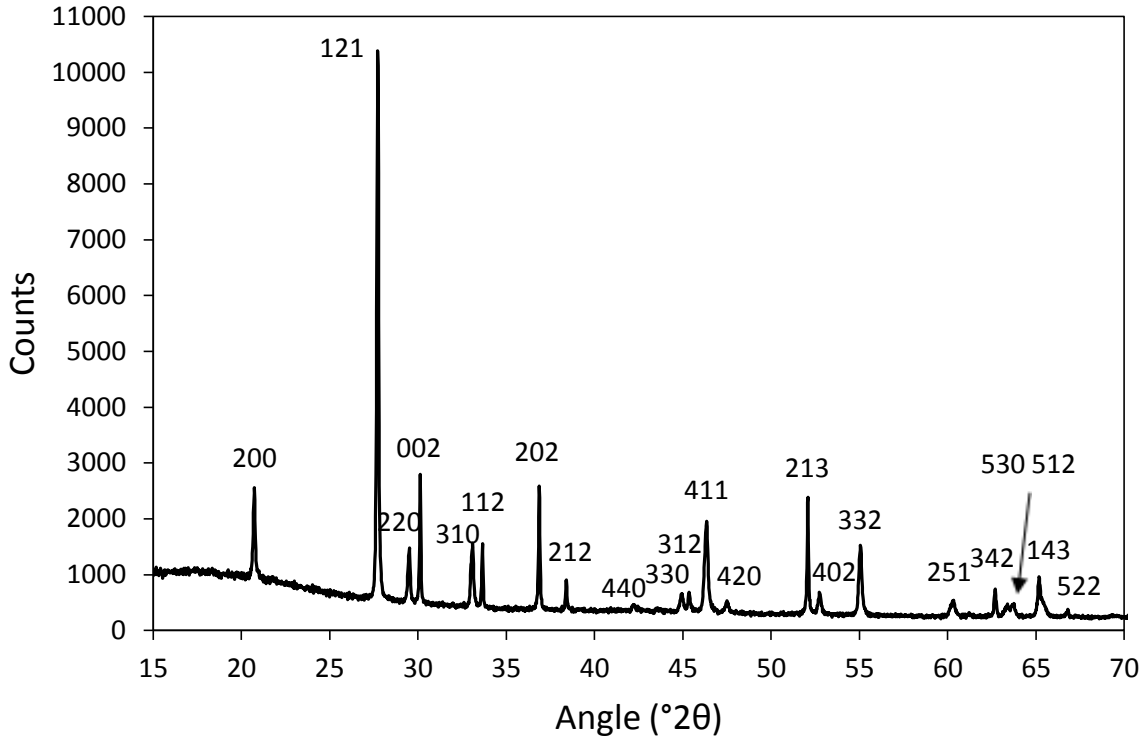

Fig. 5.2: *X-ray powder diffraction pattern for $Fe_{0.5}Mg_{0.5}Sb_2O_4$ with hkl values labelled.*

The profile function was therefore switched from type 2 to type 4 for the mixed Fe/Mg samples as function 4 contains anisotropic strain broadening parameters S_{HKL}[7]. These parameters are S_{400}, S_{004}, S_{220} and S_{202} for a tetragonal system and for the mixed Fe/Mg samples only S_{004} remained as zero. Broadening is likely to arise from needle shaped particles which, as they are smaller in the *a*- and *b*- directions than in the *c*-direction, cause broadening of reflections in which *h* or *k* is non-zero. This was investigated further using SEM (Section 5.3.2). Preferred orientation effects were also seen for the mixed Fe/Mg samples and this was refined using the March Dollase function[8-9]. Preferred orientation is seen when the arrangement of the crystallites in a polycrystalline sample is not completely random causing some reflections to be increased in intensity and others decreased in intensity. This is commonly seen for platelet or needle shaped

crystallites because platelets preferentially lie with their faces aligned parallel to the surface of the XRPD sample and needles preferentially lie with their long axis parallel to the surface of the sample. As an increase in intensity was mainly seen for the (002) reflection this suggests that the crystallites are needle shaped as the (00*l*) planes would be preferentially lined up for diffraction by the X-ray beam in transmission mode. The unit cell size, atomic coordinates, fractional occupancies and preferred orientation values obtained from Rietveld refinement of XRPD data for $Fe_{1-x}Mg_xSb_2O_4$ are given in Table 5.1; the final refinement of $Fe_{0.5}Mg_{0.5}Sb_2O_4$ is shown in Fig. 5.3.

***Table 5.1**: Parameters refined from XRPD data for $Fe_{1-x}Mg_xSb_2O_4$ taken at room temperature*

		$FeSb_2O_4$	$Fe_{0.75}Mg_{0.25}Sb_2O_4$	$Fe_{0.5}Mg_{0.5}Sb_2O_4$	$Fe_{0.25}Mg_{0.75}Sb_2O_4$	$MgSb_2O_4$
a (Å)		8.59621(7)	8.5689(1)	8.5472(2)	8.5031(1)	8.4602(1)
c (Å)		5.91014(5)	5.91455(7)	5.91942(9)	5.92477(7)	5.92069(9)
volume (Å³)		436.729(9)	434.28(2)	432.44(2)	428.38(2)	423.77(2)
Sb	*x*	0.1763(2)	0.1773(3)	0.1765(3)	0.1762(3)	0.1753(3)
Sb	*y*	0.1660(2)	0.1654(3)	0.1656(3)	0.1648(3)	0.1648(3)
O1	*x*	0.6793(9)	0.686(1)	0.682(1)	0.678(1)	0.680(1)
O1	*y*	0.1793(9)	0.186(1)	0.182(1)	0.178(1)	0.180(1)
O2	*x*	0.100(1)	0.093(6)	0.100(2)	0.101(2)	0.100(2)
O2	*y*	0.644(1)	0.632(2)	0.628(2)	0.633(2)	0.635(2)
U_{iso} (Å²)		0.0199(4)	0.0121(7)	0.0126(6)	0.0076(6)	0.0095(6)
Fe occupancy		-	0.73(1)	0.57(1)	0.29(1)	-
Mg occupancy		-	0.27(1)	0.43(1)	0.71(1)	-
Preferred Orientation (001)		-	0.845(3)	0.933(3)	0.973(3)	-
χ^2		2.763	1.490	1.292	1.884	1.963
R_{wp}		0.047	0.049	0.048	0.064	0.077
R_F^2		0.041	0.078	0.063	0.052	0.060

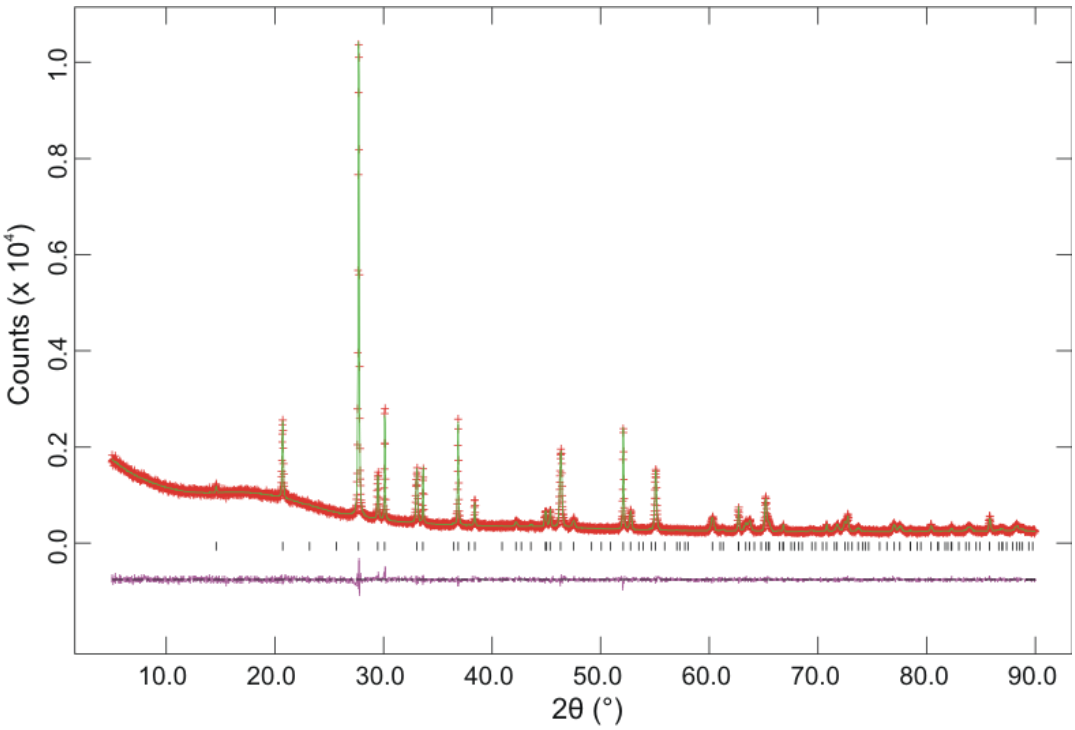

***Fig. 5.3**: Observed, calculated and difference plots for room temperature XRPD data recorded from $Fe_{0.5}Mg_{0.5}Sb_2O_4$.*

The fractional occupancies reported in Table 5.1 are close to the expected values and confirm that increasing amounts of magnesium have been substituted onto the octahedral sites. The preferred orientation was not seen for the end members of the series, $FeSb_2O_4$ and $MgSb_2O_4$, and therefore was not refined for these two compounds; for the mixed Fe/Mg schafarzikites the preferred orientation is higher with increasing iron content. The changes in unit cell parameters with Mg content, x, in $Fe_{1-x}Mg_xSb_2O_4$ are shown in Fig. 5.4. With increasing x in $Fe_{1-x}Mg_xSb_2O_4$ the unit cell volume decreases as expected from the ionic radii of Fe^{2+} and Mg^{2+} of 0.78 Å and 0.72 Å respectively (Fig. 5.4a). It can be seen from Fig. 5.4b that the contraction occurs in the *a*-direction and that the *c*-parameter changes very little as x is varied. As described previously the octahedral cations in the schafarzikite structure are much closer within the chains along the *c*-axis than within the layers perpendicular to the chains. The amount of contraction possible in the *c*-direction may therefore be restricted by the smaller Fe/Mg cation-cation distances.

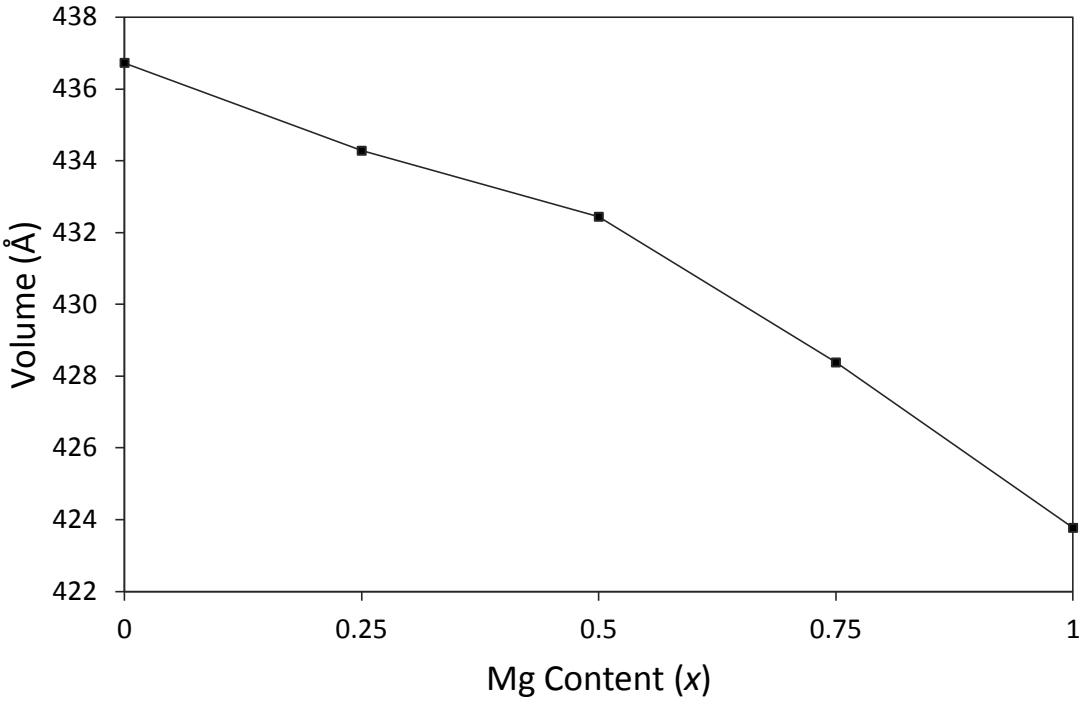

(a)

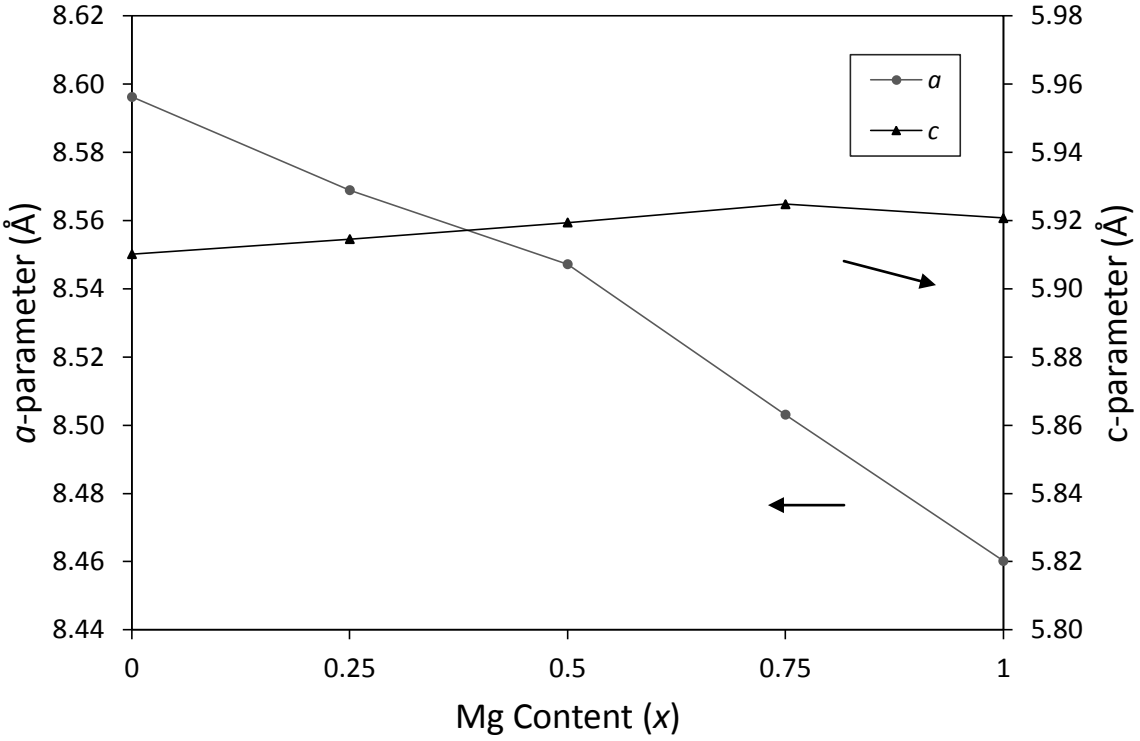

(b)

***Fig. 5.4**: Changes in unit cell data with increasing Mg content in $Fe_{1-x}Mg_xSb_2O_4$ derived from Rietveld refinement using XRPD data. (The values for the estimated standard deviations are smaller than the symbols on the graph.)*

5.3.2 Scanning Electron Microscopy (SEM) Study

Images of $Fe_{1-x}Mg_xSb_2O_4$ were taken at high levels of magnification to study the morphologies of the samples on the μm scale. Fig. 5.5 shows SEM images of $FeSb_2O_4$ at two different levels of magnification; Fig. 5.6 shows SEM images of the four magnesium containing samples $Fe_{0.75}Mg_{0.25}Sb_2O_4$, $Fe_{0.5}Mg_{0.5}Sb_2O_4$, $Fe_{0.25}Mg_{0.75}Sb_2O_4$ and $MgSb_2O_4$. The images confirm the findings from XRPD refinements that the samples with a mix of Fe and Mg on the octahedral sites form needle-shaped crystallites, which are thin in the *a*- and *b*-directions and elongated along *c* (Fig. 5.6a-c), whereas the pure Fe and pure Mg schafarzikites form crystallites which have much more equal lengths in all directions (Fig. 5.5 and Fig. 5.6d). The needle shaped particles can be seen best for $Fe_{0.75}Mg_{0.25}Sb_2O_4$ (Fig. 5.6a) which was the sample found to have the highest degree of preferred orientation from the XRPD refinement (Table 5.1).

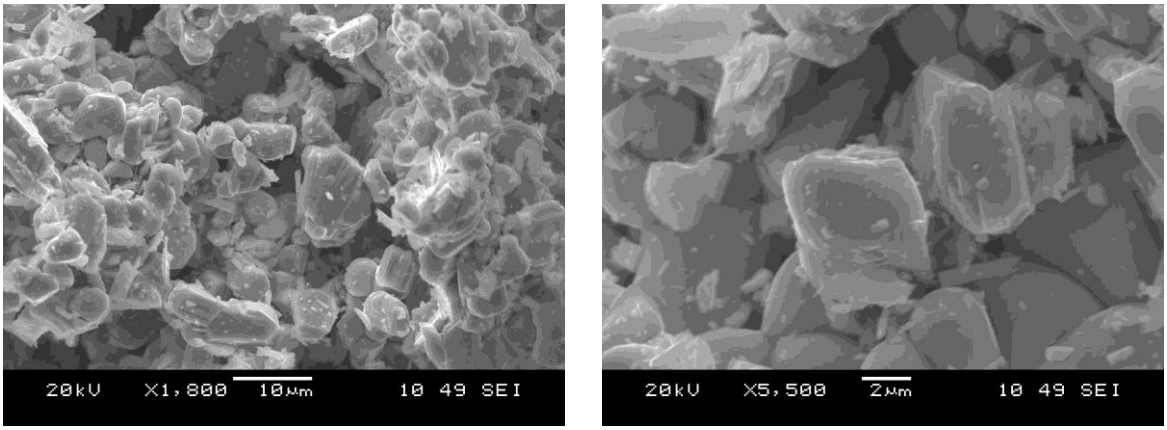

(a) *(b)*

***Fig. 5.5**: SEM images of $FeSb_2O_4$ at (a) lower magnification and (b) higher magnification.*

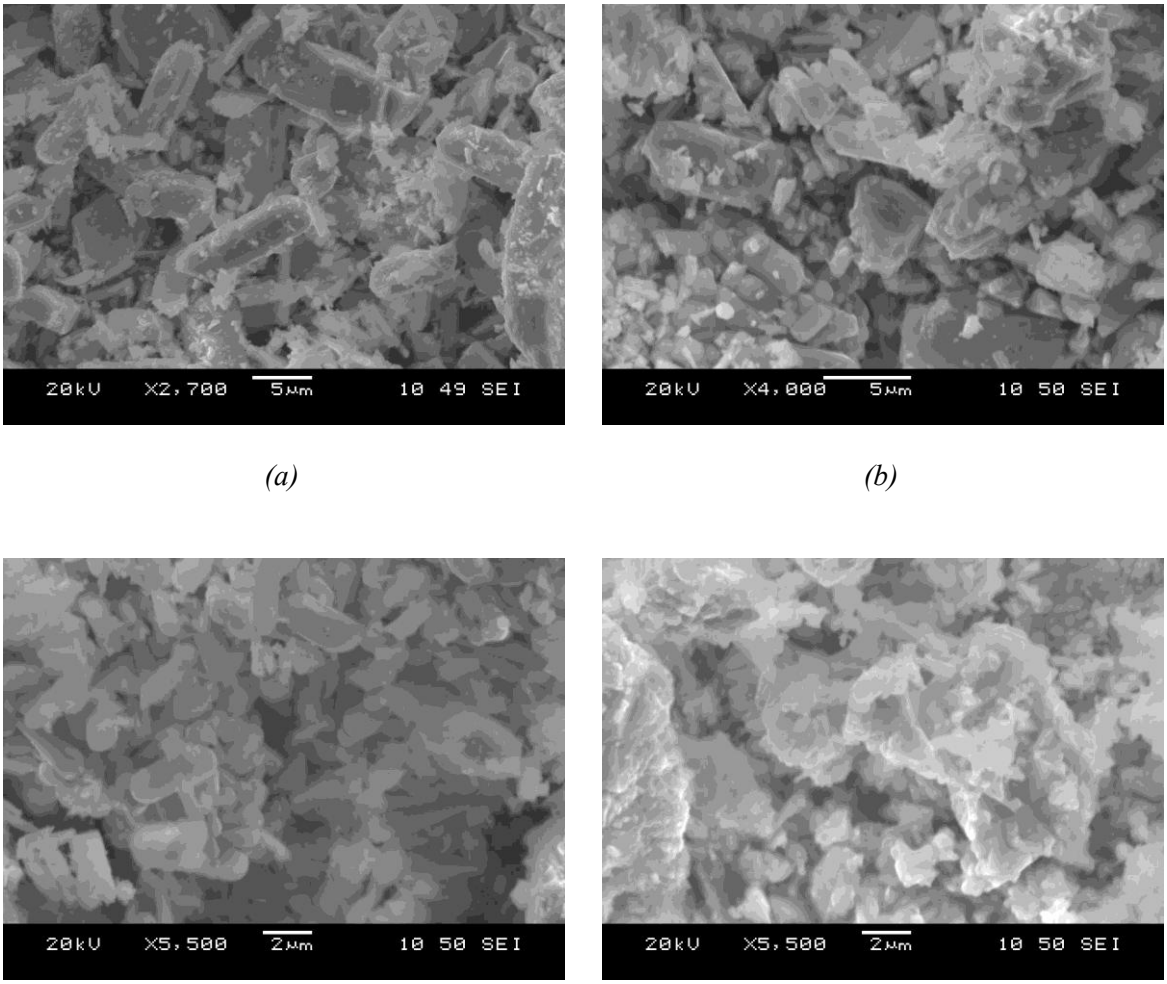

***Fig. 5.6**: SEM images of (a) $Fe_{0.75}Mg_{0.25}Sb_2O_4$, (b) $Fe_{0.5}Mg_{0.5}Sb_2O_4$, (c) $Fe_{0.25}Mg_{0.75}Sb_2O_4$ and (d) $MgSb_2O_4$.*

Elemental analysis, using energy-dispersive X-ray spectroscopy (EDS), was carried out for all the samples as well as imaging. This was done to check that the composition of the mixed Fe/Mg samples was uniform throughout and that there were not regions rich in Fe or Mg. Spectra were recorded from various different-sized areas of the sample and the results are summarised in Table 5.2. For each sample the weight percentages from each scan, the average percentages and the expected percentages are given. The values for a given sample are fairly consistent indicating that there is no inhomogeneity within the sample and the increase in magnesium content and decrease in iron content is seen as expected with increasing x in $Fe_{1-x}Mg_xSb_2O_4$.

***Table 5.2**: Results obtained from elemental analysis of $Fe_{1-x}Mg_xSb_2O_4$ using EDS*

$FeSb_2O_4$

Element	weight %					
	Scan 1	Scan 2	Scan 3	Scan 4	Average	Expected
O	5.12	8.96	7.71	6.61	7.10	18
Fe	17.31	16.65	16.67	17.12	16.94	15
Sb	77.57	74.39	75.62	76.27	75.96	67

$Fe_{0.75}Mg_{0.25}Sb_2O_4$

Element	weight %						
	Scan 1	Scan 2	Scan 3	Scan 4	Scan 5	Average	Expected
O	5.6	9.32	9.04	7.05	8.51	7.90	18
Mg	0.76	1.33	1.50	1.01	0.86	1.09	2
Fe	13.64	13.32	11.72	12.92	14.07	13.13	11
Sb	79.99	76.02	77.74	79.02	76.57	77.87	68.5

$Fe_{0.5}Mg_{0.5}Sb_2O_4$

Element	weight %						
	Scan 1	Scan 2	Scan 3	Scan 5	Scan 6	Average	Expected
O	5.91	6.43	8.09	5.49	7.53	6.69	18
Mg	1.62	1.67	2.02	1.25	1.75	1.66	3
Fe	10.83	10.93	10.81	12.54	11.85	11.39	8
Sb	81.64	80.97	79.09	80.73	78.87	80.26	70

$Fe_{0.25}Mg_{0.75}Sb_2O_4$

Element	weight %								
	Scan 1	Scan 2	Scan 3	Scan 4	Scan 5	Scan 6	Scan 7	Average	Expected
O	6.32	7.41	7.21	9.44	6.86	8.97	9.65	7.98	19
Mg	3.11	3.60	3.12	3.70	2.95	4.73	4.92	3.73	5
Fe	5.75	5.29	5.79	7.88	5.86	4.79	4.95	5.76	4
Sb	84.82	83.69	83.88	78.98	84.34	81.51	80.48	82.53	72

$MgSb_2O_4$

Element	weight %				
	Scan 1	Scan 2	Scan 3	Average	Expected
O	6.74	4.16	5.45	5.45	19
Mg	4.90	3.17	3.35	3.81	7
Sb	88.35	92.67	91.20	90.74	73

For all the samples the percentages of the light atoms, O and Mg, are lower than the expected values and the percentages of the heavier atoms, Fe and Sb, are higher than expected. This is perhaps not surprising as EDS relies on the emission of X-rays which is more efficient for heavier elements and the antimony ions may be expected to overshadow the contribution from the light oxygen ions. The ratio of Fe:Sb would therefore be a more reliable indicator of the sample compositions. The Fe:Sb ratios are reported in Table 5.3 and are very close to the expected values.

***Table 5.3**: Fe:Sb ratios determined for $Fe_{1-x}Mg_xSb_2O_4$ using EDS*

x	Average Fe:Sb ratio	Expected Fe:Sb ratio
0	0.22	0.22
0.25	0.17	0.16
0.5	0.14	0.11
0.75	0.07	0.06

5.3.3 Oxygen Insertion

As mentioned in Section 5.1, insertion of oxygen into the channels of $Fe_{1-x}Mg_xSb_2O_4$ may be possible, resulting in oxidation of Fe^{2+} ions to Fe^{3+}. Thermogravimetric analysis of the samples was therefore carried out under flowing oxygen gas. The compounds were heated to 700 °C and it can be seen in Fig. 5.7 that, similarly to the lead substituted schafarzikites, oxygen is taken up in two stages corresponding to oxidation of Fe^{2+} at lower temperatures and Sb^{3+} at higher temperatures.

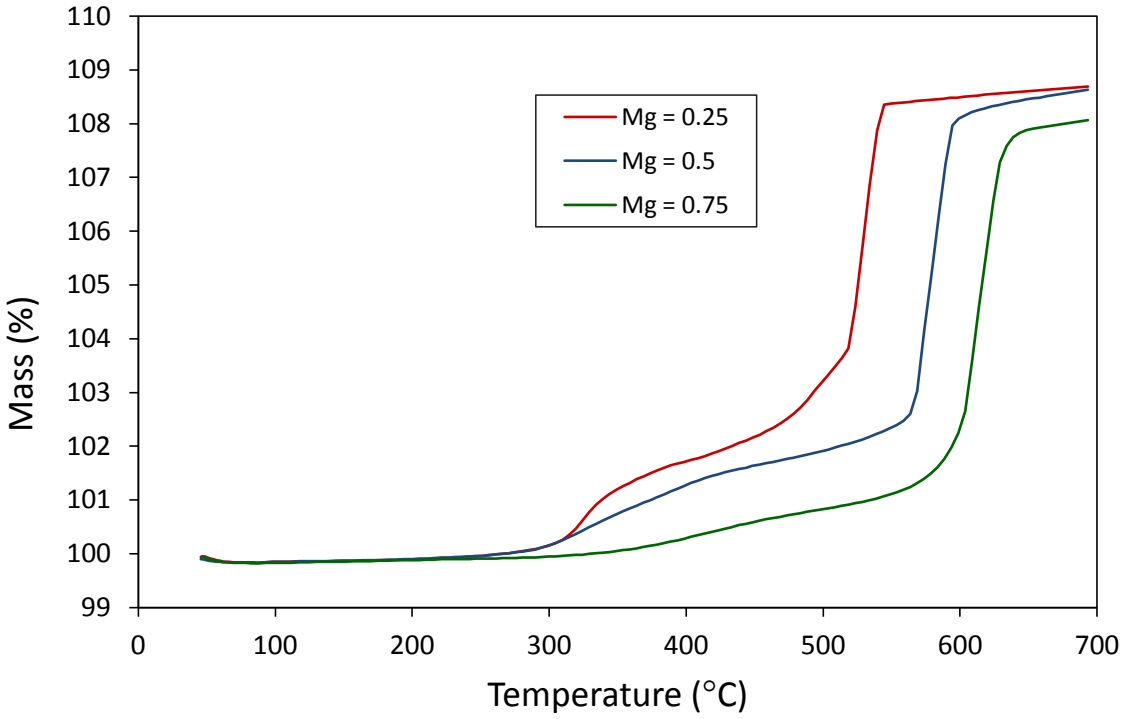

***Fig. 5.7**: Thermogravimetric analysis of $Fe_{1-x}Mg_xSb_2O_4$ (x = 0.25, 0.5, 0.75) up to 700 °C.*

The compounds are stable in air up to 250-300 °C then partial oxidation occurs at intermediate temperatures of 300-500 °C. Further oxidation occurs at 500-600 °C and X-ray diffraction revealed that after heating to 700 °C in oxygen, Sb_2O_4, $MgSb_2O_6$ and $FeSbO_4$ are formed.

To see whether the oxygen taken up at intermediate temperatures was being incorporated into the original schafarzikite structure, the samples were heated to 400 °C

under flowing oxygen gas and held there for 10 minutes before cooling (Fig. 5.8), then XRPD patterns were taken of the product (Fig. 5.9).

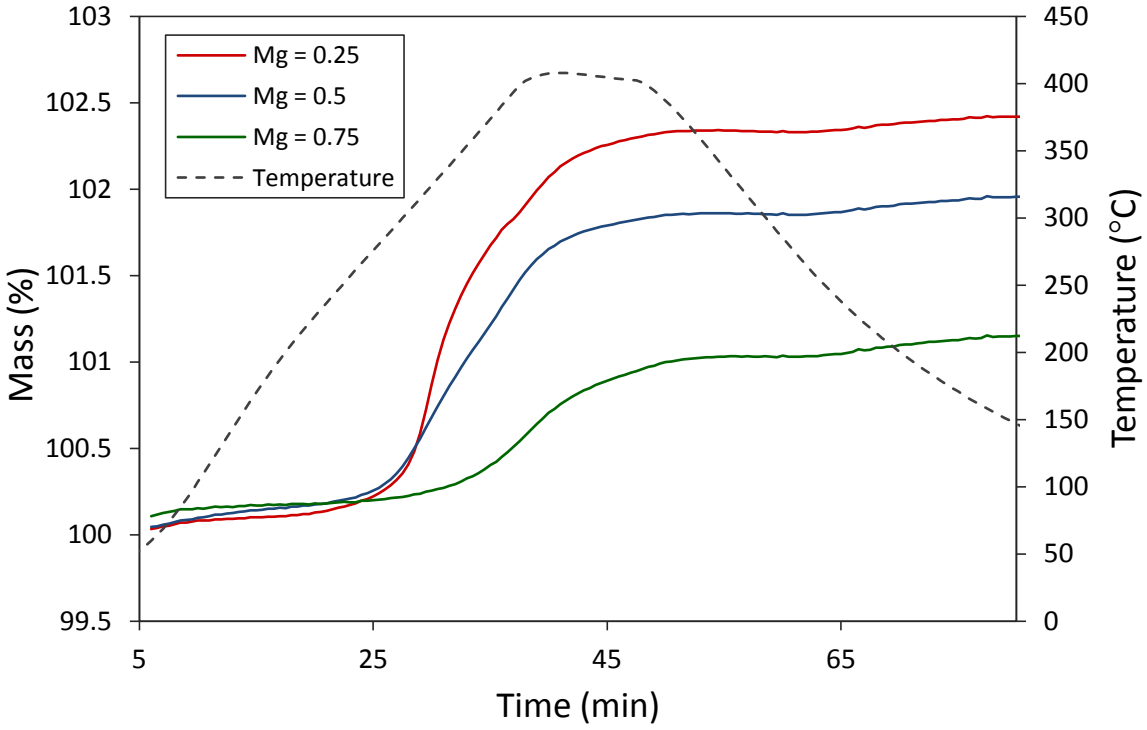

***Fig. 5.8**: Thermogravimetric analysis of $Fe_{1-x}Mg_xSb_2O_4$ (x = 0.25, 0.5, 0.75) up to 400 °C.*

The XRPD patterns show that the samples still have schafarzikite structures. The sample $Fe_{0.25}Mg_{0.75}Sb_2O_{4+x}$, which is expected to contain the lowest amount of excess oxygen ions, is the most crystalline and has the smallest shift in peak positions. For samples with higher iron contents, $Fe_{0.5}Mg_{0.5}Sb_2O_{4+x}$ and $Fe_{0.75}Mg_{0.25}Sb_2O_{4+x}$, the increased amount of oxygen taken up causes a large shift in peak positions and a loss of crystallinity as the structure begins to break down.

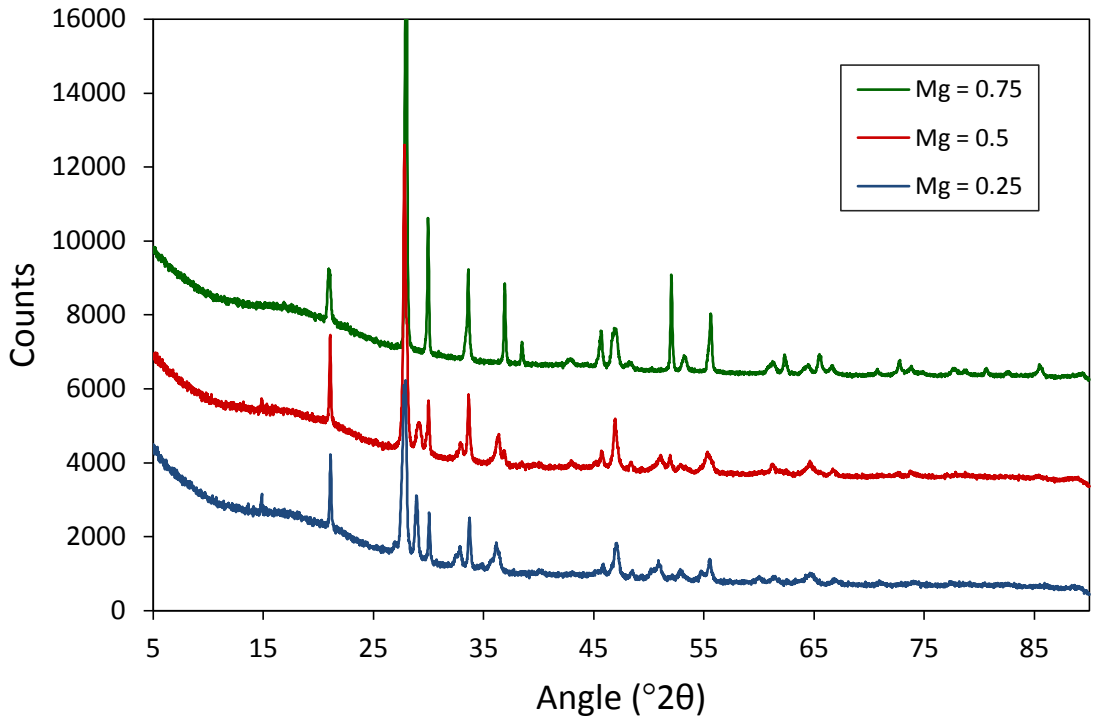

***Fig. 5.9**: Stack plot of XRPD patterns for $Fe_{1-x}Mg_xSb_2O_{4+y}$ where x = 0.25, 0.5, 0.75.*

The XRPD pattern for $Fe_{0.25}Mg_{0.75}Sb_2O_{4+x}$ was indexed using the program *DICVOL*04[10] but indexing for $Fe_{0.5}Mg_{0.5}Sb_2O_{4+x}$ and $Fe_{0.75}Mg_{0.25}Sb_2O_{4+x}$ was unsuccessful. Rietveld refinement was carried out for all the samples (using the schafarzikite structure with space group $P4_2/mbc$) to identify the problems and obtain unit cell parameters. Rietveld refinement plots for $Fe_{0.5}Mg_{0.5}Sb_2O_{4+x}$ and $Fe_{0.25}Mg_{0.75}Sb_2O_{4+x}$ are shown in Fig. 5.10. The extra oxygen ions were not included in the refinements as their positions were uncertain and location using X-ray diffraction data would have been unreliable, especially in the presence of heavy Sb^{3+} ions. Thermal parameters for all the ions were also constrained to remain equal for this reason. As the Fe and Mg atoms share the same site their atomic coordinates were constrained to be equal and the overall occupancy of the site was constrained to 1.

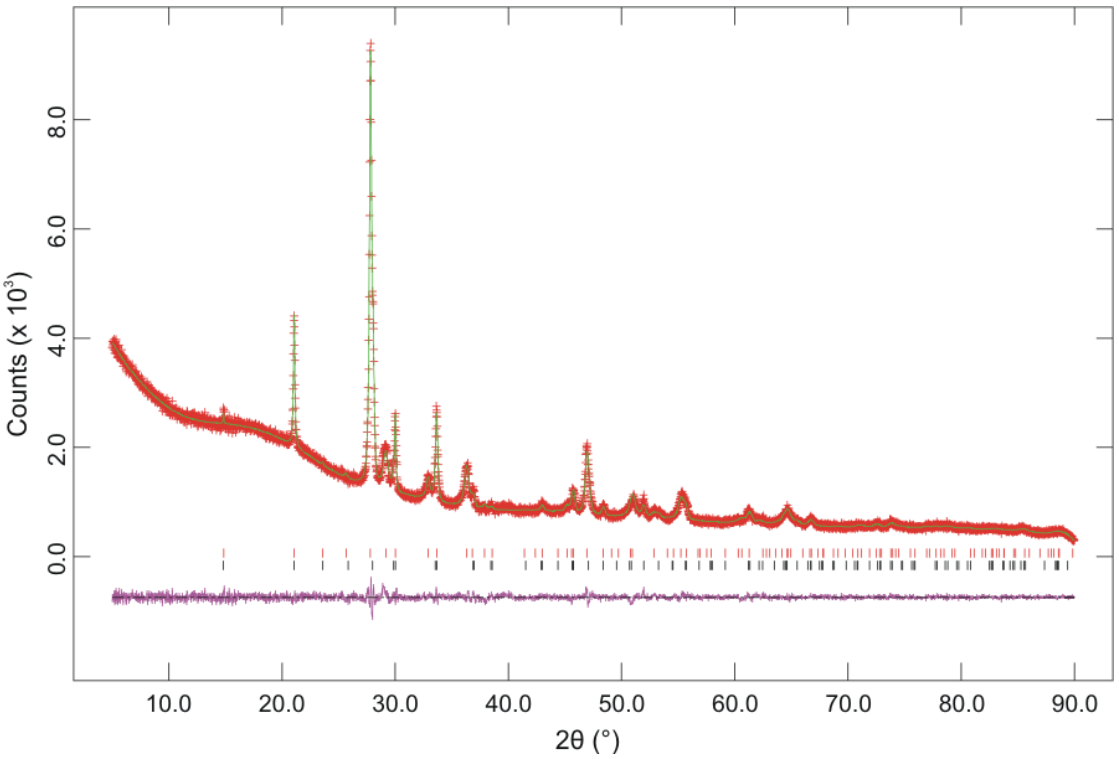

(a)

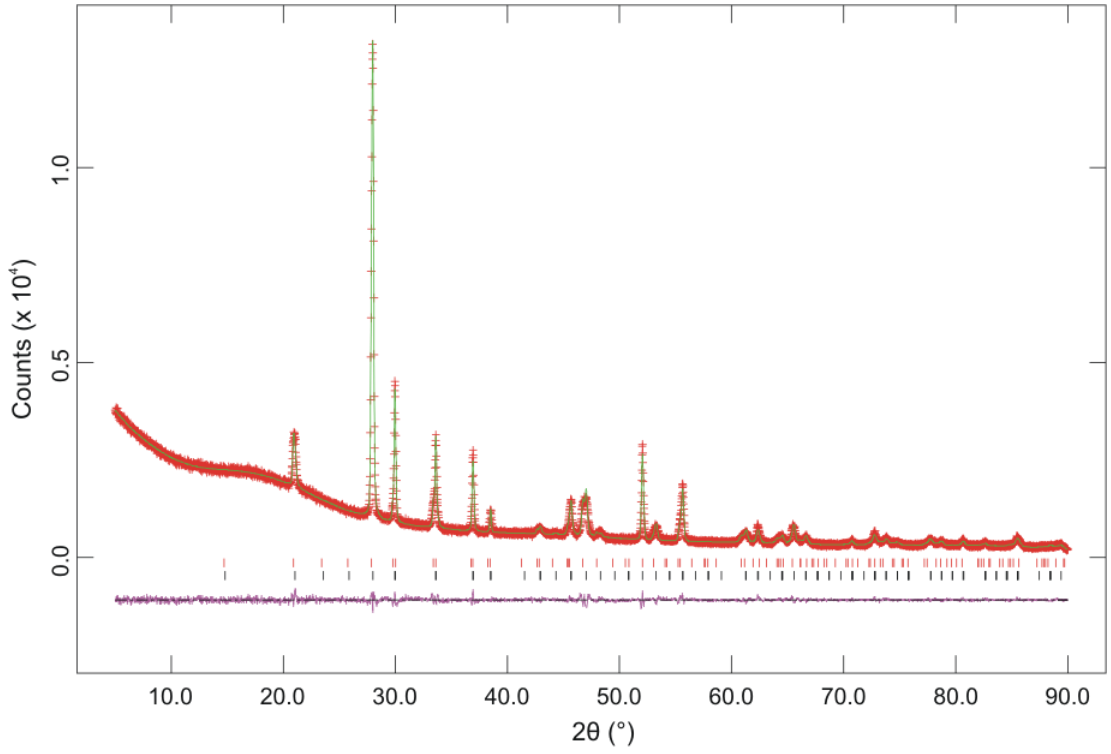

(b)

***Fig. 5.10**: Observed, calculated and difference plots for room temperature XRPD data recorded from (a) $Fe_{0.5}Mg_{0.5}Sb_2O_{4+x}$ and (b) $Fe_{0.25}Mg_{0.75}Sb_2O_{4+x}$.*

It was found from the Rietveld refinements that multiple schafarzikite-related phases were present with different unit cell parameters suggesting different oxygen contents. Initially the samples were refined using a single phase model but large differences were seen between the observed and calculated data. For $Fe_{0.25}Mg_{0.75}Sb_2O_{4+x}$, which is the most crystalline sample with the sharpest diffraction peaks, shoulders were seen on some of the peaks and the model was changed from a tetragonal one ($P4_2/mbc$) to an orthorhombic one (*Pbam*), with anisotropic broadening parameters, significantly improving the goodness of fit. However a model containing two tetragonal phases with slightly different unit cell parameters gave an equally good fit (Fig. 5.10b and Table 5.4). Although both models fit the data equally well, the two-phase model is preferred because a sample of $Fe_{0.25}Mg_{0.75}Sb_2O_{4+x}$ previous prepared at 350 °C was found to contain two phases each making up 50 % of the overall sample. The previous sample was heated under flowing oxygen gas to 350 °C but the experiment was repeated as it was found that the temperature was not high enough to complete the oxidation. Rietveld refinement for the sample prepared at 350 °C was attempted using an orthorhombic model but some of the peaks were not being modelled and the model with two tetragonal phases gave a much better fit. This suggests that heating $Fe_{0.25}Mg_{0.75}Sb_2O_4$ to a slightly higher temperature results in an increase of the phase containing more oxygen and a two phase model therefore seems more likely. $Fe_{0.5}Mg_{0.5}Sb_2O_{4+x}$ had much broader diffraction peaks and a model with two tetragonal phases with a large difference in *c*-parameter fit the data well (Fig. 5.10a and Table 5.4). $Fe_{0.75}Mg_{0.25}Sb_2O_{4+x}$ also had very broad diffraction peaks and a single phase refinement using anisotropic broadening parameters gave a χ^2 value of 2.291 and unit cell parameters of a = 8.382(2) and c = 6.156(1) for the main phase (compared to a = 8.5689(1) and c = 5.91455(7) for the original sample, $Fe_{0.75}Mg_{0.25}Sb_2O_4$). This is the largest difference in cell parameters as this sample has the highest Fe content and therefore

incorporates the most oxygen which causes the structure to break down. Models with secondary phases were considered but additional peaks were still present indicating that there are multiple phases in this sample.

***Table 5.4**: Unit cell parameters refined from XRPD data of $Fe_{1-x}Mg_xSb_2O_4$ before and after heating to 400 °C in flowing oxygen gas; after heating, two schafarzikite-related phases were formed*

	$Fe_{0.5}Mg_{0.5}Sb_2O_4$		$Fe_{0.25}Mg_{0.75}Sb_2O_4$	
before	a = 8.5472(2)	c = 5.91942(9)	a = 8.5031(1)	c = 5.92477(7)
after: 1st Phase	a = 8.392(1)	c = 6.0990(8)	a = 8.4034(5)	c = 5.9471(3)
after: 2nd Phase	a = 8.394(2)	c = 5.961(1)	a = 8.4610(8)	c = 5.9331(8)
% 1st Phase	80		76	
% 2nd Phase	20		24	
χ^2	1.489		1.732	
R_{wp}, R_F^2	0.034, 0.065		0.040, 0.060	

To try and obtain a uniform oxygen composition throughout, samples of $Fe_{1-x}Mg_xSb_2O_4$ were heated in air to 300 °C for 12 hr but the products were shown, using XRPD, to be the same as those produced from TGA.

The expected mass increase was calculated, corresponding to all Fe^{2+} being oxidised to Fe^{3+} by insertion of oxide ions, and compared with the observed increase from the TGA results (Table 5.5). The errors were determined, as in Section 4.3.1, by taking into account the likely errors when calculating percentage differences. The observed values are higher than the calculated values indicating that both oxide and peroxide ions are being incorporated into the structure as they were for the lead substituted samples (Section 4.3.1).

***Table 5.5**: Expected and observed mass increases of $Fe_{1-x}Mg_xSb_2O_4$ after oxygen insertion at 350 °C*

x	RMM $Fe_{1-x}Mg_xSb_2O_4$	RMM $Fe_{1-x}Mg_xSb_2O_{4+y}$	expected increase (%)	observed increase (%)
0.25	355.476	361.476	1.69	2.3(1)
0.5	347.591	351.591	1.15	1.8(1)
0.75	339.706	341.706	0.59	0.98(7)

Raman spectroscopy was performed on powder samples of $Fe_{1-x}Mg_xSb_2O_4$ both before and after oxygen insertion (Fig. 5.11). The spectra for $Fe_{1-x}Mg_xSb_2O_4$ (Fig. 5.11a) with no excess oxygen fit well with those reported for $FeSb_2O_4$ in the literature[11-12]. The bands are seen to shift to higher wavenumbers with increasing magnesium content which would be expected as magnesium is lighter than iron. The spectra are seen to get much broader on insertion of oxygen (Fig. 5.11b) and the broadening increases with increasing iron content in agreement with the broadening seen in the XRPD patterns (Fig. 5.9). Shoulder peaks at around 720 cm^{-1} are seen for all the oxygen inserted samples which could be indicative of peroxide ion insertion as suggested by TGA data (Table 5.5).

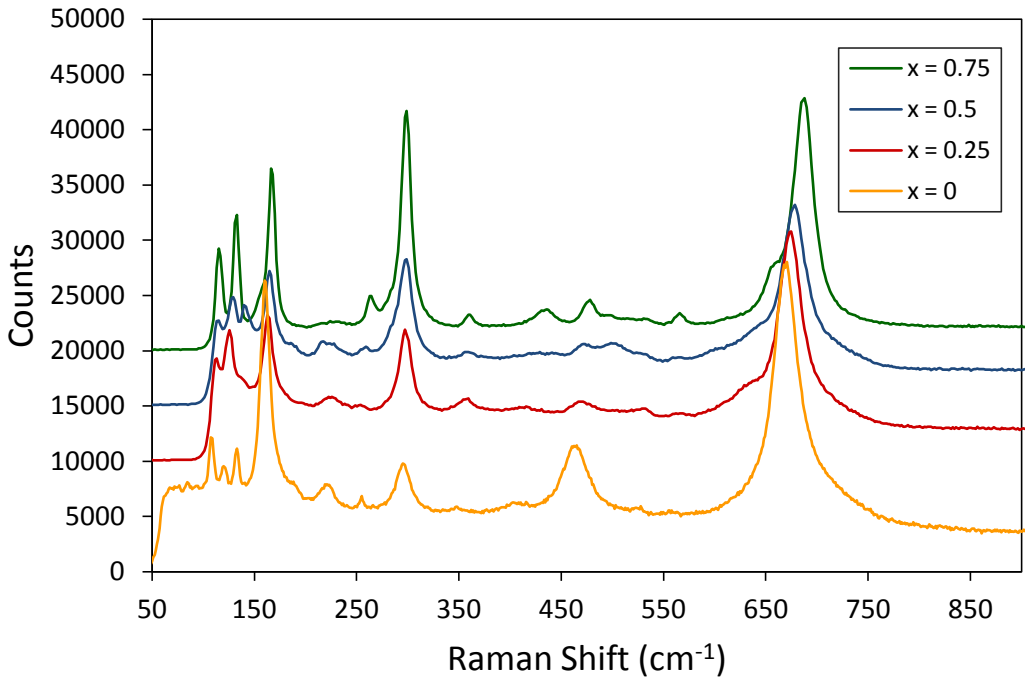

(a)

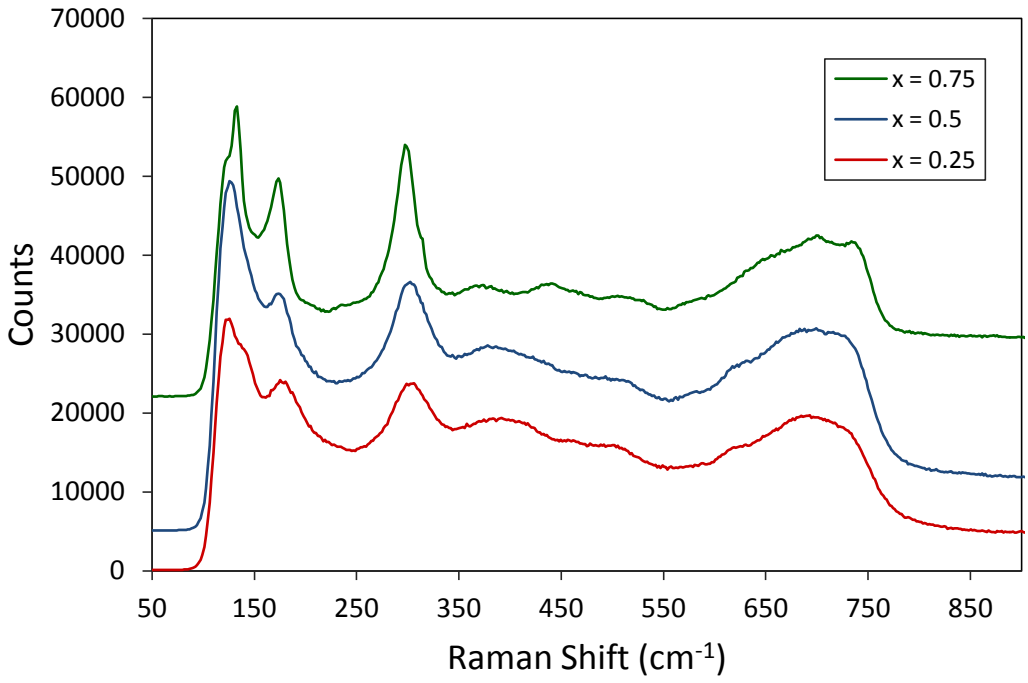

(b)

***Fig. 5.11**: Stack plot of room temperature Raman spectra recorded from (a) $Fe_{1-x}Mg_xSb_2O_4$ (x = 0, 0.25, 0.5, 0.75) and (b) $Fe_{1-x}Mg_xSb_2O_{4+y}$ (x = 0.25, 0.5, 0.75).*

5.3.4 Magnetic Properties

Field cooled (FC) and zero-field cooled (ZFC) susceptibility measurements were taken for $Fe_{1-x}Mg_xSb_2O_4$ between 5 and 300 K using an applied field of 500 Oe; plots of susceptibility versus temperature are shown in Fig. 5.12-5.14.

The plots show that for $Fe_{0.5}Mg_{0.5}Sb_2O_4$ and $Fe_{0.75}Mg_{0.25}Sb_2O_4$, magnetic transitions occur between 40 and 60 K and the divergence of the FC and ZFC measurements is indicative of a small ferromagnetic component. The sample $Fe_{0.25}Mg_{0.75}Sb_2O_4$, which has the lowest amount of iron, appears to be paramagnetic although neutron powder diffraction (NPD) would be needed to confirm this.

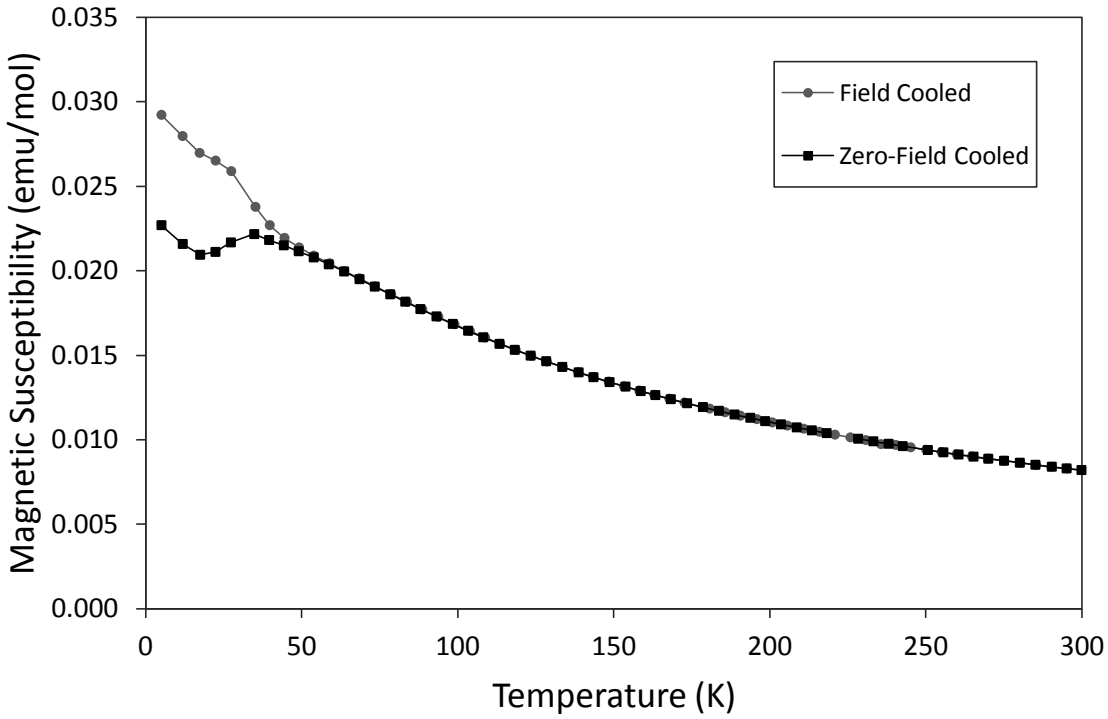

***Fig. 5.12**: Variation of magnetic susceptibility with temperature for $Fe_{0.75}Mg_{0.25}Sb_2O_4$.*

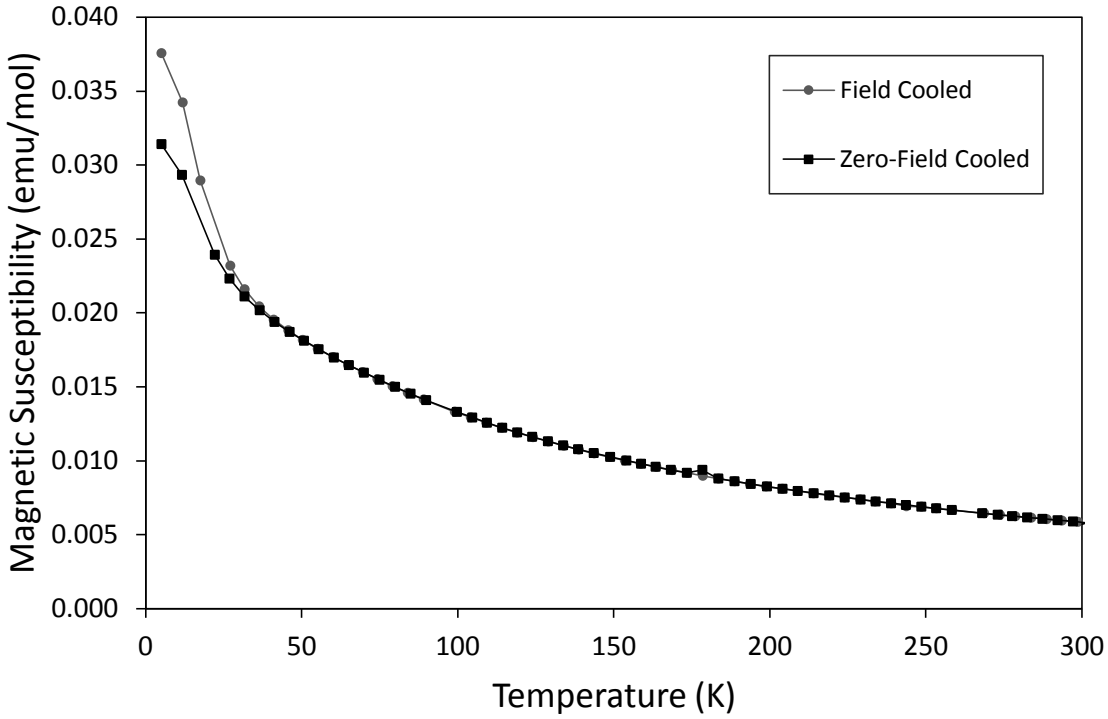

***Fig. 5.13**: Variation of magnetic susceptibility with temperature for $Fe_{0.5}Mg_{0.5}Sb_2O_4$.*

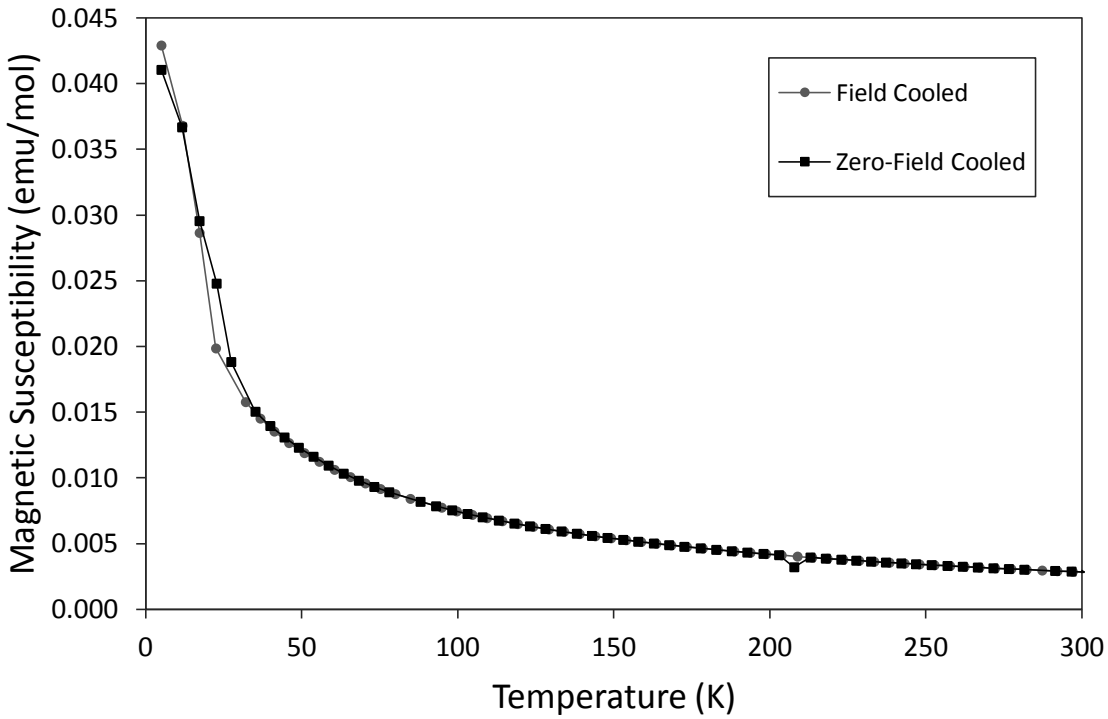

***Fig. 5.14**: Variation of magnetic susceptibility with temperature for $Fe_{0.25}Mg_{0.75}Sb_2O_4$.*

The inverse susceptibility data were plotted and fit to the Curie-Weiss law; the Weiss constant, θ, and magnetic moments obtained from the plots are reported in Table 5.6 as well as the magnetic ordering temperatures. The negative Weiss constants are characteristic of antiferromagnetic behaviour which, combined with the transitions observed from susceptibility data, suggests that $Fe_{1-x}Mg_xSb_2O_4$ (x = 0.25, 0.5) are canted antiferromagnets like the lead substituted schafarzikites (Chapter 3). The experimental magnetic moments from the Curie-Weiss plot agree with expected values for Fe^{2+} ions given in the literature. The spin only moment for high spin Fe^{2+} (d^6) of 4.90 μ_B is not used because Fe^{2+} has a T ground state and therefore an orbital contribution which increases the moment. The moments observed for $Fe_{1-x}Mg_xSb_2O_4$ are in good agreement with the experimentally determined moment given in the literature of 5.10-5.70 μ_B.[13] The transition temperature decreases with increasing Mg content, x, and is suppressed for $Fe_{0.25}Mg_{0.75}Sb_2O_4$ which is expected as the magnetic interactions between Fe^{2+} ions are weakened by the presence of non-magnetic Mg^{2+} ions.

***Table 5.6**: Magnetic parameters obtained from SQUID magnetometry data for $Fe_{1-x}Mg_xSb_2O_4$*

x	θ (K)	μ experiment per Fe (μ_B)	transition T (K)
0.75	-24.0(9)	5.32(1)	-
0.5	-59(1)	5.81(2)	41
0.25	-92.7(8)	5.73(1)	58

5.4 Conclusions

Three new schafarzikite-related compounds, $Fe_{1-x}Mg_xSb_2O_4$ (x = 0.25, 0.5, 0.75), have successfully been synthesised along with the known compounds $FeSb_2O_4$ and $MgSb_2O_4$. As Mg^{2+} is smaller than Fe^{2+}, a decrease is seen in the unit cell size of $Fe_{1-x}Mg_xSb_2O_4$ with increasing x. The XRPD data revealed anisotropic broadening of the diffraction peaks and preferred orientation effects indicating that the samples consist of needle-shaped crystallites which are smaller in *a*- and *b*-directions than in *c*. This was confirmed using SEM: the mixed Fe/Mg samples form needle-shaped particles whereas $FeSb_2O_4$ and $MgSb_2O_4$ form crystallites with equal lengths in all directions. The possibility of oxygen insertion in $Fe_{1-x}Mg_xSb_2O_4$ was also investigated, as it was for $FeSb_{2-x}Pb_xO_4$ in Chapter 4, using TGA and heating the samples in flowing oxygen gas. It was found that at low temperatures (*ca*. 350 °C) only Fe^{2+} is oxidised as oxygen ions are inserted into the original schafarzikite structure, then above *ca*. 500 °C further oxidation occurs and the structure breaks down. The oxygen-inserted phases obtained at 400 °C were studied using XRPD and were found to consist of multiple schafarzikite-type phases with different unit cell parameters. The TGA data indicate that oxygen is being taken up as a mix of oxide and peroxide ions, as was found for $FeSb_{2-x}Pb_xO_4$, and a shoulder peak was seen in the Raman data at around 720 cm^{-1} which could be assigned to peroxide vibrations. Magnetic susceptibility data suggested that $Fe_{1-x}Mg_xSb_2O_4$ (x = 0.25, 0.5) are canted antiferromagnets, similar to the lead substituted schafarzikites, whereas $FeSb_2O_4$ is antiferromagnetic. The sample $Fe_{0.25}Mg_{0.75}Sb_2O_4$ is probably paramagnetic although NPD data would be needed to confirm this. The increased presence of non-magnetic Mg^{2+} ions on the octahedral sites in $Fe_{1-x}Mg_xSb_2O_4$ weakens the magnetic interactions between Fe^{2+} ions and a subsequent decrease in the magnetic ordering temperature is seen.

5.5 References

1. A. M. Abakumov, M. G. Rozova, E. V. Antipov, J. Hadermann, G. Van Tendeloo, M. Lobanov, M. Greenblatt, M. Croft, E. V. Tsiper, A. Llobet, K. A. Lokshin and Y. Zhao, *Chem. Mater.*, 2005, **17**, 1123.

2. H. Abe, K. Yoshii and H. Kitazawa, *Phys. Stat. Sol.*, 2002, **189**, 429.

3. B. Y. Brach, N. V. Chezhina and Y. V. Shapoval, *Inorg. Mater.*, 1989, **25**, 601.

4. J. P. Vigouroux, E. Husson, G. Calvarin and N. Q. Dao, *Spectrochimica Acta*, 1982, **38A**, 393.

5. C. Giroux-Maraine and G. Perez, *Revue de Chimie Minerale*, 1975, **12**, 427.

6. R. Fischer and F. Pertlik, *Tschermaks Mineral. Petrogr. Mitt.*, 1975, **22**, 236.

7. P. W. Stephens, *J. Appl. Cryst.*, 1999, **32**, 281.

8. A. March, *Z. Kristallogr.*, 1932, **81**, 285.

9. W. A. Dollase, *J. Appl. Cryst.*, 1986, **19**, 267.

10. A. Boultif and D. Louër, *J. Appl. Cryst.*, 2004, **37**, 724.

11. S. Bahfenne, L. Rintoul and R. L. Frost, *Am. Mineral.*, 2011, **96**, 888.

12. J. Sejkora, D. Ozdín, J. Vitáloš, P. Tuček, J. Čejka and R. Ďuďa, *Eur. J. Mineral.*, 2007, **19**, 419.

13. K. Burger, *Coordination Chemistry: Experimental Methods*, Butterworth & Co Publishers Ltd, London, 1973.

6 Displacements and Disorder in $A_{1-x}Fe_x(FeSb)O_7$ Pyrochlores

6.1 Background

The pyrochlore structure was described in detail in Section 1.2.2 and is shown in Fig. 6.1. Pyrochlores have the general formula $A_2B_2O_7$ (or $A_2B_2O_6O'$ to distinguish between the two different sites for the oxygen anions) and cubic symmetry with space group *Fd*-3*m*. The ideal atomic sites in the pyrochlore structure are A 16*d*, B 16*c*, O 48*f* and O' 8*b*, the only variable positional parameter being the O anion *x*-value (48*f*, *x*,1/8,1/8) which falls between 0.319 and 0.343.[1] Substitutions can be made at the A, B and O sites giving a large variety of pyrochlore materials with a range of different properties.

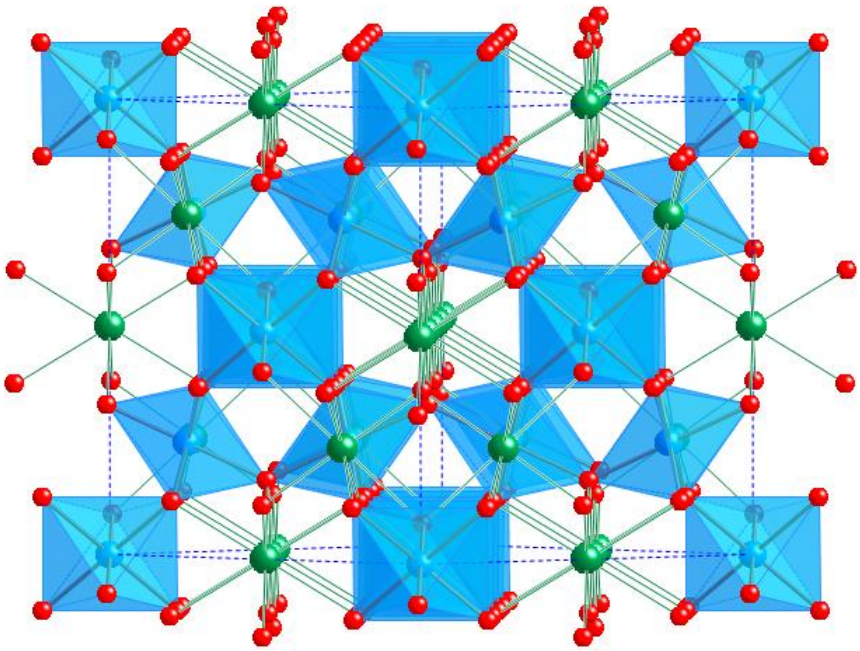

***Fig. 6.1**: The pyrochlore $A_2B_2O_7$ structure: A-cations are shown in green, BO_6 octahedra are shaded and oxygen ions are shown in red.*

6.1.1 Static Displacive Disorder

Although many pyrochlore compositions are known, there is a stability range outside which the pyrochlore structure does not form dependent on the ionic radius ratio of the A cation to the B cation (r_A/r_B). There is some variation in the limits reported[1-2] but the

A cation must be larger than the B cation for the structure to form. Typically A is a rare-earth cation or a cation with a lone pair of electrons and B is a transition or *p*-block metal but more recently pyrochlores accommodating up to 25 % of ions which are traditionally B-site cations on the A-sites have been reported such as $Bi_{2-x}M_xRu_2O_7$ (M = Mn, Fe, Co, Ni, Cu) and $Bi_{1.5}Zn_{0.92}Nb_{1.5}O_{6.92}$.[3-7] To allow these small transition-metal ions to sit on the A site, the pyrochlore structure undergoes a distortion known as static displacive disorder which has the effect of reducing the coordination number[6]. The distortion occurs in the A_2O' network: the A and O' ions are displaced from their ideal sites of 6 *d* and 8*b* respectively. As well as for pyrochlores in which the A-site is partially occupied by smaller cations, this distortion is also proposed to be a common feature for pyrochlores where the A-site cation has an s^2 electronic lone pair[4].

In this chapter some bismuth and lanthanide $A_2(FeSb)O_7$ pyrochlores are studied. The stability of the previously reported pyrochlore Bi_2FeSbO_7,[8] whose radius ratio falls outside the generally accepted stability range, and formation of compounds in the series $Bi_{2-x}Fe_x(FeSb)O_7$, which contain Fe^{3+} ions on both the A- and B-sites, is investigated. The possibility of introducing Fe^{3+} ions onto the A-sites of some known pyrochlore compounds at the upper end of the stability range, and the effect this has on the structure, is also explored.

6.2 Synthesis

Initially, 1 g samples of $Bi_{2-x}Fe_x(FeSb)O_7$ (x = 0.1, 0.2, 0.3, 0.4, 0.5) were prepared by heating Fe_2O_3 (99+ %) and Sb_2O_3 (99 %) in an alumina boat in air at 925 °C for 1 week with one intermediate regrind and then heating the resultant $FeSbO_4$ with Bi_2O_3 (99.9 %) and Fe_2O_3 (99+ %), in the correct proportions, in an alumina boat in air for 20 hours at 900 °C. Larger samples of $Bi_{2-x}Fe_x(FeSb)O_7$ (x = 0.1, 0.2) were prepared by heating stoichiometric amounts of Bi_2O_3 (99.9 %), Fe_2O_3 (99+ %) and Sb_2O_4 in air at 900 °C for 80-120 hours with one intermediate regrind.

Pr_2FeSbO_7 and $Nd_{1.8}Fe_{0.2}(FeSb)O_7$ were prepared by heating Pr_6O_{11} or Nd_2O_3 (99.997 %) with Fe_2O_3 (99+ %) and Sb_2O_4 in air at 1200 °C for 120 hours with one intermediate regrind.

6.3 Results and Discussion

6.3.1 Sample Preparation and Structural Characterisation

When investigating the possibility of synthesising bismuth-containing schafarzikite materials, an impure, cubic pyrochlore phase was formed containing iron, antimony and bismuth ions. The product was thought to be the previously-reported pyrochlore Bi_2FeSbO_7 [8] and synthesis of the pure material was attempted. However X-ray powder diffraction data revealed the presence of small amounts of Bi-rich impurity phases such as $Fe_{0.5}Bi_{12}Sb_{0.5}O_{20}$ which did not disappear after reheating or trying different synthesis methods. Rietveld refinement of XRPD data was performed for the sample using the ideal cubic pyrochlore structure (space group *Fd*-3*m*) as a starting model. Refined parameters included the background, zero-point error, scale factor, unit cell *a*-parameter, O1 *x* value, thermal parameters and profile parameters relating to the halfwidth, asymmetry and crystallite size. The B-site Fe:Sb ratio was constrained as 1:1 and the oxygen U_{iso} values were constrained to remain equal. For the first model (Table 6.1) the site occupancies were fixed according to the ideal formula Bi_2FeSbO_7 giving a χ^2 value of 6. 70. Refining the occupancy of the A-site reduced the Bi occupancy below and reduced the value of χ^2 indicating that the scattering from this site was lower than expected. A second model (Table 6.1) in which Fe^{3+} ions were introduced onto the A-site gave a better fit to the data. The Bi:Fe A-site ratio was refined while constraining the overall A-site occupancy to be equal to and a lower χ^2 value of 5.890 was achieved (the values of χ^2 are naturally large due to the presence of impurities). These data suggested that the composition Bi_2FeSbO_7 does not form and that the true composition of the sample approaches $Bi_{1.75}Fe_{0.25}(FeSb)O_7$. The lattice parameter obtained from the refinements fits well with the reported value of 10.428 Å [8] but no X-ray diffraction patterns were previously shown which would confirm the absence of impurity phases.

***Table 6.1**: Parameters refined from XRPD data using two different structural models for the sample initially thought to be Bi_2FeSbO_7*

	Model 1	Model 2
a (Å)	10.4630(1)	10.4630(1)
Bi1 occupancy	1	0.871(8)
Fe1 occupancy	-	0.129(8)
A-site U_{iso} (Å²)	0.064(1)	0.052(1)
B-site U_{iso} (Å²)	0.006(1)	0.022(1)
O U_{iso} (Å²)	0.006(4)	0.047(5)
O1 *x*	0.3125(9)	0.323(1)
χ^2	6.170	5.890
R_{wp}, R_F^2	0.073, 0.060	0.071, 0.038

Formation of $Bi_{2-x}Fe_x(FeSb)O_7$ was therefore investigated and samples where x = 0.1, 0.2 and 0.3 were successfully synthesised and confirmed to be single phase using XRPD. For the higher iron content samples ($x > 0.3$) small amounts of α-Fe_2O_3 were seen to be present from XRPD and SQUID magnetometry. Rietveld refinements were performed as described above and structural data from the refinement are given in Table 6.2. A graph of unit cell *a* parameter against A-site iron content, *x*, is shown in Fig. 6.2.

***Table 6.2**: Parameters refined from XRPD data for $Bi_{2-x}Fe_x(FeSb)O_7$*

	$x = 0.1$	$x = 0.2$	$x = 0.3$	$x = 0.4$	$x = 0.5$
a (Å)	10.46403(7)	10.44665(7)	10.43456(7)	10.42440(7)	10.41889(7)
Bi1 occupancy	0.854(8)	0.838(8)	0.821(6)	0.787(6)	0.750(8)
Fe1 occupancy	0.146(8)	0.162(8)	0.179(6)	0.213(6)	0.250(8)
A-site U_{iso} (Å²)	0.0496(9)	0.0502(9)	0.0517(8)	0.0503(8)	0.050(1)
B-site U_{iso} (Å²)	0.024(1)	0.024(1)	0.023(1)	0.025(1)	0.025(1)
O U_{iso} (Å²)	0.054(5)	0.051(4)	0.050(4)	0.054(4)	0.053(5)
O1 *x*	0.326(1)	0.326(1)	0.3256(9)	0.3286(9)	0.328(1)
χ^2	2.680	2.528	3.418	3.442	1.983
R_{wp}, R_F^2	0.068, 0.035	0.065, 0.035	0.052, 0.029	0.052, 0.027	0.057, 0.031

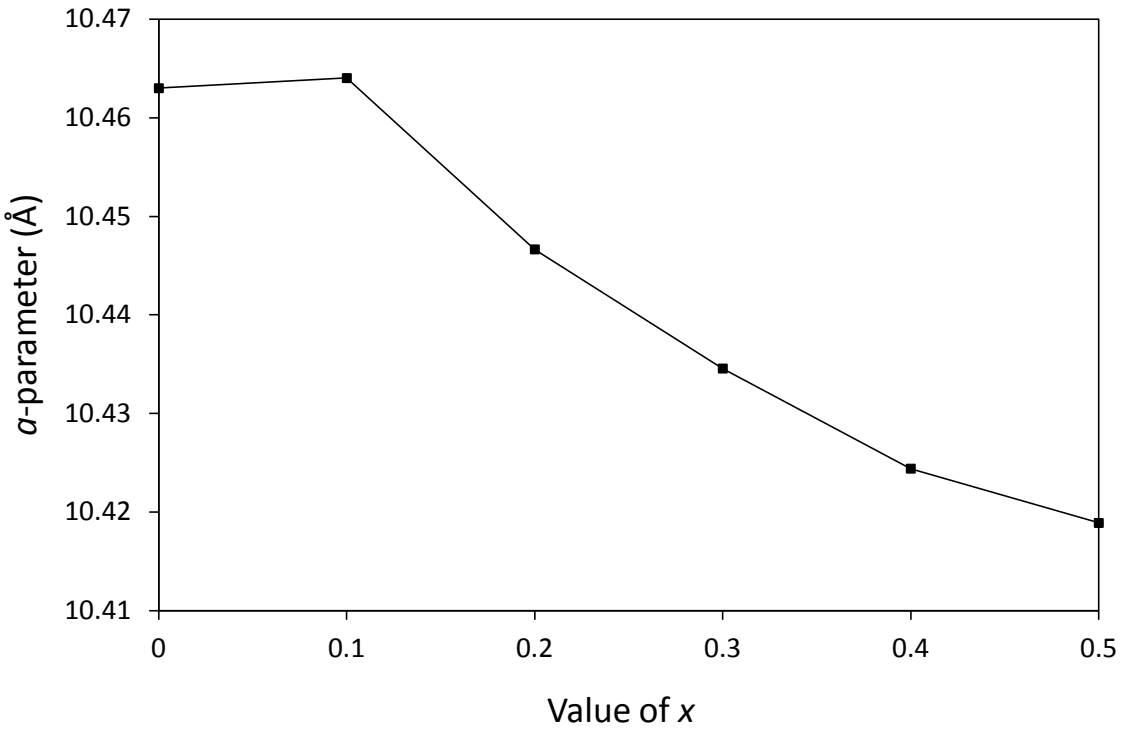

***Fig. 6.2**: Variation of unit cell a-parameter with x for $Bi_{2-x}Fe_x(FeSb)O_7$. (The values for the estimated standard deviations are smaller than the symbols on the graph.)*

The *a*-parameter decreases with increasing *x* which is expected because smaller Fe^{3+} ions are replacing larger Bi^{3+} ions on the A sites (the ionic radii of 8-coordinate Fe^{3+} and Bi^{3+} are 0.78 Å and 1.17 Å respectively[9]). The *a* parameter for the $x = 0$ compound does not fit the trend but this supports the idea that this composition does not form; instead, Fe^{3+} ions are present on both the A and B sites. The refined Bi:Fe ratios are slightly low for the samples with higher Bi contents but they are close to the ideal values and vary as expected as the composition is altered.

The radius ratio for Bi_2FeSbO_7 is calculated to be 1.88 when using values of 1.17 Å for 8-coordinate Bi^{3+}, 0.78 Å for 8-coordinate Fe^{3+}, 0.645 Å for 6-coordinate Fe^{3+} and 0.6 Å for 6-coordinate Sb^{5+}.[9] As mentioned previously this falls above the generally accepted stability range for formation of a pyrochlore material. The presence of impurities when trying to form Bi_2FeSbO_7 and the formation of single-phase $Bi_{2-x}Fe_x(FeSb)O_7$ compounds strongly indicates that the ideal composition of Bi_2FeSbO_7 does not form and

that smaller Fe^{3+} ions are actually required to stabilise the structure. The radius ratios calculated for the materials formed here, $Bi_{1.9}Fe_{0.1}(FeSb)O_7$, $Bi_{1.8}Fe_{0.2}(FeSb)O_7$ and $Bi_{1.7}Fe_{0.3}(FeSb)O_7$, fall either at the top or outside the stability range but will still be lower than that calculated for Bi_2FeSbO_7. As all these materials contain both small B-site cations on the A-sites and Bi^{3+}, which has a lone pair of electrons, they are likely to undergo static displacive disorder where the A-site cations are displaced from their ideal sites. This is also true of the compound Bi_2FeSbO_7 due to the Bi^{3+} lone pair. The distortion helps to accommodate the smaller ions on the A-site by reducing the coordination number from 8 to (5+3) where the cation has five nearest neighbours and three that are further away[5-6]. The radius ratios must be used with caution because the uncertainty in the exact structure and coordination number of the ions leads to inaccuracies in the calculations. The presence of Fe^{3+} ions on the A-site will, however, reduce the overall size on this site and is therefore expected to stabilise the structure.

An ^{57}Fe Mössbauer spectrum was recorded from the sample $Bi_{1.8}Fe_{0.2}(FeSb)O_7$ and interpreted by Professor Frank J. Berry. The spectrum is shown in Fig. 6.3 and is best fit to two quadrupole split absorptions with chemical isomer shifts characteristic of Fe^{3+}. One doublet has a chemical isomer shift, δ, of 0.38 mm s^{-1}, a quadrupole splitting, Δ, of 0.54 mm s^{-1} and accounts for *ca*. 90 % of the spectral area; this doublet is associated with Fe^{3+} on the 6-coordinate B-sites. The other doublet has δ = 0.32 mm s^{-1}, a larger quadrupole splitting, Δ = 1.87 mm s^{-1} and accounts for 10 % of the spectral area; this doublet is associated with Fe^{3+} on the 8-coordinate A-sites. The presence of two Fe^{3+} doublets with a large difference in quadrupole splitting values strongly supports the evidence from XRPD of iron being present on both the A- and B-sites. Within error, the Fe^{3+} occupancies of the A- and B-sites indicated by the Mössbauer spectrum agree well with the expected values of 17 % and 83 % respectively.

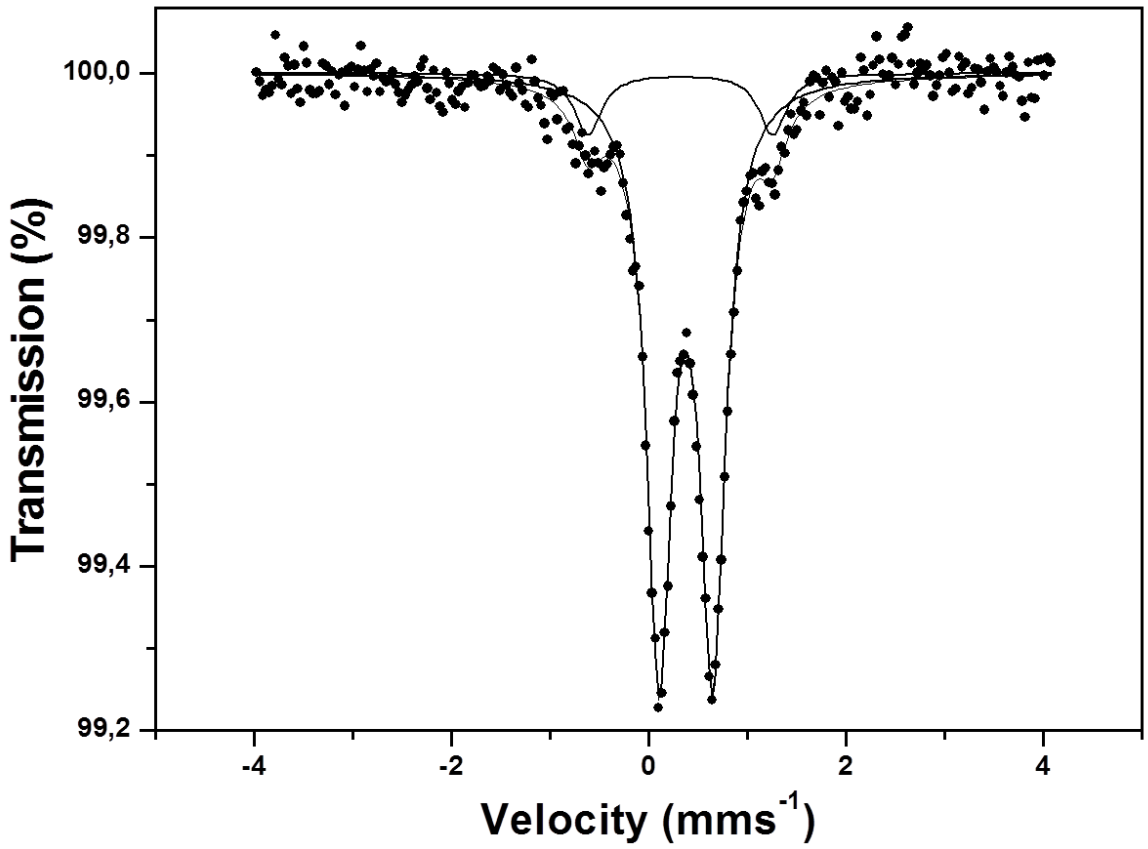

***Fig. 6.3**: ^{57}Fe Mössbauer spectrum recorded from $Bi_{1.8}Fe_{0.2}(FeSb)O_7$ at 298 K.*

Pyrochlores of the type $A_2(FeSb)O_7$ where A = Pr, Nd, Sm, Eu, Gd, Tb, Dy, Ho, Er, Yb, Lu and Y are already known[10-11] and for all these compositions the radius ratio requirements are satisfied. The compound where A = La is not known due to the larger size of 1.16 Å for 8-coordinate La^{3+}. However, as La^{3+} and Bi^{3+} have similar sizes, substitution of La by a smaller ion on the A-site could be expected to stabilise a pyrochlore structure. Formation of $La_{2-x}Fe_x(FeSb)O_7$ (x = 0.25, 0.5) was therefore attempted but no pyrochlore phase was formed and instead a multi-phase product containing different forms of $LaFeO_3$ and $LaFe_{0.5}Sb_{1.5}O_6$ was obtained. Although partial occupancy by iron on the A-sites is not necessary for the stability of the known $A_2(FeSb)O_7$ pyrochlores, formation of $A_{1.8}Fe_{0.2}(FeSb)O_7$ was attempted for A = Pr and Nd and XRPD patterns were taken of the products. The sample $Nd_{1.8}Fe_{0.2}(FeSb)O_7$ was successfully formed and confirmed to be single phase. For the compound $Pr_{1.8}Fe_{0.2}(FeSb)O_7$ a pyrochlore phase was formed which

was shown to contain a minor $PrFeO_3$ impurity phase but a reduction was seen in the unit cell size of the main phase. Rietveld refinement of the X-ray data gave a unit cell *a*-parameter of 10.40164(8) Å, compared with 10.43945(8) for the sample Pr_2FeSbO_7. This suggests that Fe^{3+} can be introduced onto the A-sites of Pr_2FeSbO_7 as it was for Nd_2FeSbO_7 but due to the impurity phase present this has not been studied further.

To investigate the structures of the materials formed and the possibility of static displacive disorder, neutron powder diffraction data were obtained at 300 K and 1.5 K for the samples $Bi_{1.9}Fe_{0.1}(FeSb)O_7$, $Bi_{1.8}Fe_{0.2}(FeSb)O_7$, $Nd_{1.8}Fe_{0.2}(FeSb)O_7$ and $Pr_2(FeSb)O_7$. As bismuth and iron have very similar neutron scattering lengths, Rietveld refinements of combined X-ray and neutron powder diffraction data were performed to allow accurate determination of the oxygen positions, the Bi:Fe ratio and any ion displacements in the A_2O' network. Structural data from the final refinements are given in Table 6.3 and Rietveld refinements for $Bi_{1.8}Fe_{0.2}(FeSb)O_7$ and $Nd_{1.8}Fe_{0.2}(FeSb)O_7$ are shown in Fig. 6.4 and Fig. 6.5 respectively.

The samples were shown to be single phase from the X-ray and neutron data and refinements were initially performed using models based on the ideal cubic pyrochlore structure. The data for Pr_2FeSbO_7 fit well with this model confirming that the A site is only occupied by praseodymium, the B site is only occupied by iron and antimony and all the ions sit on their ideal sites (Table 6.3). This is the first detailed characterisation of Pr_2FeSbO_7 and the *a*-parameter of 10.43945(8) compares with the value of 10.405 Å given in the literature from a report containing little data[10].

***Table 6.3**: Structural parameters from combined refinements of XRPD and NPD data at 300 K*

		Pr_2FeSbO_7	$Nd_{1.8}Fe_{0.2}FeSbO_7$		$Bi_{1.8}Fe_{0.2}FeSbO_7$	$Bi_{1.9}Fe_{0.1}FeSbO_7$
a (Å)		10.43945(8)	10.38463(5)		10.44945(6)	10.46793(5)
A-site	Wyckoff	16*d*	Nd1:16*d*	Fe1:96*g*	96*g*	96*g*
	x	½	½	0.517(2)	0.5126(5)	0.5124(5)
	y	½	½	0.517(2)	0.5126(5)	0.5124(5)
	z	½	½	0.445(2)	0.4697(5)	0.4701(6)
	occupancy	1	Nd1: 0.857(7)		Bi1: 0.150(1)	Bi1: 0.151(1)
			Fe1: 0.024(1)		Fe1: 0.016(1)	Fe1: 0.015(1)
	U_{iso} (Å²)	0.0170(4)	0.0083(6)		0.0136(6)	0.0124(6)
B-site	Wyckoff	16*c*	16*c*		16*c*	16*c*
	x, y, z	0, 0, 0	0, 0, 0		0, 0, 0	0, 0, 0
	occupancy	Sb1: 0.494(5)	Sb1: 0.487(6)		Sb1: 0.474(7)	Sb1: 0.477(7)
		Fe1: 0.506(5)	Fe2: 0.513(6)		Fe2: 0.526(7)	Fe2: 0.523(7)
	U_{iso} (Å²)	0.0073(3)	0.0106(4)		0.0089(3)	0.0085(3)
O1-site	Wyckoff	48*f*	48*f*		48*f*	48*f*
	x	0.32699(6)	0.32818(6)		0.32326(5)	0.32300(6)
	y, z	⅛, ⅛	⅛, ⅛		⅛, ⅛	⅛, ⅛
	occupancy	1	1		1	1
	U_{iso} (Å²)	0.0100(3)	0.0121(3)		0.0133(2)	0.0126(2)
O2-site	Wyckoff	8*b*	8*b*		96*g*	96*g*
	x	⅜	⅜		0.3530(3)	0.3544(2)
	y	⅜	⅜		0.3530(3)	0.3544(2)
	z	⅜	⅜		0.3820(9)	0.3780(9)
	occupancy	1	0.894(7)		0.083	0.083
	U_{iso} (Å²)	0.0099(6)	0.0121(3)		0.0133(2)	0.0126(2)
O3-site	Wyckoff	-	96*g*		-	-
	x, y	-	0.314(4), 0.314(4)		-	-
	z	-	0.389(4)		-	-
	occupancy	-	0.009(1)		-	-
	U_{iso} (Å²)	-	0.0121(3)		-	-
χ^2		5.168	4.759		4.454	4.199
R_{wp} NPD (H1)		0.061	0.052		0.048	0.045
R_{wp} XRPD (H2)		0.048	0.044		0.064	0.068
R_F^2 NPD (H1)		0.026	0.017		0.030	0.030
R_F^2 XRPD (H2)		0.020	0.032		0.034	0.022

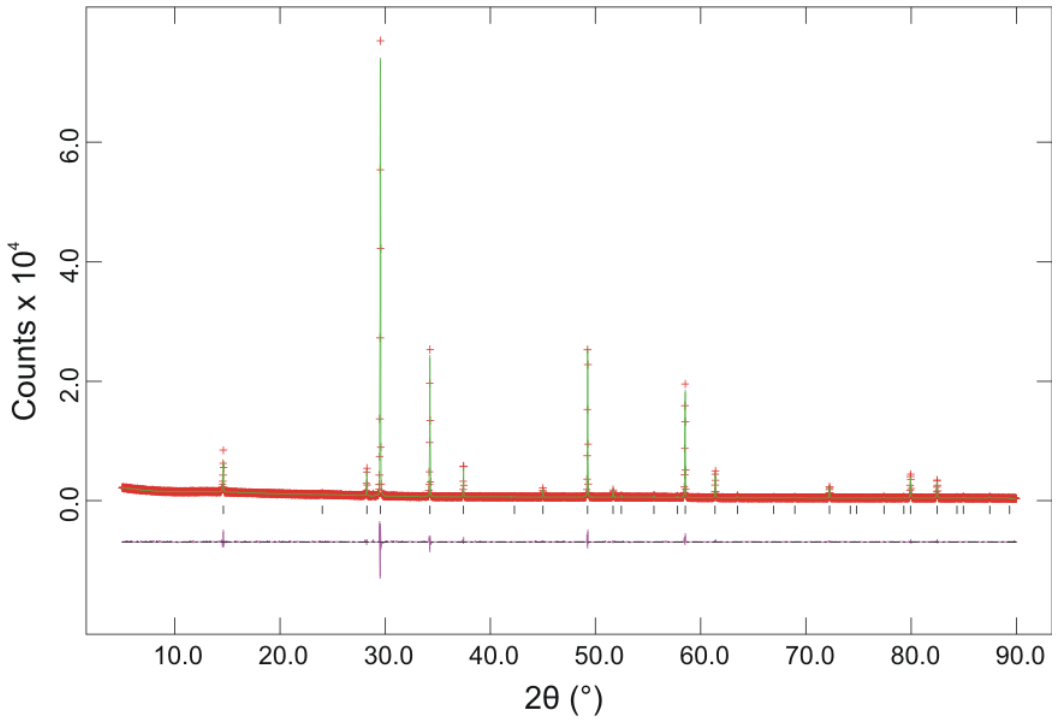

(a)

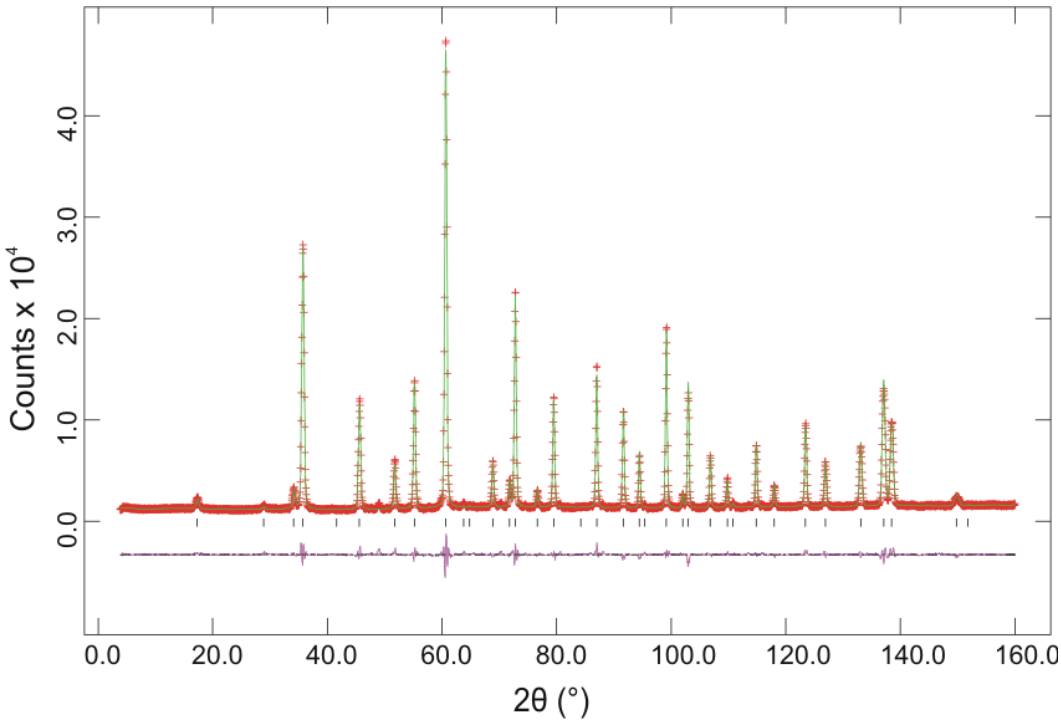

(b)

***Fig. 6.4**: Observed, calculated and difference plots obtained from a joint refinement based on XRPD and NPD data for $Bi_{1.8}Fe_{0.2}(FeSb)O_7$ at 300 K: (a) XRPD (b) NPD.*

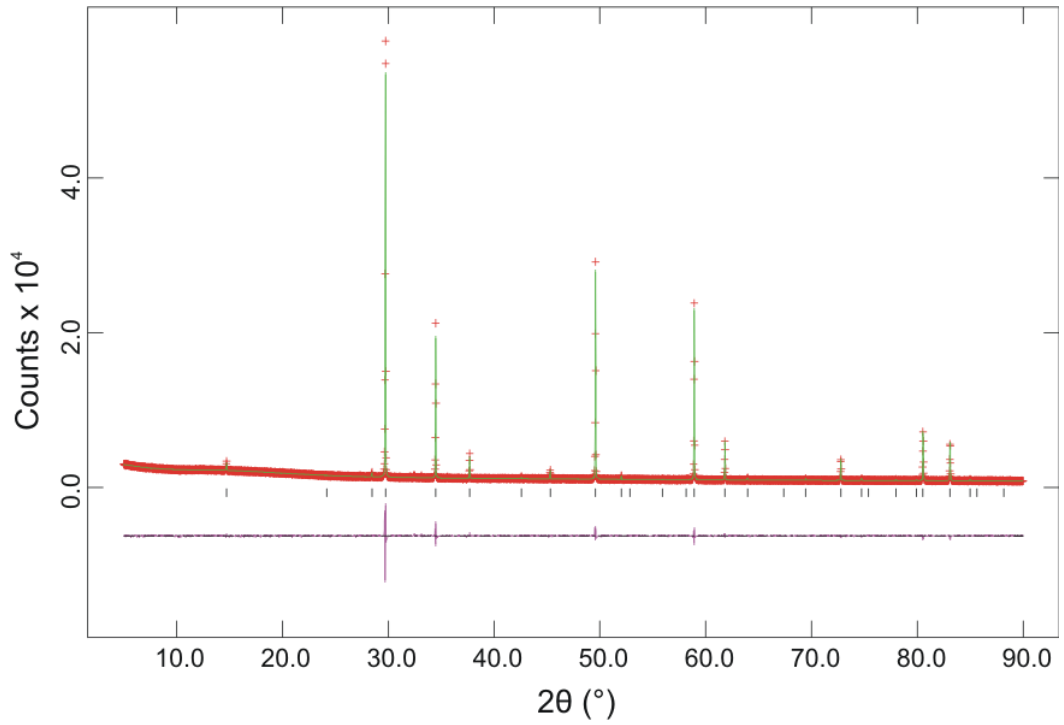

(a)

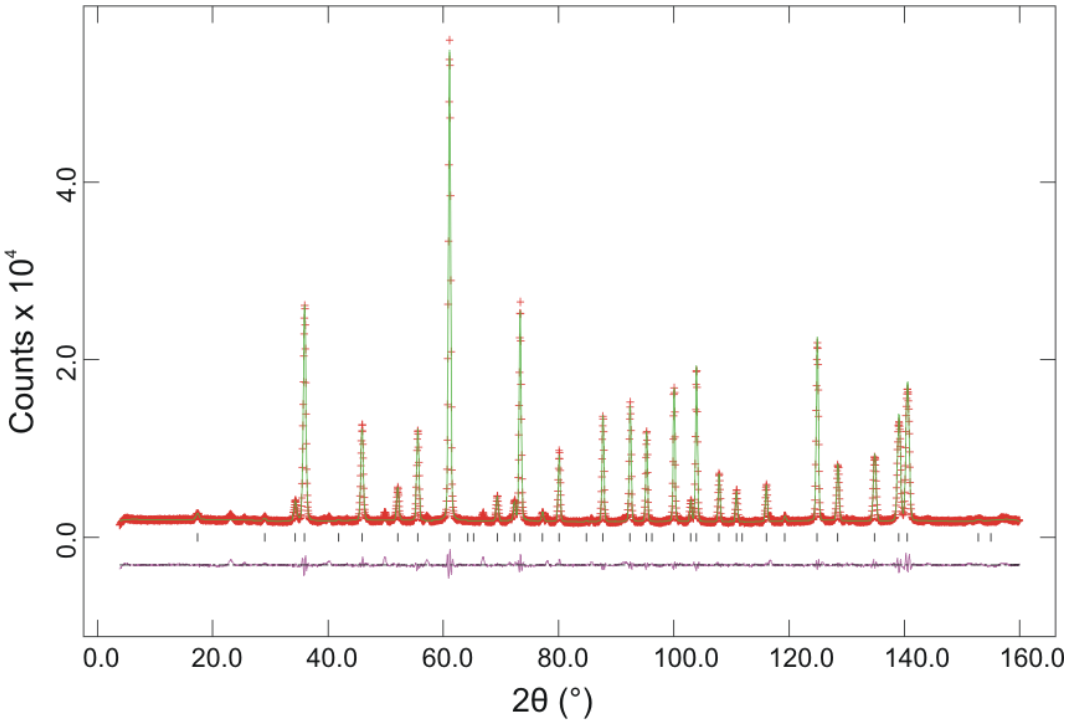

(b)

***Fig. 6.5**: Observed, calculated and difference plots obtained from a joint refinement based on XRPD and NPD data for $Nd_{1.8}Fe_{0.2}(FeSb)O_7$ at 300 K: (a) XRPD (b) NPD.*

Refinements for the two bismuth-containing pyrochlores revealed a mismatch in intensities between the observed data and the calculated model in the NPD refinement. The U_{iso} values for the A-site cations and O2 anion were also found to be significantly higher than those for the other atoms in both the room and low temperature data, indicative of static displacive disorder in the A_2O' chains. A model in which the A-site cations were displaced from the 16*d* site to the 96*g* site and the O2 anions were displaced from the 8*b* to the 96*g* site (Table 6.3), as seen previously for similar pyrochlores[4-5], gave a superior fit to the data. The fractional occupancies for the A-site cations obtained from the refinement were around 0.9 for Bi^{3+} and 0.1 for Fe^{3+} for both compounds. However the unit cell size for $Bi_{1.8}Fe_{0.2}(FeSb)O_7$ is smaller than for $Bi_{1.9}Fe_{0.1}(FeSb)O_7$ confirming that the samples have different compositions. For all the samples the B-site fractional occupancy was refined giving an Fe:Sb ratio of around 1:1, as expected. For the samples containing a mixture of cations on both the A- and B-sites, the Fe:Sb B-site ratio was initially fixed at 1:1 as the A-site occupancies were refined before refining both the A- and B-site occupancies together.

The presence of Fe^{3+} ions on the A-sites in $Nd_{1.8}Fe_{0.2}(FeSb)O_7$ suggests that this phase also exhibits static displacive disorder. The ideal cubic model gave a satisfactory fit to the data and a χ^2 value of 5. 03. The model which gave a successful fit to the data for the bismuth-containing samples did not give a good fit for $Nd_{1.8}Fe_{0.2}(FeSb)O_7$ indicating that the Bi^{3+} lone pair of electrons has a significant effect on the structure and displacement of the Nd^{3+} ions from the ideal 16*d* sites is not required. However as there is a large difference in size between Nd^{3+} and Fe^{3+} (1.11 Å and 0.78 Å respectively for 8-coordinate ions), displacement of the Fe^{3+} ions could be expected to reduce the Fe^{3+} coordination number and stabilise the structure. A third model in which only the A-site Fe^{3+} ions are displaced onto the 96*g* site, similar to that applied to the pyrochlore

$Zn_{2-x}Bi_{2.96-(x-y)}Sb_{3.04-y}O_{4+\delta}$,[12] was tested. As the displacement occurs in the A_2O' chains, some of the O' ions were allowed to be displaced onto a third oxygen site, O3, the fractional occupancy of which corresponds to that of the Fe^{3+} A-site ions. This model gave the best fit to the data, reducing the χ^2 value to 4.759, and is reported in Table 6.3.

6.3.2 Magnetic Properties

The neutron powder diffraction patterns taken at 1.5 K for the samples $Bi_{1.9}Fe_{0.1}(FeSb)O_7$, $Bi_{1.8}Fe_{0.2}(FeSb)O_7$, $Nd_{1.8}Fe_{0.2}(FeSb)O_7$ and $Pr_2(FeSb)O_7$ showed no extra reflections that would indicate the presence of long range magnetic ordering at low temperatures. Field cooled (FC) and zero-field cooled (ZFC) susceptibility measurements were taken for the samples between 5 and 300 K using an applied field of 1000 Oe. The data showed that $Nd_{1.8}Fe_{0.2}(FeSb)O_7$ and $Pr_2(FeSb)O_7$ were paramagnetic but for the bismuth-containing samples a separation of the FC and ZFC curves was observed at low temperatures indicative of a spin-glass type magnetic state (Fig. 6.6).

Spin-glass is a disordered magnetic state often observed in magnetically-frustrated systems such as those with trigonally- or tetrahedrally-related magnetic atoms. Pyrochlores with magnetic ions on the A or B sites can be very highly frustrated because the structure contains two interlinking networks of A_4 and B_4 tetrahedra (Section 1.5.3). Triangles and tetrahedra of magnetic atoms are described as frustrated because they cannot form an antiferromagnetic ground state and there are therefore competing antiferromagnetic and ferromagnetic interactions and no single, lowest-energy ground state. In a spin-glass material, at high temperatures the spins are fluctuating due to thermal energy and the material behaves like a paramagnet. Then below a freezing temperature, T_f, the random orientations of the moments are frozen in giving rise to a highly irreversible and disordered magnetic state and a transition in the susceptibility data where the FC and ZFC curves diverge. As the magnetic state is disordered no additional reflections are observed in the

NPD pattern. Spin-glass magnetic states have been confirmed for the similar pyrochlores $Bi_{1.89}Fe_{0.11}(Fe_{1.05}Nb_{0.95})O_{6.95}$ and $Bi_{1.88}Fe_{0.12}(Fe_{1.42}Te_{0.58})O_{6.87}$.[13-14]

To study the possibility of spin-glass behaviour in $Bi_{2-x}Fe_x(FeSb)O_7$ further, a SQUID magnetometry study was carried out on the samples $Bi_{1.9}Fe_{0.1}(FeSb)O_7$, $Bi_{1.8}Fe_{0.2}(FeSb)O_7$ and $Bi_{1.7}Fe_{0.3}(FeSb)O_7$ by Christina Raith, the results of which are summarised here.

As mentioned above the spin-glass state was indicated by the divergence in FC and ZFC curves (Fig. 6.6). The inverse susceptibility is also plotted and the high temperature region fit to the Curie-Weiss law. The lines deviate from the linear Curie-Weiss behaviour below 150 K which was assumed to be due to the development of ferromagnetic clusters. This plot is representative of all the samples but an anomaly is seen in the data for $Bi_{1.7}Fe_{0.3}(FeSb)O_7$ at around 250 K which is most likely to be due to the Morin transition in α-Fe_2O_3 impurities. However no impurity peaks were seen in the XRPD data so the amounts are expected to be very small. The region above 250 K was left out when fitting the inverse susceptibility data to the Curie-Weiss law for $Bi_{1.7}Fe_{0.3}(FeSb)O_7$.

The spin-glass transition for all the samples can be seen in Fig. 6.7. The freezing temperature, T_f, is strongly dependent on the applied field so measurements were taken using various applied fields between 5000 and 20000 Oe. The zero-field freezing temperature can then be determined from a plot of field dependent freezing temperature as a function of applied field. Using the Weiss constant, obtained from the Curie-Weiss plot, and the freezing temperature, a frustration parameter, $f = |\theta|/T_f$, can be determined[15]. These three values for all the samples are reported in Table 6.4.

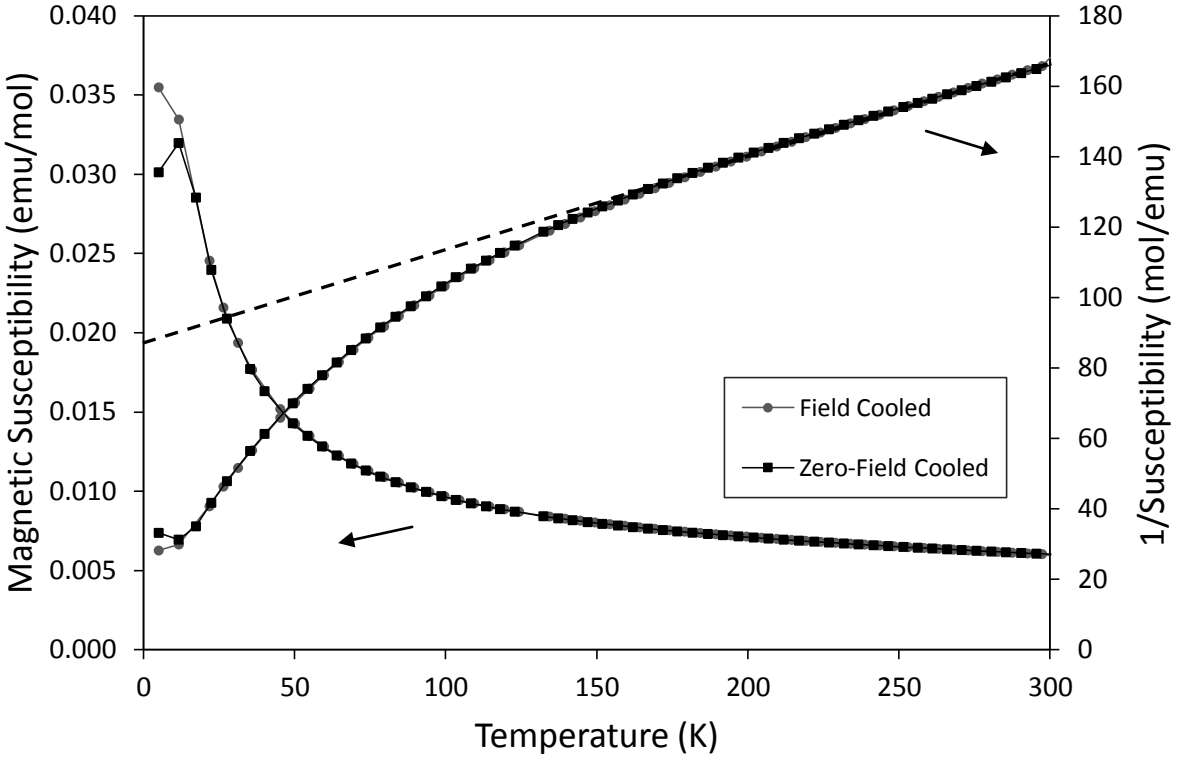

***Fig. 6.6**: Variation of magnetic susceptibility and inverse susceptibility with temperature for $Bi_{1.8}Fe_{0.2}(FeSb)O_7$.*

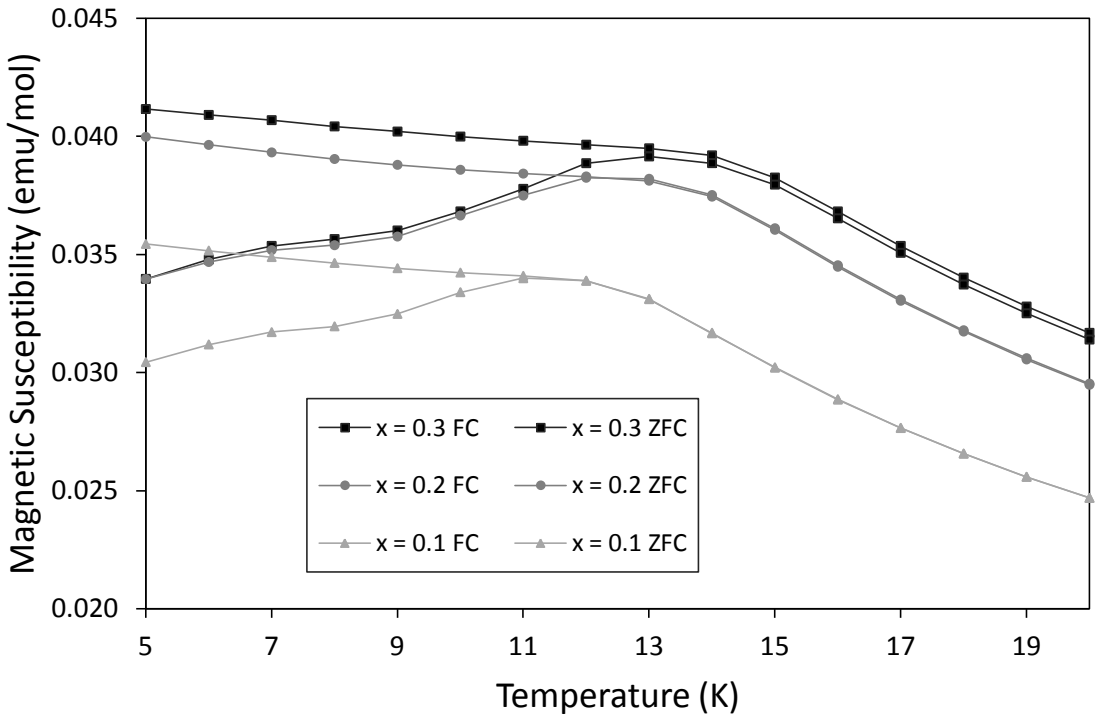

***Fig. 6.7**: Variation of magnetic susceptibility with temperature between 5 and 20 K for $Bi_{2-x}Fe_x(FeSb)O_7$ (x = 0.1, 0.2 and 0.3) using an applied field of 500 Oe.*

***Table 6.4**: Weiss constants, freezing temperatures and frustration parameters obtained from SQUID magnetometry data for $Bi_{2-x}Fe_x(FeSb)O_7$*

x	θ (K)	T_f (K)	f
0.1	-435.9(3)	12.5(2)	35
0.2	-368(2)	13.4(3)	27
0.3	-305(5)	13.9(2)	22

For all the samples the Weiss constant is very large and negative indicating that at high temperatures antiferromagnetic interactions are dominant. The Weiss constant becomes less negative with increasing iron content suggesting that the ferromagnetic exchange interactions are becoming stronger as more iron is present. The freezing temperature also increases with increasing iron content. The frustration parameter is seen to decrease with increasing iron content but the values of *f* are large showing that all the samples are highly frustrated[15].

To confirm the spin-glass magnetic state, AC susceptibility measurements were taken between 5 and 20 K for all three samples using various frequencies between 0.3 and 900 Hz and no applied DC field. Measurements were taken for the sample $Bi_{1.7}Fe_{0.3}(FeSb)O_7$ using frequencies of 0.3 Hz, 1.75 Hz, 9 Hz, 39 Hz and 100 Hz and the real part of the AC susceptibility against temperature for all these frequencies is shown in Fig. 6.8. A peak is seen in the susceptibility at the freezing temperature, the location of which is dependent on the frequency of the AC susceptibility. This shift of this peak with frequency is a signature for a spin-glass magnetic system and was seen for all three materials. The real and imaginary parts of the AC susceptibility for all three samples are shown in Fig. 6.9 between 5 and 20 K at a frequency of 9 Hz.

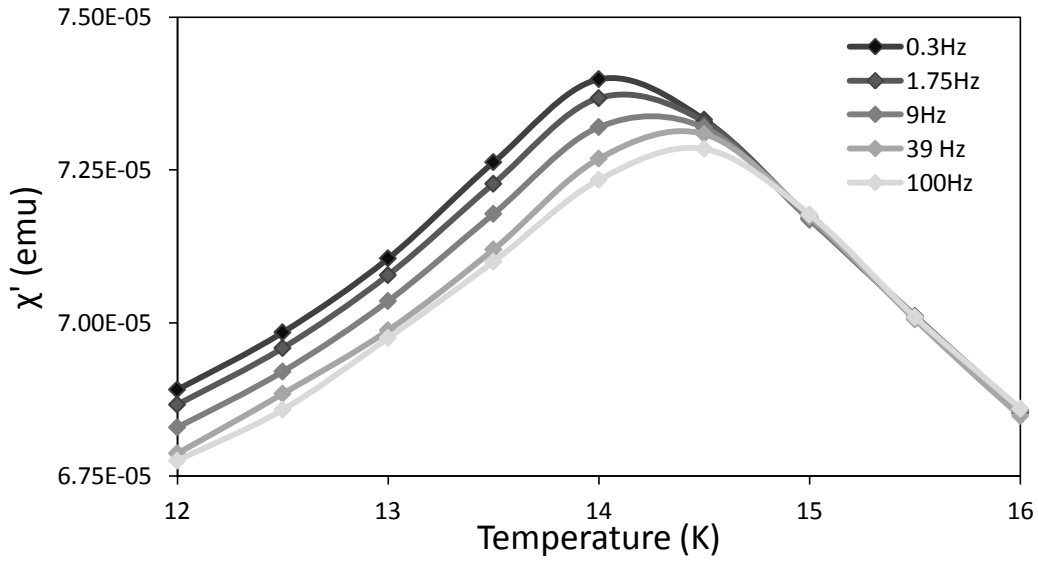

***Fig. 6.8**: Real part of the AC susceptibility, χ', as a function of temperature for different frequencies for $Bi_{1.7}Fe_{0.3}(FeSb)O_7$.*

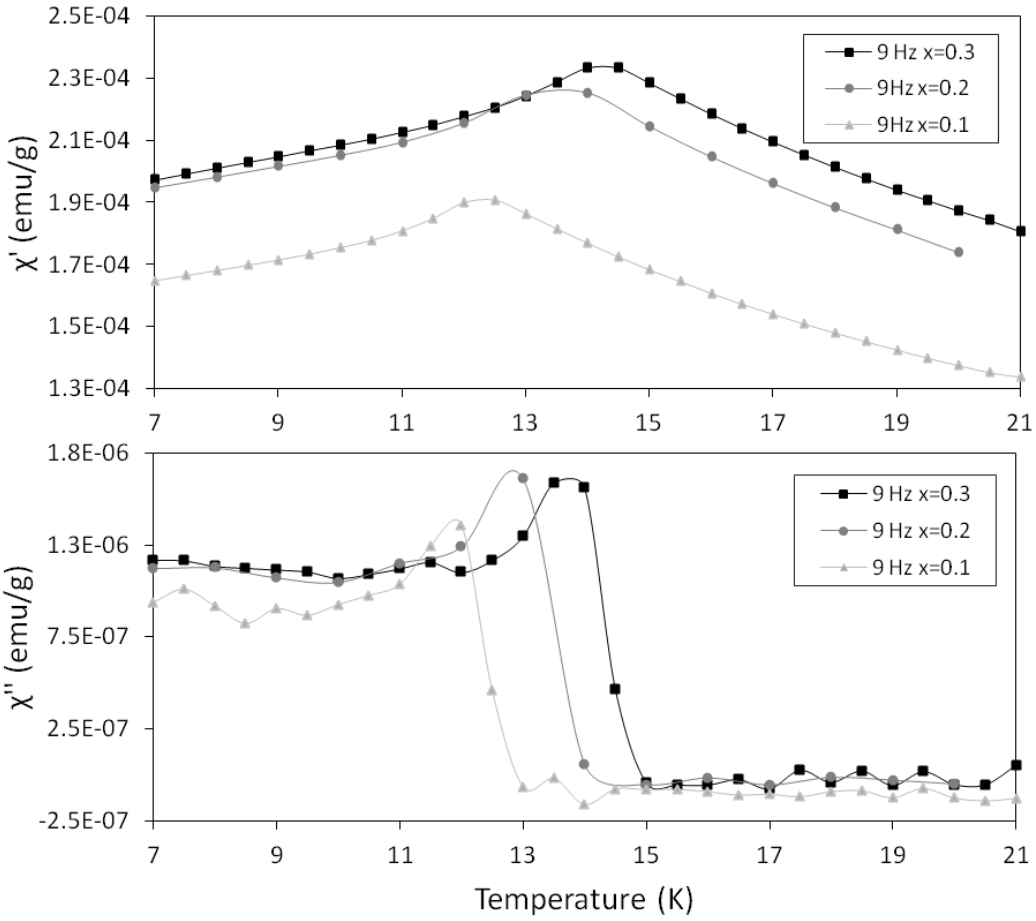

***Fig. 6.9**: Real part of the AC susceptibility, χ', (above) and imaginary part of the AC susceptibility, χ'', (below) at 9 Hz for $Bi_{2-x}Fe_x(FeSb)O_7$.*

6.4 Conclusions

Four new antimony-containing pyrochlores, $Bi_{2-x}Fe_x(FeSb)O_7$ (x = 0.1, 0.2, 0.3) and $Nd_{1.8}Fe_{0.2}(FeSb)O_7$ have been synthesised, along with the known compound Pr_2FeSbO_7, and their structural properties investigated. Formation of the previously-reported material Bi_2FeSbO_7, which falls outside the stability range for formation of a pyrochlore from radius-ratio rules, was attempted but impurity phases were present and it has been concluded that this composition does not form. Instead partial occupancy of the A site by smaller Fe^{3+} ions is required for stabilisation of the structure. The compounds $Bi_{2-x}Fe_x(FeSb)O_7$, which were single phase for x = 0.1-0.3, were prepared and studied using XRPD, Mössbauer spectroscopy and NPD. The samples were found to undergo static displacive disorder, a phenomenon observed in similar pyrochlores, to allow the structure to accommodate the Bi^{3+} lone pair of electrons and to allow the smaller, traditionally B-site, Fe^{3+} ions to sit on the A sites in the structure. The distortion is seen in the A_2O' network, the A-site cations and O' anions are displaced from their ideal sites. The sample $Nd_{1.8}Fe_{0.2}(FeSb)O_7$ was also found to undergo a distortion but for this sample only the Fe^{3+} ions are displaced from the A-site while the Nd^{3+} ions remain in their ideal positions. For Pr_2FeSbO_7 all the ions sit on their ideal sites. The magnetic properties of the samples were also studied and the samples $Nd_{1.8}Fe_{0.2}(FeSb)O_7$ and Pr_2FeSbO_7 were found to be paramagnetic. Transitions were seen in the susceptibility data for $Bi_{2-x}Fe_x(FeSb)O_7$ (x = 0.1, 0.2, 0.3) between around 12-14 K indicative of spin-glass behaviour. A SQUID magnetometry study carried out by Christina Raith confirmed the spin-glass magnetic state for all three samples.

6.5 References

1. M. A. Subramanian, G. Aravamudan and G. V. Subba Rao, *Prog. Solid St. Chem.*, 1983, **15**, 55.

2. J. S. Gardner, M. J. P. Gingras and J. E. Greedan, *Rev. Mod. Phys.*, 2010, **82**, 53.

3. M. K. Haas, R. J. Cava, M. Avdeev and J. D. Jorgensen, *Phys. Rev. B*, 2002, **66**, 094429.

4. M. Avdeev, M. K. Haas, J. D. Jorgensen and R. J. Cava, *J. Solid State Chem.*, 2002, **169**, 24.

5. I. Levin, T. G. Amos, J. C. Nino, T. A. Vanderah, C. A. Randall and M. T. Lanagan, *J. Solid State Chem.*, 2002, **168**, 69.

6. T. A. Vanderah, I. Levin and M. W. Lufaso, *Eur. J. Inorg. Chem.*, 2005, 2895.

7. M. W. Lufaso, T. A. Vanderah, I. M. Pazos, I. Levin, R. S. Roth, J. C. Nino, V. Provenzano and P. K. Schenck, *J. Solid State Chem.*, 2006, **179**, 3900.

8. M. D. Sundararajan, A. Narayanasamy, T. Nagarajan, G. V. Subba Rao, A. K. Singh and L. Häggström, *Solid State Commun.*, 1983, **48**, 657.

9. R. D. Shannon, *Acta Cryst.*, 1976, **A32**, 751.

10. M. C. Montmory and F. Bertaut, *C. R. Hebd. Seances Acad. Sci. C*, 1961, **252**, 4171.

11. O. Knop, F. Brisse, R. E. Meads and J. Bainbridge, *Can. J. Chem.*, 1968, **46**, 3829.

12. G. C. Miles and A. R. West, *Solid State Sciences*, 2006, **8**, 1422.

13. W. Miiler, L. Causeret and C. D. Ling, *J. Phys.: Condens. Matter*, 2010, **22**, 486004.

14. G. S. Babu, M. Valent, K. Page, A. Llobet, T. Kolodiazhnyi and A. K. Axelsson, *Chem. Mater.*, 2011, **23**, 2619.

15. A. P. Ramirez, *Annu. Rev. Mater. Sci.*, 1994, **24**, 453.

7 Magnetic Properties of RE_2CrSbO_7 Pyrochlores

7.1 Background

As mentioned in Section 1.5.3, the A and B ions in the pyrochlore structure form two interlinking lattices of A_4 and B_4 tetrahedra (Fig. 7.1) and if these ions are magnetic this can give highly-frustrated systems and unusual magnetic properties.

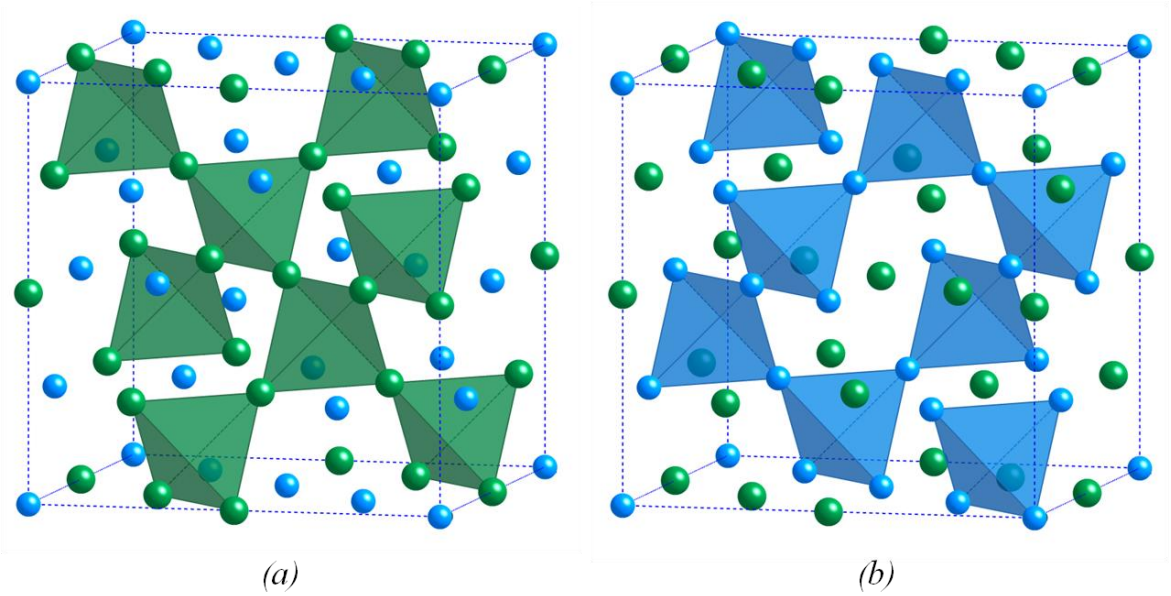

***Fig. 7.1**: The pyrochlore structure showing the A- and B-cations only. The tetrahedral arrangement of (a) A-cations (green) and (b) B-cations (blue) is shown.*

One of the more unusual types of magnetic behaviour observed in some pyrochlore materials is the spin-ice magnetic state which was first discovered for the pyrochlore $Ho_2Ti_2O_7$.[1] In a spin-ice pyrochlore the magnetic moments are constrained to lie along the ⟨111⟩ directions: either pointing in to or out from the centre of a given tetrahedron (Fig. 7.2a).[2] For each tetrahedron, two spins point in and two spins point out, and each tetrahedron has an overall ferromagnetic moment. However, as the *x*, *y* and *z* directions are equivalent in a cubic structure there is no preferred direction for the moments to align themselves in unless a magnetic field is applied.[2] This gives a disordered structure with the moments on neighbouring tetrahedra pointing in different directions while obeying the

two-in, two-out condition. Spin-ice materials therefore have many degenerate ground states which prevents a long-range ordered structure from forming[2]. This type of magnetic behaviour is known as spin-ice because it is analogous to the ordering of protons in hexagonal water ice.[3] Each oxygen ion is tetrahedrally surrounded by four hydrogen ions and forms two short and two long O-H bonds (Fig. 7.2b). Hexagonal water ice and spin-ice pyrochlores both have similar disordered ground states and residual entropies at extremely low temperatures.[2] So far only the pyrochlores $Ho_2Ti_2O_7$,[1] $Dy_2Ti_2O_7$ [4] and $Ho_2Sn_2O_7$ [5] have been confirmed to be spin-ices. The spin-ice pyrochlores are of interest because their structure has been suggested as a host for magnetic monopoles[6].

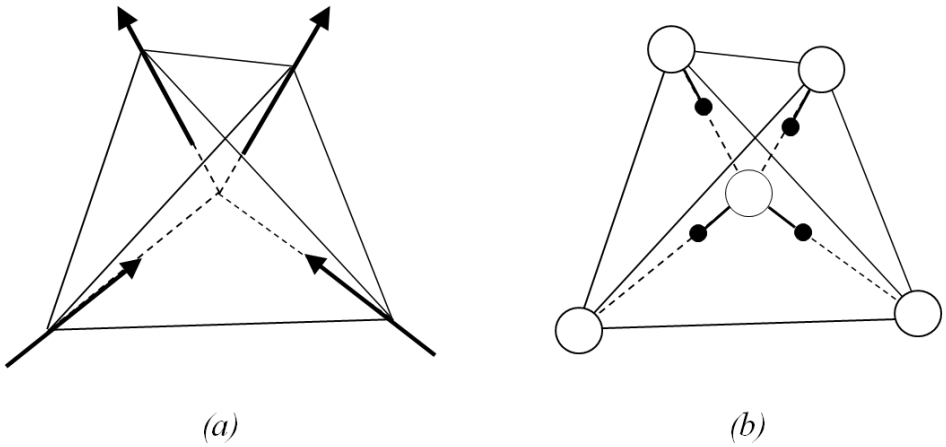

Fig. 7.2*: (a) The arrangement of magnetic spins for a given tetrahedron in a spin-ice pyrochlore structure; (b) the arrangement of hydrogen ions in water ice: oxygen ions are shown as large white spheres and hydrogen ions are shown as small black spheres.*

Pyrochlores which form long-range ordered magnetic states despite the inherent geometric frustration are also of interest, and in a previous study of magnetic rare earth pyrochlores the compounds Ho_2CrSbO_7 and Dy_2CrSbO_7 were shown to be ferromagnetic below 10 K and 16 K respectively[7]. The magnetic susceptibility and magnetisation of the pyrochlores RE_2CrSbO_7 (where RE = Y, Pr, Nd, Sm, Eu, Gd, Tb, Dy, Ho, Er, Tm and Yb) were measured and all the compounds were found to have positive Weiss temperatures, θ, between +4 and +16 K indicative of ferromagnetic interactions.[7] These pyrochlores

contain rare earth ions on the A-sites and a mix of magnetic Cr^{3+} and non-magnetic Sb^{5+} ions on the B-sites. For the samples Ho_2CrSbO_7 and Dy_2CrSbO_7 remanence was observed below the transition temperature and saturated moments of around 12 μ_B per formula unit were obtained[7] which is much lower than the expected value of 23 μ_B per formula unit. For the sample Y_2CrSbO_7 no remanence was observed at 4 K but a magnetic moment of 2.6 μ_B per formula unit was obtained at an applied field of 3 T and it was suggested that clusters of Cr^{3+} moments are coupled parallel in the structure.[7]

These materials order at relatively high temperatures for pyrochlore materials (see Section 1.5.3) but the exact type of magnetic ordering and magnetic structure has never been investigated. In this chapter the previously reported[8] rare earth pyrochlore compounds RE_2CrSbO_7 (RE = Y, Tb, Dy, Ho and Er) and Ho_2FeSbO_7 have been synthesised and their structural and magnetic properties further investigated. A neutron diffraction study of the compound Ho_2CrSbO_7 has been performed to determine the low temperature magnetic structure. As Ho_2CrSbO_7 shows magnetic ordering and Ho_2FeSbO_7 does not, some new mixed Fe-Cr analogues have been prepared with the composition $Ho_2Cr_{1-x}Fe_xSbO_7$ and the structure and magnetic properties examined.

7.2 Synthesis

Ho_2CrSbO_7 was prepared by heating stoichiometric amounts of Ho_2O_3 (≥99.9 %), Cr_2O_3 (99 %) and Sb_2O_4 powders in air for 3 days at 950 °C then regrinding and reheating at 1200 °C for 4.5 days with several intermediate regrindings. The starting material Sb_2O_4 was prepared by heating Sb_2O_3 (99 %) in air at 640 °C.

To synthesise Y_2CrSbO_7, Tb_2CrSbO_7, Dy_2CrSbO_7 and Er_2CrSbO_7, initially $CrSbO_4$ was prepared by heating Cr_2O_3 (99 %) and Sb_2O_3 (99 %) in air for 7 days at 1200 °C. Several intermediate regrindings with addition of excess Sb_2O_3 were necessary when synthesising $CrSbO_4$ to compensate for a loss of Sb_2O_3 due to volatilisation. Stoichiometric amounts of $CrSbO_4$ and RE_2O_3 (99.9 % - 99.99+ %) powders were then heated in air for 5.5 days at 1200 °C with one intermediate regrind. Samples of Ho_2CrSbO_7 were also prepared using this method as well as the one described above.

To synthesise Ho_2FeSbO_7, stoichiometric amounts of Fe_2O_3 (99+ %) and Sb_2O_3 (99 %) were heated in air for 2 days at 925 °C. The resultant $FeSbO_4$ was then heated with Ho_2O_3 (≥99.9 %) in the correct proportions for 7 days at 1000 °C then at 1200 °C for 2.5 days with several intermediate regrindings.

Samples of $Ho_2Cr_{1-x}Fe_xSbO_7$ were prepared by heating Ho_2O_3 (≥99.9 %), Cr_2O_3 (99 %), Fe_2O_3 (99+ %) and Sb_2O_4 in air for 4 days at 1000 °C then at 1200 °C for 8-10 days with several intermediate regrindings.

7.3 Results and Discussion

7.3.1 Sample Preparation

That the rare earth pyrochlores were successfully synthesised as described in Section 7.2 was confirmed using X-ray powder diffraction. However, it was seen from the XRPD patterns that for some of the samples very small impurity peaks were present. The impurity peaks did not fit to a single phase: a peak was seen at around 29 °2θ due to RE_2O_3 impurities and peaks were seen between 33 and 35 °2θ due to $RECrO_3$ impurities.

Samples of $Ho_2Cr_{1-x}Fe_xSbO_7$ (where x = 0, 0.25, 0.5 and 0.75) were initially prepared using mixtures of the corresponding binary metal oxides and the XRPD patterns, along with that of Ho_2FeSbO_7, are shown in Fig. 7.3. Ho_2O_3 and $HoCrO_3$ impurities were seen to be present in these samples (x = 0-0.75) but it was found that the amounts of the impurity phases were significantly reduced by initially heating at a lower temperature (900-1000 °C) before heating at 1200 °C.

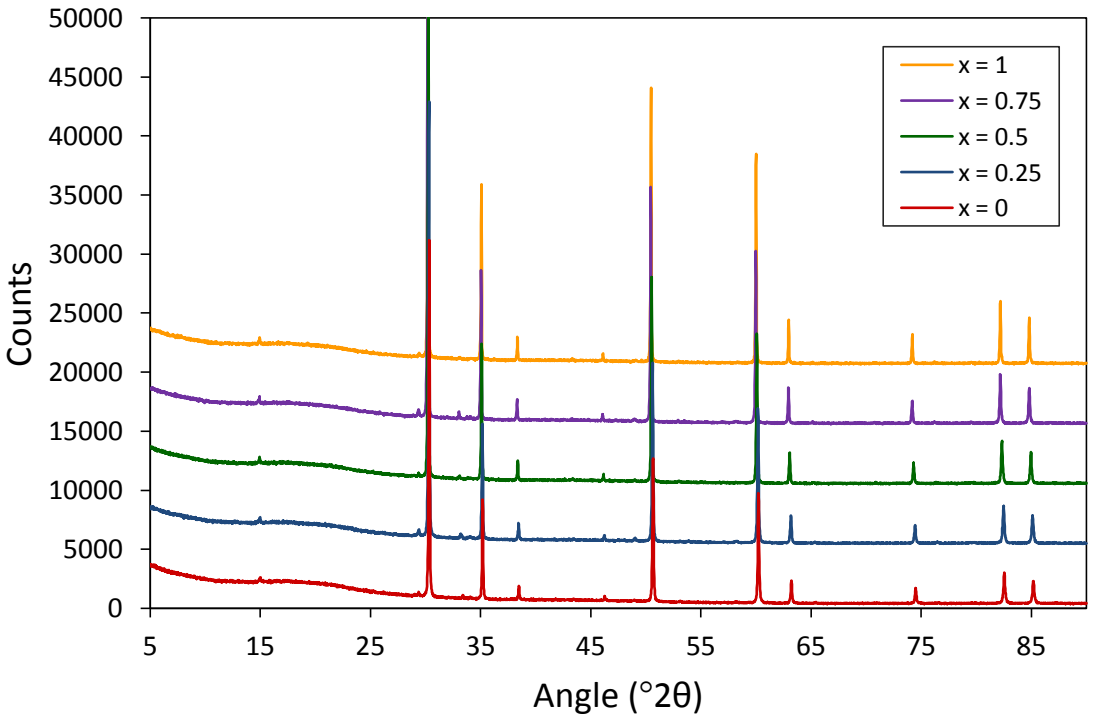

***Fig. 7.3**: Stack plot of XRPD patterns for $Ho_2Cr_{1-x}Fe_xSbO_7$ where x = 0, 0.25, 0.5, 0.75, 1.*

When synthesising the samples, the antimony oxide Sb_2O_4 was used instead of Sb_2O_3 as it is stable to much higher temperatures[9]. Although Sb_2O_3 converts to Sb_2O_4 when heated in air there are likely to be losses due to volatilisation. Problems with Sb_2O_3 volatilisation were seen when synthesising the lead substituted schafarzikite materials (Section 3.3.1) but Sb_2O_4 could not be used because these samples are prepared in sealed tubes at much lower temperatures and Sb_2O_4 would not react at these temperatures. A second method of making Ho_2CrSbO_7 was also tried using $CrSbO_4$ as a starting material. This was done because the sample Ho_2FeSbO_7 was prepared using $FeSbO_4$, which forms readily at 925 °C, and the XRPD pattern showed that this sample had no impurity phases (Fig. 7.3). The XRPD patterns of Ho_2CrSbO_7 formed using the two different synthesis methods are compared in Fig. 7.4 and it can be seen that using $CrSbO_4$ as a starting material gave single phase Ho_2CrSbO_7.

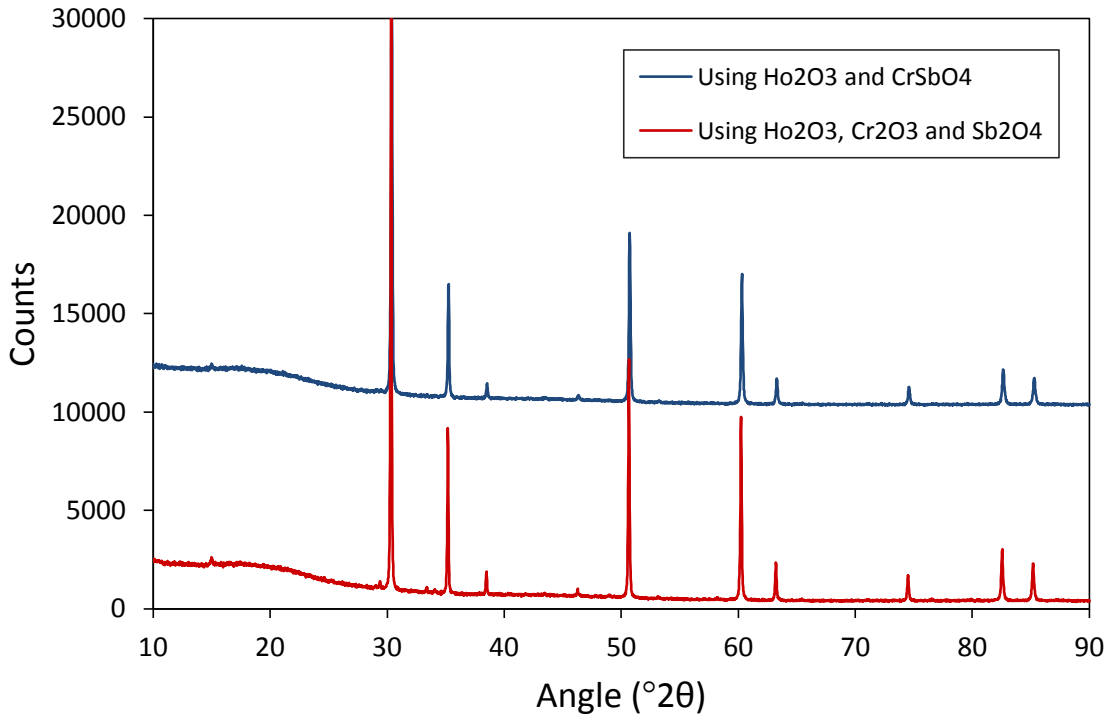

***Fig. 7.4**: Stack plot of XRPD patterns for Ho_2CrSbO_7 formed using two different synthesis methods.*

This method was therefore used to synthesise RE_2CrSbO_7 for RE = Y, Tb, Dy, Er. The sample Y_2CrSbO_7 was single phase but Tb_2CrSbO_7, Dy_2CrSbO_7 and Er_2CrSbO_7 had very small RE_2O_3 and $RECrO_3$ impurity phases (Fig. 7.5).

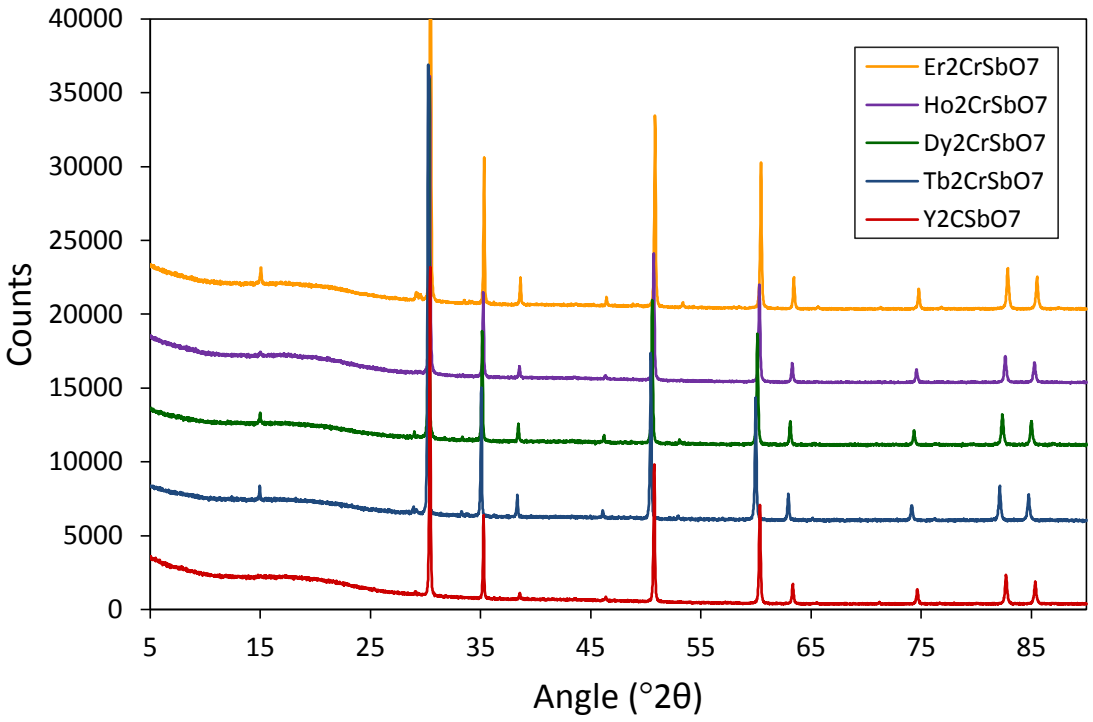

***Fig. 7.5**: Stack plot of XRPD patterns for RE_2CrSbO_7 where RE = Y, Tb, Dy, Ho, Er.*

The $CrSbO_4$ starting material was reported to form at 1200 °C by heating Cr_2O_3 and Sb_2O_3 in air[10] but the product obtained was shown using XRPD to have a large impurity phase. This was identified as Cr_2O_3 indicating a large loss of Sb_2O_3 due to volatilisation. This was also seen by looking at the sample because the brown $CrSbO_4$ product had a green Cr_2O_3 layer at the surface. The sample was therefore reheated several times, each time adding excess Sb_2O_3, which reduced the amount of Cr_2O_3 impurity (Fig. 7.6). After the fourth heat treatment no traces of Cr_2O_3 were seen in the XRPD pattern.

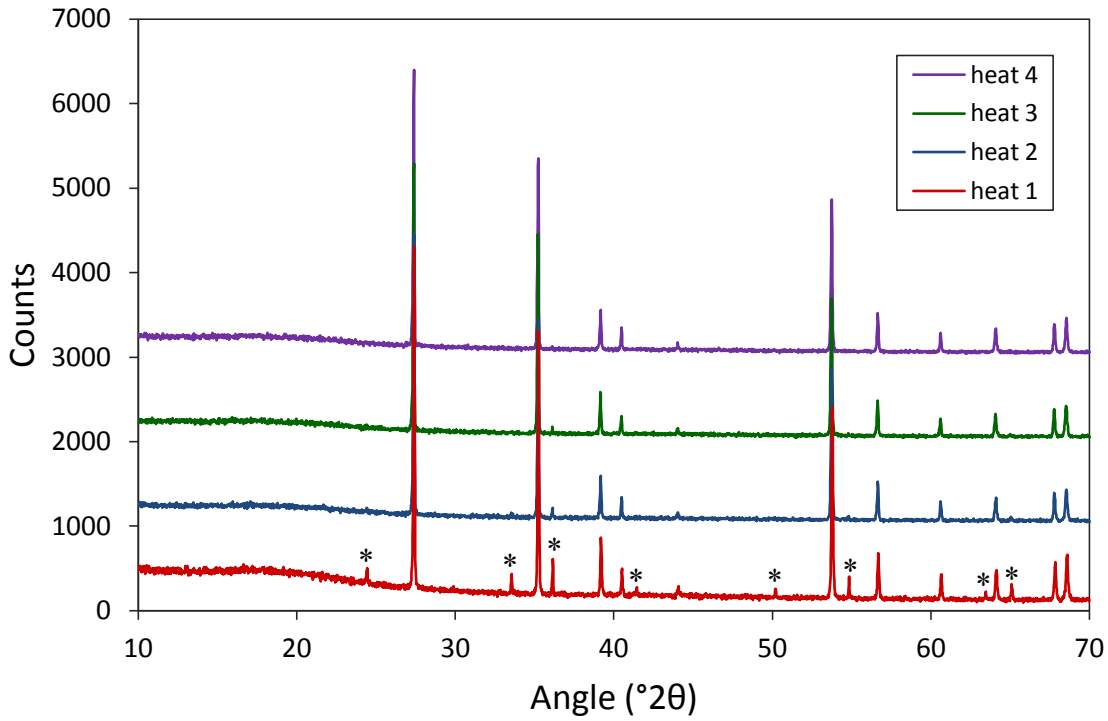

***Fig. 7.6**: Stack plot of XRPD patterns for each heat treatment in the synthesis of $CrSbO_4$. Asterisks show the positions of the Cr_2O_3 impurity peaks.*

7.3.2 Structural Characterisation

Structural refinements were performed on XRPD data for all the samples using the ideal cubic pyrochlore structure with space group *Fd*-3*m* as the starting model. Refined parameters included the background, zero-point error, scale factor, unit cell parameter, O1 *x*-value, thermal parameters and various profile parameters. The fractional occupancies of the B-site ions were constrained to remain at the ideal values and U_{iso} values were constrained to remain equal for all atoms.

The refined structural parameters for RE_2CrSbO_7 are given in Table 7.1. These samples contain RE^{3+} ions on the A-sites and a 1:1 mix of Cr^{3+} and Sb^{5+} ions on the B-sites. As expected the change in unit cell parameter corresponds to the change in ionic radius of the rare earth ion.

***Table 7.1**: Parameters refined from XRPD data for RE_2CrSbO_7 and RE^{3+} ionic radii values*

	Y_2CrSbO_7	Tb_2CrSbO_7	Dy_2CrSbO_7	Ho_2CrSbO_7	Er_2CrSbO_7
a (Å)	10.1621(1)	10.2199(1)	10.1954(1)	10.1675(1)	10.1464(1)
volume (Å³)	1049.41(4)	1067.45(3)	1059.78(3)	1051.10(3)	1044.57(3)
O1 *x*	0.3466(6)	0.3315(6)	0.3319(6)	0.3375(5)	0.3329(6)
U_{iso} (Å²)	0.0057(3)	0.0114(4)	0.0104(3)	0.0140(3)	0.0112(3)
χ^2	1.921	1.847	1.364	1.383	2.838
R_{wp}	0.043	0.034	0.028	0.036	0.051
R_F^2	0.049	0.021	0.022	0.022	0.022
RE^{3+} ionic radius (Å)[11]	1.019	1.04	1.027	1.015	1.004

The refined structural parameters for $Ho_2Cr_{1-x}Fe_xSbO_7$ are given in Table 7.2. In these materials the B-site is occupied by a mix of Cr^{3+}, Fe^{3+} and Sb^{5+} ions. The change in unit cell size indicates that the mixed Cr^{3+}/Fe^{3+} samples have successfully been formed; the unit cell size increases with increasing iron content as expected because 6-coordinate high spin Fe^{3+} (ionic radius = 0.645 Å) is larger than 6-coordinate Cr^{3+} (0.615 Å)[11]. The variation of the unit cell parameter with increasing *x* in $Ho_2Cr_{1-x}Fe_xSbO_7$ is shown in Fig. 7.7.

***Table 7.2**: Parameters refined from XRPD data for $Ho_2Cr_{1-x}Fe_xSbO_7$*

	Ho_2FeSbO_7	$Ho_2Cr_{0.25}Fe_{0.75}SbO_7$	$Ho_2Cr_{0.5}Fe_{0.5}SbO_7$	$Ho_2Cr_{0.75}Fe_{0.25}SbO_7$	Ho_2CrSbO_7
a (Å)	10.21237(6)	10.20811(8)	10.19343(8)	10.18075(9)	10.1675(1)
volume (Å³)	1065.07(2)	1063.74(2)	1059.16(2)	1055.21(3)	1051.10(3)
O1 *x*	0.3362(6)	0.3360(6)	0.3360(5)	0.3360(5)	0.3375(5)
U_{iso} (Å²)	0.0069(3)	0.0064(3)	0.0116(3)	0.0071(3)	0.0140(3)
χ^2	3.176	2.833	2.144	2.486	1.383
R_{wp}	0.047	0.045	0.041	0.045	0.036
R_F^2	0.024	0.025	0.021	0.028	0.022

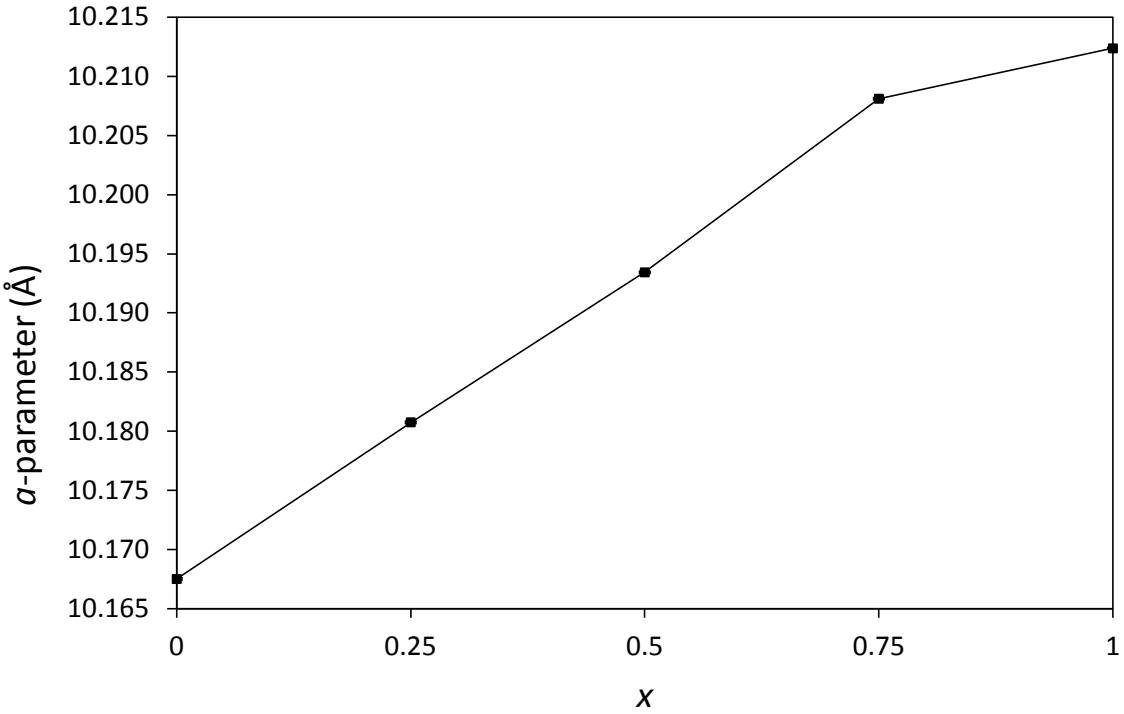

***Fig. 7.7**: Variation in unit cell a-parameter with x for $Ho_2Cr_{1-x}Fe_xSbO_7$ where x = 0, 0.25, 0.5, 0.75, 1. (The values for the estimated standard deviations are smaller than the symbols on the graph.)*

Neutron powder-diffraction data were collected for the sample Ho_2CrSbO_7 at 300 K, 50 K and 2 K. The compounds Dy_2CrSbO_7 and Ho_2CrSbO_7 were both reported to magnetically order at low temperatures[7] and Ho_2CrSbO_7 was chosen for study using neutron diffraction because dysprosium has a high neutron absorption cross-section. Structural parameters from Rietveld refinement of NPD data at different temperatures are given in Table 7.3 and the final refinement at 300 K is shown in Fig. 7.8. Thermal parameters were constrained to remain equal for Cr^{3+} and Sb^{5+} as they lie on the same site and the Cr:Sb ratio was refined but constrained so that overall the occupancy of the B-site remained at 1. From the refinement it can be seen that the unit cell size decreases with decreasing temperature due to thermal contraction and the ratio of the B-site ions, within error, remains at around 1:1.

***Table 7.3**: Parameters refined from NPD data recorded from Ho_2CrSbO_7 at 300 K, 50 K and 2 K*

	300 K	50 K	2 K
a (Å)	10.1739(3)	10.1668(3)	10.1648(1)
volume (Å³)	1053.08(8)	1050.89(8)	1050.26(5)
O1 *x*	0.3318(1)	0.3323(1)	0.3324(1)
Cr occupancy	0.44(3)	0.43(3)	0.51(3)
Sb occupancy	0.56(3)	0.57(3)	0.49(3)
Ho U_{iso} (Å²)	0.0089(4)	0.0059(4)	0.0046(4)
Cr/Sb U_{iso} (Å²)	0.0042(8)	0.0008(8)	0.003(1)
O1 U_{iso} (Å²)	0.0063(3)	0.0030(3)	0.0033(3)
O2 U_{iso} (Å²)	0.0052(9)	0.001(1)	0.006(1)
Ho-O1 (Å) x 6	2.4822(7)	2.4777(7)	2.4761(7)
Ho-O2 (Å) x 2	2.20271(4)	2.20119(4)	2.20074(2)
Cr/Sb-O1 (Å) x 6	1.9819(4)	1.9823(4)	1.9825(5)
χ^2	1.924	2.323	2.979
R_{wp}, R_F^2	0.040, 0.039	0.032, 0.029	0.042, 0.020

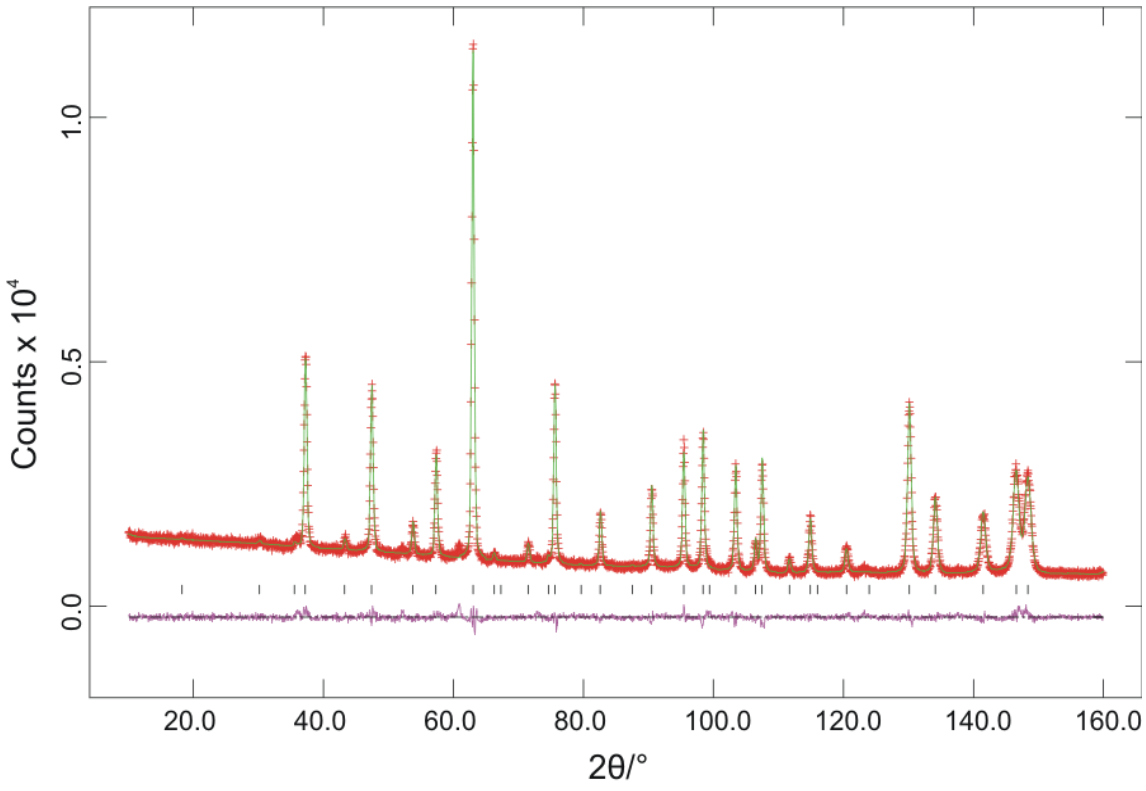

***Fig. 7.8**: Observed, calculated and difference plots for NPD data recorded from Ho_2CrSbO_7 at 300 K.*

7.3.3 Magnetic Properties

Field cooled (FC) and zero-field cooled (ZFC) susceptibility measurements were taken for the samples RE_2CrSbO_7 (RE = Y, Tb, Dy, Ho and Er) and $Ho_2Cr_{1-x}Fe_xSbO_7$ (x = 0.25, 0.5, 0.75 and 1) using applied fields of 500 Oe.

Plots of susceptibility against temperature are shown in Fig. 7.9a and 7.9b for the samples Ho_2CrSbO_7 and Dy_2CrSbO_7 respectively which have both been reported to order magnetically[7]. A large increase is seen in the magnetic susceptibility at low temperatures followed by a divergence of the FC and ZFC curves, confirming that these samples have ferromagnetic components at low temperatures.

Susceptibility data for Y_2CrSbO_7 are shown in Fig. 7.10a and no obvious ferromagnetic transition can be seen although the increase in susceptibility at low temperatures (T < 25 K) looks larger than may be expected for a paramagnetic material. Magnetisation against field measurements were taken at 5 K up to applied fields of 50000 Oe and showed no remanence (Fig. 7.10b). The magnetisation is still increasing and a magnetic moment of 2.5 μ_B per formula unit was obtained consistent with the literature which reported that ferromagnetic Cr^{3+} clusters are formed[7].

Plots of susceptibility against temperature are shown in Fig. 7.11a and 7.11b for the samples Tb_2CrSbO_7 and Er_2CrSbO_7 respectively. The data for Tb_2CrSbO_7 look very similar to those for Ho_2CrSbO_7 and Dy_2CrSbO_7; an upturn is seen in the magnetic susceptibility before the FC and ZFC curves diverge indicating that the sample may exhibit the same kind of magnetic ordering as Ho_2CrSbO_7 and Dy_2CrSbO_7. For Er_2CrSbO_7 no magnetic transition or FC-ZFC divergence is observed but, similar to Y_2CrSbO_7, the increase in susceptibility below *ca*. 25 K looks larger than may be expected for a paramagnetic material. This suggests that some magnetic interactions could be occurring either between the Er^{3+} ions, the Cr^{3+} ions or both.

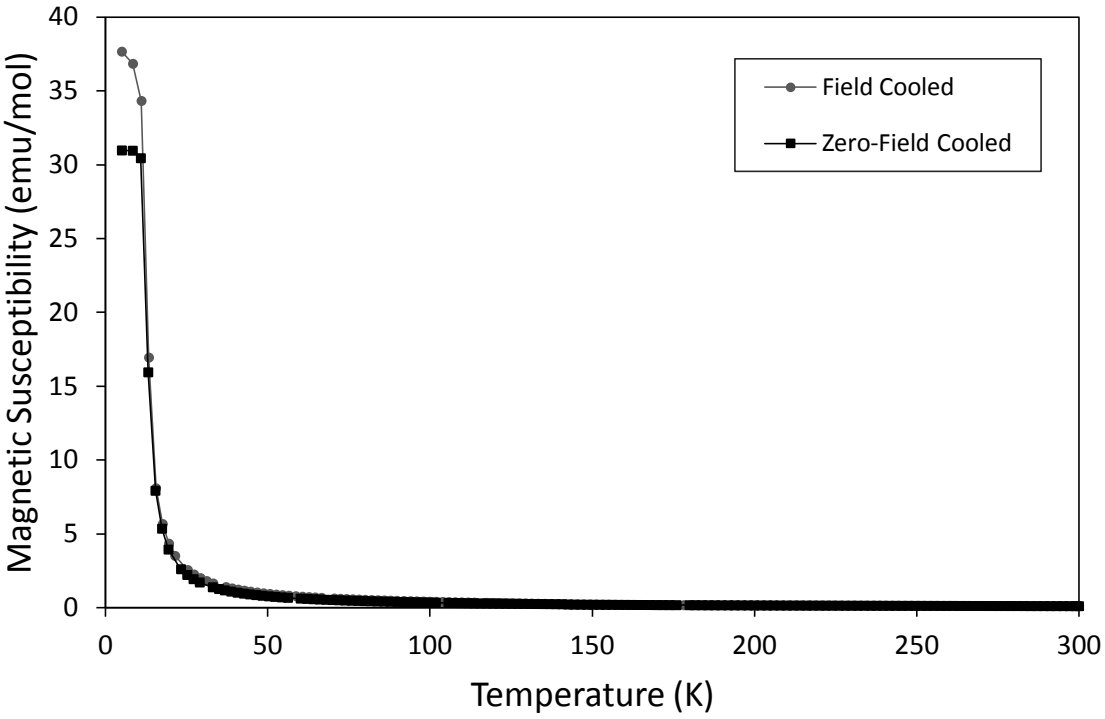

(a)

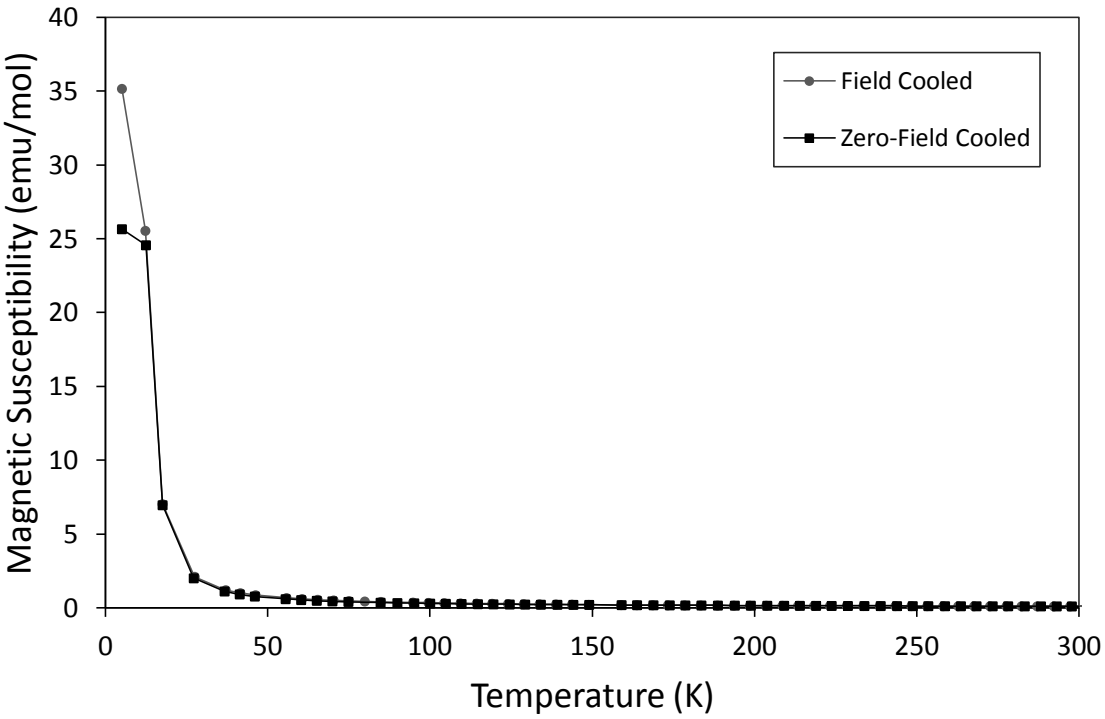

(b)

***Fig. 7.9**: Variation of magnetic susceptibility with temperature for (a) Ho_2CrSbO_7 and (b) Dy_2CrSbO_7.*

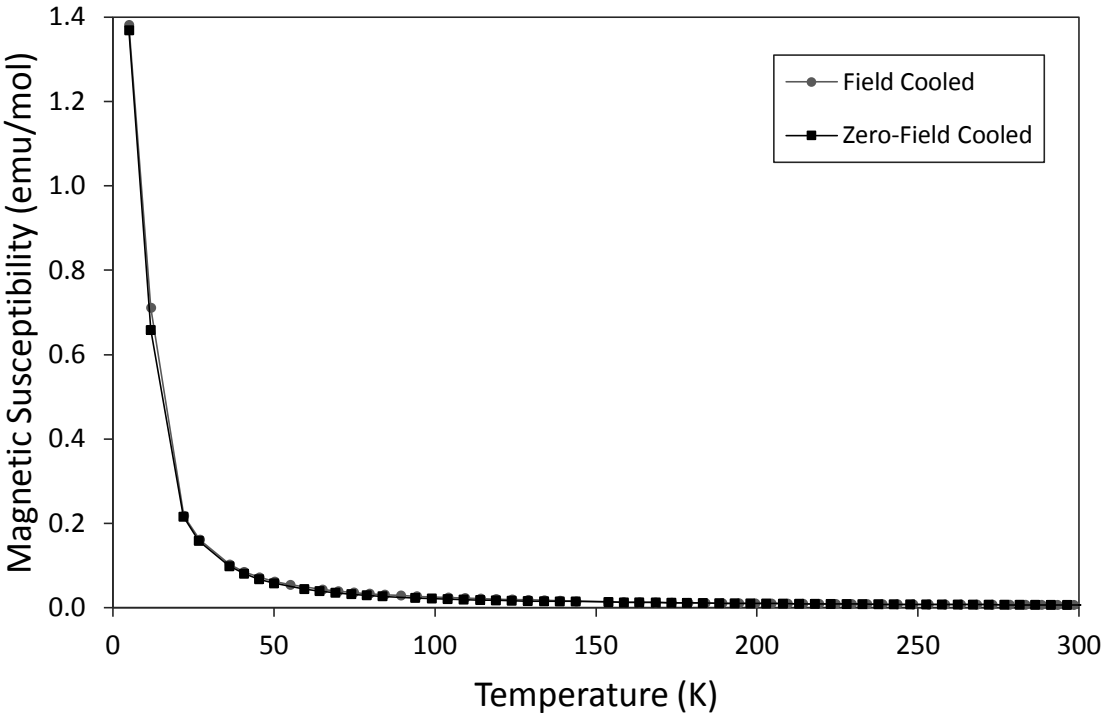

(a)

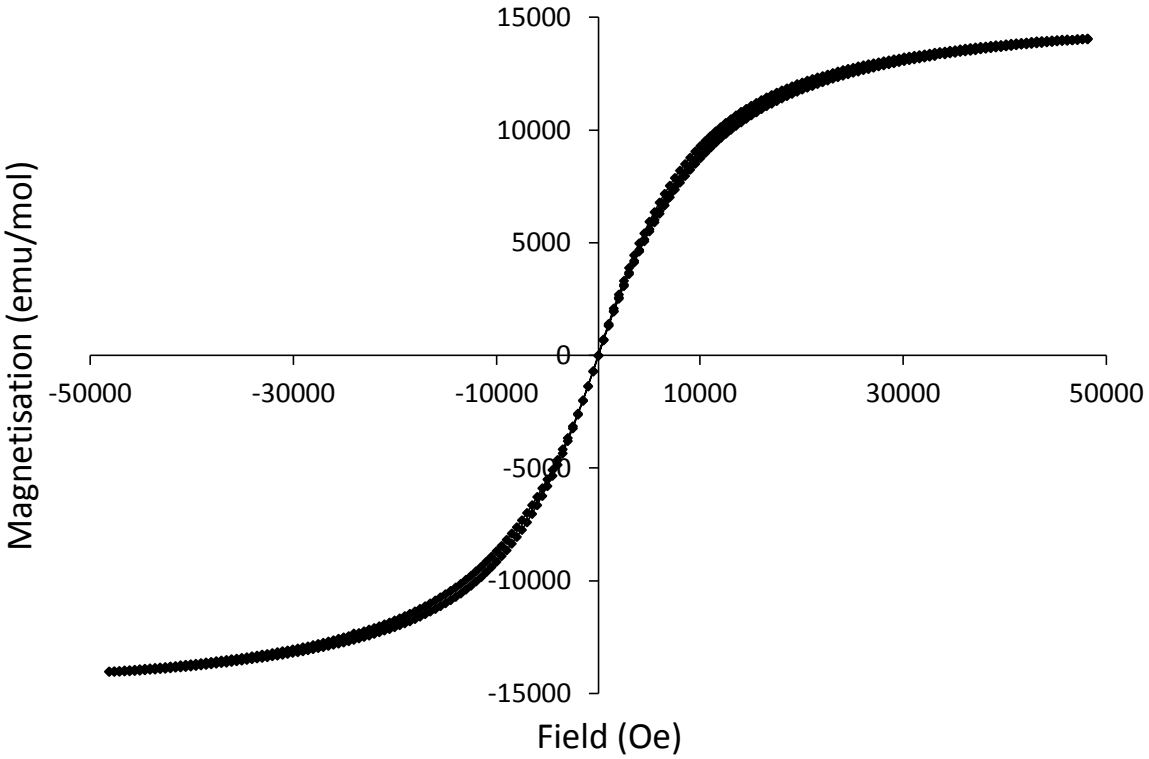

(b)

***Fig. 7.10**: (a) Variation in magnetic susceptibility with temperature and (b) variation in magnetisation with applied field (at 5 K) for Y_2CrSbO_7.*

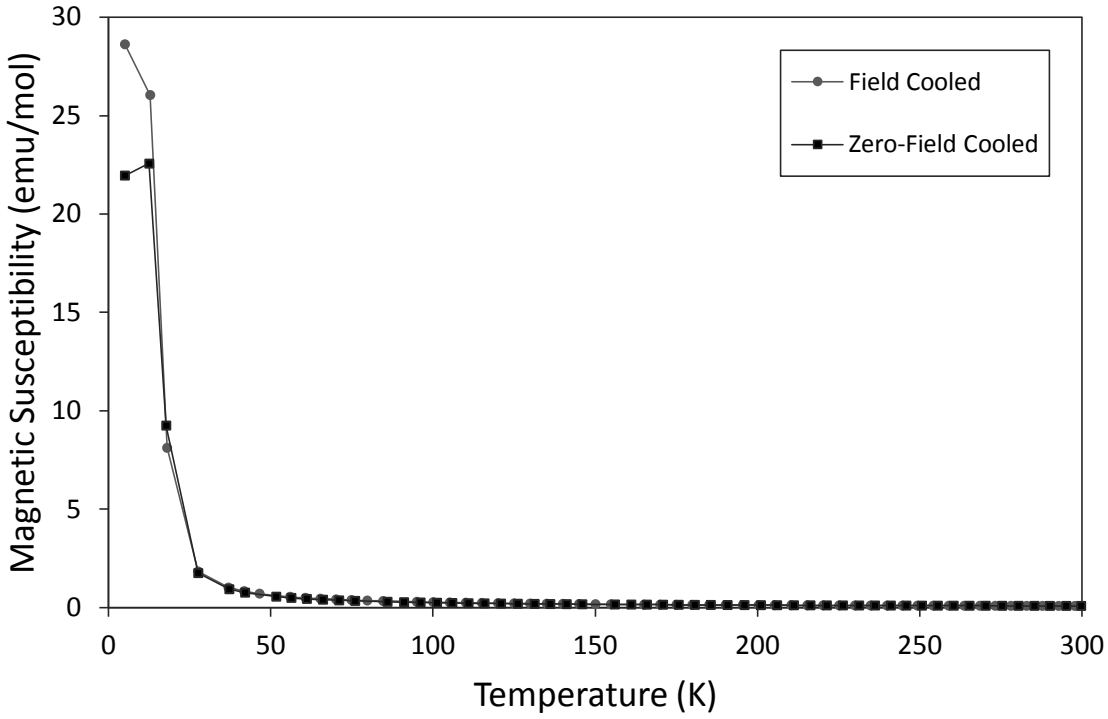

(a)

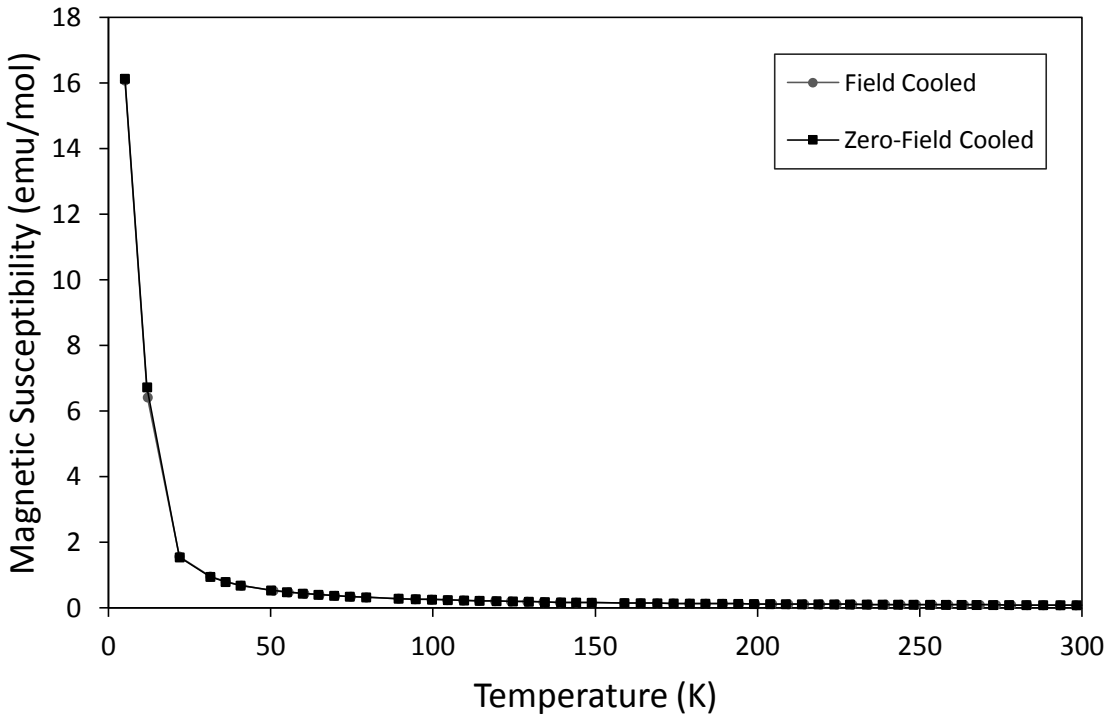

(b)

***Fig. 7.11**: Variation of magnetic susceptibility with temperature for (a) Tb_2CrSbO_7 and (b) Er_2CrSbO_7.*

Inverse susceptibility data were plotted for the samples and fit to the Curie-Weiss law. Magnetic moments, μ, and Weiss temperatures, θ, were calculated and are shown in Table 7.4. The experimental magnetic moments fit very well with the theoretical values for all the samples. The Weiss temperature is positive for Y_2CrSbO_7 indicating that ferromagnetic interactions are dominant in this sample, consistent with the idea that the Cr^{3+} ions are coupled parallel to one another[7]. The Weiss temperatures are negative for all the other samples indicative of antiferromagnetic behaviour. If the Cr^{3+} ions interact in the same way in all the samples the data would suggest that the lanthanide interactions are AFM and dominate the Curie-Weiss plot but the Cr^{3+} interactions are FM which is revealed for Y_2CrSbO_7 as the A-sites are now non-magnetic. The Cr^{3+} ions can interact via superexchange interactions through Cr-O-Cr links. Exchange interactions for Cr^{3+} are expected to be AFM for a cation-anion-cation angle of 180 ° and FM for an angle of 90 °.[12] In the pyrochlore structure the B-O-B angle is 130 ° and is therefore intermediate between the two situations; d^3-d^3 cation-anion-cation interactions are predicted to change from AFM to FM in the region of 125-150 ° making the type of superexchange interaction expected in these samples uncertain[13].

***Table 7.4**: Magnetic parameters obtained from SQUID magnetometry data for RE_2CrSbO_7*

Sample	μ theory (μ_B)	μ experiment (μ_B)	θ (K)
Y_2CrSbO_7	3.87	3.707(5)	+24.5(5)
Tb_2CrSbO_7	14.28	14.297(6)	-3.7(2)
Dy_2CrSbO_7	15.52	15.64(2)	-2.8(5)
Ho_2CrSbO_7	15.48	15.430(7)	-3.4(2)
Er_2CrSbO_7	14.08	14.20(1)	-12.2(3)

When plotting the inverse susceptibility data for Ho_2CrSbO_7 an anomaly was seen at about 145 K where there is a transition and divergence of the FC and ZFC data (Fig. 7.12). The transition was seen for both Ho_2CrSbO_7 samples, prepared using different methods. Similar transitions were found in the inverse susceptibility plots for all the

RE_2CrSbO_7 samples between 140 and 160 K and only data collected above these temperatures were used for the Curie-Weiss plot. Initially it was thought that the transition may correspond to high temperature ferromagnetic ordering of the Cr^{3+} moments which is overshadowed in the susceptibility data by the large Ln^{3+} magnetic moments, but the transition is also masked in the susceptibility data for Y_2CrSbO_7 and calculations of the ferromagnetic upturn in Ho_2CrSbO_7 gave a value of 2.2 x 10^{-3} μ_B per Cr^{3+} ion. The moment is much smaller than would be expected for a ferromagnetic arrangement of Cr^{3+} ions and a canted antiferromagnetic state with a small net moment was considered. However FM ordering of Cr^{3+} ions was observed in the NPD data at 2 K (discussed later) and spin reorientation under the influence of the strong ferromagnetic Ho moment would not be energetically possible at this temperature. It is therefore likely that the transition is due to the small impurity phases present rather than the bulk sample.

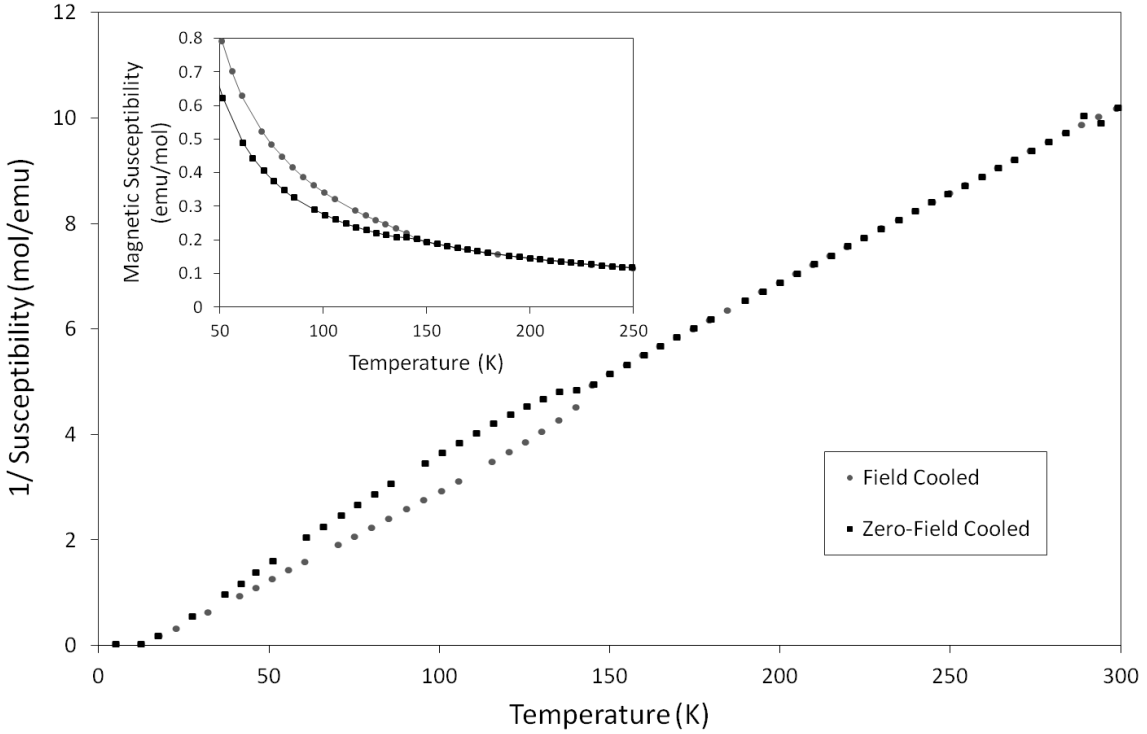

***Fig. 7.12**: Inverse susceptibility data for Ho_2CrSbO_7 showing 145 K anomaly. Inset shows variation of magnetic susceptibility with temperature for Ho_2CrSbO_7 between 50 and 250 K.*

Raman spectroscopic measurements were performed on the sample Ho_2CrSbO_7 at temperatures between 295 K and 105 K to look for spin-phonon coupling which would give evidence for a magnetic transition. Measurements are taken at various temperatures and the positions of the Raman bands plotted as a function of temperature, which can then be fitted to a straight line. If magnetic ordering of the spins occurs this will influence the phonons and a deviation from the straight line plot will be observed. The Raman spectra are shown in Fig. 7.13. For the *Fd*-3*m* pyrochlore structure there are six Raman active modes and the most intense peak in the spectrum is the A_{1g} mode which is found at around 520 cm^{-1}.[14] The positions of the bands were plotted against temperature but no effects of spin-phonon coupling were seen.

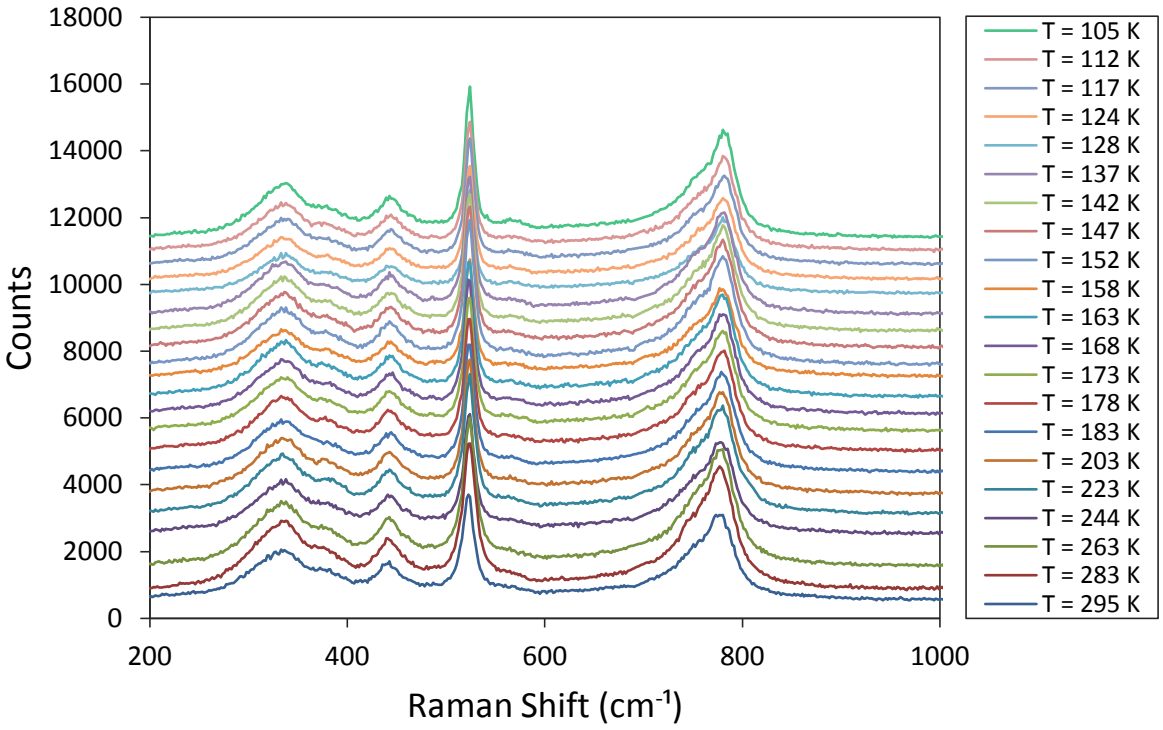

***Fig. 7.13**: Stack plot of Raman spectra recorded from Ho_2CrSbO_7 at various temperatures.*

The high temperature transitions could be due to $RECrO_3$ impurity phases. The $RECrO_3$ compounds show magnetic transitions at around 130-140 K where the Cr^{3+} ions order to canted antiferromagnetic states[15-17]; these temperatures correspond to the

anomalies seen in the susceptibility data. The magnetic field generated by the Cr^{3+} ordering then causes the lanthanide ions in $RECrO_3$ to magnetically order at lower temperatures[15-17].

A plot of susceptibility against temperature for the samples $Ho_2Cr_{1-x}Fe_xSbO_7$ where x = 0.25, 0.5, 0.75 and 1 is shown in Fig. 7.14. The compound Ho_2CrSbO_7 magnetically orders and Ho_2FeSbO_7 is paramagnetic. From Fig. 7.14 it can be seen that for $Ho_2Cr_{1-x}Fe_xSbO_7$, as more Fe^{3+} ions are introduced onto the B-sites the susceptibility values decrease and the magnetic ordering is lost. This suggests that the Cr^{3+} ions induce ordering of the Ho^{3+} ions, presumably by magnetically ordering, whereas the Fe^{3+} ions do not. The Cr-Cr interaction and ordered structure would then be weakened by the Fe^{3+} ions until it is no longer sufficient to cause the Ho^{3+} ions to order.

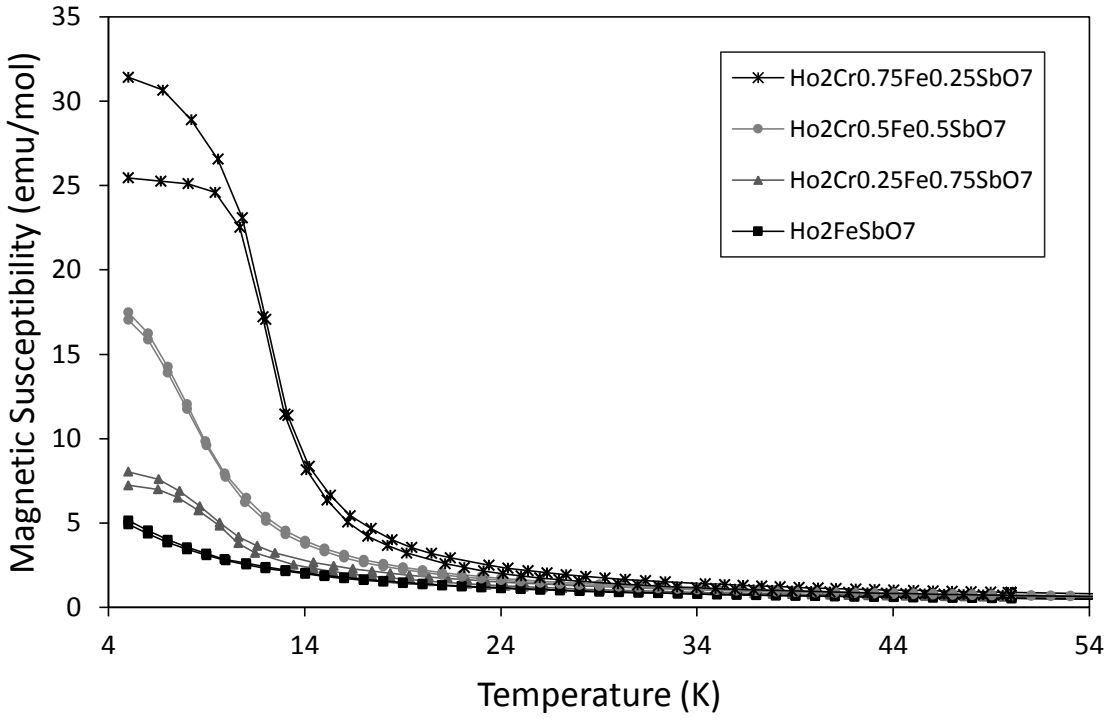

***Fig. 7.14**: Variation in magnetic susceptibility with temperature for $Ho_2Cr_{1-x}Fe_xSbO_7$ where x = 0.25, 0.5, 0.75 and 1.*

Higher temperature transitions where the FC and ZFC plots diverge were seen for the mixed Cr/Fe samples (x = 0.25, 0.5 and 0.75) as they were for RE_2CrSbO_7. However unlike these samples, where the ordering temperatures corresponded to that of the $RECrO_3$ impurity phases, the transition temperature changes as the Cr:Fe ratio is altered. Transition temperatures of 73 K, 145 K and 180 K were seen for the samples $Ho_2Cr_{0.25}Fe_{0.75}SbO_7$, $Ho_2Cr_{0.5}Fe_{0.5}SbO_7$ and $Ho_2Cr_{0.75}Fe_{0.25}SbO_7$ respectively. The nature of the transitions in these samples is uncertain and to investigate this further additional data such as neutron powder diffraction would be needed. As mentioned above NPD measurements were recorded from one of the pyrochlore samples, Ho_2CrSbO_7, at 300 K, 50 K and 2 K but this material shows no signs of magnetic ordering at 50 K.

A Rietveld refinement of the NPD data collected at 2 K from Ho_2CrSbO_7 is shown in Fig. 7.15. This can be compared to the room temperature data shown in Fig. 7.8.

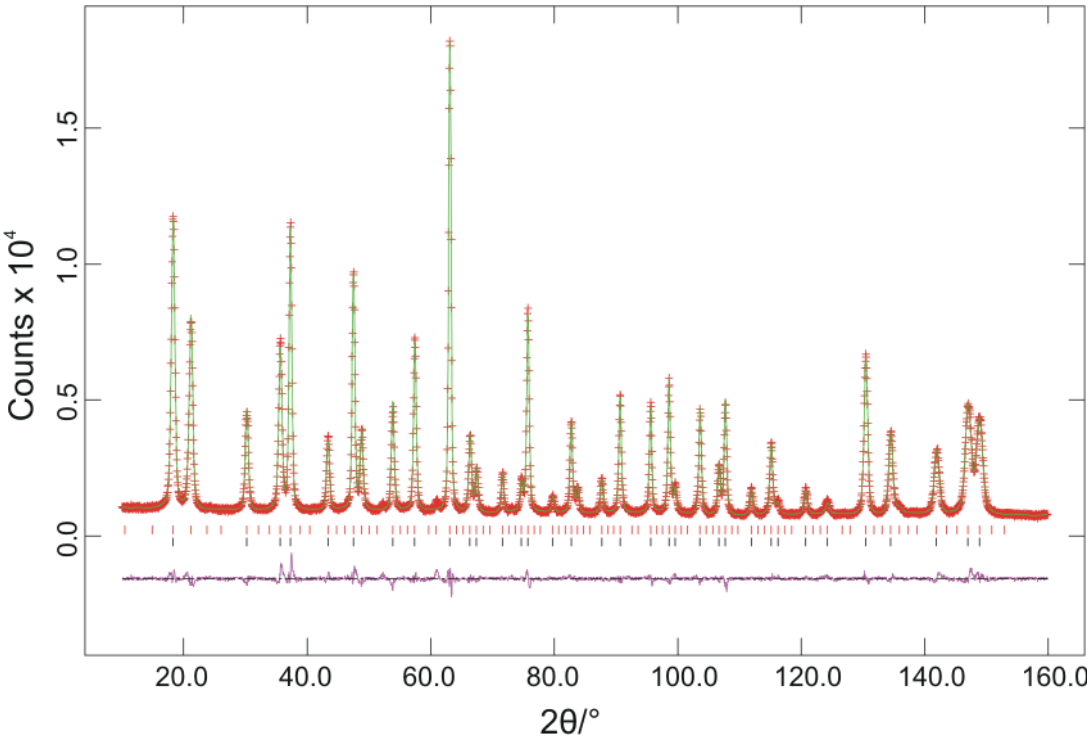

***Fig. 7.15**: Observed, calculated and difference plots for NPD data recorded from Ho_2CrSbO_7 at 2 K.*

Very large magnetic ordering peaks are present in the NPD pattern and the data show that Ho_2CrSbO_7 is not a simple ferromagnetic. The nuclear structure was refined with space group *Fd*-3*m* and the magnetic structure was refined as a separate phase with *P*1 symmetry such that the directions of the moments were unrestricted. Moments were initially input for the Ho^{3+} ions on the A sites with a component aligned along one axis only, similar to the magnetic model for the antiferromagnetic pyrochlore $Er_2Ru_2O_7$[18] which also has magnetic A and B sites Neither a simple ferromagnetic nor an antiferromagnetic structure would allow all the magnetic peaks to be modelled. Looking at the low temperature neutron diffraction pattern of Ho_2CrSbO_7, it appeared similar to that of the pyrochlore $Tb_2Sn_2O_7$ taken at 0.1 K[19]. $Tb_2Sn_2O_7$ is a spin-liquid which undergoes a transition at 0.87 K to an ordered spin-ice state with both ferromagnetic and antiferromagnetic order[19]. Therefore a model with an antiferromagnetic component along one axis and a ferromagnetic component along a second axis was tested which modelled all the peaks. The final model which gave the best fit to the data was an ordered spin-ice structure in which the moments are constrained to lie along the ⟨111⟩ crystallographic axes with the ferromagnetic component along the *z*-axis. The contribution from Cr^{3+} ions to the magnetic reflections was expected to be small due to the much larger Ho^{3+} moment and the Ho:Cr ratio of 2:1. The Cr^{3+} ions occupy half the B-sites and the best fit was obtained using a model in which the Cr^{3+} ions are ordered ferromagnetically along the *z*-axis. The ordered magnetic structures on Ho_4 and Cr_4 tetrahedra are shown in Fig. 7.16 (although the B-site tetrahedra are occupied 50 % by Cr^{3+} ions and 50 % by Sb^{5+} ions, a tetrahedron of four Cr^{3+} ions is shown for simplicity). In a true spin-ice pyrochlore material the magnetic moments are constrained along the ⟨111⟩ axes but due to the cubic symmetry no one direction is favoured, giving a disordered magnetic structure. In Ho_2CrSbO_7 the Cr^{3+} ordering along the *z*-axis removes this degeneracy and provides a field in a particular

direction for the Ho^{3+} moments to align themselves with. The ordered spin-ice structure is shown in Fig. 7.17. This would explain why the material shows rare earth magnetic ordering at a relatively high temperature for a pyrochlore. This is similar to the effect seen in $Er_2Ru_2O_7$ where it was suggested that the increased ordering temperature of the Er^{3+} ions was due to the high temperature Ru^{4+} ordering[18].

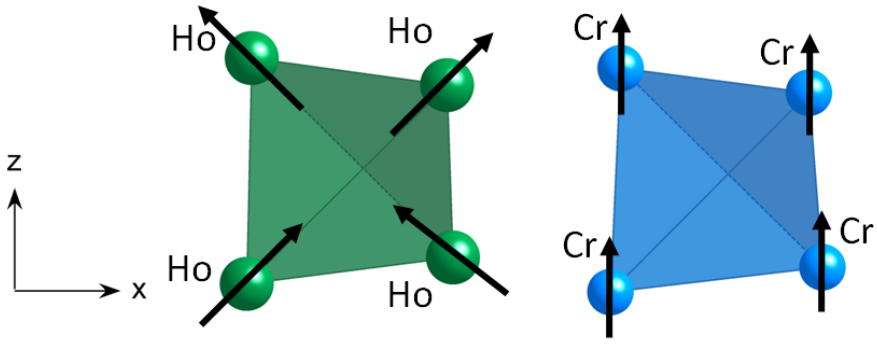

***Fig. 7.16**: Representations of the magnetic structure of Ho_2CrSbO_7 showing the arrangement of magnetic moments on single Ho and Cr tetrahedra. The Ho^{3+} moments are pointing in and out from the centre of the tetrahedron along the ⟨111⟩ axis and the Cr^{3+} ions lie solely along the z-axis.*

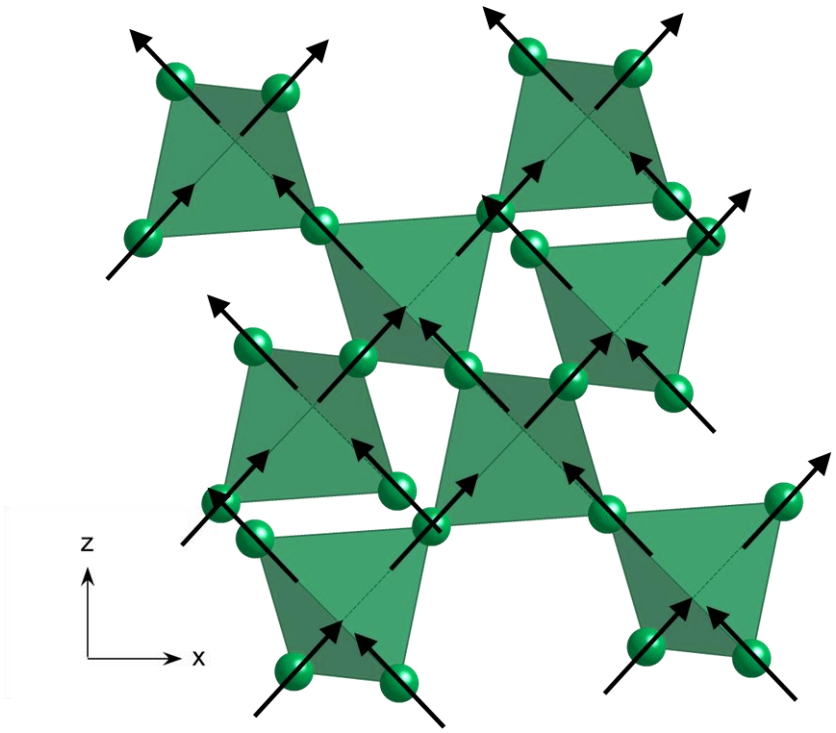

***Fig. 7.17**: Ordered spin-ice structure of Ho_2CrSbO_7 showing only the Ho_4 tetrahedra. The Ho^{3+} moments are pointing in to and out from the centre of the tetrahedron along the ⟨111⟩ axis with the ferromagnetic component aligned along the z-axis.*

The final moments from the Rietveld refinement of NPD data are given in Table 7.5. The values are in excellent agreement with the saturated moments expected from neutron diffraction of 10 μ_B for Ho^{3+} and 3 μ_B for Cr^{3+}.

***Table 7.5**: Magnetic moments and unit cell a-parameter obtained from Rietveld refinement of NPD data recorded from Ho_2CrSbO_7 at 2 K*

Magnetic Ion	M_x (μ_B)	M_y (μ_B)	M_z (μ_B)	M_{total} (μ_B)
Ho^{3+}	5.78(3)	5.78(3)	5.78(3)	10.02(5)
Cr^{3+}	2.72(5)	-	-	2.72(5)
a = 10.1648(1) Å	χ^2 = .978	R_{wp} = 0.042		R_F^2 = 0.020

Magnetisation against field measurements were performed for Ho_2CrSbO_7 and Dy_2CrSbO_7 using a SQUID magnetometer. Measurements were taken at 5 K using applied fields between -20000 Oe and 20000 Oe for Ho_2CrSbO_7 and between -50000 Oe and 50000 Oe for Dy_2CrSbO_7. Saturation was observed but there was little remanence. For the measurements small sample sizes of approximately 6 mg had to be used as the lanthanide moments were too large to give good quality hysteresis data when using a sample size of around 60-80 mg. Saturated moments of 23 μ_B would be expected for both compounds and moments of 11.3 μ_B and 12.0 μ_B were obtained from the hysteresis plots for Ho_2CrSbO_7 and Dy_2CrSbO_7 respectively which is similar to the values reported in the literature[7]. Reduced moments for the lanthanide ions in these types of pyrochlores have been reported previously due to a local ⟨ ⟩ Ising anisotropy[1, 5, 19-20]. The full moment cannot be seen because the magnetic moments are constrained along the ⟨ ⟩ axes and the field applied is too weak to turn them away from this direction. Assuming the moments lie along the ⟨ ⟩ axis with the ferromagnetic component in the *z*-direction, the reduced moment observed in the *z*-direction is calculated to be 5.8 μ_B. This gives a total calculated saturated moment of 14.6 μ_B which is much closer to the observed values of 11.3 μ_B and 12.0 μ_B.

The calculated value is still too high but could be expected to be reduced further due to the average arrangement of the crystallites in a powder sample.

7.4 Conclusions

The previously reported pyrochlore compounds, RE_2CrSbO_7 (RE = Y, Tb, Dy, Ho, Er) and Ho_2FeSbO_7 have successfully been synthesised as well as three new compounds $HoCr_{1-x}Fe_xSbO_7$ (x = 0.25, 0.5, 0.75) and their magnetic properties examined. Ho_2CrSbO_7 and Dy_2CrSbO_7 show transitions to magnetically ordered states with ferromagnetic components at low temperatures, and ferromagnetic interactions between Cr^{3+} ions are indicated by the susceptibility data for Y_2CrSbO_7 consistent with the literature. The sample Tb_2CrSbO_7 appears to undergo a magnetic transition similar to those seen for Ho_2CrSbO_7 and Dy_2CrSbO_7 at low temperatures and some magnetic ordering may also be occurring in the sample Er_2CrSbO_7. Although Ho_2CrSbO_7 magnetically orders, the related compound Ho_2FeSbO_7 is paramagnetic which suggests that the Cr^{3+} ions are important for inducing magnetic ordering of the lanthanide ion. Samples with compositions intermediate between the two materials, $HoCr_{1-x}Fe_xSbO_7$, showed a loss of magnetic ordering with increasing iron content which suggests that the Fe^{3+} does not magnetically order in these samples and instead weakens the interactions between Cr^{3+} ions. NPD data for Ho_2CrSbO_7 recorded at 2 K show large magnetic ordering peaks. The magnetic structure was found from Rietveld refinement to be an ordered spin-ice structure with the Ho^{3+} moments constrained along the ⟨ ⟩ axis and the ferromagnetic component aligned in the z-direction. The Cr^{3+} moments were found to be ferromagnetically ordered along the z-axis. It is thought that the moment generated by the FM Cr^{3+} ordering removes the degeneracy of the spin-ice state and induces ordering of the Ho^{3+} moments. The ⟨ ⟩ anisotropy was also seen in magnetisation against field measurements where a reduced moment was observed because the Ho^{3+} moments could not be turned away from the ⟨ ⟩ axis.

7.5 References

1. M. J. Harris, S. T. Bramwell, D. F. McMorrow, T. Zeiske and K. W. Godfrey, *Phys. Rev. Lett.*, 1997, **79**, 2554.

2. S. T. Bramwell and M. J. P. Gingras, *Science*, 2001, **294**, 1495.

3. L. Pauling, *J. Am. Chem. Soc.*, 1935, **57**, 2680.

4. A. P. Ramirez, A. Hayashi, R. J. Cava, R. Siddharthan and B. S. Shastry, *Nature*, 1999, **399**, 333.

5. K. Matsuhira, Y. Hinatsu, K. Tenya and T. Sakakibara, *J. Phys.: Condens. Matter*, 2000, **12**, L649.

6. C. Castelnovo, R. Moessner and S. L. Sondhi, *Nature*, 2008, **451**, 42.

7. P. F. Bongers and E. R. Van Meurs, *J. Appl. Phys.*, 1967, **38**, 944.

8. M. C. Montmory and F. Bertaut, *C. R. Hebd. Seances Acad. Sci. C*, 1961, **252**, 4171.

9. S. E. Golunski, T. G. Nevell and M. I. Pope, *Thermochim. Acta*, 1981, **51**, 153.

10. J. Amador and I. Rasines, *J. Appl. Cryst.*, 1981, **14**, 348.

11. R. D. Shannon, *Acta Cryst.*, 1976, **A32**, 751.

12. J. Kanamori, *J. Phys. Chem. Solids*, 1959, **10**, 87.

13. J. B. Goodenough, *Magnetism and the Chemical Bond*, Interscience-Wiley, New York, 1963.

14. H. C. Gupta, S. Brown, N. Rani and V. B. Gohel, *J. Raman Spectrosc.*, 2001, **32**, 41.

15. T. Morishita and K. Tsushima, *Phys. Rev. B*, 1981, **24**, 341.

16. I. B. Krynetskiĭ and V. M. Matveev, *Phys. Solid State*, 1997, **39**, 584.

17. Y. Su, J. Zhang, Z. Feng, Z. Li, Y. Shen and S. Cao, *J. Rare Earth*, 2011, **29**, 1060.

18. N. Taira, M. Wakeshima, Y. Hinatsu, A. Tobo and K. Ohoyama, *J. Solid State Chem.*, 2003, **176**, 165.

19. I. Mirebeau, A. Apetrei, J. Rodríguez-Carvajal, P. Bonville, A. Forget, D. Colson, V. Glazkov, J. P. Sanchez, O. Isnard and E. Suard, *Phys. Rev. Lett.*, 2005, **94**, 246402.

20. C. Bansal, H. Kawanaka, H. Bando and Y. Nishihara, *Physica B*, 2003, **329**, 1034.

8 Conclusions and Further Work

8.1 Conclusions

In this work the chemical modification of metal-oxide minerals to form new functional materials has been investigated. Primarily the effect of cation substitution has been studied to see whether the physical properties of the materials can be enhanced and to gain a better understanding of structure-property relationships. Two structure types have been examined: schafarzikite, which has been little studied but due to its interesting structure could potentially exhibit some appealing properties, and pyrochlore, which, on the contrary, has been very well studied and which has a structure very amenable to chemical modifications resulting in a diverse range of properties.

Schafarzikite, $FeSb_2O_4$, was successfully modified in three ways: by making substitutions at the pyramidal sites, by inserting excess oxygen ions into the channels and by making substitutions at the octahedral sites.

In Chapter 3, the partial replacement of Sb^{3+} ions by Pb^{2+} ions to form $FeSb_{2-x}Pb_xO_4$ was investigated. To balance the charge some of the Fe^{2+} ions were oxidised to Fe^{3+} giving two competing trends for the change in unit cell size. This caused an overall decrease in *a*-parameter and increase in *c*-parameter to be observed. The magnetic properties of the lead-substituted samples are different from those of the parent material. The magnetic ordering changes from predominantly A-type antiferromagnetic order in $FeSb_2O_4$ to C-type canted antiferromagnetic order in $FeSb_{2-x}PbO_4$. All the samples showed semiconducting behaviour and the conductivity was increased by introducing lead into the structure. Thermogravimetric analysis, carried out by heating $FeSb_{2-x}PbO_4$ in flowing oxygen gas, revealed that the samples take up oxygen in two stages corresponding to oxidation of Fe^{2+} at *ca*. 300-400 °C and Sb^{3+} above *ca*. 500 °C. The way that oxygen was being taken up by the samples was studied further in Chapter 4. It was seen using XRPD

that at 400 °C oxygen was being incorporated into the original schafarzikite structure before the structure broke down at higher temperatures. Fourier mapping of NPD data was used to locate the excess oxygen ions for the sample $FeSb_{1.25}Pb_{0.75}O_{4+x}$ and they were found in the channels. Both the TGA and NPD data indicated that more oxygen was being taken up into the structures than would be expected for oxidation by insertion of oxide, O^{2-}, ions, which suggested that the samples may also be taking up some oxygen as peroxide, O_2^{2-}, ions. The oxygen inserted sample, $FeSb_{1.25}Pb_{0.75}O_{4+x}$, was seen to be antiferromagnetic with a mix of A- and C-type AFM ordering which is different from that of $FeSb_{2-x}Pb_xO_4$ before oxygen ion insertion.

In Chapter 5 samples with a mix of Fe^{2+} and Mg^{2+} on the octahedral sites of the schafarzikite structure were prepared. Anisotropic broadening and preferred orientation effects were observed in the XRPD patterns, and SEM images confirmed that $Fe_{1-x}Mg_xSb_2O_4$ form needle shaped particles whereas $FeSb_2O_4$ and $MgSb_2O_4$ form particles which have equal lengths in all directions. Thermogravimetric analysis showed that the samples behave in the same way as $FeSb_{2-x}Pb_xO_4$ when heated in flowing oxygen gas; they take up oxygen in two stages forming schafarzikite-related phases containing excess oxygen at 400 °C. However Rietveld refinement of the XRPD patterns revealed that the products formed at 400 °C actually consisted of multiple schafarzikite-type phases with slightly different unit cell parameters. Canted AFM behaviour was indicated from susceptibility measurements for $Fe_{1-x}Mg_xSb_2O_4$ and the Fe^{2+}-Fe^{2+} interactions were weakened by increased levels of non-magnetic Mg^{2+} ions on the octahedral sites.

The structure and magnetic properties of some pyrochlore materials were also studied in this work. For the pyrochlore structure to form, the A-cation must be larger than the B-cation and stability ranges have been reported which depend on the ionic radius ratio of the A-cation to the B-cation (r_A/r_B). The stability of some pyrochlore phases with

radius-ratio values at the top or outside of this range were investigated in Chapter 6. It was found that a previously reported pyrochlore Bi_2FeSbO_7 [1] did not form and that to stabilise the structure and reduce the radius-ratio values, incorporation of smaller Fe^{3+} ions on the Bi^{3+} site was required and the series of compounds, $Bi_{2-x}Fe_x(FeSb)O_7$ (x = 0.1, 0.2, 0.3), was successfully prepared. Introduction of smaller transition metals on the A sites of some lanthanide pyrochlores was also investigated. Pyrochlores are magnetically frustrated systems due to the tetrahedral arrangement of A and B cations and the samples $Bi_{2-x}Fe_x(FeSb)O_7$ (x = 0.1, 0.2, 0.3) were shown to exhibit spin-glass behaviour.

In Chapter 7, the magnetic properties of RE_2CrSbO_7 (RE = Y, Tb, Dy, Ho, Er) were examined. The compound Ho_2CrSbO_7 had previously been reported to magnetically order at a relatively high temperature for a frustrated pyrochlore material of 10 K [2] but the magnetic structure had not been studied. NPD data showed that at 2 K the Ho^{3+} moments form an ordered spin-ice structure with the ferromagnetic component along the z-axis and the Cr^{3+} moments order ferromagnetically in the z-direction. It is thought that the Cr^{3+} moments influence the Ho^{3+} moments causing them to magnetically order. The compound Ho_2FeSbO_7 is paramagnetic at all temperatures and samples of $Ho_2Cr_{1-x}Fe_xSbO_7$ (x = 0.25, 0.5, 0.75) were also prepared; with increasing Fe content the magnetic ordering in these samples was lost.

8.2 Further Work

It was shown in this work that the oxidation state of the transition metal cation in schafarzikite can be controlled by making substitutions at the pyramidal site and that the physical properties can therefore be modified. To further enhance the properties of schafarzikite for useful applications, the preparation of materials more stable with respect to oxidation in air is required. Oxidation of schafarzikite begins at around 200 °C but some of the related compounds are stable to higher temperatures. For example oxygen uptake is

not observed for the compound $CoSb_2O_4$ until higher temperatures of around 500 °C.[3] Another goal for schafarzikite materials would be to reduce the toxicity which arises from the pyramidal ions such as antimony, lead and arsenic. Formation of a bismuth analogue was attempted in this work but has so far been unsuccessful. Another avenue of research that would be particularly interesting would be single crystals synthesis of the schafarzikite-related materials prepared. As the schafarzikite structure is pseudo one-dimensional, single-crystal work would allow anisotropic properties such as enhanced conductivity along the octahedral chains to be studied. However, the instability with respect to oxidation makes single crystal work challenging. Another possible area of research is the study of materials containing ions within the channels, such as the related versiliaite and apuanite minerals and the schafarzikite samples containing excess oxygen. The stability is, again, a problem for schafarzikite samples containing excess oxygen as the structure is seen to break down for samples containing higher levels of oxygen. Sealed tube synthesis at higher temperatures using stoichiometric amounts of starting materials, which account for the excess oxygen, could result in more crystalline samples. Sealed tube synthesis of oxygen inserted schafarzikite samples with different 2+ and 3+ cations in the octahedral chains could be another way of making these types of materials. This was attempted in this work with Al^{3+} and Ga^{3+} but no change was seen in the unit cell parameters to indicate that the samples had successfully formed. The collection of NPD data for more samples of $FeSb_{2-x}Pb_xO_{4+y}$ would also be interesting to determine how much oxygen is being taken up and how it is incorporated into the structure for different compositions.

For the pyrochlore materials in Chapter 6, the incorporation of small transition metal ions on the A-sites to stabilise materials with large cations on this site, such as the lanthanide pyrochlores, could be further investigated. In Chapter 7 the elimination of

impurity phases in the samples RE_2CrSbO_7 would be desirable to confirm whether the higher temperature magnetic transition observed in the susceptibility data arises from $RECrO_3$ impurities. Further NPD measurements for the sample Y_2CrSbO_7 would confirm whether this material orders magnetically and, if so, allow the low-temperature Cr^{3+} magnetic ordering to be studied in the absence of large magnetic lanthanide moments. The possible magnetic ordering in the materials Er_2CrSbO_7 and Tb_2CrSbO_7 has also not been confirmed. Performing magnetisation against field measurements at various temperatures could allow transition temperatures to be determined for these samples and for Y_2CrSbO_7, and NPD measurements would allow the magnetic structures to be studied. NPD measurements could also be performed for the samples in the series $Ho_2Cr_{1-x}Fe_xSbO_7$ to study the low temperature ordering and more samples with intermediate values of x could be prepared to study the loss in magnetic ordering with increasing Fe^{3+} content.

8.3 References

1. M. D. Sundararajan, A. Narayanasamy, T. Nagarajan, G. V. Subba Rao, A. K. Singh and L. Häggström, *Solid State Commun.*, 1983, **48**, 657.

2. P. F. Bongers and E. R. Van Meurs, *J. Appl. Phys.*, 1967, **38**, 944.

3. B. P. de Laune and C. Greaves, *J. Solid State Chem.*, 2012, **187**, 225.

List of Publications Arising from this Thesis

. " The synthesis, structure, magnetic and electrical properties of $FeSb_{2-x}Pb_xO_4$"

M. J. Whitaker, R. D. Bayliss, F. J. Berry and C. Greaves

J. Mater. Chem., 2011, **21**, 14523

. " Magnetic Interaction in Ferrous Antimonite, $FeSb_2O_4$, and Some Derivatives"

R. D. Bayliss, F. J. Berry, B. P. de Laune, C. Greaves, Ö. Helgason, J. F. Marco, M. F. Thomas, L. Vergara and M. J. Whitaker

J. Phys.: Condens. Matter, 2012, **24**, 276001

3. "Structural and Magnetic Characterisation of the Pyrochlores $Bi_{2-x}Fe_x(FeSb)O_7$ (x = 0.1, 0.2, 0.3), $Nd_{1.8}Fe_{0.2}(FeSb)O_7$ and $Pr_2(FeSb)O_7$"

M. J. Whitaker, J. F. Marco, F. J. Berry, C. R. Raith, E. Blackburn and C. Greaves

J. Solid State Chem., 2013, **198**, 316

4. "Magnetic Properties of the Rare Earth Pyrochlores RE_2CrSbO_7"

M. J. Whitaker, V. Pomjakushin, E. Blackburn, M. Long and C. Greaves

In preparation

5. "Crystal Structure and Magnetic Properties of Chemically Modified Schafarzikites Containing Excess Oxygen"

C. Greaves, B. P. de Laune, M. J. Whitaker and F. J. Berry

In preparation

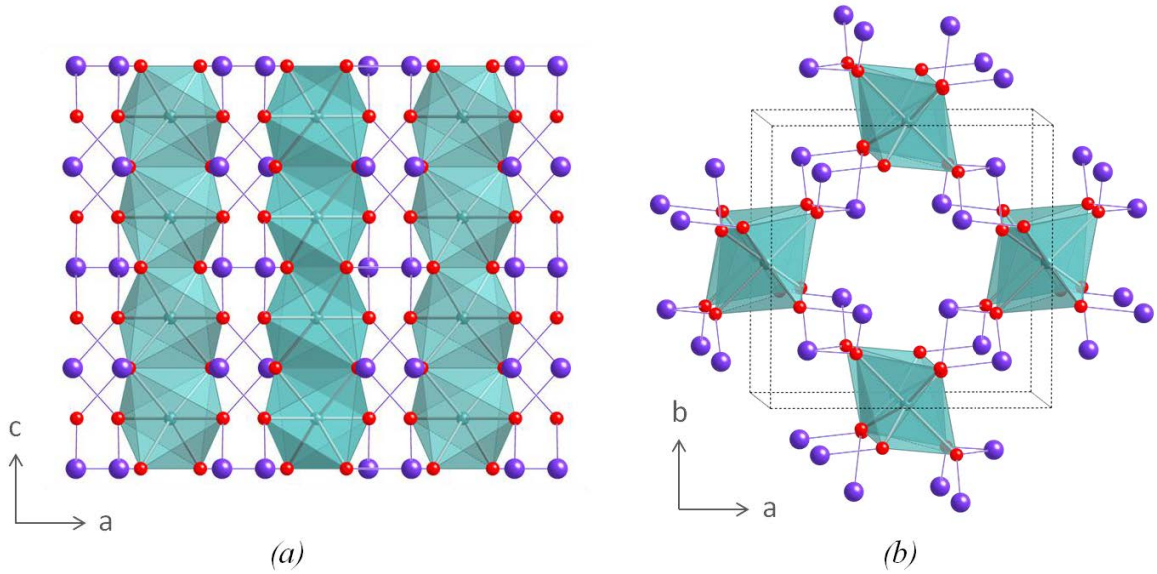

***Fig. 1.1**: The structure of schafarzikite, $FeSb_2O_4$ (a) showing the edge-linked chains and (b) looking down the c-axis. FeO_6 octahedra are shaded. Fe ions are located within the octahedra, O ions are shown as red spheres and Sb ions are shown as purple spheres.*

The schafarzikite structure is interesting for many reasons and one of these is its relationship to the rutile structure. The rutile structure (Fig. 1.2) has an MO_2 stoichiometry and the same edge-linking chains of MO_6 octahedra along the *c*-axis that are found in schafarzikite. However in the schafarzikite structure these chains are separated and linked by cations in pyramidal sites. The presence of a significantly different second cation that will not mix with the M cations in the octahedral chains could potentially provide a way of controlling the M oxidation state in the chains which is not possible in the rutile structure. Therefore structural modifications by cation substitution at the pyramidal site could be made for the schafarzikite materials to alter the properties as has been done for perovskites. Other interesting features arise due to the separation of the chains. The intrachain Fe-Fe distance (2.96 Å) is much shorter than the nearest Fe-Fe distance within the layers perpendicular to the chains (6.07 Å) suggesting that some one-dimensional character could be expected in schafarzikite. Low dimensional materials are of interest for electronic devices because they can have new and unusual electronic and magnetic properties which are anisotropic.

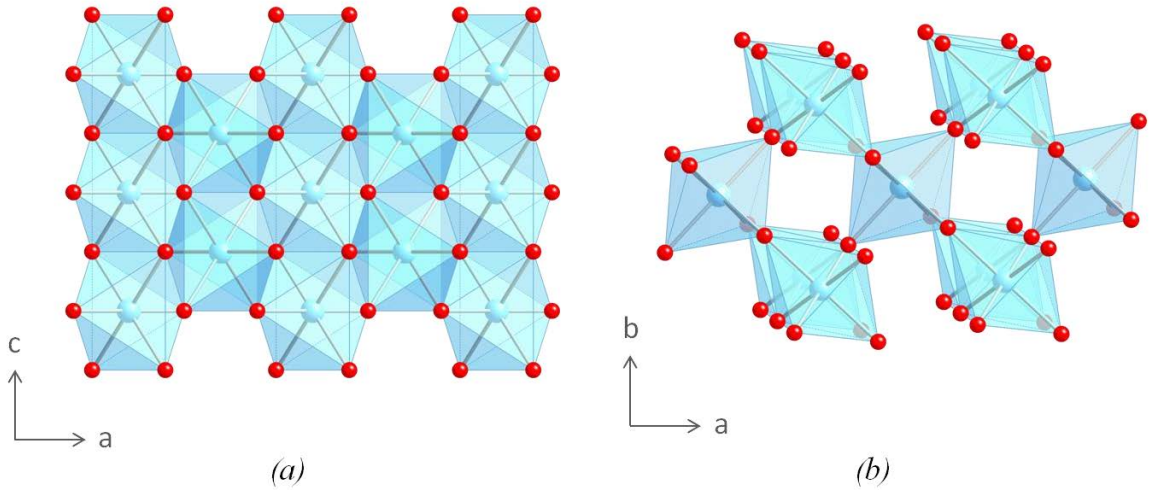

***Fig. 1.2**: The rutile, MO_2, structure (a) showing the edge-linked chains and (b) looking down the c-axis. MO_6 octahedra are shaded, M ions are located within the octahedra and O ions are shown as red spheres.*

The separation of the chains in schafarzikite also gives rise to channels within the structure along the *c*-axis. Insertion of ions into these channels to give mixed oxidation state materials may also be possible. Modifications of the schafarzikite structure in this way have not been studied before. There is only one previous report exploring substitutions on the pyramidal site;[5] this was for the material $MnSb_2O_4$ which was unsuccessful and is discussed further in Section 3.1.1.

1.2.1.1 Orthorhombic Distortion in Pb_3O_4

As mentioned previously the MX_2O_4 schafarzikites are isostructural with Pb_3O_4, which has Pb^{4+} ions within the octahedral chains and Pb^{2+} ions on the pyramidal sites. Pb_3O_4 is tetragonal at room temperature but undergoes a tetragonal to orthorhombic transition at 170 K[6-7]. The tetragonal structure has space group $P4_2/mbc$ and unit cell parameters a = 8.811(5) Å and c = 6.563(3) Å,[6] and the orthorhombic structure has space group *Pbam* (no. 55) and unit cell parameters a = 9.124(1) Å, b = 8.467(1) Å and c = 6.5667(5) Å[7]. So far no similar transitions have been observed for any other MX_2O_4 schafarzikite materials[3]. The structure of the similar compound $SnPb_2O_4$ was studied at various temperatures using X-ray and neutron diffraction.[2] No phase transition was seen

but both tetragonal and orthorhombic structures were reported at each temperature, the latter only having small differences in the *a*- and *b*-parameters.

1.2.2 Pyrochlore

The term pyrochlore refers to a family of mixed oxides isostructural with the mineral pyrochlore, $NaCaNb_2O_6F$. The general formula is $A_2B_2O_7$ (or $A_2B_2O_6O'$ to distinguish between the two crystallographically different O1 and O2 sites) where A is a larger 8-coordinate cation and B is a smaller 6-coordinate cation. The structure is shown in Fig 1.3. There are various different ways of describing the pyrochlore structure and two examples are given here: it can be described as two interlinking networks of BO_6 octahedra and A_2O' chains or as an oxygen-deficient fluorite superstructure. Pyrochlores have cubic symmetry with space group *Fd*-3*m* (no. 227) and unit cell *a*-parameter between 10-11 Å.[8]

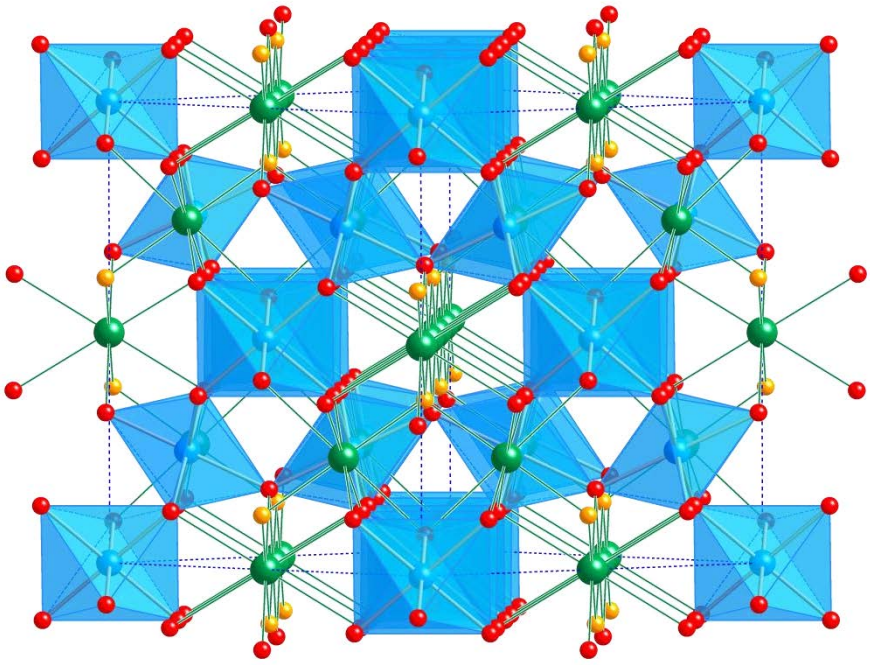

***Fig. 1.3**: The pyrochlore $A_2B_2O_7$ structure: A-cations are shown in green, BO_6 octahedra are shaded, O1 anions are shown in red and O2 anions are shown in orange.*

The atomic positions for the pyrochlore structure are given in Table 1.2, the only variable positional parameter in the structure is the O1 *x*-value which falls between 0.319 and 0.343[9]. There are different possible choices of origin for the pyrochlore structure but most commonly the B-cation is chosen and this is used as the origin throughout this work.

***Table 1.2**: Atomic positions for the pyrochlore $A_2B_2O_7$ structure in Fd-3m (origin at the B-site)*

	Wyckoff Position	*x*	*y*	*z*
A	16*d*	½	½	½
B	16*c*	0	0	0
O1	48*f*	*x*	⅛	⅛
O2	8*b*	⅜	⅜	⅜

The geometry around the A-cations is described as scalenohedral rather than cubic because the A-ion forms six longer A-O1 bonds and two shorter A-O2 bonds (Fig. 1.4a). The B-ion forms six equal B-O1 bonds and although the BO_6 units will be referred to as octahedra they are distorted and therefore are in fact trigonal antiprisms (Fig. 1.4b).

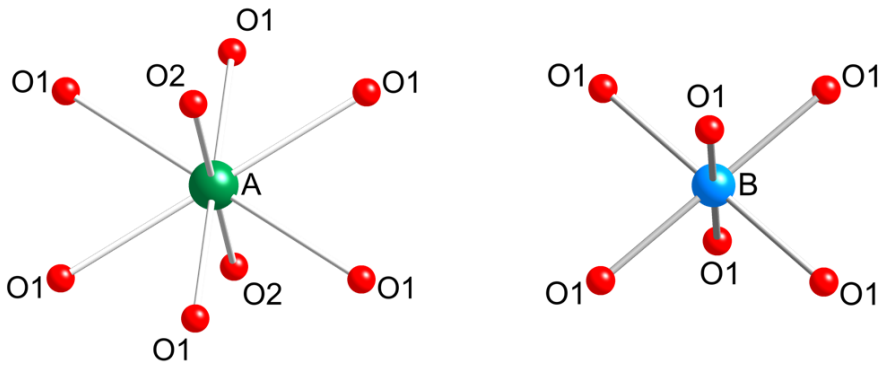

(a) *(b)*

***Fig. 1.4**: Coordination environment around cations in the pyrochlore structure showing (a) the 8-coordinate A-ion and (b) the 6-coordinate B-ion.*

Mixed metal oxides with the pyrochlore structure are well studied and of great interest because of their susceptibility to chemical modifications. Pyrochlores can be substituted at the A-, B- and O-sites and can tolerate vacancies at the A and O2 sites giving

octahedral Fe^{2+} and Fe^{3+} ions are aligned parallel to one another but antiparallel to the tetrahedral Fe^{3+} ions so the moments therefore do not cancel out and an increase is observed in the susceptibility. Another type of ordering that gives rise to an increased susceptibility at the ordering temperature is canted antiferromagnetism (Fig. 1.6d). The moments are aligned antiferromagnetically but do not cancel out as they are all slightly tilted in one direction causing there to be an overall magnetic moment.

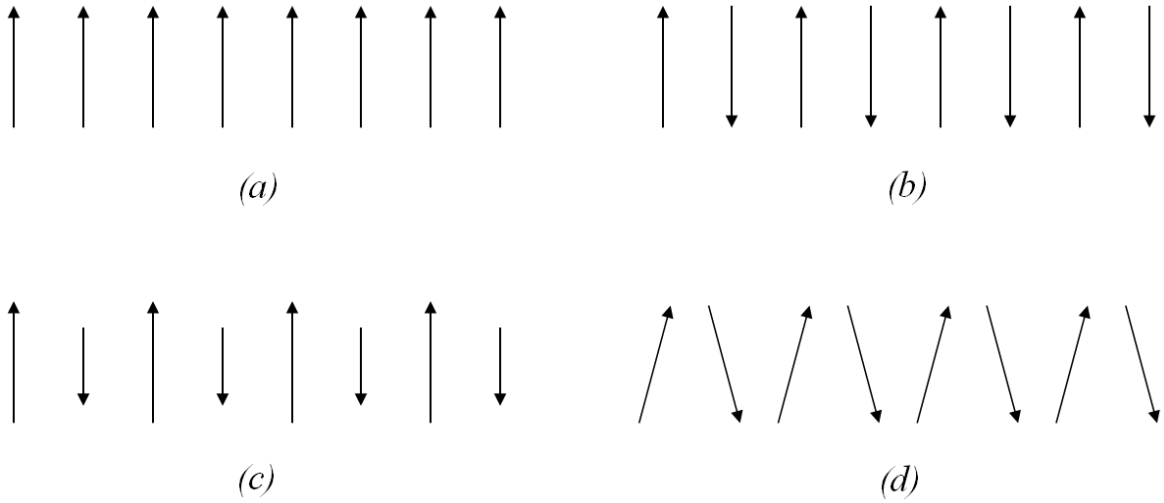

Fig. 1.6*: Diagrams to represent different types of magnetic ordering showing (a) ferromagnetism, (b) antiferromagnetism, (c) ferrimagnetism and (d) canted antiferromagnetism.*

The Curie law is modified to take into account the interactions between magnetic moments to give the Curie-Weiss law:

$$\chi = \frac{C}{T - \theta} \tag{1.6}$$

Plots of inverse susceptibility against temperature that follow the Curie-Weiss law are linear in the high temperature paramagnetic region then a deviation is seen at the ordering temperature. The plot (Fig. 1.7) can be used to calculate magnetic moments and to obtain the Weiss temperature, θ, the sign of which indicates whether the interactions

occurring in the material are ferromagnetic (positive value of θ) or antiferromagnetic (negative value of θ).

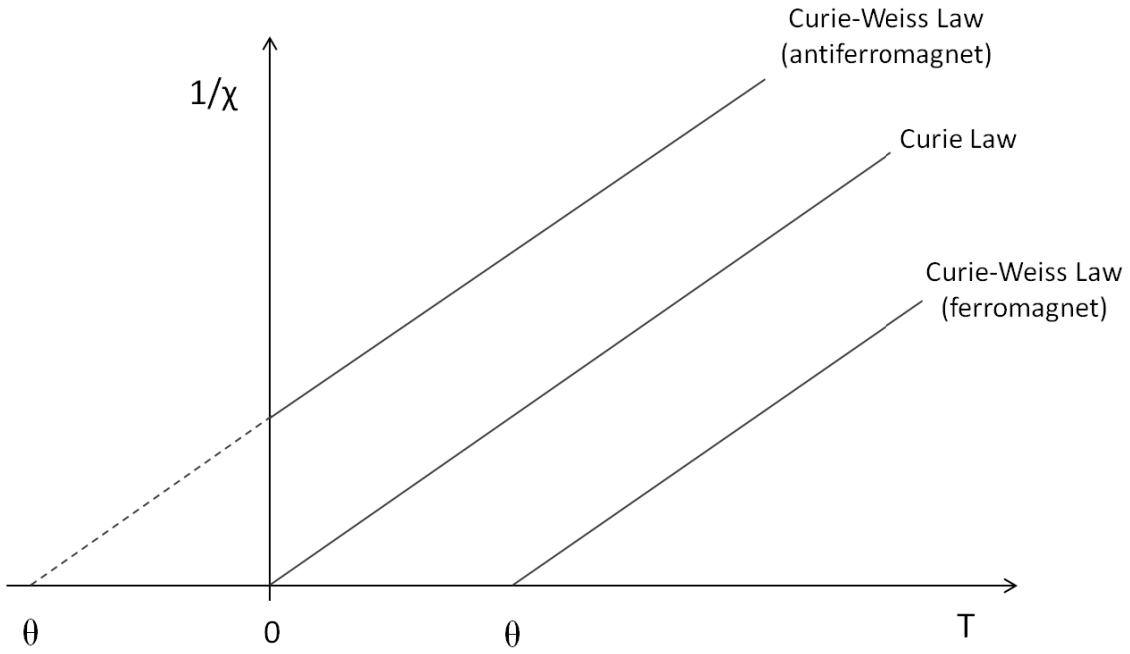

Fig. 1.7*: Plot of inverse susceptibility against temperature showing the Curie law for paramagnetic materials and the Curie-Weiss law for ferromagnetic and antiferromagnetic materials.*

1.5.1 Superexchange

To rationalise the ways in which magnetic materials order, the interactions between magnetic ions need to be considered. Magnetic ions in metal-oxide materials can either interact directly if they are close enough, for example in face- or edge-sharing chains, or indirectly through the oxide ions. The interaction through oxide ions is known as superexchange where virtual electron transfer occurs between the metal *d*-orbitals and oxygen 2*p* orbitals.[30-33] The type of ordering resulting from superexchange interactions depends on the geometry of the ions and the electron configuration of the metal ions. Various types of magnetic superexchange interactions are shown in Fig. 1.8.

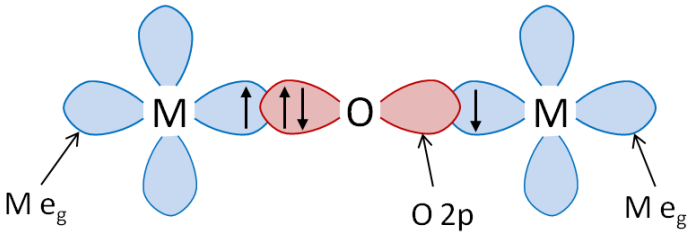

(a)

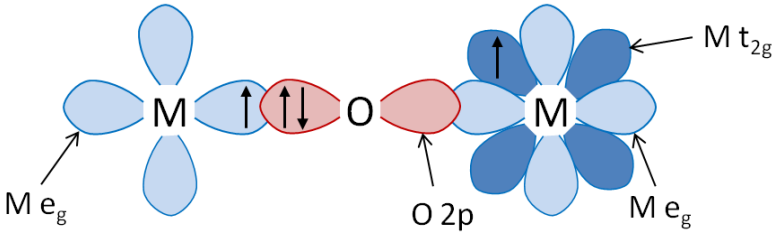

(b)

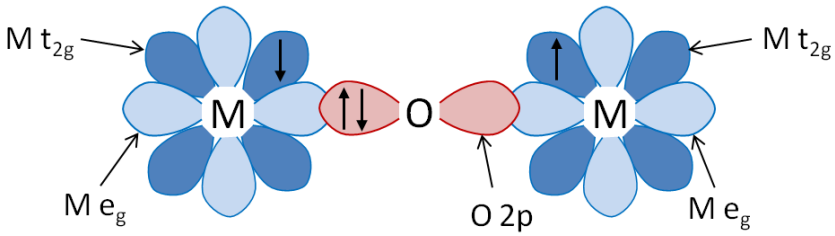

(c)

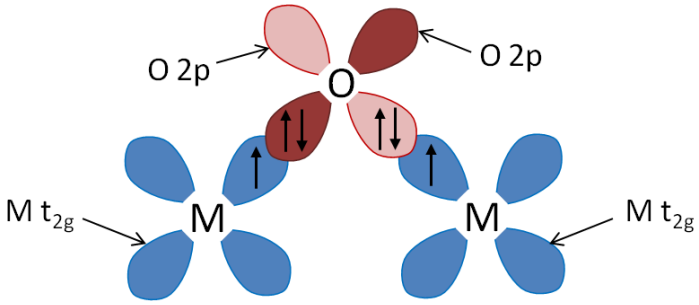

(d)

***Fig. 1.8**: Magnetic superexchange diagrams showing: (a) 180 ° AFM e_g-2p-e_g superexchange, (b) 180 ° FM e_g-2p-t_{2g} superexchange (c) 180 ° AFM t_{2g}-2p-t_{2g} superexchange and (d) 90 ° FM t_{2g}-2p-2p-t_{2g} superexchange.*

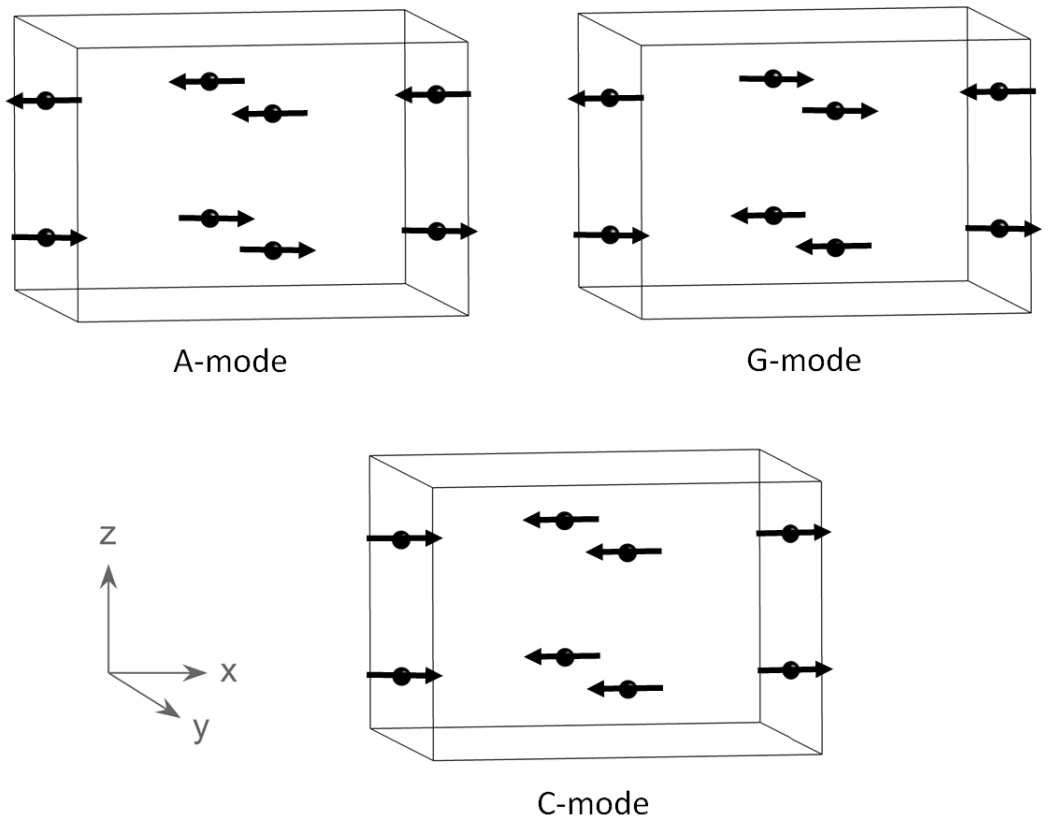

***Fig 1.9**: The three antiferromagnetic modes for MX_2O_4 structures. The magnetic moments are shown here to be aligned along the x-axis.*

$MnSb_2O_4$ also exhibits A-type antiferromagnetic order with a Néel temperature of around 60 K[35-36]. The moments are collinear and lie in the *ab* plane. $NiSb_2O_4$ orders antiferromagnetically at approximately 46 K[35-36], the moments are collinear and are aligned primarily along the *c*-axis. Unlike $FeSb_2O_4$ and $MnSb_2O_4$ the ordering is C-type (Fig. 1.9). In a C-type magnetic structure the moments are aligned parallel within the chains along the *c*-axis and antiparallel within the layers. In the final antiferromagnetic mode, the G-mode (Fig 1.9), the moments are aligned antiparallel in both the chains and the layers.

The differences in magnetic ordering can be rationalised by considering how the transition metal cations interact with one another. The magnetic ions within a chain can interact by direct cation-cation exchange (Fig 1.10a) and through 90º M-O-M

superexchange interactions (Fig 1.10b). Within a layer the ions interact through much weaker M-O-Sb-O-M links, giving long range magnetic order.

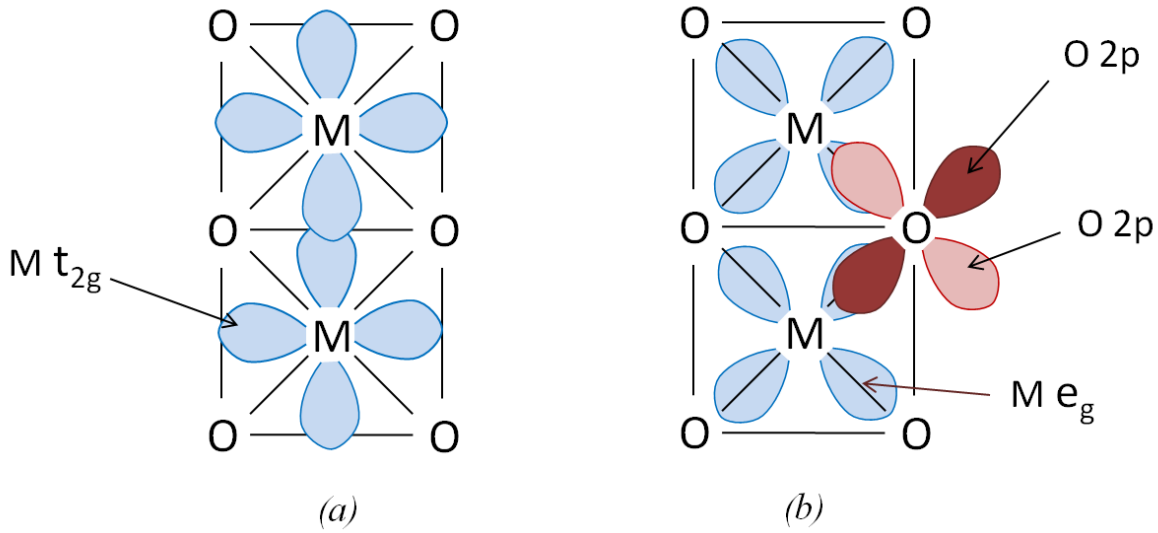

***Fig. 1.10**: Mechanisms of magnetic exchange throughout the chains of MO_6 octahedra. Magnetic moments on adjacent ions in a chain can interact by (a) direct cation-cation exchange and (b) 90° superexchange interactions.*

As the octahedra in the chains share edges, the t_{2g} orbitals on neighbouring transition metal ions point directly towards each other and overlap (Fig. 1.10a). If the unpaired electrons between the two cation centres are arranged antiferromagnetically, this will maximise the electronic charge in this region and stabilise the bonding[39]. This exchange mechanism competes with the 90º superexchange interaction which favours ferromagnetic ordering (Section 1.5.1). In $MnSb_2O_4$ and $FeSb_2O_4$ the Mn^{2+} (d^5) and Fe^{2+} (d^6) t_{2g} orbitals are partially filled and antiferromagnetic coupling is observed throughout the octahedral chains which is consistent with direct exchange occurring between adjacent ions. In $NiSb_2O_4$ the Ni^{2+} (d^8) t_{2g} orbitals are completely filled and therefore there is no direct exchange occurring and the ordering seen within the chains is ferromagnetic, as predicted by the superexchange interactions.

This type of direct exchange is also seen for the related compound $MnPb_2O_4$.[40] $MnPb_2O_4$ has a slightly different structure from $FeSb_2O_4$: it is tetragonal with space group $P\bar{4}2_1c$ (no. 114) and the MnO_6 octahedra form zigzag chains along the *c*-axis which are linked by Pb^{2+} ions in pyramidal sites (Fig 1.11)[41]. It is an interesting material because it is piezoelectric and also has magnetic properties. The moments on the Mn^{4+} ions order antiferromagnetically below $T_N = 18$ K[40]; the moments align antiparallel both within the chains and within the layers perpendicular to the chains. The octahedra share edges and antiferromagnetic ordering within the chains would be expected for Mn^{4+} as it has a d^3 configuration and therefore three unpaired electrons in the t_{2g} orbitals.

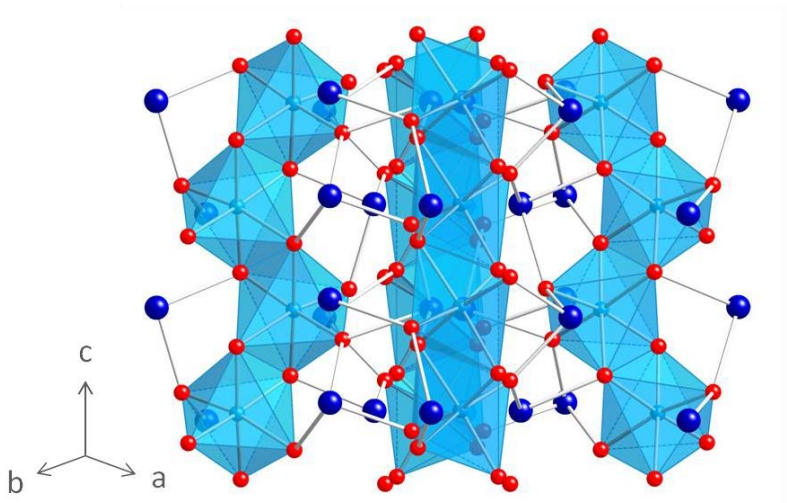

***Fig. 1.11**: The structure of $MnPb_2O_4$. MnO_6 octahedra are shaded. Mn ions are located within the octahedra, O ions are shown as red spheres and Pb ions are shown as dark blue spheres.*

1.5.3 Magnetic Properties of Pyrochlores

As mentioned in Section 1.2.2 there are many different ways of describing the pyrochlore structure. It is useful when looking at magnetic properties to view the structure as two sublattices of A_4 and B_4 corner-sharing tetrahedra (Fig. 1.12). If these sites are occupied by magnetic ions the tetrahedral relationship can cause them to be frustrated giving unusual magnetic properties.

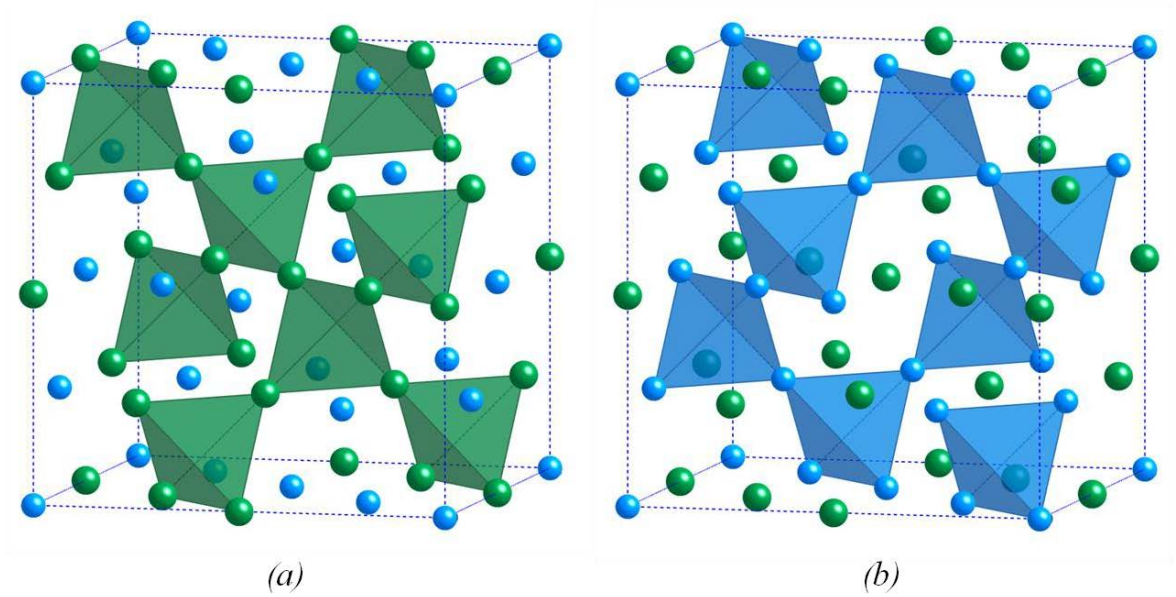

***Fig. 1.12**: The pyrochlore structure showing the A- and B-cations only. The tetrahedral arrangement of (a) A-cations (green) and (b) B-cations (blue) is shown.*

Triangles and tetrahedra of magnetic atoms are described as frustrated because they cannot form an antiferromagnetic ground state. It can be seen from Fig. 1.13 that it is impossible for all the nearest neighbour interactions to be antiferromagnetic. There are therefore competing antiferromagnetic and ferromagnetic interactions and no single lowest energy ground state.

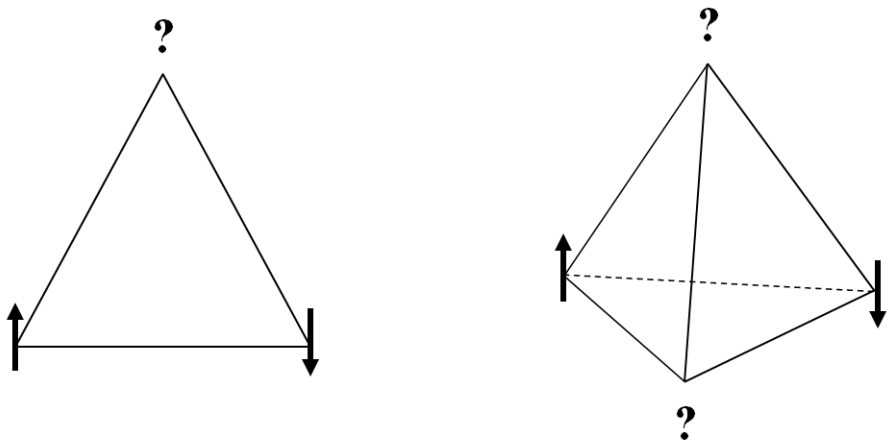

***Fig. 1.13**: Geometric frustration shown by antiferromagnetic arrangement of spins on a triangle and on a tetrahedron.*

Although magnetic pyrochlore materials are highly geometrically frustrated there are still some materials which exhibit long-range magnetic ordering at low temperatures[12]. Some examples of this are the material $Er_2Ti_2O_7$ which orders below T_N = 1.173 K to an antiferromagnetic state where the moments are perpendicular to the ⟨111⟩ axes[42], the material $Gd_2Sn_2O_7$ in which the Gd^{3+} moments are aligned parallel to the edges of the tetrahedron below a Néel temperature of around 1 K[43] and the material $Tb_2Sn_2O_7$ which displays magnetic ordering below 0.87 K with both ferromagnetic and antiferromagnetic character[44]. Other interesting magnetic pyrochlores are those which contain magnetic ions on both the A and B sites of the structure, such as $A_2Ru_2O_7$ (where A = rare earth), as they can interact with one another influencing the magnetic properties. In the material $Er_2Ru_2O_7$ both the Ru^{4+} and Er^{3+} moments order magnetically at temperatures of 90 K and 10 K respectively and the moments are arranged antiferromagnetically along the ⟨110⟩ directions[45]. The rare-earth ions in the pyrochlore structure will often only order at very low temperatures of around 1 K or lower, as seen for the materials mentioned above, and it was suggested that the increased ordering temperature of the Er^{3+} moments in $Er_2Ru_2O_7$ is due to the interaction with Ru^{4+} moments[45].

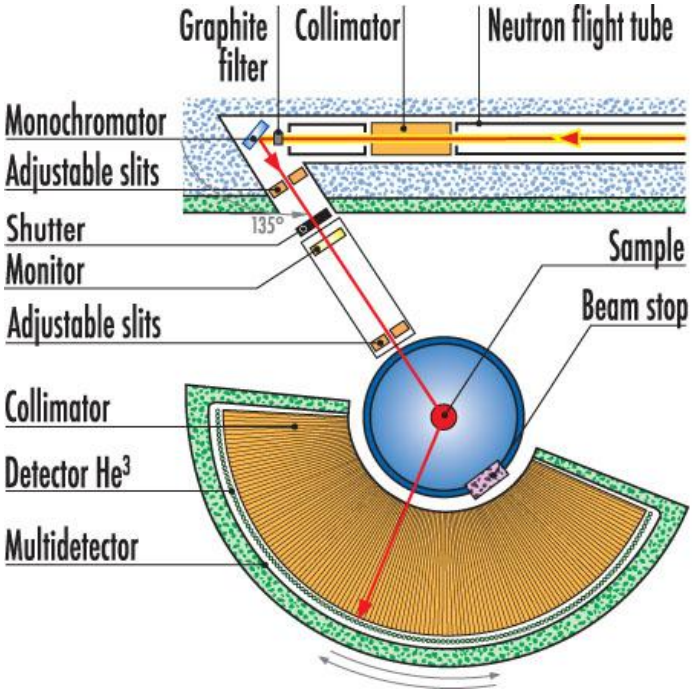

***Fig. 2.1**: Diagram of D2B instrument layout.*[5]

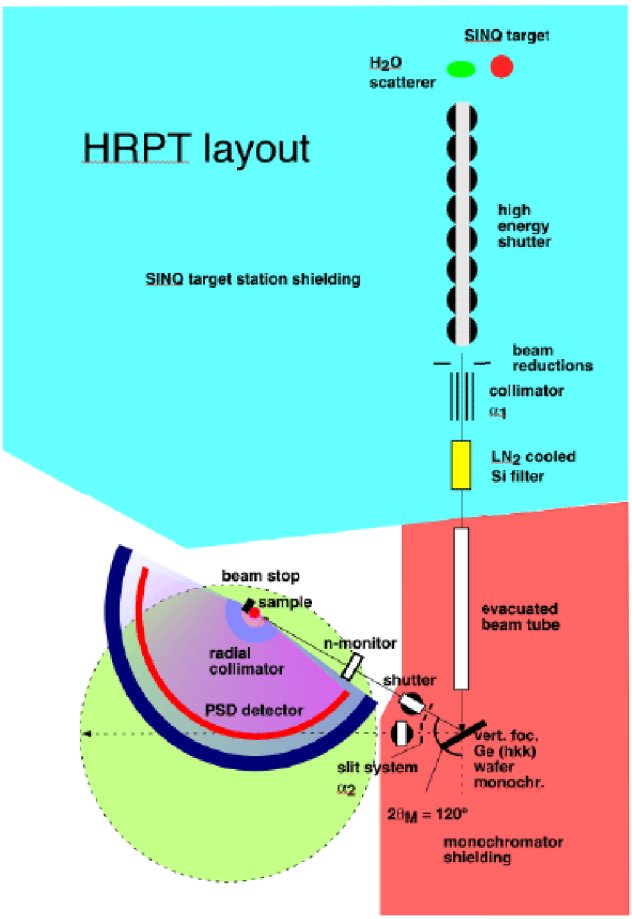

***Fig. 2.2**: Diagram of HRPT instrument layout.*[6]

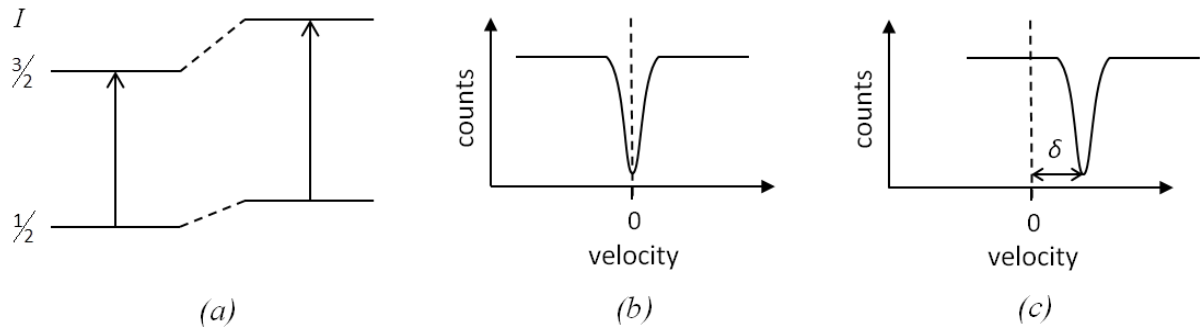

***Fig. 2.3**: (a) Modification of ^{57}Fe nuclear energy levels by chemical isomer shift and the transition that occurs, (b) Mössbauer spectrum with sample and source in the same environment and (c) the effect of chemical isomer shift on the Mössbauer spectrum.*

The quadrupole splitting, Δ, is seen if a nucleus has a nuclear spin quantum number, $I > ½$ as it will have a non-spherical charge distribution and a nuclear quadrupole moment. If an asymmetric electric field is present, from an asymmetric arrangement of electrons or surrounding atoms, the nuclear quadrupole moment will interact with it causing the nuclear energy levels to split. This results in splitting of absorption lines in the Mössbauer spectrum by an amount, Δ, and gives information about bonding and local structure. For ^{57}Fe a two-line spectrum is seen as the excited state splits into two substates giving rise to two possible transitions (Fig. 2.4). High spin Fe^{2+} has a larger quadrupole splitting than high spin Fe^{3+} as Fe^{2+} has an asymmetric d^6 configuration whereas Fe^{3+} has a symmetric d^5 configuration.

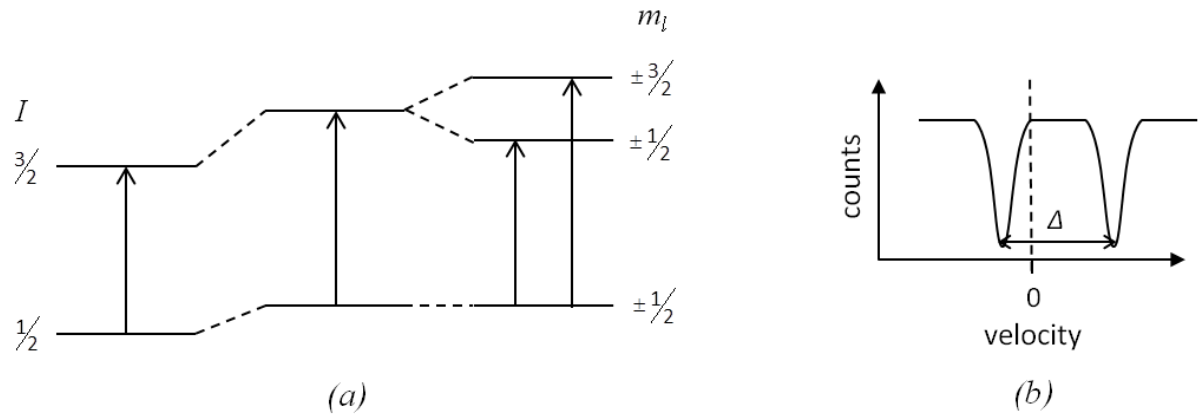

***Fig. 2.4**: (a) The effect of quadrupole splitting on the nuclear energy levels of ^{57}Fe and the transitions that occur and (b) the resultant Mössbauer spectrum.*

The magnetic hyperfine splitting is observed because nuclei with spin, $I > 0$ interact with magnetic fields via a magnetic dipole interaction. This interaction splits the absorption lines in the Mössbauer spectrum as it removes the degeneracy of the nuclear energy levels causing them to split into $2I + 1$ substates. The magnetic hyperfine field at the nucleus is caused by the spin of unpaired electrons therefore the magnetic splitting gives information about electronic structure and magnetic properties. In ^{57}Fe the ground state splits into two substates and the excited state splits into four substates resulting in six possible transitions and a six line spectrum due to selection rules (Fig. 2.5).

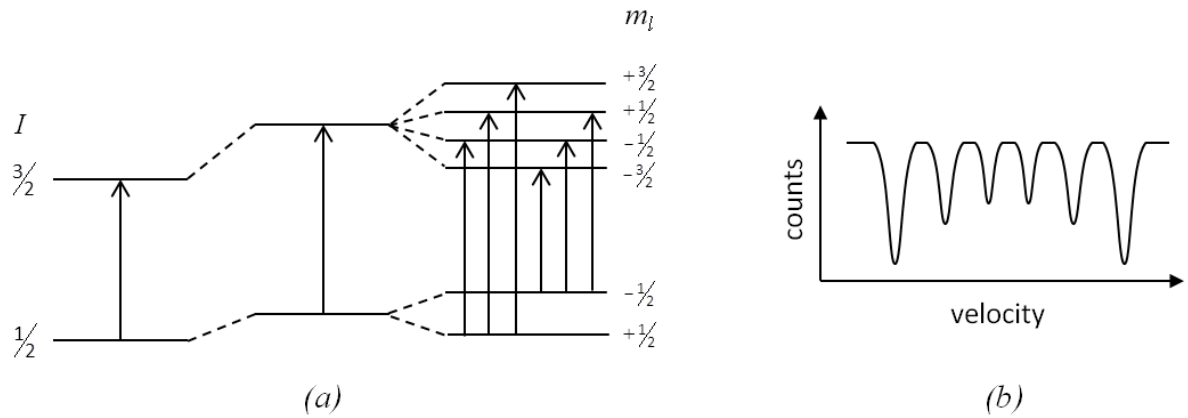

***Fig. 2.5**: (a) The effect of magnetic splitting on the nuclear energy levels of ^{57}Fe and the transitions that occur, (b) the resultant Mössbauer spectrum.*

2.7 Thermogravimetric Analysis

Thermogravimetric analysis (TGA) is used to measure precise changes in the mass of a sample as a function of temperature or time. The sample is heated at a constant rate in a controlled atmosphere under the flow of a gas such as nitrogen, oxygen or hydrogen. A decrease in mass may be seen if the sample decomposes or if volatiles are lost, which can be measured by linking the thermogravimetric analyser to a mass spectrometer; however if the sample becomes oxidised or adsorbs gas molecules an increase in mass is observed.

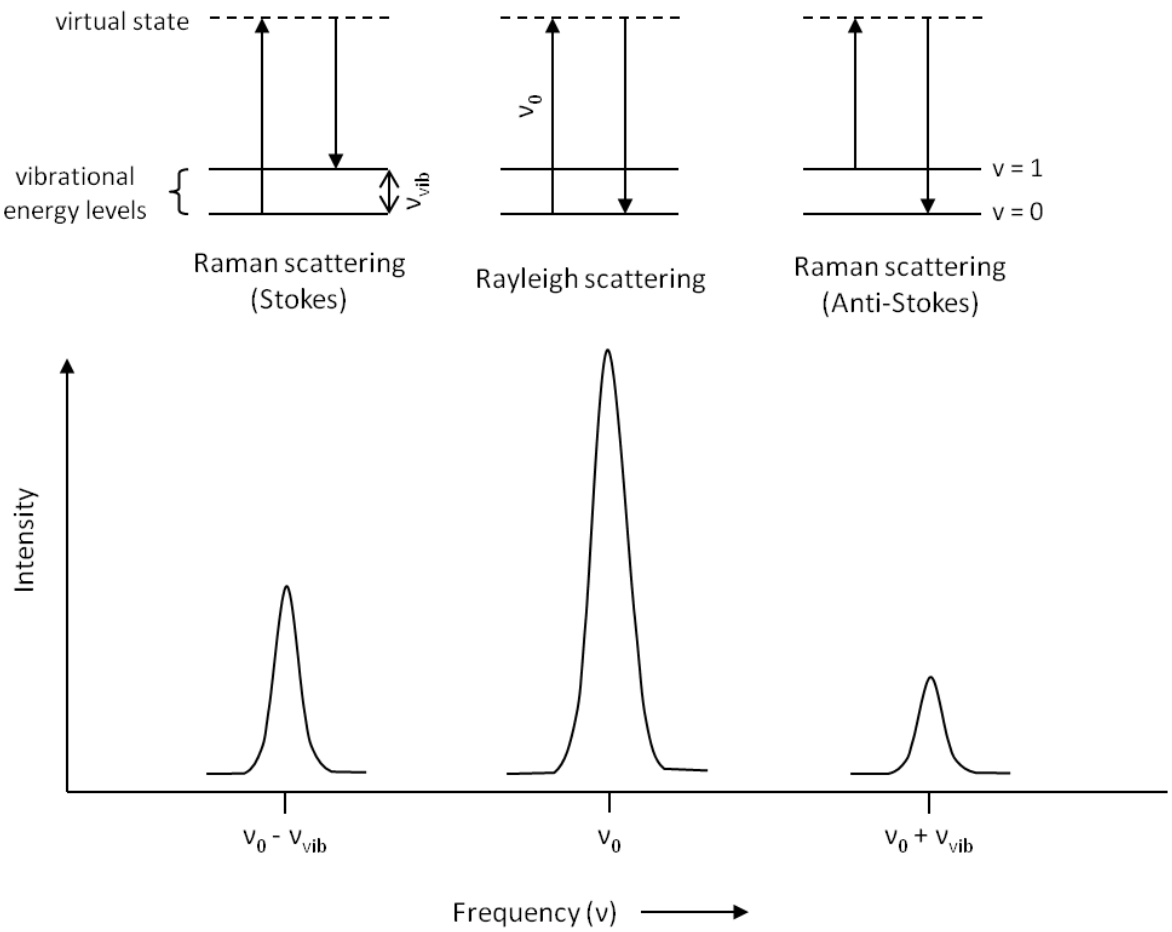

***Fig. 2.6**: Diagram showing the different scattering processes that can occur and the resultant spectrum.*

3 Lead-Substituted Schafarzikites, $FeSb_{2-x}Pb_xO_4$

3.1 Background

The structure of $FeSb_2O_4$ was described in detail in Section 1.2.1 and is shown in Fig. 3.1. Schafarzikite belongs to a family of compounds isostructural with red lead, Pb_3O_4, which have the general formula MX_2O_4 where M = Pb^{4+}, Sn^{4+} and X = Pb^{2+} or M = Mn^{2+}, Fe^{2+}, Co^{2+}, Ni^{2+}, Cu^{2+}, Zn^{2+}, Mg^{2+} and X = Sb^{3+}, As^{3+}.[1-3]

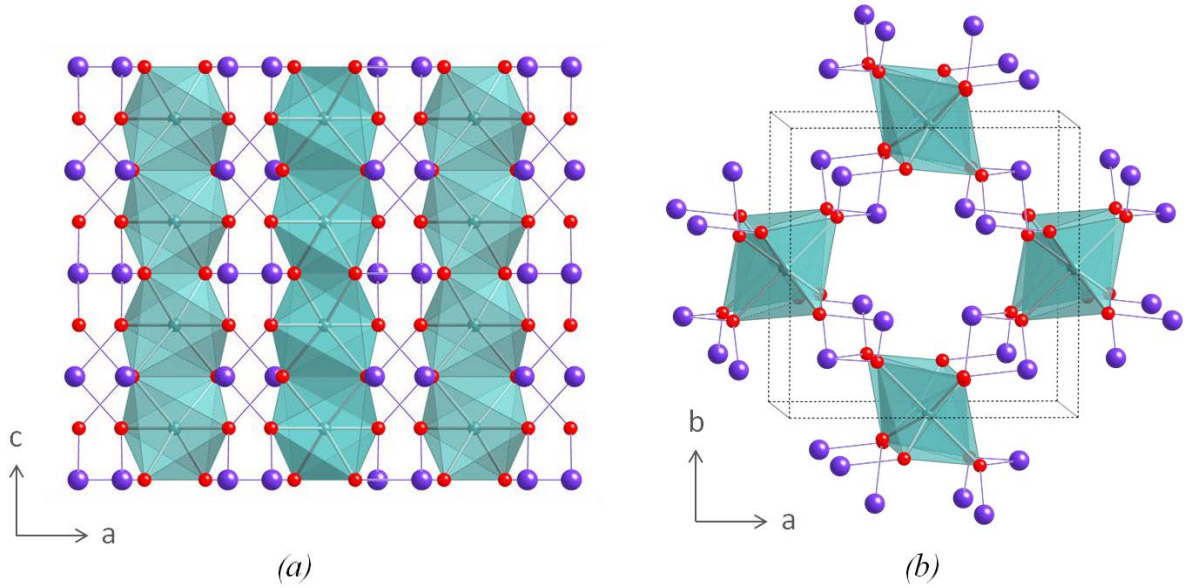

Fig. 3.1*: The structure of schafarzikite, $FeSb_2O_4$ (a) showing the edge-linked chains and (b) looking down the c-axis. FeO_6 octahedra are shaded. Fe ions are located within the octahedra, O ions are shown as red spheres and Sb ions are shown as purple spheres.*

3.1.1 Cation Substitution in the Schafarzikite Structure

Due to the chemical similarities of Sb^{3+} and Pb^{2+} in the MX_2O_4 schafarzikites, chemical modification of the structure may be possible by substituting Pb^{2+} for Sb^{3+} with consequential oxidation of transition metal cations. So far there has only been one report of lead substitution in MX_2O_4 structures, for the compound $MnSb_2O_4$, but this resulted in oxidation of Sb^{3+}, rather than Mn^{2+}, ions[4]. The Pb^{2+} ions replaced Sb^{3+} ions on the pyramidal sites and to compensate for the loss of charge, Sb^{3+} ions were oxidised to Sb^{5+} ions. The Sb^{5+} ions then replaced Mn^{2+} ions in the octahedral chains to give multi-phase

more Fe^{3+} than Fe^{2+} (Fe^{3+}:Fe^{2+} ≈ 2:1) which suggested that there was a deficiency of either lead or antimony in the sample. As antimony oxide is fairly volatile it was assumed to be the latter and the formation of a schafarzikite with antimony vacancies, $FeSb_{2-x}O_4$, was attempted. This was unsuccessful and instead $FeSb_2O_4$ was formed with Fe_3O_4 and other small impurities. The lead substituted samples were remade using a small excess of Sb_2O_3 to compensate for the loss and ^{57}Fe Mössbauer spectroscopy measurements were retaken. The ^{57}Fe Mössbauer spectrum of $FeSb_{1.5}Pb_{0.5}O_4$ recorded at 298 K is shown in Fig. 3.3 and is best fit to two quadrupole split absorptions. The first doublet has a chemical isomer shift, δ, of 0.49(2) mm s^{-1} and quadrupole splitting, Δ, of 0.87(4) mm s^{-1}; it is characteristic of Fe^{3+} and accounts for 58 % of the spectral area. The second doublet has δ = 1.01(2) mm s^{-1} and Δ = 1.74(4) mm s^{-1}; it is characteristic of Fe^{2+} and accounts for 42 % of the spectral area. Within the errors (±5 %) the result is indicative of nearly equal amounts of iron in each oxidation state and is consistent the composition $FeSb_{1.5}Pb_{0.5}O_4$. The ^{57}Fe Mössbauer spectrum of $FeSb_2O_4$ is reported in the literature.[5]

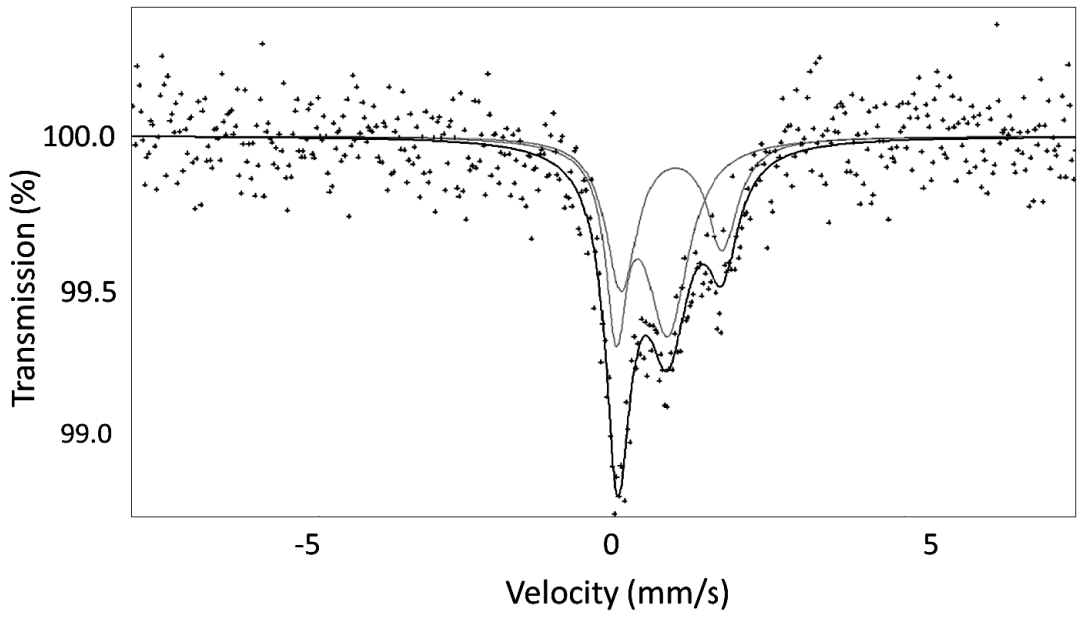

***Fig. 3.3**: ^{57}Fe Mössbauer spectrum recorded from $FeSb_{1.5}Pb_{0.5}O_4$ at 298 K.*

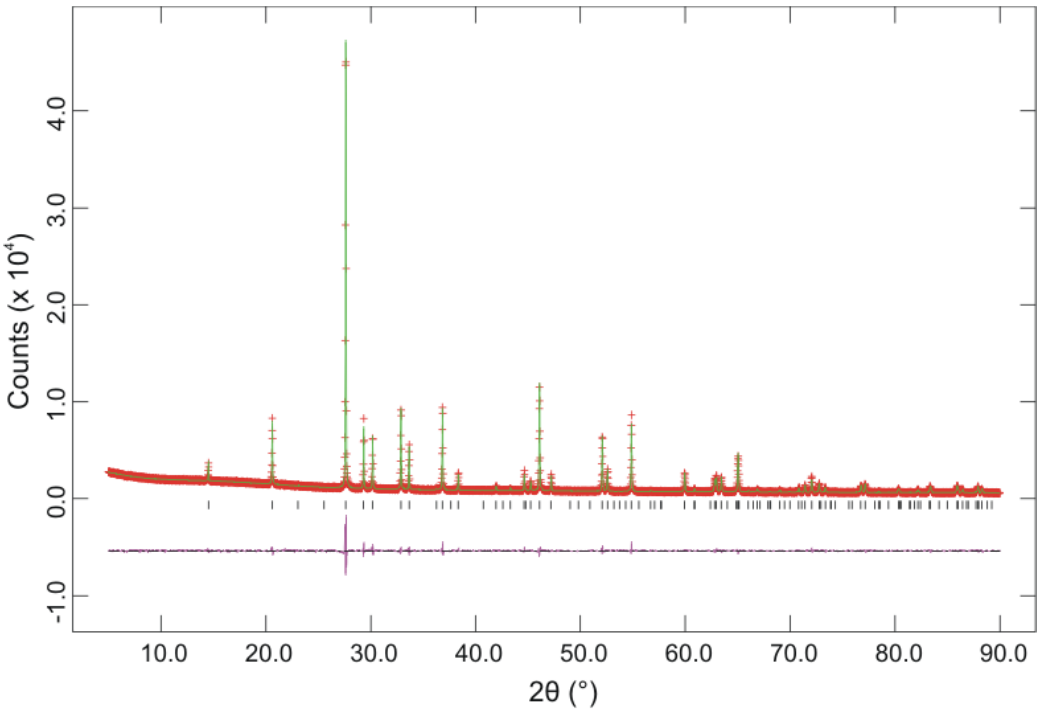

(a)

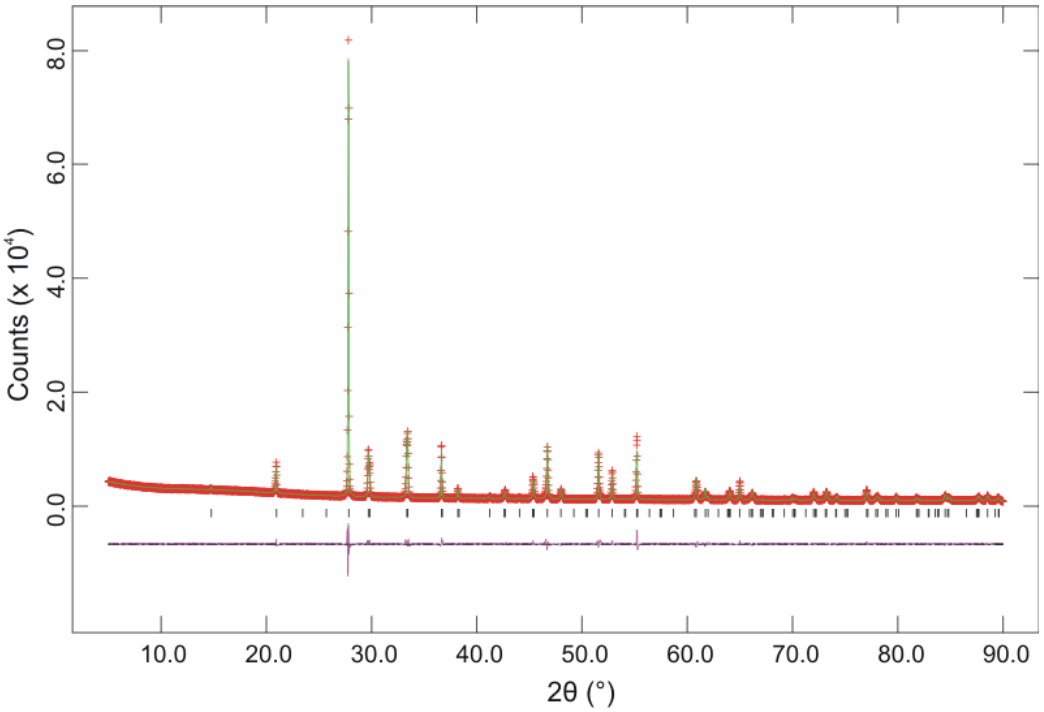

(b)

***Fig. 3.4**: Observed, calculated and difference plots for room temperature XRPD data recorded from (a) $FeSb_2O_4$ and (b) $FeSb_{1.5}Pb_{0.5}O_4$.*

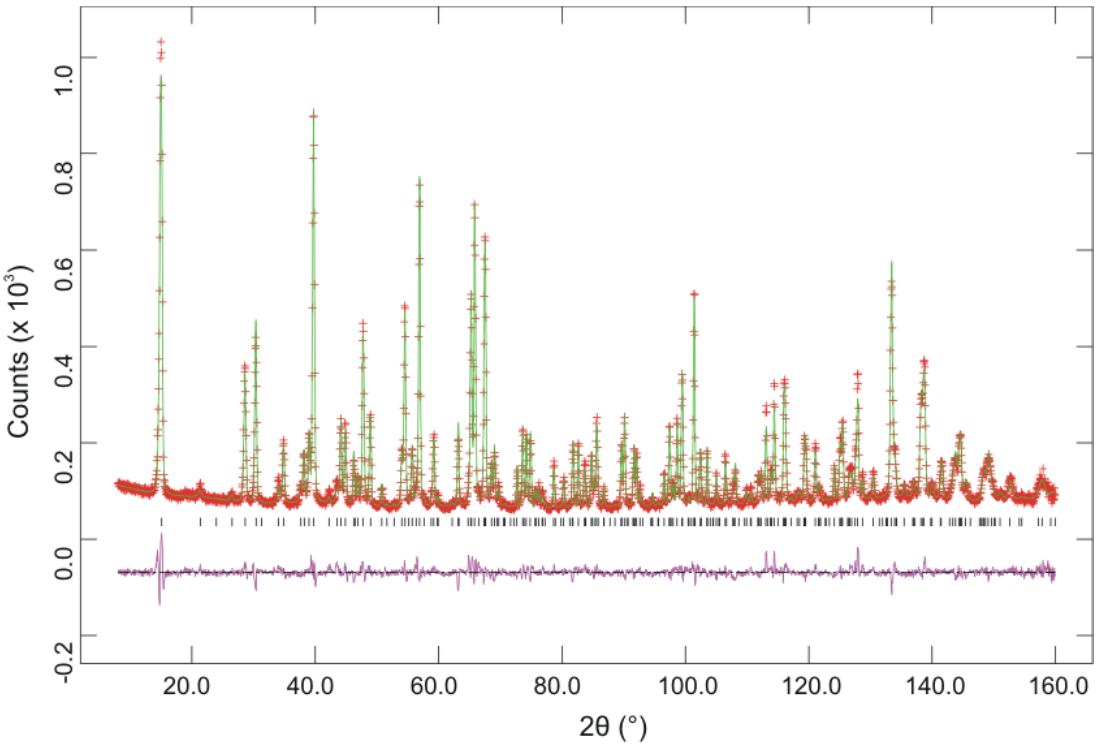

(a)

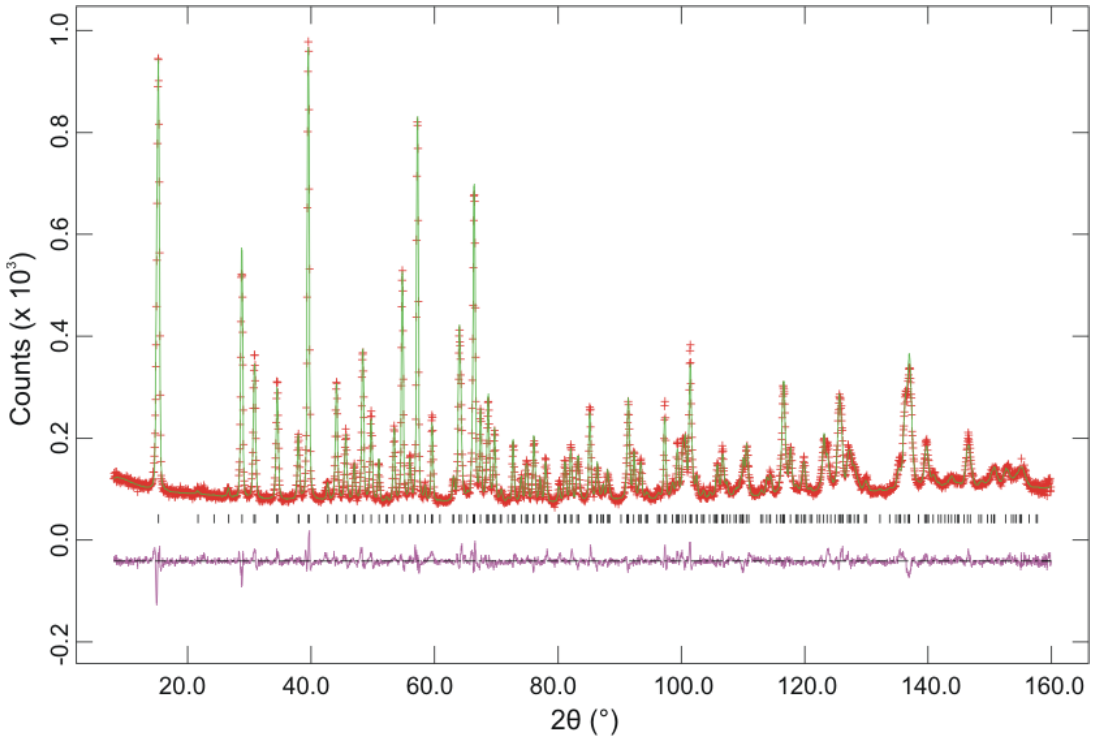

(b)

***Fig. 3.5**: Observed, calculated and difference plots for high resolution NPD data recorded from (a) $FeSb_2O_4$ and (b) $FeSb_{1.5}Pb_{0.5}O_4$ at 298 K.*

As more lead is introduced into the schafarzikite structure the FeO_6 octahedra become increasingly distorted (Fig. 3.6); this is seen by the deviation in O2-Fe-O2 angles from 90 º. With increasing levels of lead, all the Fe-O bond lengths decrease consistent with the presence of more Fe^{3+} ions. This is mainly seen for the Fe-O1 (apical) bond length which causes the FeO_6 octahedra to contract in the *a*-direction. The Fe-O2 (equatorial) bonds also contract slightly but to a lesser extent. As the Fe ions are found in octahedral edge-linked chains along the *c*-axis, the increasing *c*-parameter directly reflects an increase in Fe-Fe distances. This is caused by an increasing repulsion throughout the chains due to the presence of more highly charged Fe^{3+} ions. This is also observed by the change in Fe-O2-Fe bond angle which increases as the FeO_6 octahedra expand in the *c*-direction and limits the reduction possible in the Fe-O2 bond lengths. As Pb substitutes for Sb, the Sb/Pb position is altered and longer Sb/Pb-O bond lengths are observed due to the increased size and reduced charge on the pyramidal sites. The shorter Fe-O1 bonds are dominant over the longer Sb/Pb-O bonds in the *ab* plane and an overall contraction is seen in the *a*-direction with increasing lead content.

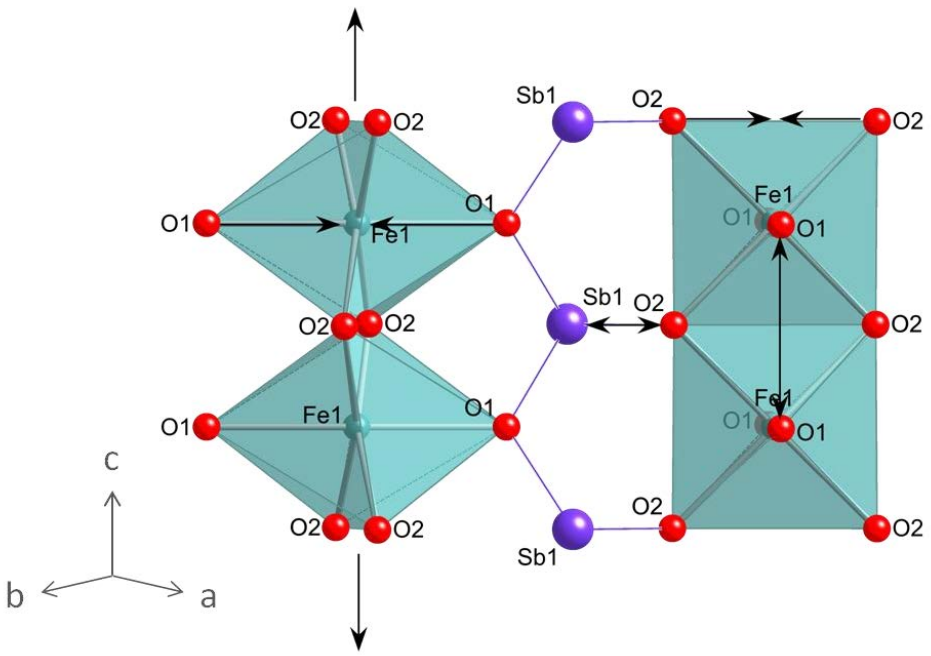

***Fig. 3.6**: Changes in $FeSb_{2-x}Pb_xO_4$ bond lengths and angles as the lead content is increased.*

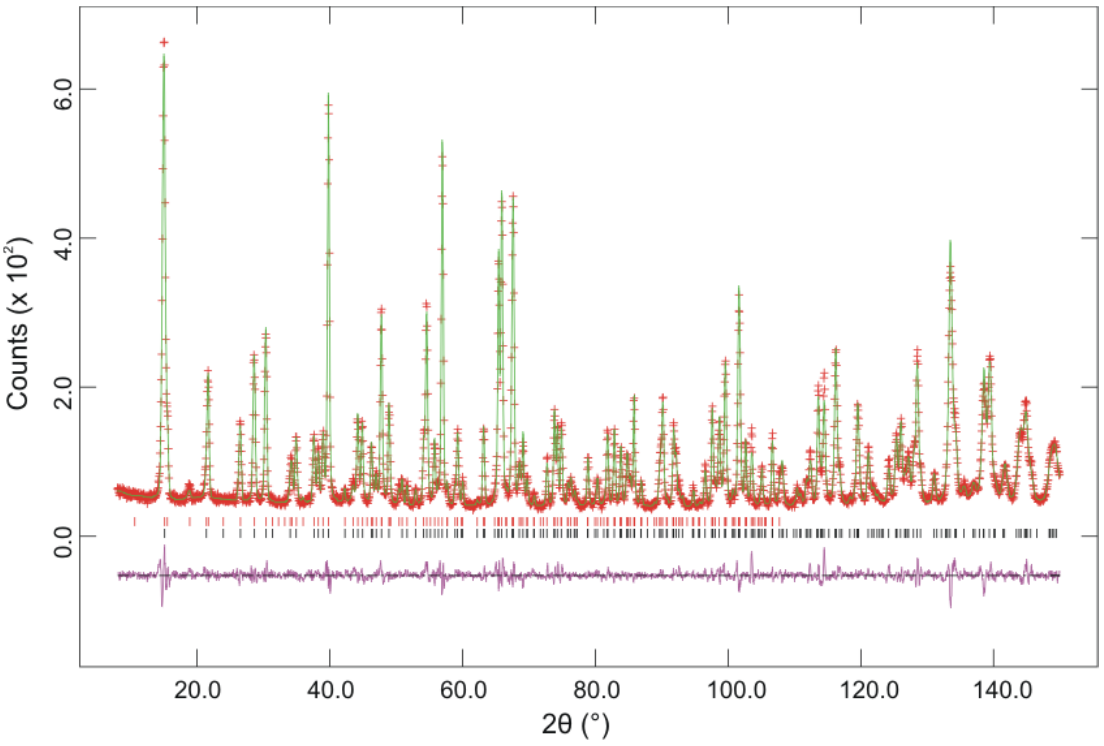

(a)

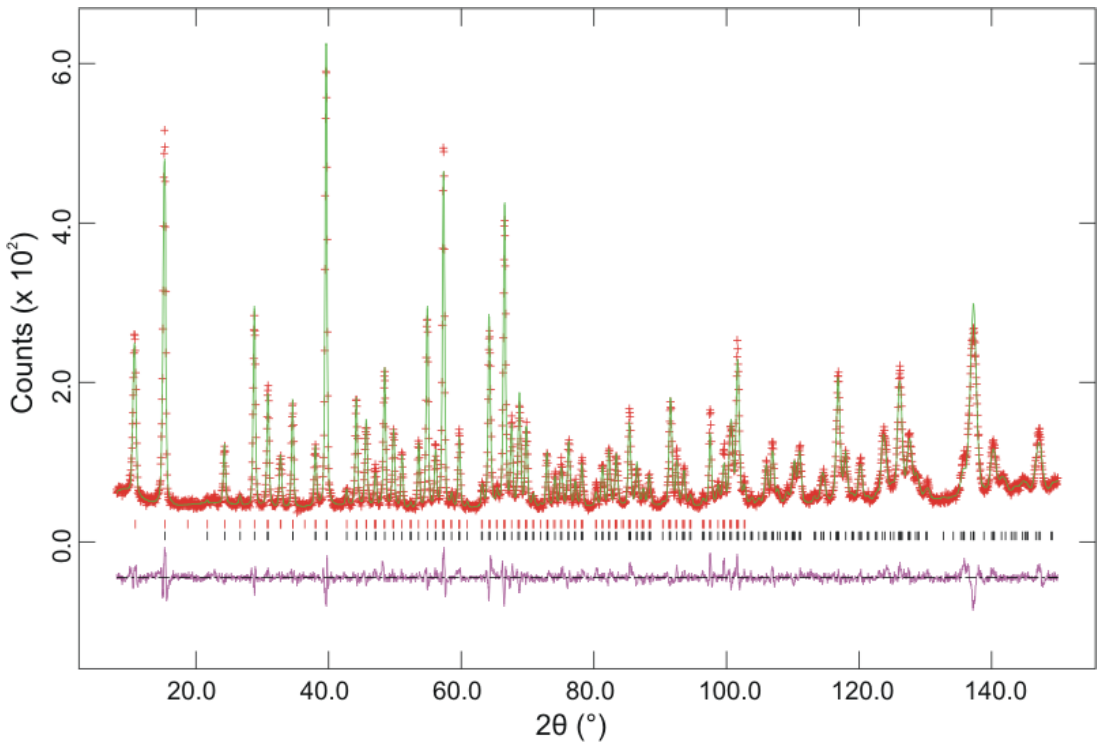

(b)

***Fig. 3.13**: Observed, calculated and difference plots for high resolution NPD data recorded from (a) $FeSb_2O_4$ and (b) $FeSb_{1.5}Pb_{0.5}O_4$ at 4 K.*

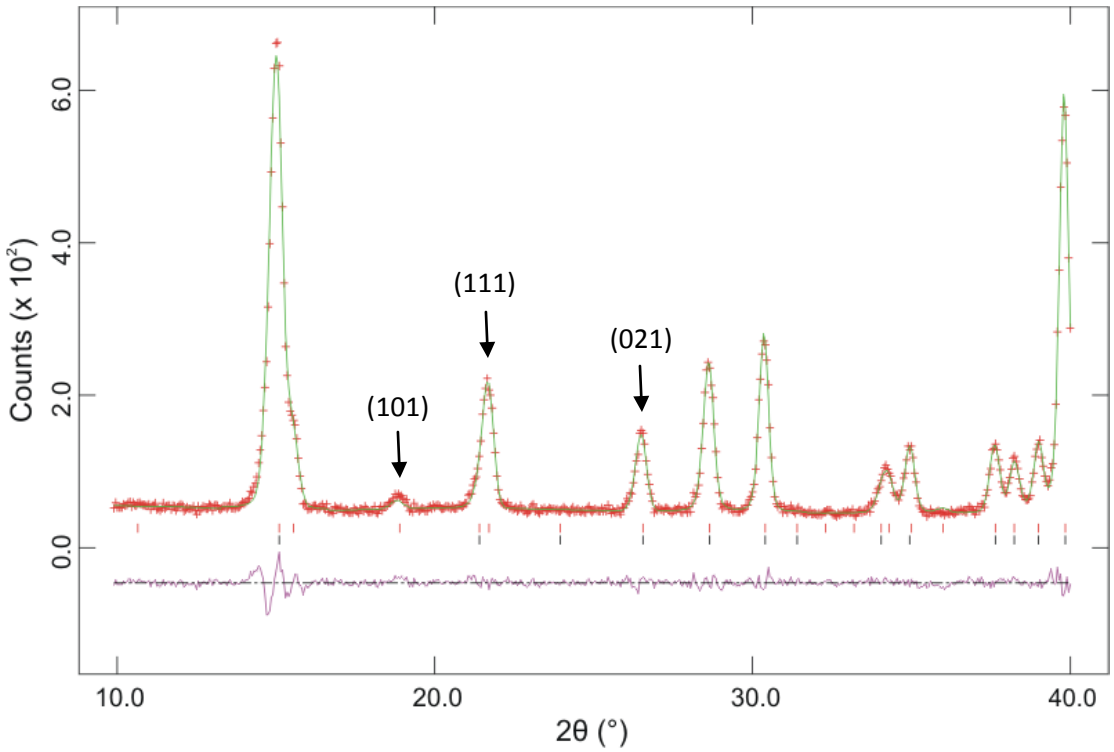

(a)

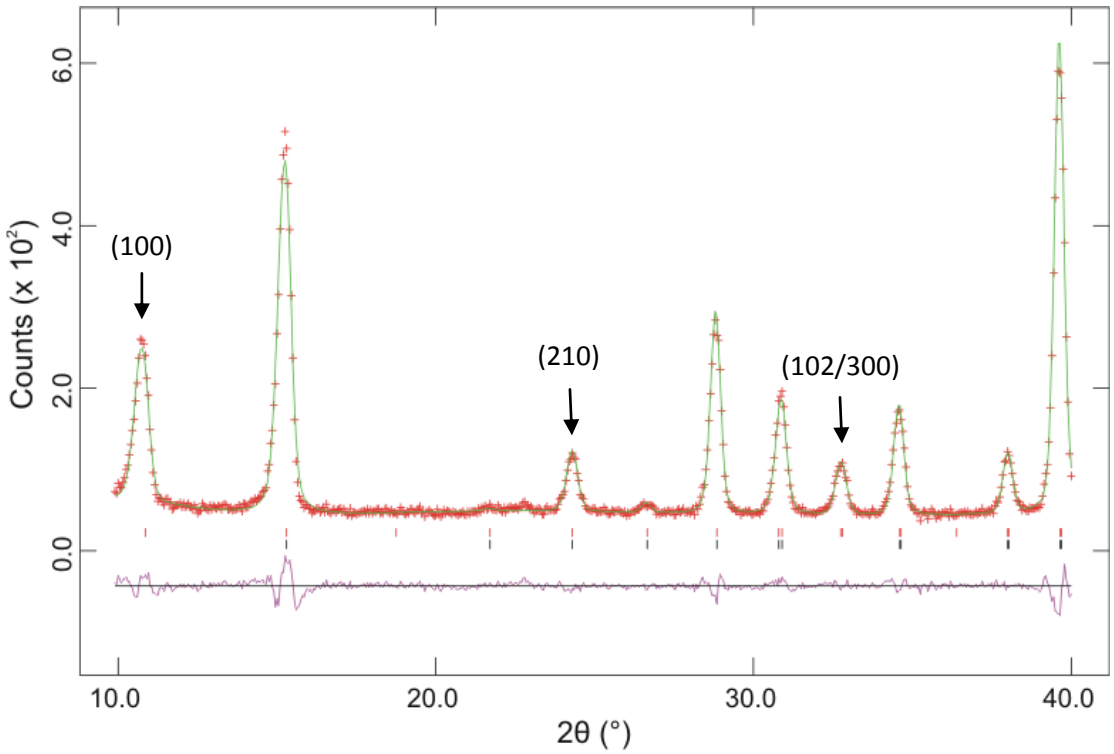

(b)

***Fig. 3.14**: Observed, calculated and difference plots (between 10 and 40 °2θ) for high resolution NPD data recorded from (a) $FeSb_2O_4$ and (b) $FeSb_{1.5}Pb_{0.5}O_4$ at 4 K.*

Previous work on neutron diffraction data of $FeSb_2O_4$ reported that the low temperature magnetic structure is predominantly A-type, but that C-type and G-type components are also present.[8] These three modes are combined to give a magnetic structure with orthorhombic symmetry and small moments along the *y*- and *z*-axes in addition to the major component along *x*.[8] As the {100} peak is absent there is no evidence for a C-type component in the sample studied here, but a peak just below 19 ° θ could be indexed as the {101} peak which would indicate a G-type component (Fig. 3.14a). This peak could also be due to Fe_3O_4 impurities, which were shown to be present from the SQUID magnetometry data, as it is close to the position of the most intense magnetic reflection of magnetite. However, the peak is absent from the room temperature (Fig. 3.15) data and a refinement with Fe_3O_4 added as an impurity phase did not model the peak well, indicating that it relates to a bulk feature.

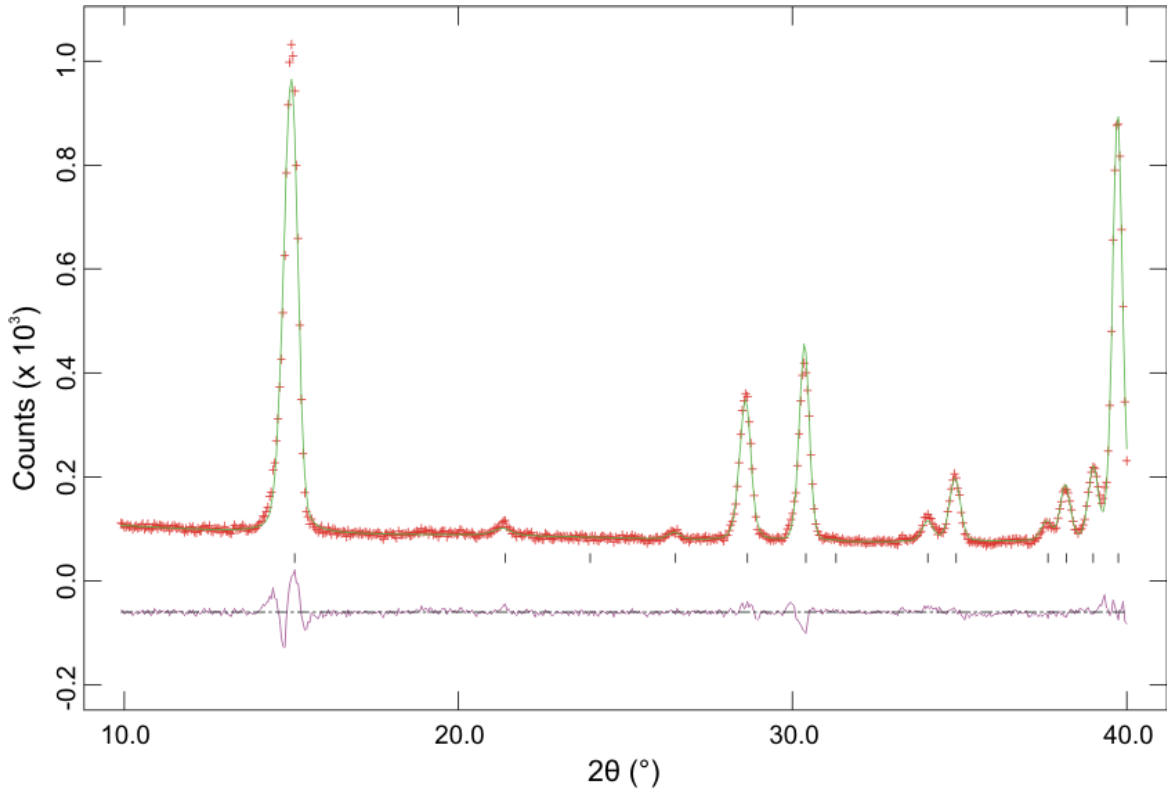

***Fig. 3.15**: Low angle region of observed, calculated and difference plots for high resolution NPD data recorded from $FeSb_2O_4$ at 298 K.*

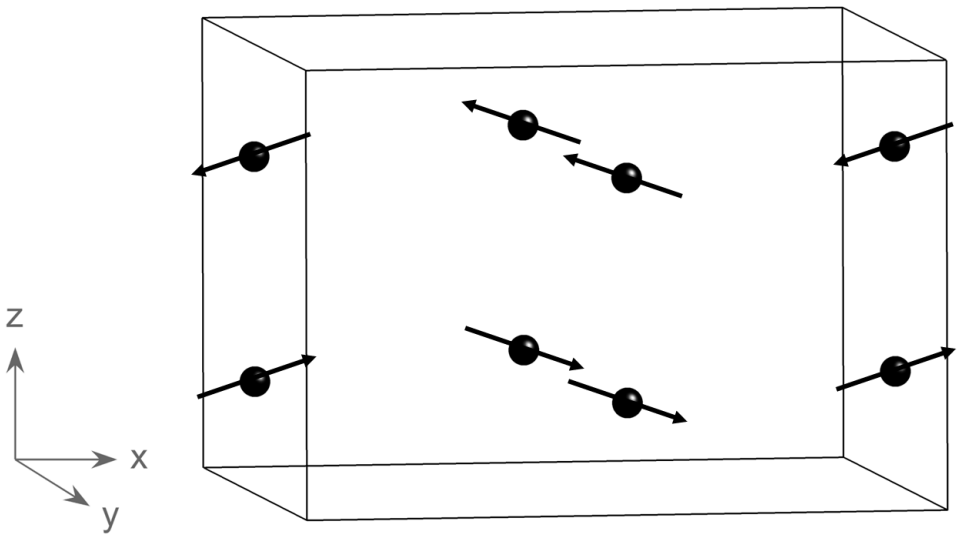

(a)

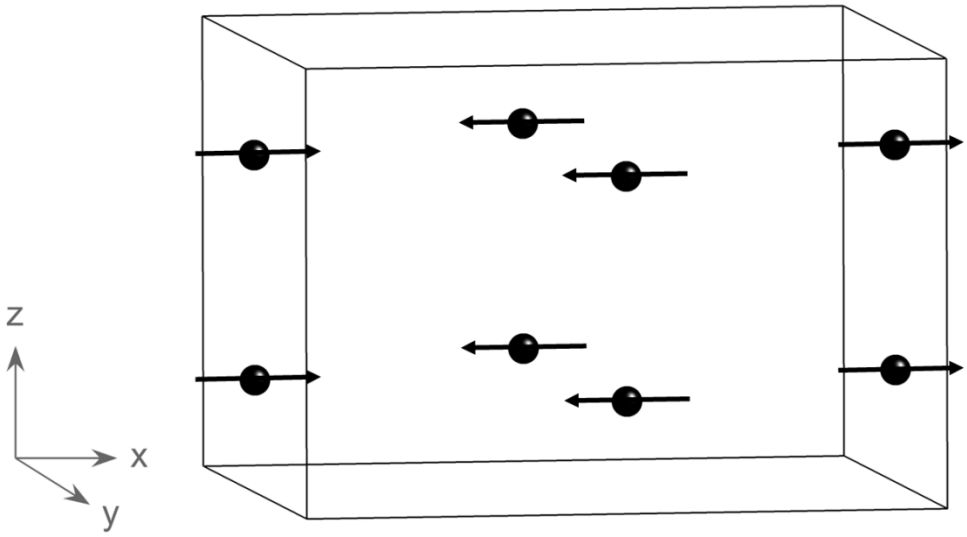

(b)

***Fig. 3.16**: Magnetic structure models (a) for $FeSb_2O_4$ showing predominantly A-type ordering with a G-type component and (b) for $FeSb_{2-x}Pb_xO_4$ showing C-type ordering.*

As described in Section 1.5.2 and Fig. 1.10, within a chain the Fe ions interact both directly through the t_{2g} orbitals and also through 90 º Fe-O-Fe superexchange interactions, and within a layer the Fe ions interact through weaker Fe-O-Sb/Pb-O-Fe links. The A-type ordering of $FeSb_2O_4$ was explained by the partially filled t_{2g} orbitals which favour AFM ordering within the FeO_6 chains (Section 1.5.2). Introducing lead into $FeSb_2O_4$ results in partial oxidation of Fe^{2+} giving a mixed Fe^{2+}/Fe^{3+} oxidation state throughout the chains and C-type magnetic order. The FM ordering within the chains can then either be explained by a reduction in the direct exchange or by a double exchange mechanism. Direct exchange occurs as the t_{2g} orbitals on neighbouring Fe ions within the edge-sharing chains point directly at each other. With increasing lead content the t_{2g} overlap decreases due to the *d*-orbital contraction in Fe^{3+} and the increase in Fe-Fe distance along *c*. This could then cause the 90 ° superexchange interaction, which favours FM interactions, to become dominant. A double exchange mechanism[12], by which electron migration between Fe^{2+} and Fe^{3+} ions can occur, is possible throughout the chains of $FeSb_{2-x}Pb_xO_4$ as a result of the mixed Fe^{2+}/Fe^{3+} oxidation state (Fig. 3.17). As Fe^{2+} has a d^6 configuration and Fe^{3+} has a d^5 configuration, a parallel arrangement of spins throughout the chains allows electron transfer between neighbouring Fe ions and is therefore favoured over an antiparallel arrangement. In $FeSb_2O_4$, as all the Fe is present as Fe^{2+}, this is not possible.

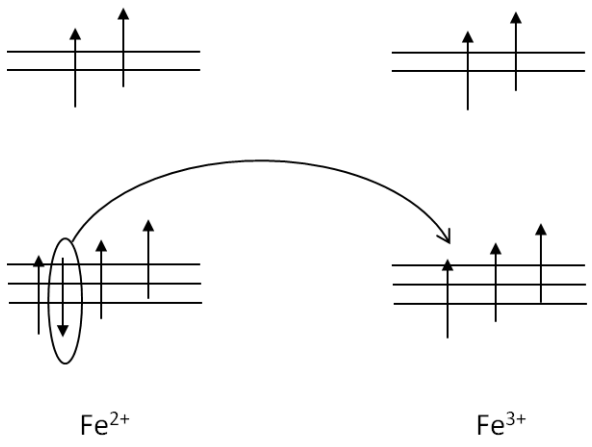

***Fig. 3.17**: Double exchange mechanism.*

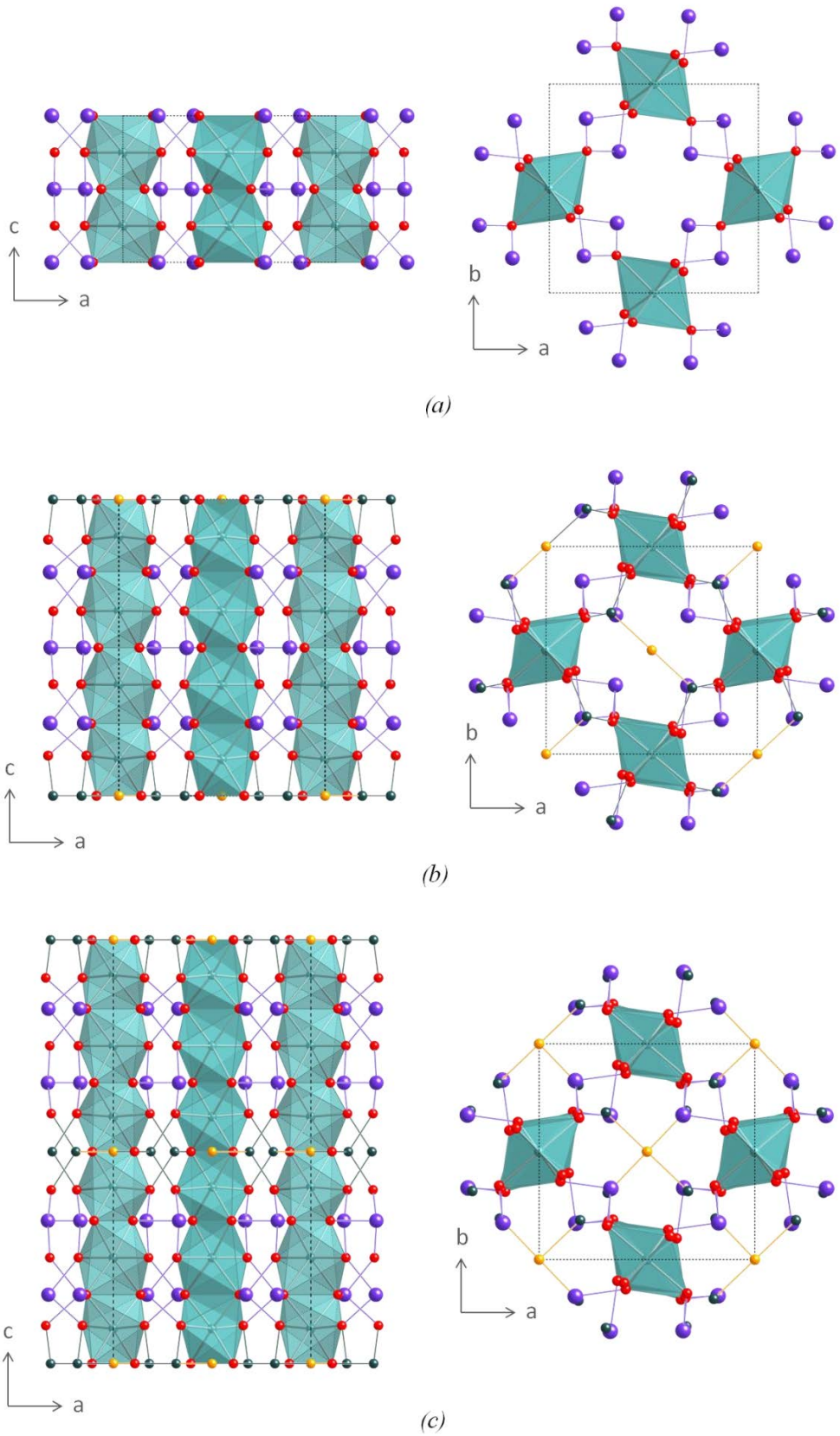

***Fig. 4.1**: Structure of (a) schafarzikite, (b) versiliaite and (c) apuanite unit cells. FeO_6 octahedra are shaded, O ions are shown as red spheres and Sb ions are shown as purple spheres. For versiliaite and apuanite, pyramidal Fe^{3+} ions are shown in dark green and S^{2-} ions are shown in orange.*

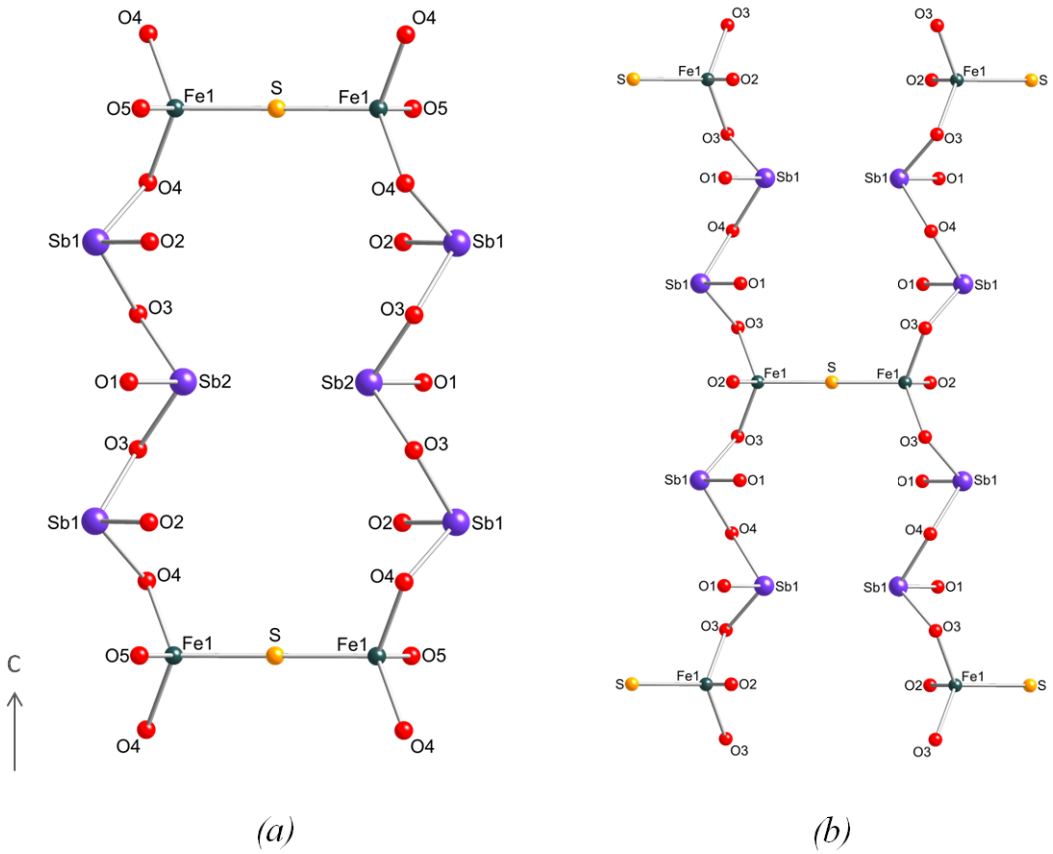

***Fig. 4.2**: Structures of schafarzikite-related minerals: the formation of (a) two chain ribbons in versiliaite and (b) infinite sheets in apuanite by Fe-S-Fe links is shown.*

In the apuanite structure, every third Sb^{3+} ion is replaced to give pyramidal Fe^{3+} ions within a chain facing in alternating directions (Fig. 4.2b). Infinite sheets are formed in (110) directions by the Fe-S-Fe links (Fig. 4.1c and 4.2b) resulting in a tetragonal structure (space group $P4_2/mbc$) and tripling of the unit cell (a = 8.372(5), c = 17.97(1)[3]).

The formulae of versiliaite and apuanite can be written as $Fe(Sb_{1.5}Fe_{0.5})O_4S_{0.25}$ and $Fe(Sb_{1.33}Fe_{0.67})O_4S_{0.33}$ respectively. Little research has been carried out on these materials: both versiliaite and apuanite have been investigated using Mössbauer spectroscopy[4] and apuanite has also been studied using Raman spectroscopy[5].

In this chapter insertion of oxygen into the schafarzikite structure is investigated. The lead-substituted schafarzikites, $FeSb_{2-x}Pb_xO_4$, have been shown to incorporate oxygen

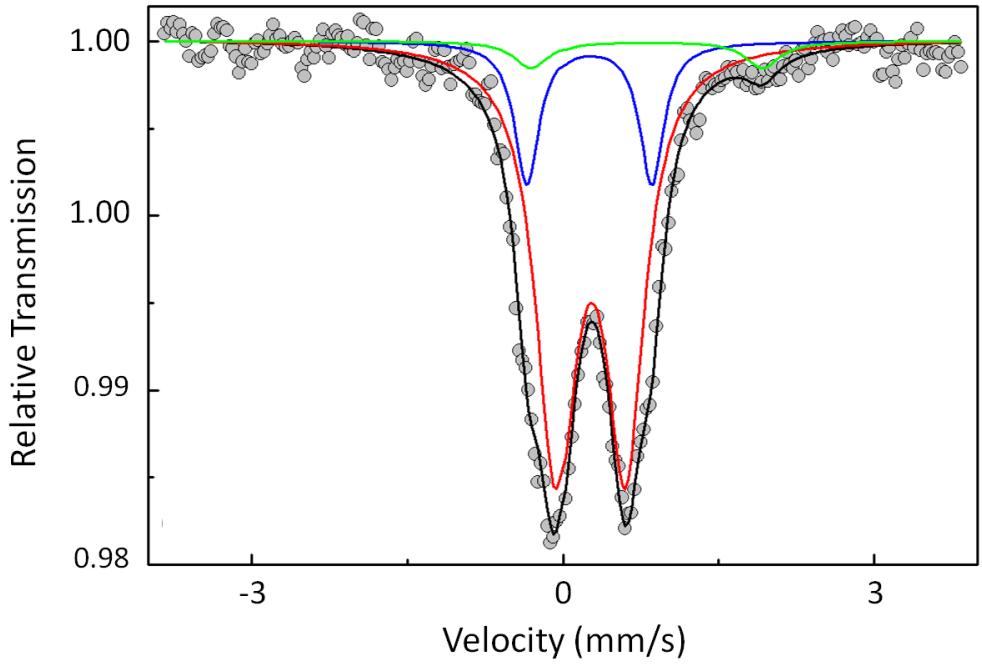

***Fig. 4.10**: ^{57}Fe Mössbauer spectrum recorded from $FeSb_{1.25}Pb_{0.75}O_{4+x}$ at 298 K.*

Structure refinement of NPD data was performed using the model obtained for $FeSb_{1.25}Pb_{0.75}O_4$ (space group $P4_2/mbc$) with no excess oxygen added and refining the unit cell along with other parameters as described for $FeSb_{2-x}Pb_xO_4$ in Section 3.3.1. The refinement gave a good fit with values of $\chi^2 = .6$, $R_{wp} = 0.055$ and $R_F^2 = 0.052$.

To locate oxygen ions in the structure, difference Fourier maps were plotted. Fourier maps can be calculated from data obtained during the Rietveld refinement. For each reflection the structure factor, F_{calc}, and phase are calculated; the observed intensity is also extracted which can be used to calculate an observed structure factor, F_{obs}. Using these values, calculated and observed maps of the structure can be plotted and by subtracting the calculated data from the observed data a difference Fourier map can be plotted which is used to find missing atoms in the structure. Two-dimensional difference Fourier maps were plotted at various intervals along the *c*-axis to locate the extra oxygen ions. The Fourier maps are shown in Fig. 4.11 and are compared with the structure of $FeSb_2O_4$.

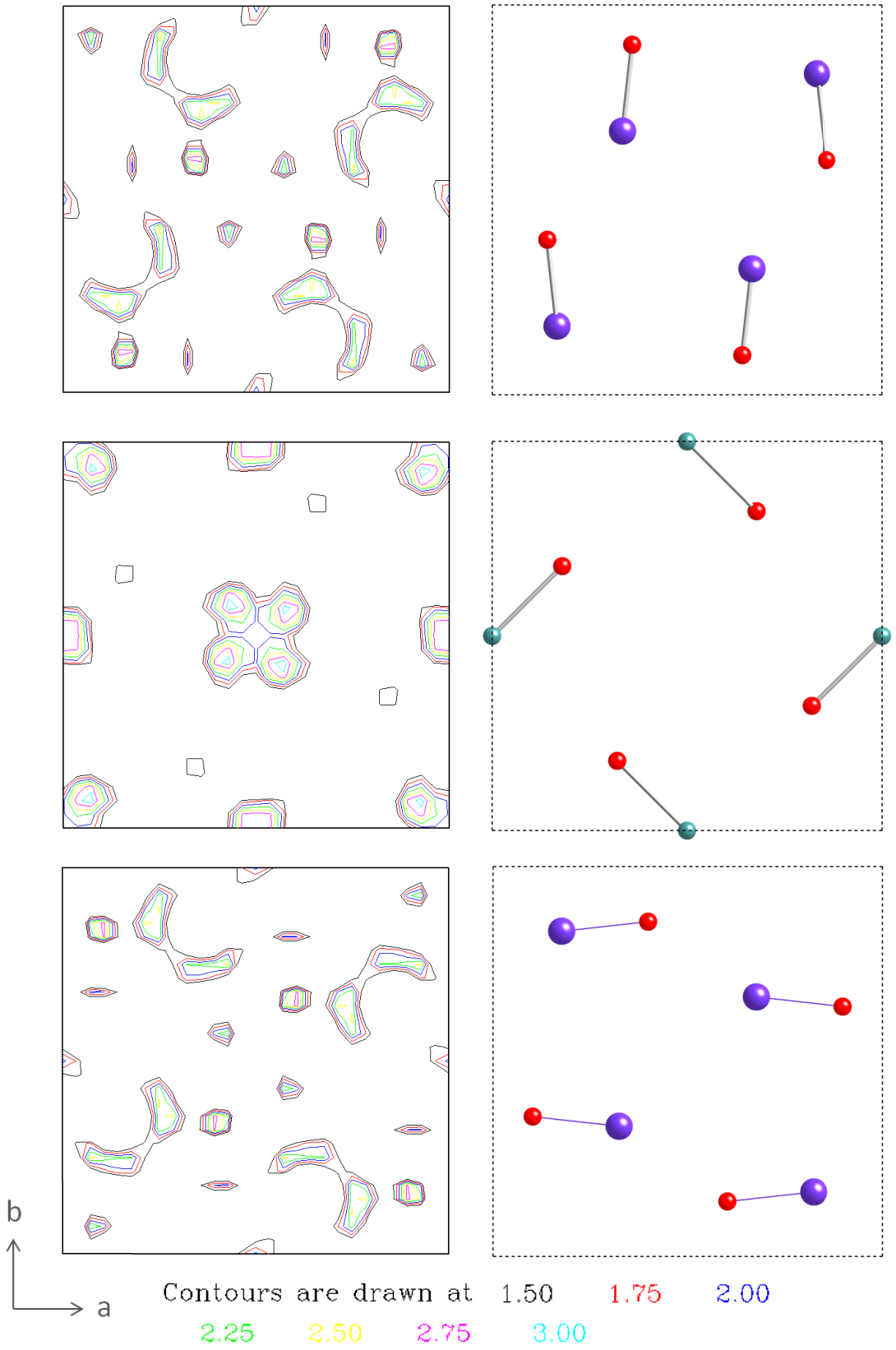

***Fig. 4.11**: Left hand side: 2D difference Fourier maps for $FeSb_{1.25}Pb_{0.75}O_{4+x}$ obtained from Rietveld refinement of room temperature NPD data at c = 0 Å (top), c = 1.5 Å (middle) and c = 3 Å (bottom). Right hand side: corresponding structure diagrams of $FeSb_2O_4$; Fe ions are shown as green spheres, Sb as purple spheres and O as red spheres.*

Three maps are shown at c = 0 Å, c = 1.5 Å and c = 3 Å which, since c = 6.04 Å, correspond to 0, ¼ and ½ along the c-axis respectively. The region of highest neutron scattering density not being accounted for in the model was found at c = ¼ and slightly off centre within the channels. Due to the space group symmetry, four oxygen ion positions are generated and this corresponds to a partially occupied 16*i* site (Fig. 4.12).

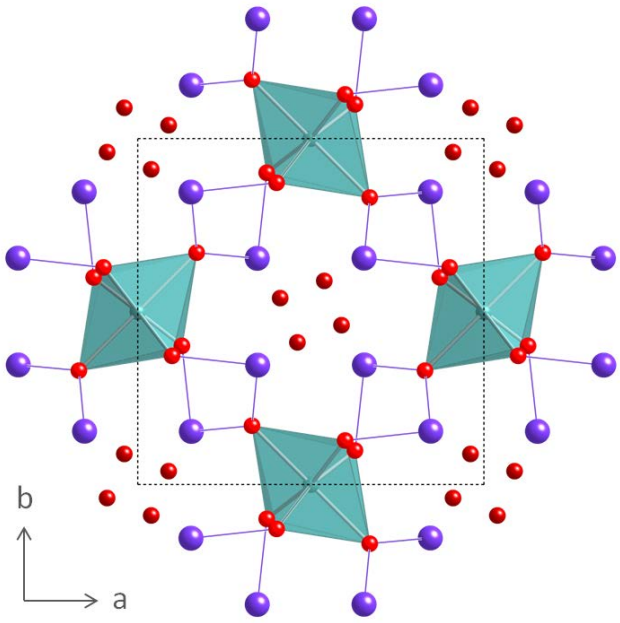

***Fig. 4.12**: The structure of $FeSb_{1.25}Pb_{0.75}O_{4+x}$ looking down the c-axis. FeO_6 octahedra are shaded. Fe ions are located within the octahedra, Sb/Pb ions are shown as purple spheres and O ions are shown as red spheres. The O3 ions within the channels are shown in dark red and only partially occupy a 16i site.*

A third oxygen position was therefore added to the model and the atomic coordinates and fractional occupancy were refined. The model fits the data well (Fig. 4.13), reducing the value of χ^2 to .900, and the parameters obtained from the refinement are summarised in Table 4.3. The Fourier maps initially plotted revealed a splitting of the O1 anion site as electron density was seen either side of the O1 anion in the *ab* plane. Anisotropic temperature factors were therefore used for this ion in all room temperature $FeSb_{1.25}Pb_{0.75}O_{4+x}$ refinements and gave larger values in the a-direction than in the c-direction (Table 4.3).

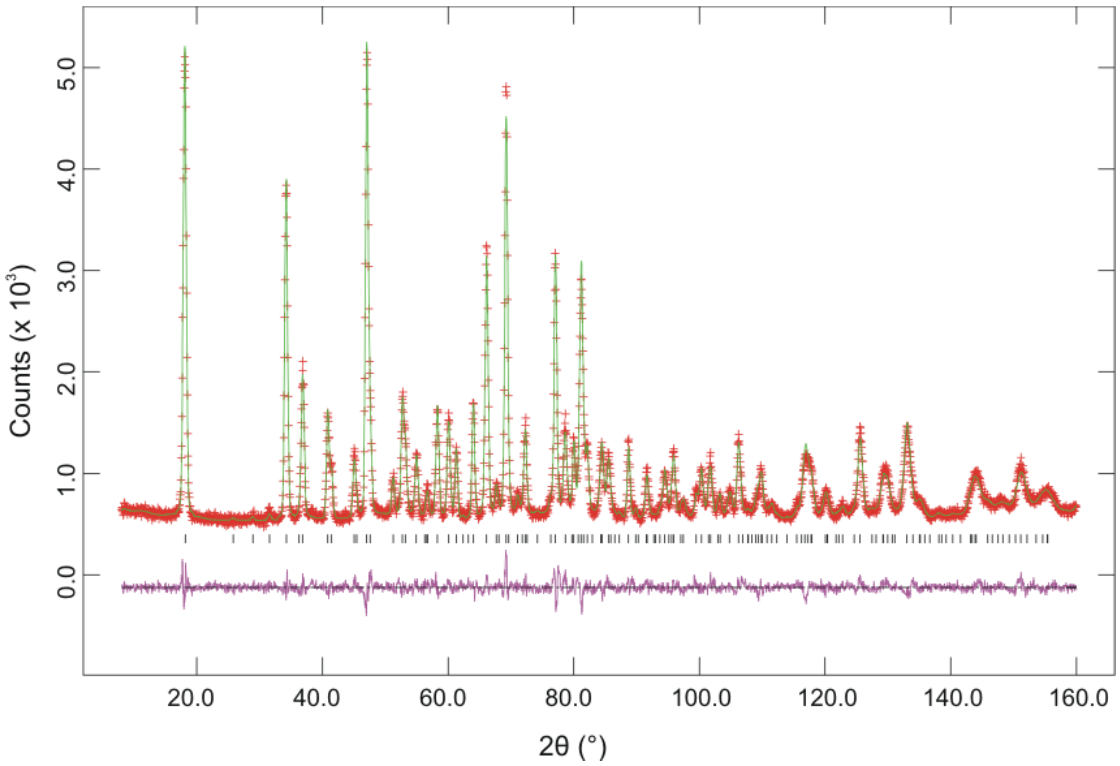

***Fig. 4.13**: Observed, calculated and difference plots for high resolution NPD data recorded from $FeSb_{1.25}Pb_{0.75}O_{4+x}$ at 298 K.*

Assuming all the Fe^{2+} is oxidised to Fe^{3+} by insertion of oxide ions, the composition of the sample would be $FeSb_{1.25}Pb_{0.75}O_{4.125}$ which gives half an excess oxygen ion per unit cell. Overall a fractional occupancy of 0.03125 would be expected on the O3 16*i* site. The fractional occupancy given from refinement of NPD data (Table 4.3) is slightly more than double the expected value. This, along with the value from TGA, supports the idea that oxygen is being taken up as peroxide. The bond lengths and angles obtained from the refinement show that a model with peroxide in the channels bonded to Sb ions is sensible. The Sb-O3 bond to the nearest of the four possible oxygen sites is 1.92(4) Å, the bond length between the O3 ions opposite one another is 1.63(4) Å and the Sb-O3-O3 bond angle is 118(2) °. Compared to other compounds these values look reasonable[10] and the O3-O3 bond length corresponds to a long peroxide bond as the O-O bond length of peroxo groups is typically 1.40-1.48 Å [11]. The coordination of the Sb^{3+}/Pb^{2+} ion and location of O3 ions is shown in Fig. 4.14.

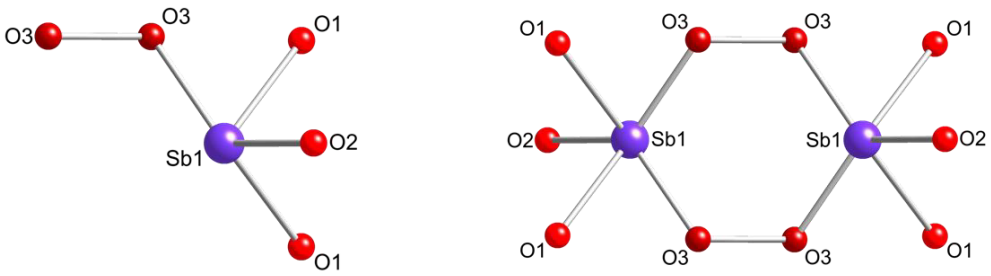

***Fig. 4.14**: Left: coordination of the Sb/Pb ion in $FeSb_{1.25}Pb_{0.75}O_{4+x}$ showing bonding to peroxide oxygen ions (O3) in the channels; right: location of O3 ions and possible links to Sb/Pb in adjacent chains.*

4.3.2 Magnetic Properties

Field cooled (FC) and zero-field cooled (ZFC) susceptibility measurements were taken between 5 and 300 K for the samples $FeSb_{1.5}Pb_{0.5}O_{4+x}$ and $FeSb_{1.25}Pb_{0.75}O_{4+x}$. An applied field of 500 Oe was used and plots of susceptibility versus temperature are shown in Fig. 4.15 and 4.16.

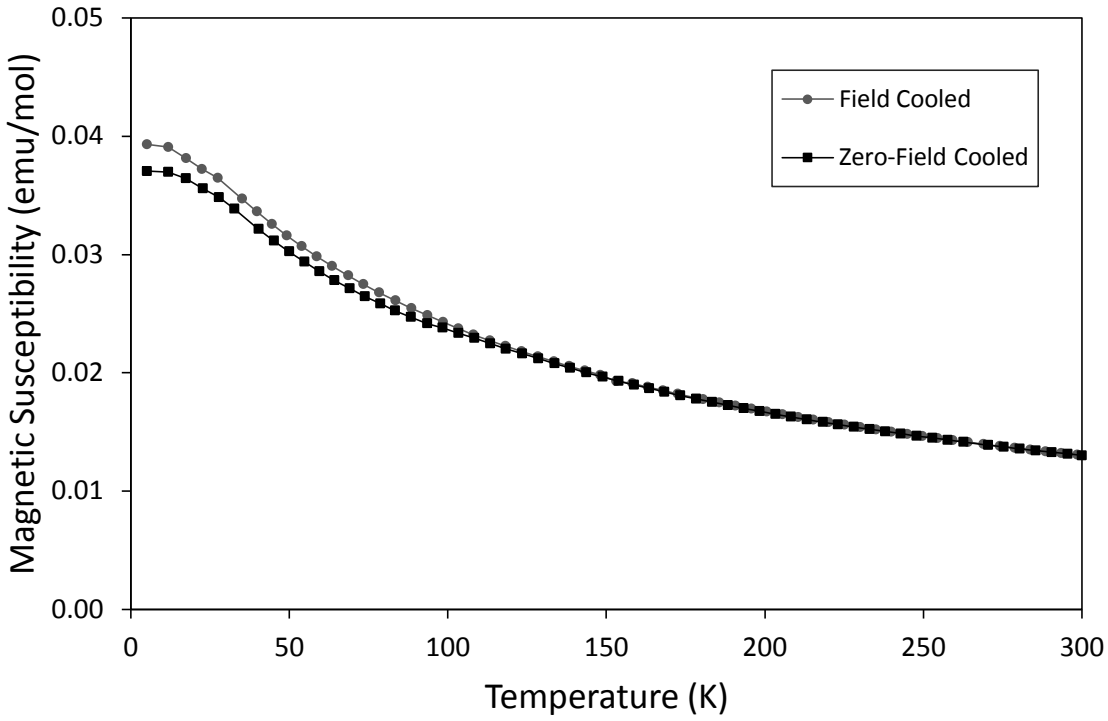

***Fig. 4.15**: Variation of magnetic susceptibility with temperature for $FeSb_{1.5}Pb_{0.5}O_{4+x}$.*

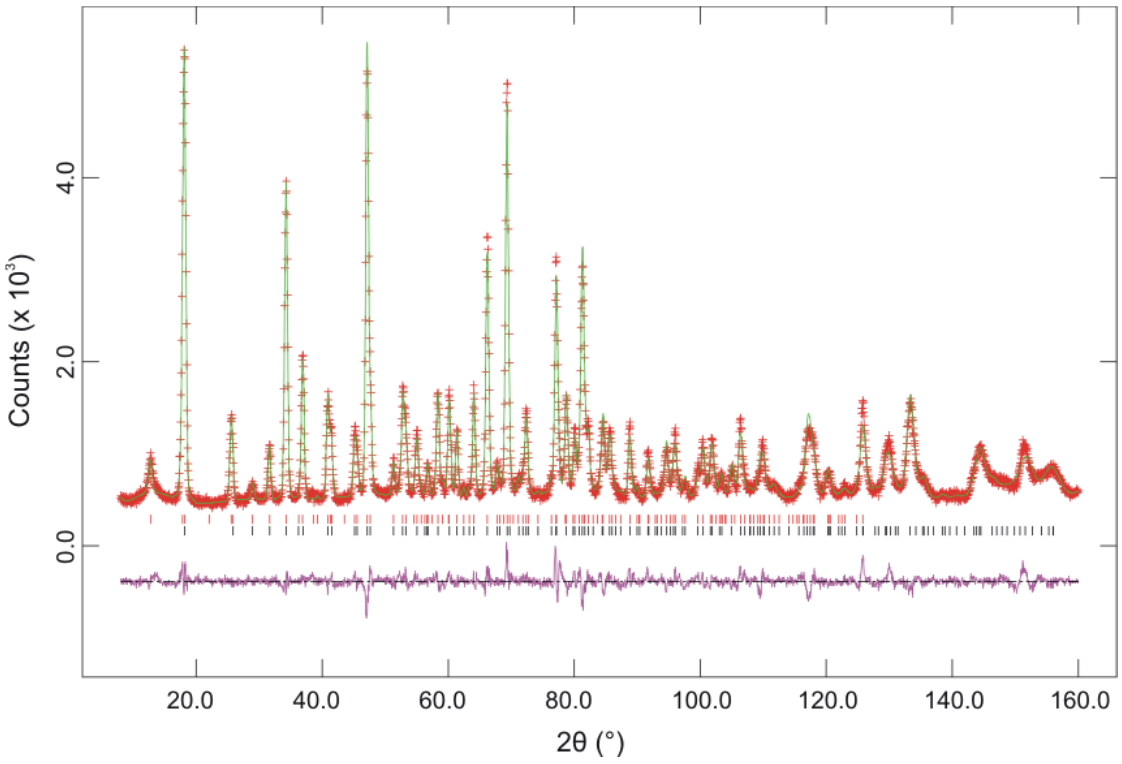

(a)

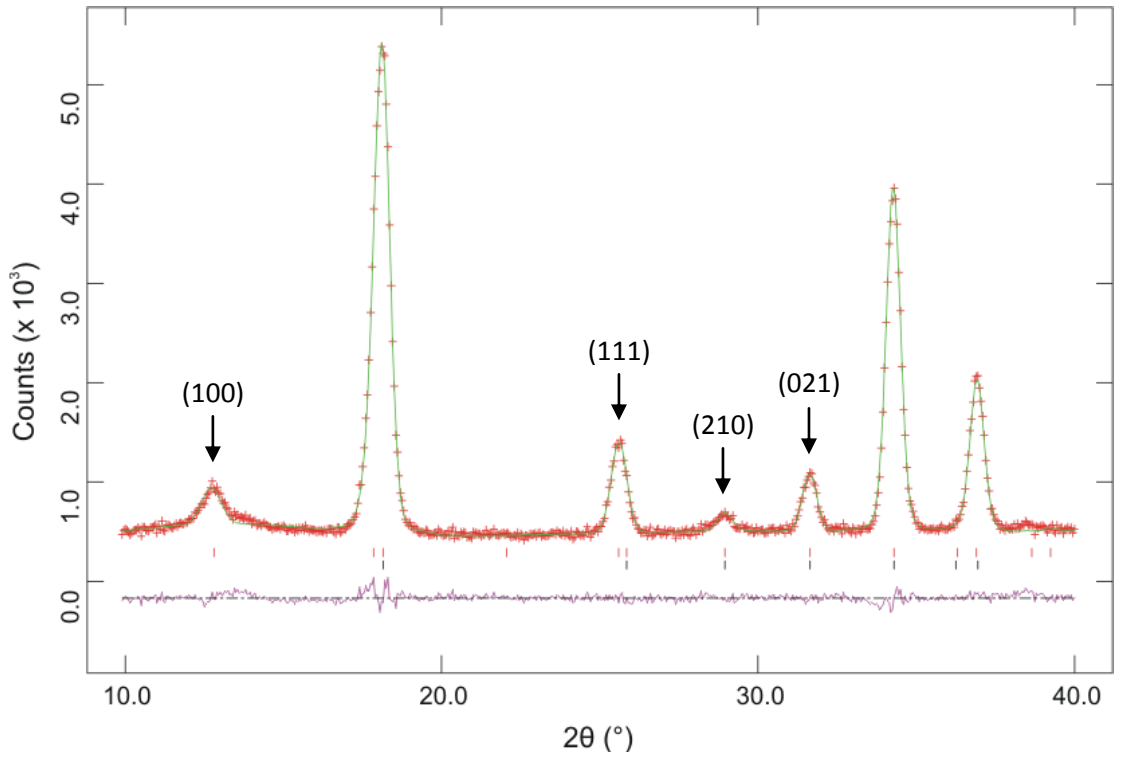

(b)

***Fig. 4.17**: Observed, calculated and difference plots for high resolution NPD data recorded from $FeSb_{1.25}Pb_{0.75}O_{4+x}$ at 2 K showing (a) the full plot from 10 to 160 °2θ and (b) 10 to 40 °2θ with magnetic reflections labelled.*

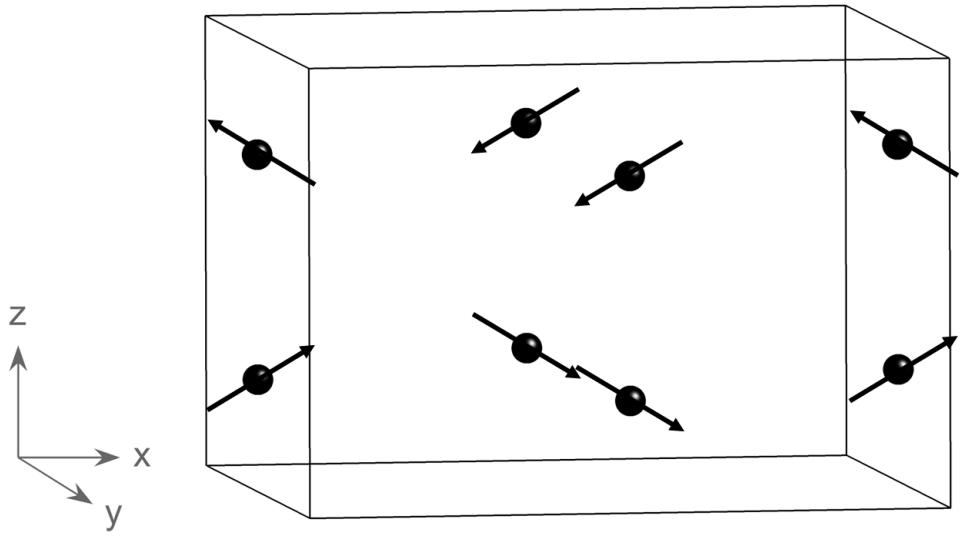

***Fig. 4.18**: Magnetic structure model for $FeSb_{1.25}Pb_{0.75}O_{4+x}$ showing A-type ordering along x with a strong C-type component along z.*

This is different from the magnetic structures of $FeSb_{2-x}Pb_xO_4$ before oxygen insertion, which show C-type magnetic ordering only. Of these samples the highest lead composition for which NPD data were collected was 0.7 and the magnetic structure of $FeSb_{1.3}Pb_{0.7}O_4$ is shown in Fig. 4.19 for comparison with $FeSb_{1.25}Pb_{0.75}O_{4+x}$.

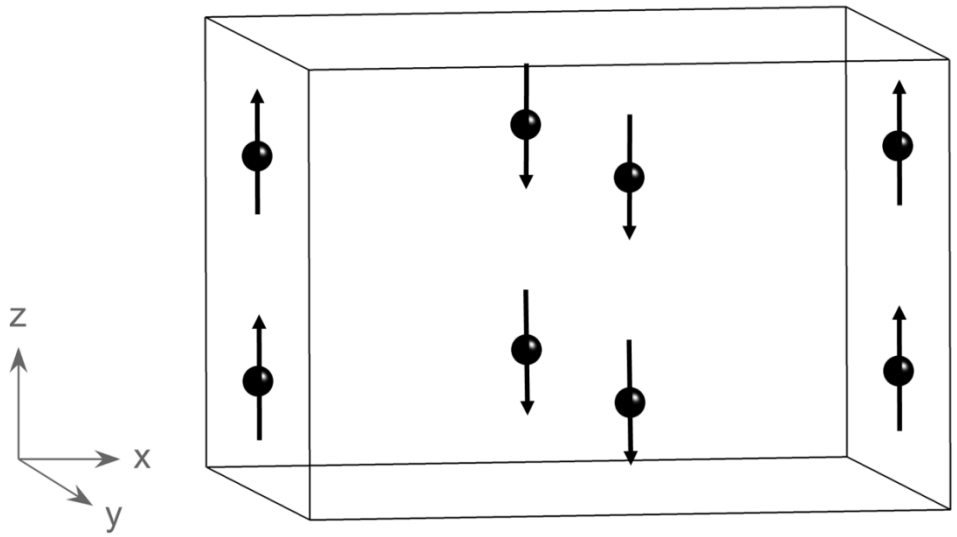

***Fig. 4.19**: Magnetic structure model for $FeSb_{1.3}Pb_{0.7}O_4$ showing C-type ordering. The moment is aligned predominantly along the z-axis with a small component along x (not shown).*

the diffraction peaks (Fig. 5.2), for example the (220) and (310) reflections are broader than the (002) and (112) reflections.

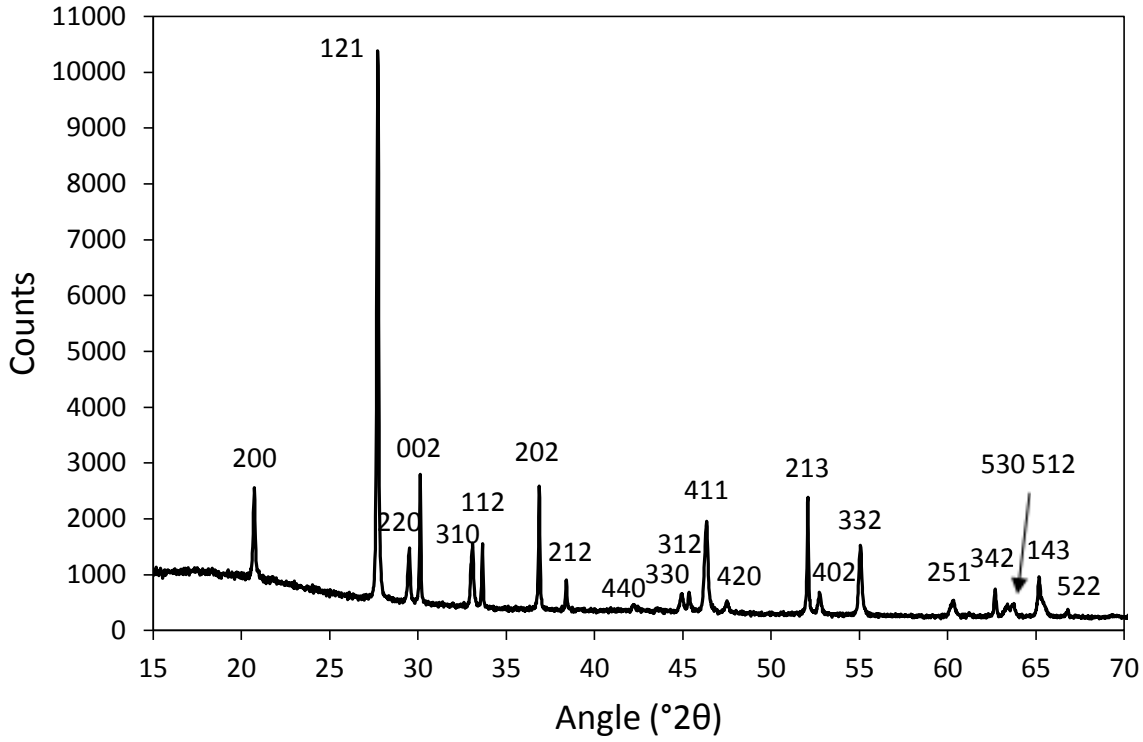

Fig. 5.2: *X-ray powder diffraction pattern for $Fe_{0.5}Mg_{0.5}Sb_2O_4$ with hkl values labelled.*

The profile function was therefore switched from type 2 to type 4 for the mixed Fe/Mg samples as function 4 contains anisotropic strain broadening parameters S_{HKL}[7]. These parameters are S_{400}, S_{004}, S_{220} and S_{202} for a tetragonal system and for the mixed Fe/Mg samples only S_{004} remained as zero. Broadening is likely to arise from needle shaped particles which, as they are smaller in the *a*- and *b*- directions than in the *c*-direction, cause broadening of reflections in which *h* or *k* is non-zero. This was investigated further using SEM (Section 5.3.2). Preferred orientation effects were also seen for the mixed Fe/Mg samples and this was refined using the March Dollase function[8-9]. Preferred orientation is seen when the arrangement of the crystallites in a polycrystalline sample is not completely random causing some reflections to be increased in intensity and others decreased in intensity. This is commonly seen for platelet or needle shaped

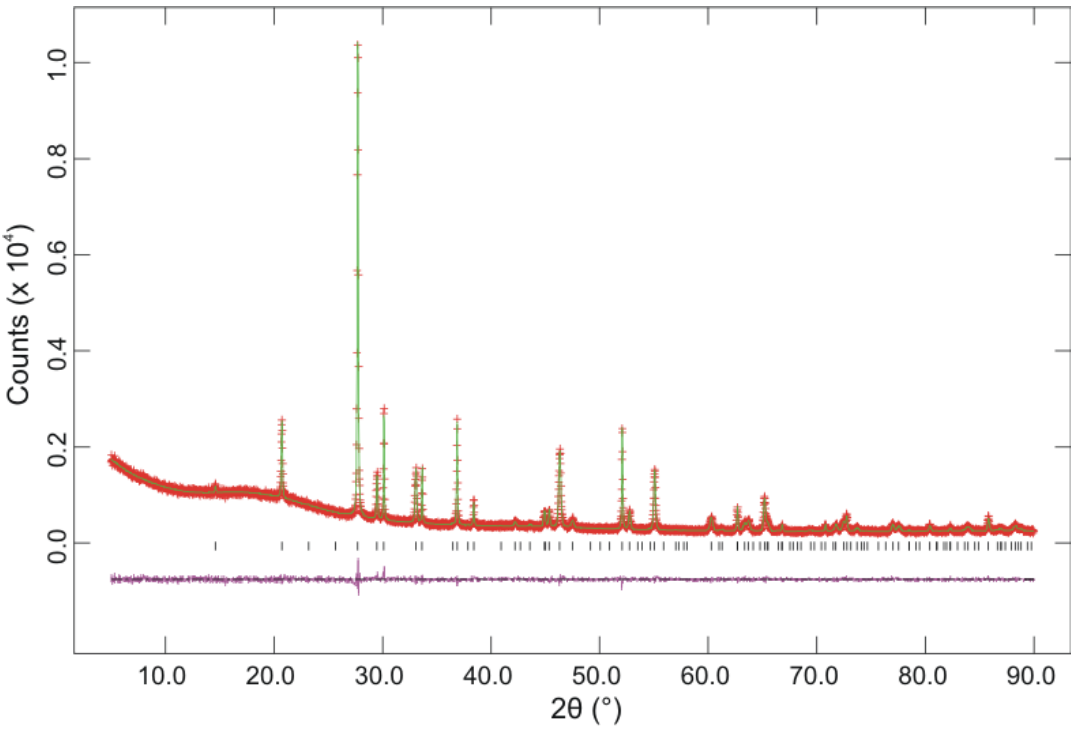

***Fig. 5.3**: Observed, calculated and difference plots for room temperature XRPD data recorded from $Fe_{0.5}Mg_{0.5}Sb_2O_4$.*

The fractional occupancies reported in Table 5.1 are close to the expected values and confirm that increasing amounts of magnesium have been substituted onto the octahedral sites. The preferred orientation was not seen for the end members of the series, $FeSb_2O_4$ and $MgSb_2O_4$, and therefore was not refined for these two compounds; for the mixed Fe/Mg schafarzikites the preferred orientation is higher with increasing iron content. The changes in unit cell parameters with Mg content, x, in $Fe_{1-x}Mg_xSb_2O_4$ are shown in Fig. 5.4. With increasing x in $Fe_{1-x}Mg_xSb_2O_4$ the unit cell volume decreases as expected from the ionic radii of Fe^{2+} and Mg^{2+} of 0.78 Å and 0.72 Å respectively (Fig. 5.4a). It can be seen from Fig. 5.4b that the contraction occurs in the *a*-direction and that the *c*-parameter changes very little as x is varied. As described previously the octahedral cations in the schafarzikite structure are much closer within the chains along the *c*-axis than within the layers perpendicular to the chains. The amount of contraction possible in the *c*-direction may therefore be restricted by the smaller Fe/Mg cation-cation distances.

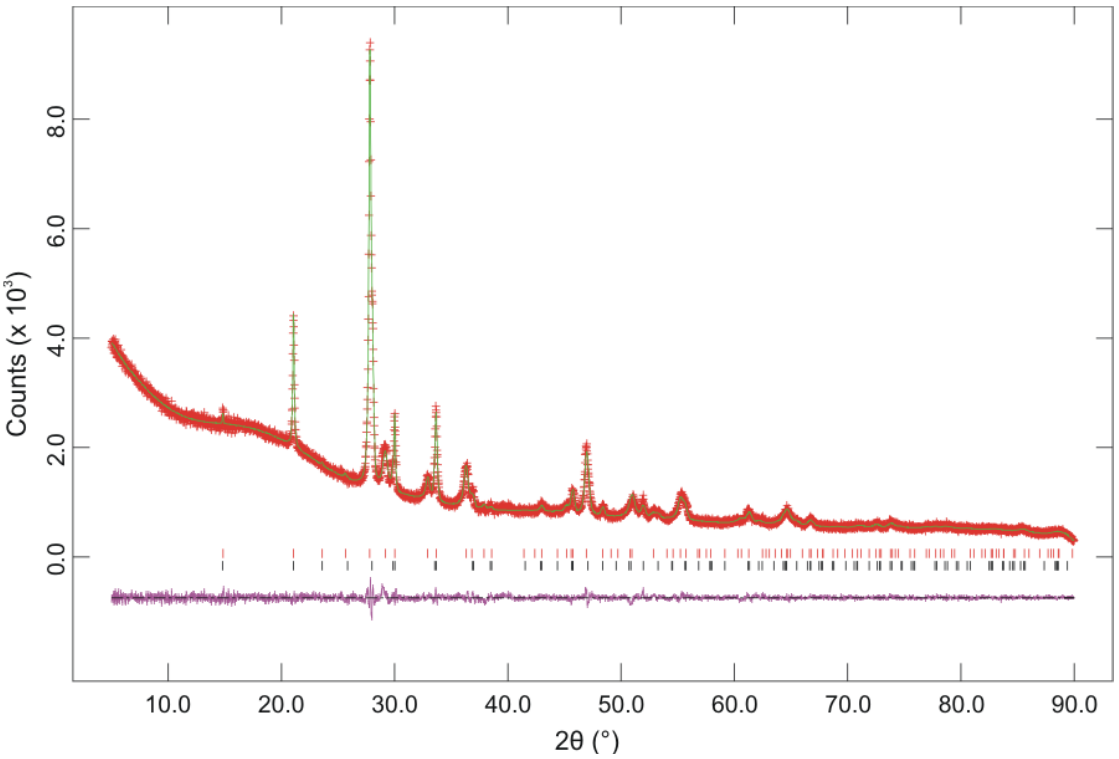

(a)

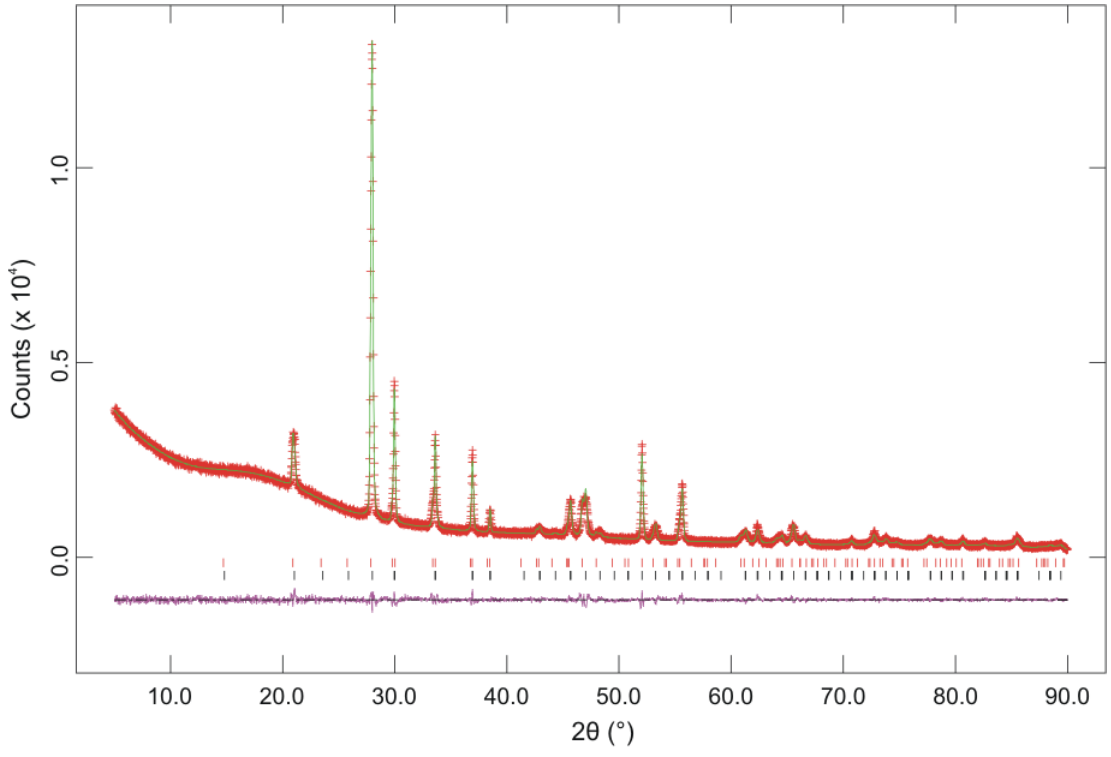

(b)

***Fig. 5.10**: Observed, calculated and difference plots for room temperature XRPD data recorded from (a) $Fe_{0.5}Mg_{0.5}Sb_2O_{4+x}$ and (b) $Fe_{0.25}Mg_{0.75}Sb_2O_{4+x}$.*

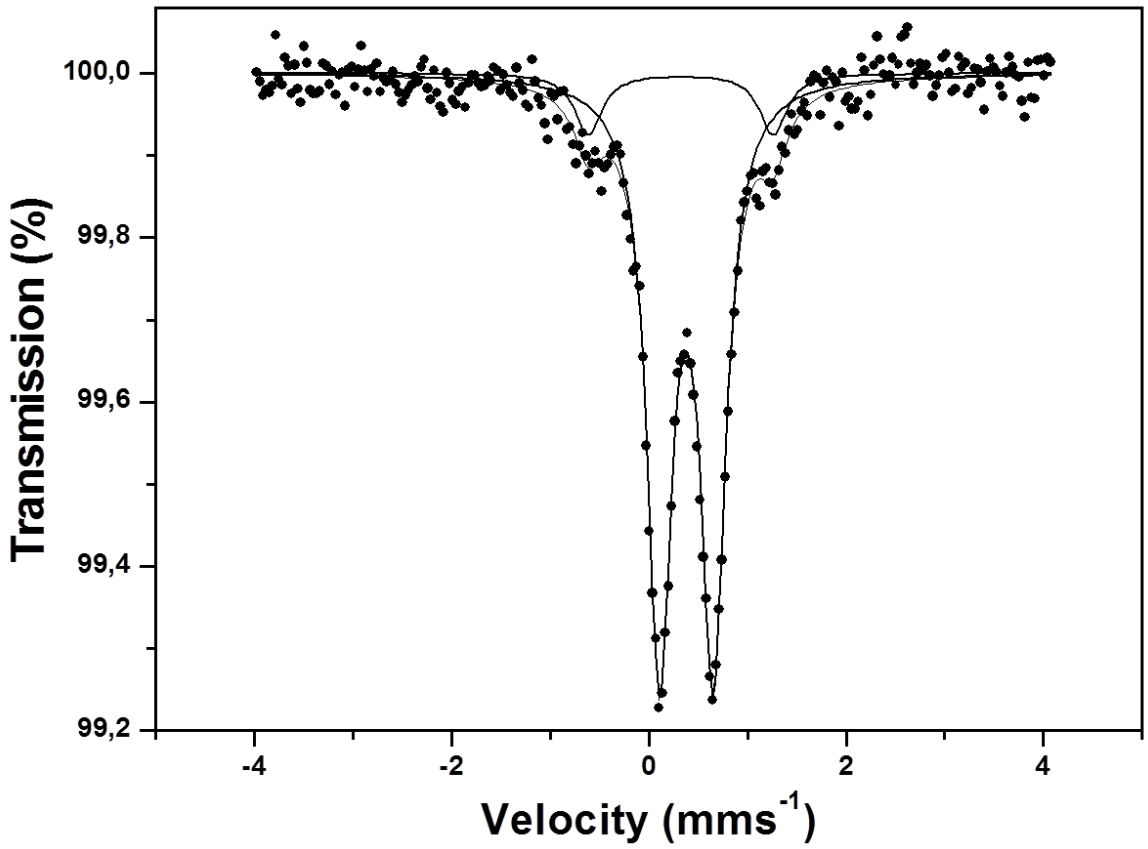

***Fig. 6.3**: ^{57}Fe Mössbauer spectrum recorded from $Bi_{1.8}Fe_{0.2}(FeSb)O_7$ at 298 K.*

Pyrochlores of the type $A_2(FeSb)O_7$ where A = Pr, Nd, Sm, Eu, Gd, Tb, Dy, Ho, Er, Yb, Lu and Y are already known[10-11] and for all these compositions the radius ratio requirements are satisfied. The compound where A = La is not known due to the larger size of 1.16 Å for 8-coordinate La^{3+}. However, as La^{3+} and Bi^{3+} have similar sizes, substitution of La by a smaller ion on the A-site could be expected to stabilise a pyrochlore structure. Formation of $La_{2-x}Fe_x(FeSb)O_7$ (x = 0.25, 0.5) was therefore attempted but no pyrochlore phase was formed and instead a multi-phase product containing different forms of $LaFeO_3$ and $LaFe_{0.5}Sb_{1.5}O_6$ was obtained. Although partial occupancy by iron on the A-sites is not necessary for the stability of the known $A_2(FeSb)O_7$ pyrochlores, formation of $A_{1.8}Fe_{0.2}(FeSb)O_7$ was attempted for A = Pr and Nd and XRPD patterns were taken of the products. The sample $Nd_{1.8}Fe_{0.2}(FeSb)O_7$ was successfully formed and confirmed to be single phase. For the compound $Pr_{1.8}Fe_{0.2}(FeSb)O_7$ a pyrochlore phase was formed which

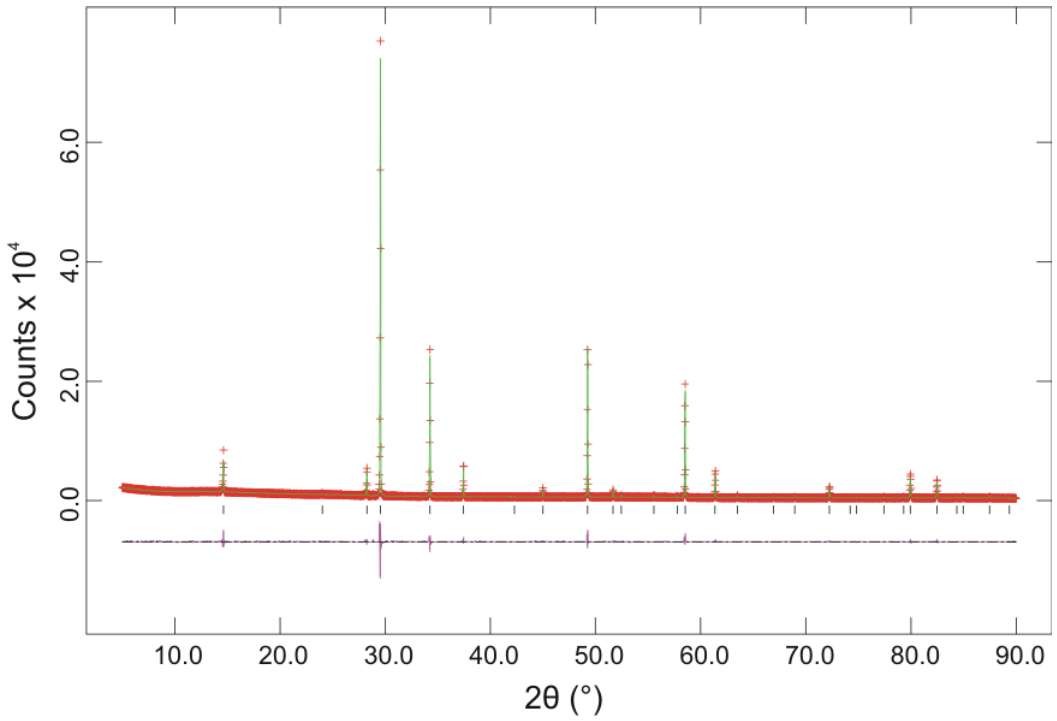

(a)

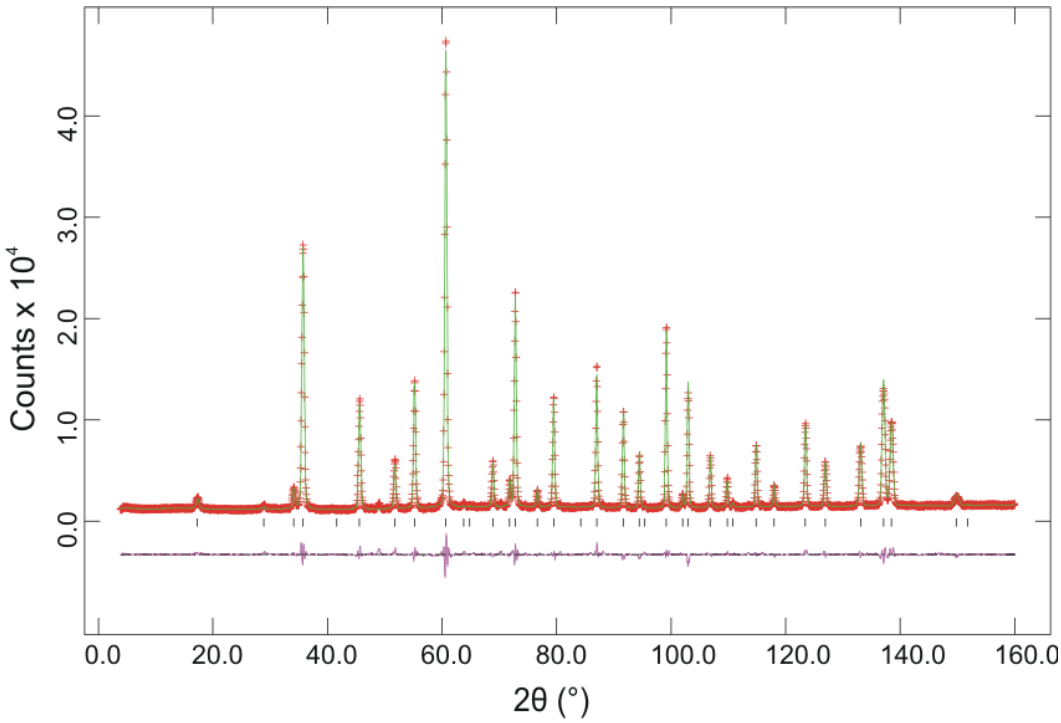

(b)

***Fig. 6.4**: Observed, calculated and difference plots obtained from a joint refinement based on XRPD and NPD data for $Bi_{1.8}Fe_{0.2}(FeSb)O_7$ at 300 K: (a) XRPD (b) NPD.*

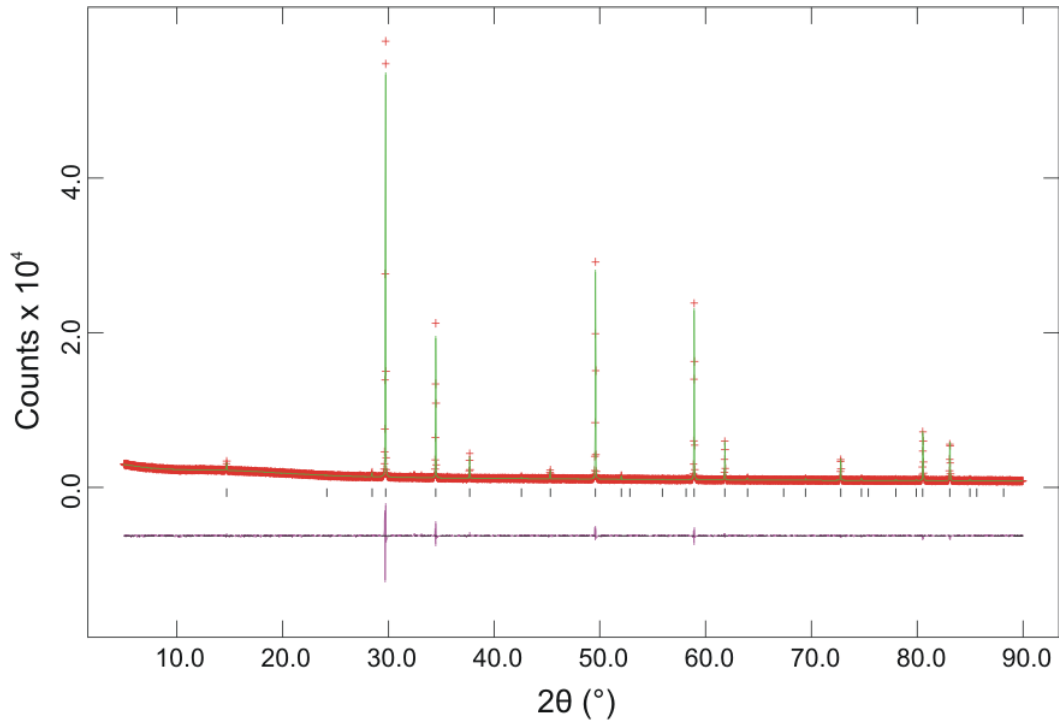

(a)

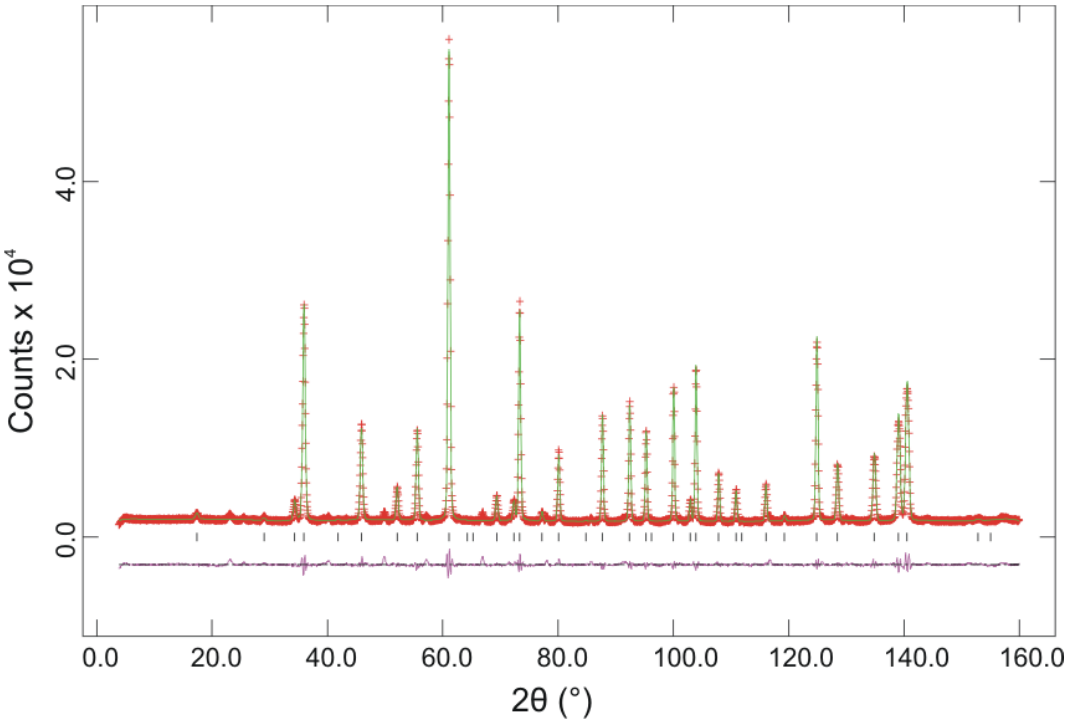

(b)

***Fig. 6.5**: Observed, calculated and difference plots obtained from a joint refinement based on XRPD and NPD data for $Nd_{1.8}Fe_{0.2}(FeSb)O_7$ at 300 K: (a) XRPD (b) NPD.*

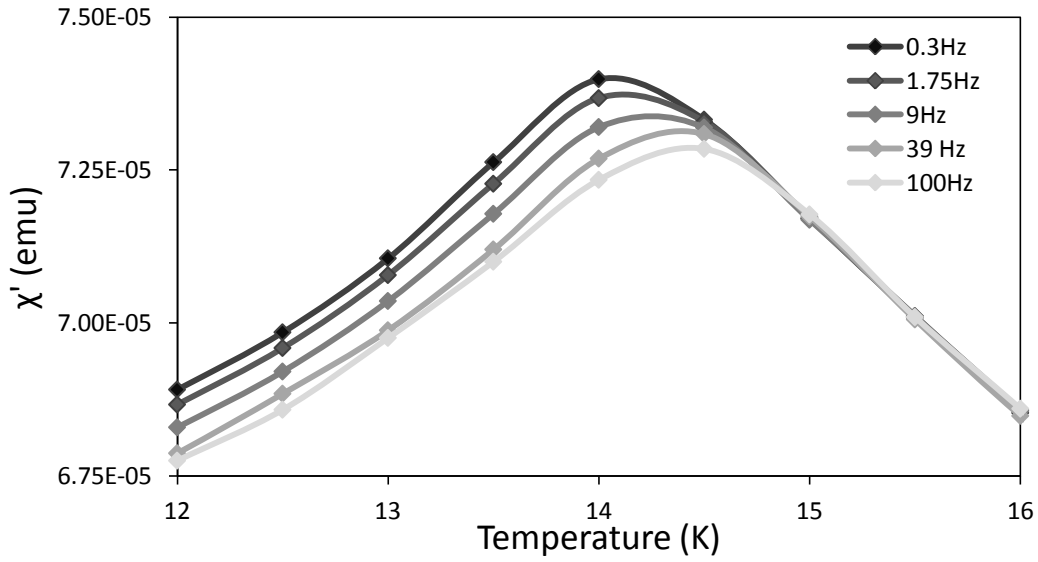

***Fig. 6.8**: Real part of the AC susceptibility, χ', as a function of temperature for different frequencies for $Bi_{1.7}Fe_{0.3}(FeSb)O_7$.*

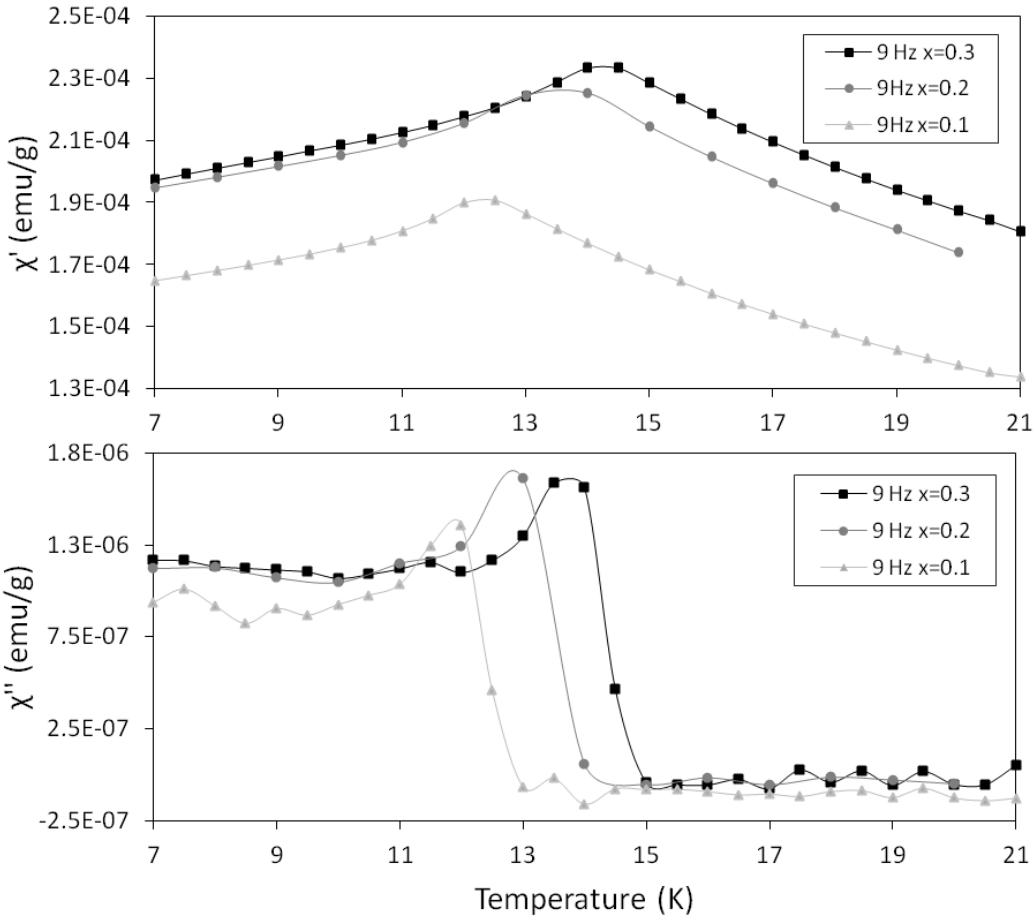

***Fig. 6.9**: Real part of the AC susceptibility, χ', (above) and imaginary part of the AC susceptibility, χ'', (below) at 9 Hz for $Bi_{2-x}Fe_x(FeSb)O_7$.*

7 Magnetic Properties of RE_2CrSbO_7 Pyrochlores

7.1 Background

As mentioned in Section 1.5.3, the A and B ions in the pyrochlore structure form two interlinking lattices of A_4 and B_4 tetrahedra (Fig. 7.1) and if these ions are magnetic this can give highly-frustrated systems and unusual magnetic properties.

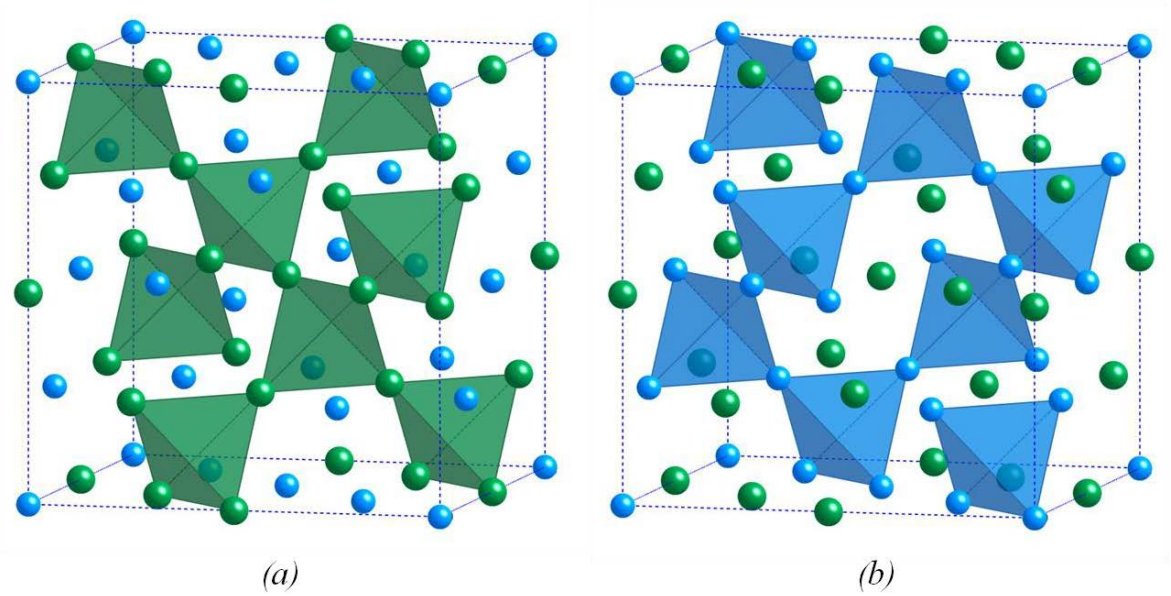

***Fig. 7.1**: The pyrochlore structure showing the A- and B-cations only. The tetrahedral arrangement of (a) A-cations (green) and (b) B-cations (blue) is shown.*

One of the more unusual types of magnetic behaviour observed in some pyrochlore materials is the spin-ice magnetic state which was first discovered for the pyrochlore $Ho_2Ti_2O_7$.[1] In a spin-ice pyrochlore the magnetic moments are constrained to lie along the ⟨111⟩ directions: either pointing in to or out from the centre of a given tetrahedron (Fig. 7.2a).[2] For each tetrahedron, two spins point in and two spins point out, and each tetrahedron has an overall ferromagnetic moment. However, as the *x*, *y* and *z* directions are equivalent in a cubic structure there is no preferred direction for the moments to align themselves in unless a magnetic field is applied.[2] This gives a disordered structure with the moments on neighbouring tetrahedra pointing in different directions while obeying the

two-in, two-out condition. Spin-ice materials therefore have many degenerate ground states which prevents a long-range ordered structure from forming[2]. This type of magnetic behaviour is known as spin-ice because it is analogous to the ordering of protons in hexagonal water ice.[3] Each oxygen ion is tetrahedrally surrounded by four hydrogen ions and forms two short and two long O-H bonds (Fig. 7.2b). Hexagonal water ice and spin-ice pyrochlores both have similar disordered ground states and residual entropies at extremely low temperatures.[2] So far only the pyrochlores $Ho_2Ti_2O_7$,[1] $Dy_2Ti_2O_7$ [4] and $Ho_2Sn_2O_7$ [5] have been confirmed to be spin-ices. The spin-ice pyrochlores are of interest because their structure has been suggested as a host for magnetic monopoles[6].

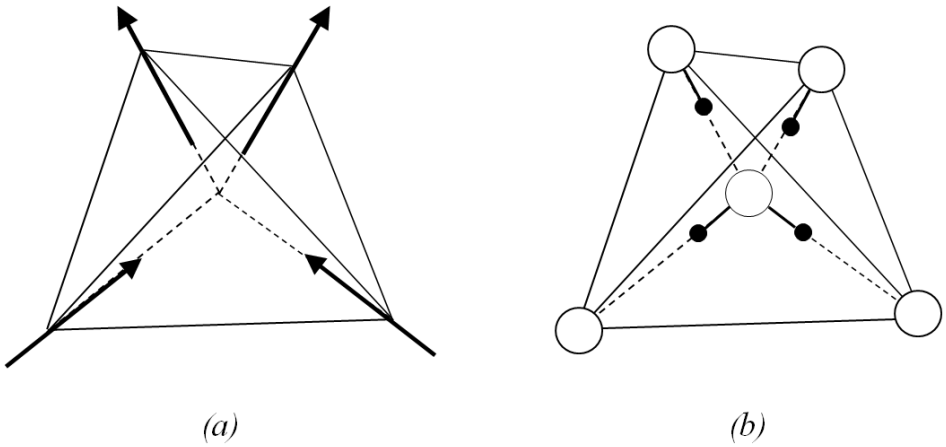

Fig. 7.2*: (a) The arrangement of magnetic spins for a given tetrahedron in a spin-ice pyrochlore structure; (b) the arrangement of hydrogen ions in water ice: oxygen ions are shown as large white spheres and hydrogen ions are shown as small black spheres.*

Pyrochlores which form long-range ordered magnetic states despite the inherent geometric frustration are also of interest, and in a previous study of magnetic rare earth pyrochlores the compounds Ho_2CrSbO_7 and Dy_2CrSbO_7 were shown to be ferromagnetic below 10 K and 16 K respectively[7]. The magnetic susceptibility and magnetisation of the pyrochlores RE_2CrSbO_7 (where RE = Y, Pr, Nd, Sm, Eu, Gd, Tb, Dy, Ho, Er, Tm and Yb) were measured and all the compounds were found to have positive Weiss temperatures, θ, between +4 and +16 K indicative of ferromagnetic interactions.[7] These pyrochlores

***Table 7.3**: Parameters refined from NPD data recorded from Ho_2CrSbO_7 at 300 K, 50 K and 2 K*

	300 K	50 K	2 K
a (Å)	10.1739(3)	10.1668(3)	10.1648(1)
volume (Å³)	1053.08(8)	1050.89(8)	1050.26(5)
O1 *x*	0.3318(1)	0.3323(1)	0.3324(1)
Cr occupancy	0.44(3)	0.43(3)	0.51(3)
Sb occupancy	0.56(3)	0.57(3)	0.49(3)
Ho U_{iso} (Å²)	0.0089(4)	0.0059(4)	0.0046(4)
Cr/Sb U_{iso} (Å²)	0.0042(8)	0.0008(8)	0.003(1)
O1 U_{iso} (Å²)	0.0063(3)	0.0030(3)	0.0033(3)
O2 U_{iso} (Å²)	0.0052(9)	0.001(1)	0.006(1)
Ho-O1 (Å) x 6	2.4822(7)	2.4777(7)	2.4761(7)
Ho-O2 (Å) x 2	2.20271(4)	2.20119(4)	2.20074(2)
Cr/Sb-O1 (Å) x 6	1.9819(4)	1.9823(4)	1.9825(5)
χ^2	1.924	2.323	2.979
R_{wp}, R_F^2	0.040, 0.039	0.032, 0.029	0.042, 0.020

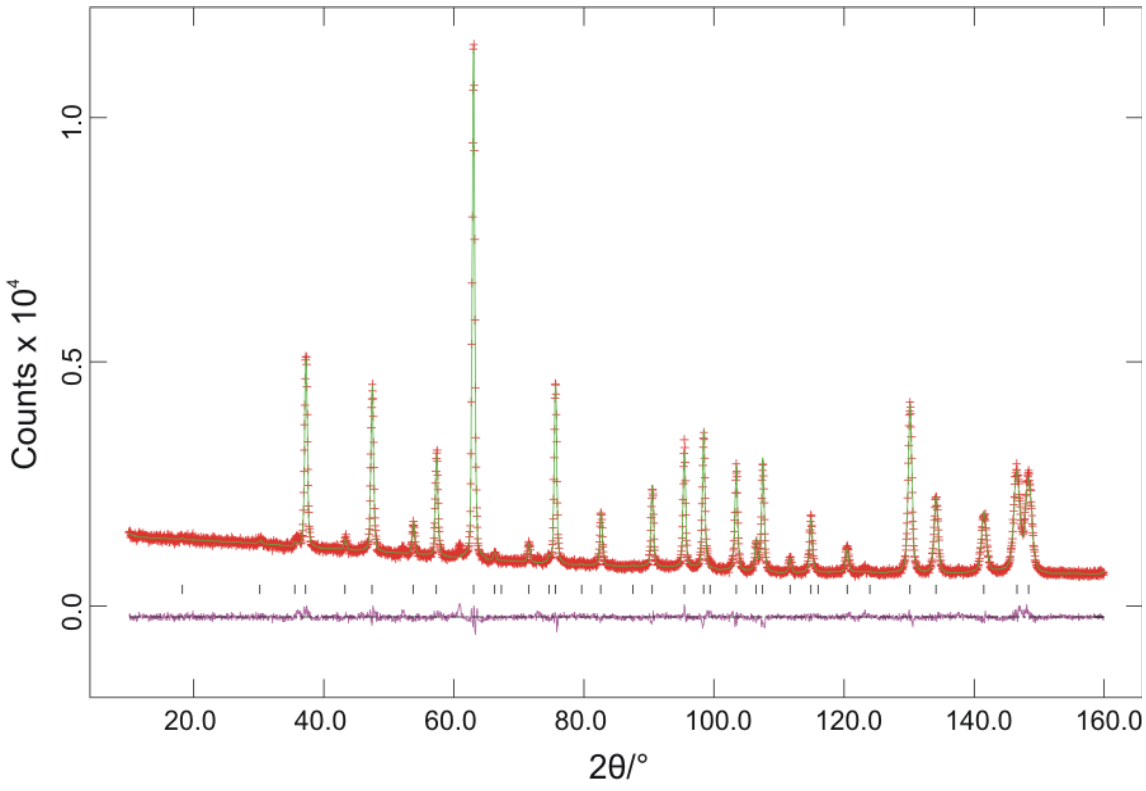

***Fig. 7.8**: Observed, calculated and difference plots for NPD data recorded from Ho_2CrSbO_7 at 300 K.*

RE_2CrSbO_7 samples between 140 and 160 K and only data collected above these temperatures were used for the Curie-Weiss plot. Initially it was thought that the transition may correspond to high temperature ferromagnetic ordering of the Cr^{3+} moments which is overshadowed in the susceptibility data by the large Ln^{3+} magnetic moments, but the transition is also masked in the susceptibility data for Y_2CrSbO_7 and calculations of the ferromagnetic upturn in Ho_2CrSbO_7 gave a value of 2.2 x 10^{-3} μ_B per Cr^{3+} ion. The moment is much smaller than would be expected for a ferromagnetic arrangement of Cr^{3+} ions and a canted antiferromagnetic state with a small net moment was considered. However FM ordering of Cr^{3+} ions was observed in the NPD data at 2 K (discussed later) and spin reorientation under the influence of the strong ferromagnetic Ho moment would not be energetically possible at this temperature. It is therefore likely that the transition is due to the small impurity phases present rather than the bulk sample.

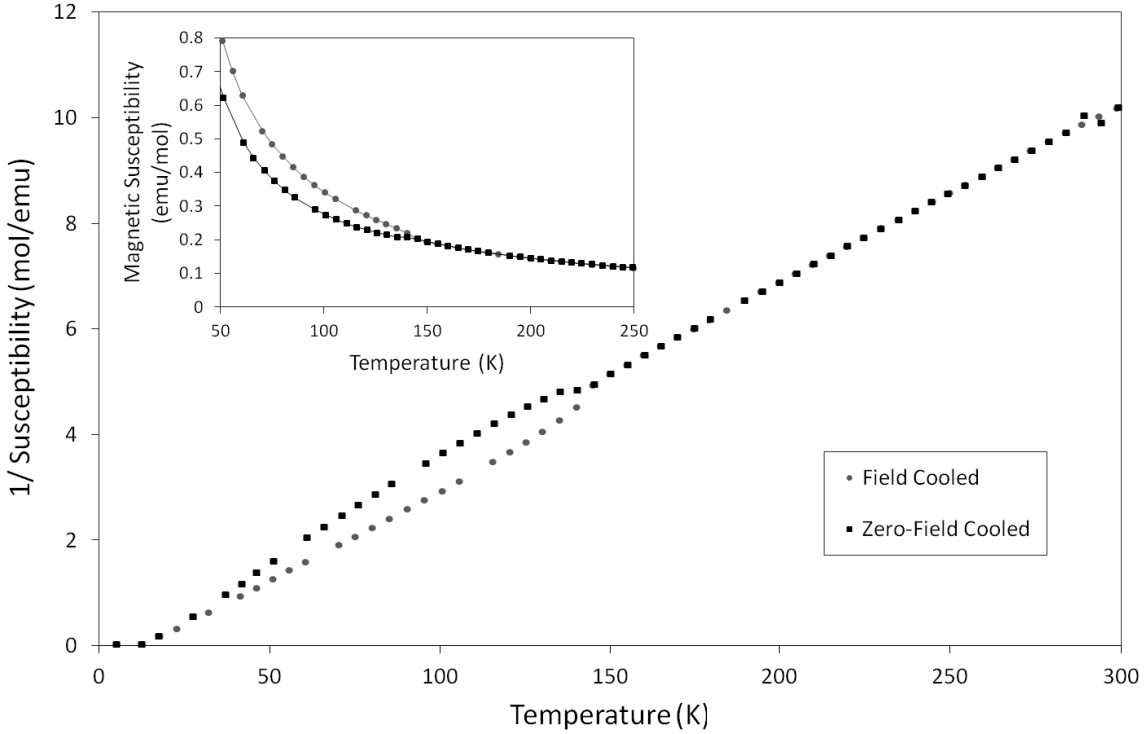

***Fig. 7.12**: Inverse susceptibility data for Ho_2CrSbO_7 showing 145 K anomaly. Inset shows variation of magnetic susceptibility with temperature for Ho_2CrSbO_7 between 50 and 250 K.*

Higher temperature transitions where the FC and ZFC plots diverge were seen for the mixed Cr/Fe samples (x = 0.25, 0.5 and 0.75) as they were for RE_2CrSbO_7. However unlike these samples, where the ordering temperatures corresponded to that of the $RECrO_3$ impurity phases, the transition temperature changes as the Cr:Fe ratio is altered. Transition temperatures of 73 K, 145 K and 180 K were seen for the samples $Ho_2Cr_{0.25}Fe_{0.75}SbO_7$, $Ho_2Cr_{0.5}Fe_{0.5}SbO_7$ and $Ho_2Cr_{0.75}Fe_{0.25}SbO_7$ respectively. The nature of the transitions in these samples is uncertain and to investigate this further additional data such as neutron powder diffraction would be needed. As mentioned above NPD measurements were recorded from one of the pyrochlore samples, Ho_2CrSbO_7, at 300 K, 50 K and 2 K but this material shows no signs of magnetic ordering at 50 K.

A Rietveld refinement of the NPD data collected at 2 K from Ho_2CrSbO_7 is shown in Fig. 7.15. This can be compared to the room temperature data shown in Fig. 7.8.

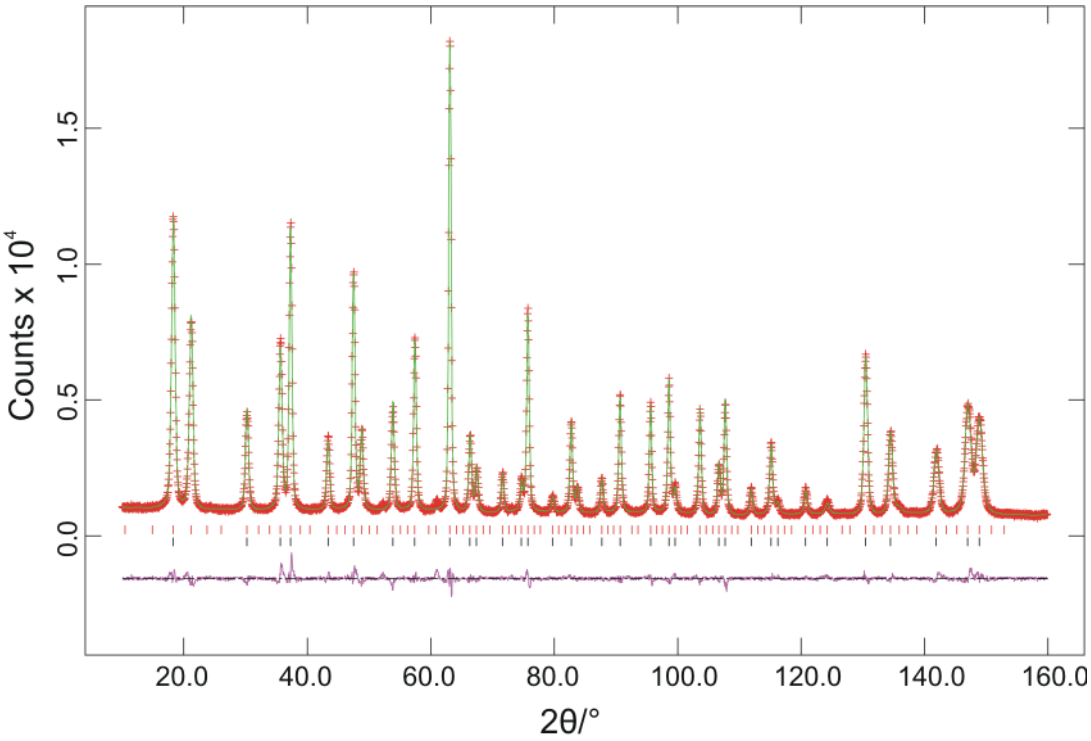

***Fig. 7.15**: Observed, calculated and difference plots for NPD data recorded from Ho_2CrSbO_7 at 2 K.*

direction for the Ho^{3+} moments to align themselves with. The ordered spin-ice structure is shown in Fig. 7.17. This would explain why the material shows rare earth magnetic ordering at a relatively high temperature for a pyrochlore. This is similar to the effect seen in $Er_2Ru_2O_7$ where it was suggested that the increased ordering temperature of the Er^{3+} ions was due to the high temperature Ru^{4+} ordering[18].

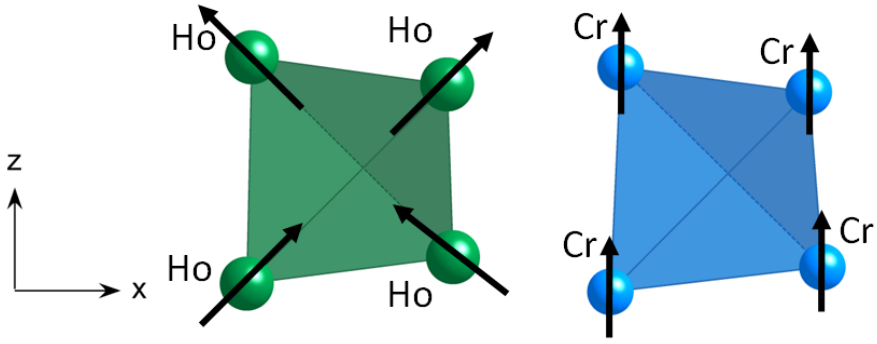

***Fig. 7.16**: Representations of the magnetic structure of Ho_2CrSbO_7 showing the arrangement of magnetic moments on single Ho and Cr tetrahedra. The Ho^{3+} moments are pointing in and out from the centre of the tetrahedron along the ⟨111⟩ axis and the Cr^{3+} ions lie solely along the z-axis.*

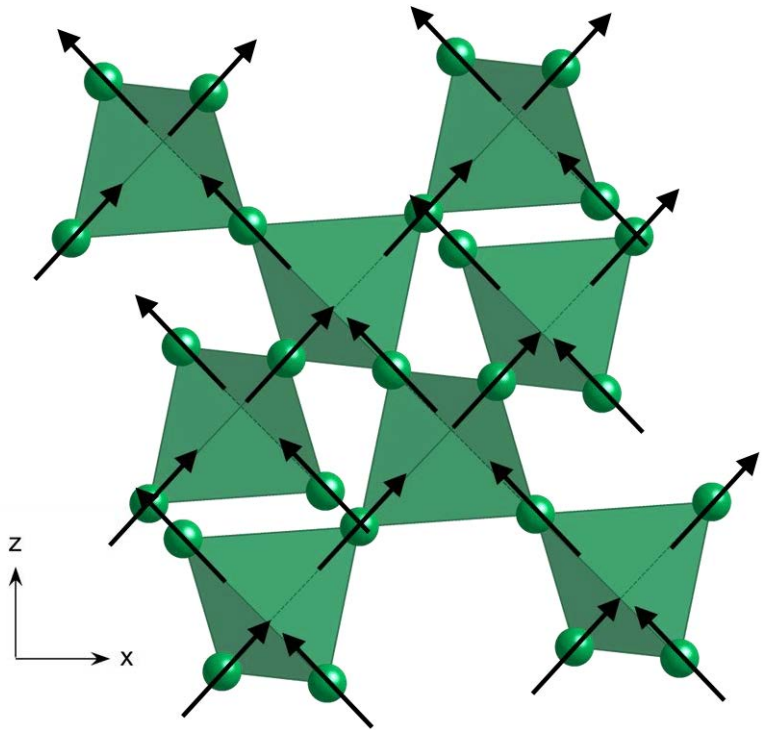

***Fig. 7.17**: Ordered spin-ice structure of Ho_2CrSbO_7 showing only the Ho_4 tetrahedra. The Ho^{3+} moments are pointing in to and out from the centre of the tetrahedron along the ⟨111⟩ axis with the ferromagnetic component aligned along the z-axis.*